ANL-GenIV-179

Generation IV Nuclear Energy System Initiative. Air-Cooled Option RCCS Studies and NSTF Preparation

Nuclear Engineering Division

About Argonne National Laboratory

Argonne is a U.S. Department of Energy laboratory managed by UChicago Argonne, LLC under contract DE-AC02-06CH11357. The Laboratory's main facility is outside Chicago, at 9700 South Cass Avenue, Argonne, Illinois 60439. For information about Argonne and its pioneering science and technology programs, see www.anl.gov.

Availability of This Report

This report is available, at no cost, at http://www.osti.gov/bridge. It is also available on paper to the U.S. Department of Energy and its contractors, for a processing fee, from:

U.S. Department of Energy
Office of Scientific and Technical Information
P.O. Box 62
Oak Ridge, TN 37831-0062
phone (865) 576-8401
fax (865) 576-5728
reports@adonis.osti.gov

Disclaimer

This report was prepared as an account of work sponsored by an agency of the United States Government. Neither the United States Government nor any agency thereof, nor UChicago Argonne, LLC, nor any of their employees or officers, makes any warranty, express or implied, or assumes any legal liability or responsibility for the accuracy, completeness, or usefulness of any information, apparatus, product, or process disclosed, or represents that its use would not infringe privately owned rights. Reference herein to any specific commercial product, process, or service by trade name, trademark, manufacturer, or otherwise, does not necessarily constitute or imply its endorsement, recommendation, or favoring by the United States Government or any agency thereof. The views and opinions of document authors expressed herein do not necessarily state or reflect those of the United States Government or any agency thereof, Argonne National Laboratory, or UChicago Argonne, LLC.

ANL-GenIV-179

Generation IV Nuclear Energy System Initiative. Air-Cooled Option RCCS Studies and NSTF Preparation

prepared by
S. Lomperski, W. D. Pointer, C. P. Tzanos, T. Y. C. Wei, A. R. Krauss
Nuclear Engineering Division, Argonne National Laboratory

September 2011

Executive Summary

The Reactor Cavity Cooling System (RCCS) is an important system to the passive safety case being incorporated in the overall safety strategy for the Next Generation Nuclear Plant (NGNP). The RCCS will be one of the new safety systems specifically designed for the next generation of nuclear power plants. In particular, it is being developed and incorporated into the proposed reactor and plant designs for the very high temperature reactor (VHTR)—a helium gas-cooled nuclear plant with a thermal-spectrum reactor. The RCCS forms a passive heat sink external to the reactor, and is located within the reactor cavity/silo surrounding the metal vessel. During emergency accident conditions when all ac (alternating current) power is lost, natural convection of the RCCS coolant removes the heat radiated or naturally convected from the metal vessel wall to the inner boundary of the RCCS facing the vessel. RCCS will be a first-of-a-kind (FOAK) passive safety system for core decay heat removal when the FOAK VHTR is built.

The work documented in this report is a follow-on to the FY 2010 work reported on the air-cooled RCCS design of the General Atomics (GA) Modular High Temperature Gas-cooled Reactor (MHTGR). This workscope focused on confirming the scaling laws selected to design the scaled experiments in the large-scale Argonne National Laboratory (ANL) Natural Convection Shutdown Heat Removal Test Facility (NSTF) and on sensitivity studies to evaluate the effect of the modeling approximations made in FY 2010 on the models developed for the experiment design supporting analysis. In addition design support analyses were performed to evaluate NSTF configuration modifications proposed to enhance instrumentation performance.

The objectives were to: (a) update and confirm the scaling relations to be used in modifying the existing NSTF facility into a scaled model of the GA-MHTGR air-cooled RCCS; and (b) provide an analytical basis for the NSTF modifications needed to conduct scaled experimental simulations of this RCCS. In summary, the scaling evaluation updated the basis that the air-cooled RCCS can be simulated at the ANL NSTF facility at a prototypic scale in the lateral direction and about half scale in the vertical direction. The density behavior of air was modified. A parallel track approach was taken with both RELAP5 system evaluations and STAR-CCM+ computational fluid dynamic (CFD) evaluations carried out as the set of instrumentation configurations were detailed.

Three groups of RELAP5 models were used: Full-Scale GA–MHTGR, Half-Scale GA-MHTGR, and NSTF experiment configuration. It is clear from the nondimensional analyses that all similarity conditions cannot be satisfied. Since, by necessity, the scaling is based on a number of approximations, and because no information is available on the performance of a reference air-cooled RCCS, the scaling laws selected need to be validated by analysis of the steady-state and transient performance of the reference air-cooled RCCS design. The analyses performed with the RELAP5 full-scale and half-scale models confirm that the magnitude of distortions imposed by the similarity conditions that are not satisfied are minimal. A model of the planned NSTF experiment initial configuration is also in place. The full-scale model was used to test the response of the system to heat fluxes at 10 and 5 kW/m^2. The heat flux of 5.0kW/m^2 represents the reference reactor case of medium heat flux. The high heat flux case corresponds to the system model with 10 kW/m^2. It should be emphasized that these are uniform heat fluxes applied at the reactor vessel outer surface over the heated height. The half-scale model was then run at

the corresponding scaled heat fluxes with the appropriate riser orifice loss coefficient. The results show quantitative agreement with the scaling analysis in terms of preservation of riser air outlet temperatures. The riser air outlet temperatures of the full-scale cases agree with the corresponding temperatures of the half-scale cases. The NSTF experiment configuration model was then used to conduct cases at various internal power generation levels. These power levels produce the proportionally full-scaled heat fluxes previously used. A number of experiment cross section configurations are under discussion but, in this report, the RELAP5 model involves varying the separation distance between the heated surface of the box and the hot risers so that the test cavity box depth varies from 18 in. (45.7 cm) to 46 in. (116.8 cm) . The model was used to examine the relative effect of the intraduct radiation and conduction. Radiation dominates.

RANS-based simulations of natural convection and radiation heat transport have been completed using the CFD code STARCCM+ to support the definition of the instrumentation layout. Previous CFD studies show that large-scale flow structures in mixing plena and chimney structures are also preserved in the NSTF baseline design. Improvements have been proposed to the NSTF configuration that should enhance conduct of the series of experiments used to evaluate the performance of an air-cooled RCCS with quality data instrumentation. The proposed baseline design of the modified NSTF test section has been shown to maintain key scaling parameters related to natural convective flow and thermal mixing. The additional CFD analyses described in this FY 2011 report provide a preliminary solution verification study to assess the uncertainty in the baseline simulations as well as evaluate the impact of alternative design options that may be considered to simplify instrumentation access or to better represent anticipated RCCS system design.

The initial baseline STAR-CCM+ CFD simulations for the air-cooled RCCS and the related NSTF experiments previously showed that the proposed NSTF design duplicates the major flow features of the anticipated RCCS design. An initial series of solution verification studies have been completed for the NSTF analyses in order to begin to quantify the uncertainty in predicted quantities of interest as a result of mesh size and modeling options. Building on this foundational work, a series of design studies have been completed to evaluate potential design options, the most promising of which have been presented. Future work will focus on the application of more realistic thermal boundary conditions for selected cases and on unsteady simulations to evaluate the stability of the natural convection flow field.

The four design cases considered are:

- Nominal geometry
- Extension of the risers through the floor of the outlet plenum by 25 cm to allow for instrumentation access
- Raised outlet plenum floor and the addition of an unheated extension of the risers between the cavity and the outlet plenum to allow for instrumentation access and better agreement with jet penetration scaling parameters.
- A modification of the raised outlet plenum model with a substantially extended inlet pipe length for improved inlet flow stability and instrumentation access.

The STAR-CCM+ results show that all four cases retain the primary flow features of the anticipated RCCS design. The introduction of extended risers to support instrumentation access

does not dramatically alter the parallel riser flows. The use of a reduced-height outlet plenum does impact the riser jet penetration and the rotational flow that develops in the plenum volume and may be an attractive option for better representing the outlet plenum flow, if desired. The extended inlet provides better inlet flow conditioning and improves the rate of simulation convergence.

As more detailed instrumentation plans for the facility have evolved, several design adaptations have been suggested to simplify placement and maintenance of instrumentation. These modifications include the addition of unheated extensions at the outlet of the riser ducts and the extension of the length of the test section inlet by several diameters. Design variations have also been suggested as a consequence of additional scaling studies examining the physical phenomena associated with the outlet plenum and piping. Three alternate designs that address these concerns are considered in this report. An evaluation of corresponding instrumentation alternatives has been carried out. A characterization of gas velocities, temperatures, and heat fluxes with the cavity and risers is desired for comparison with code simulations. Laser Doppler Velocimetry (LDV) was evaluated as a candidate in FY 2010 for local velocity and turbulence measurements. The FY 2011 focus was on bulk flow and temperature measurements.

Both the duct and stack measurements will be made with instruments positioned downstream and closer to their outlets than inlets. It is not possible to make reliable flow measurements near the test section inlet because entrance lengths are far too short. Sensors near the inlet might be able to provide indications of relative flow, such as balance between the two main inlets, but local flow patterns are likely to be unstable and so even that may not be reliable. Refraining from inlet measurements means sensors must operate at elevated rather than ambient temperature, which is more difficult and generally less accurate, but it is necessary in order to provide the instruments adequate entrance length.

LDV is normally used in open systems and forced circulation loops with either naturally suspended particles or flows that are easily seeded artificially. Without such particles to reflect light, there is no signal for the LDV to process. Measurements in the closed cavity would be problematic since they require periodic seeding injections followed by a waiting period for reestablishment of natural circulation patterns. Particles may not remain suspended long enough for high quality measurements. Perhaps more critical is the change in surface emissivity that is likely to accompany the use of seeding particles. Oils are the most promising seeding candidates as they generate strong signals, but extensive use is likely to result in a thin coating of oil over all of the cavity surfaces. LDV is more feasible for measurements within the upper plenum. Seeding can be added at the bottom end of the ducts to be swept along up towards the upper plenum, where windows allow access for the laser beams. The inner surfaces of the ducts, upper plenum, and eventually the stacks will be coated with oil, but their emissivities should have little influence on gross heat transfer, which is primarily conductive and convective.

Table of Contents

Executive Summary iii
Acronyms & Nomenclature xiii
1.0 Introduction 1
1.1 GA-MHTGR RCCS Design 2
1.2 NSTF RCCS Experiment Scaling 4
1.2.1 Top-down Scaling 4
1.2.2 Loop Steady State 4
1.2.3 Loop Transient 8
1.2.4 Cavity Steady State 11
1.3 Top-Down Scaling Laws 13
1.3.1 Baseline Scaling 13
1.3.2 Time Number Scaling 17
1.3.3 Alternate Time Number Scaling 18
1.3.4 Stanton Numbering Scaling 19
1.3.5 Cavity Scaling 20
1.4 Bottom-Up Scaling 22
1.5 Study Approach 23
References 28
2.0 Air Heat Sink System Analyses 29
2.1 RCCS Design View Factors 29
2.1.1 Reactor-Scale Geometry: Cavity 29
2.1.2 Experiment Geometry: IntraDuct 34
2.2 RELAP5 Modeling 35
2.2.1 Full-Scale Model 36
2.2.2 Half-Scale Model 36
2.2.3 1 Channel NSTF Model 36
2.2.4 2 Channel NSTF Model 39
2.3 Full/Half RCCS Model RELAP5 Results 41
2.3.1 Full-Scale Axial Power Variation 44
2.3.2 Full-Scale Isothermal Forced-Flow 50
2.3.3 Full-Scale Duct-Radiation 53
2.3.4 Full-Scale Axial Power-Variation/Duct Radiation 55
2.3.5 Half-Scale Isothermal Forced-Flow 8.8-J1574 55
2.3.6 Half-Scale 8.8-J1574 Duct-Conduction 59
2.3.7 Half-Scale 8.8-J1576 Duct-Radiation 66
2.4 NSTF Experiment RELAP5 Results 66
2.4.1 1 Channel NSTF Isothermal Forced-Flow 66
2.4.2 1 Channel NSTF Duct-Radiation 68
2.4.3 2 Channel NSTF 46″ (116.84 cm) x 52″(132.08) 73
2.4.4 2 Channel NSTF 46″ (116.84 cm) x 52″ (132.08) Emissivity Change 80
2.4.5 2 Channel NSTF 46″ (116.84 cm) x 52″ (132.08) Duct Radiation 85
2.5 Conclusions 85

References 86
3.0 Air-Cooled RCCS CFD Analysis 87
3.1 Motivation and Objective 87
3.2 Air-Cooled RCCS System Geometry 87
3.3 NSTF Baseline Geometry 87
3.4 Simulation Methodology 89
3.5 NSTF Baseline CFD Model 90
3.6 NSTF Baseline Results 91
3.7 Mesh Sensitivity Study Results 96
3.8 Turbulence Model Sensitivity Results 96
3.9 NSTF Design Studies 101
3.9.1 Extended Riser Length 101
3.9.2 Extended Riser with Reduced-Height Plenum 105
3.9.3 Extended Vertical Inlet 107
3.10 Summary and Future Work 111
References 111
4.0 Instrumentation 112
4.1 Temperature 112
4.2 Flow Rate 115
4.3 Heater Power 119
4.4 Heat Flux 120
4.5 Meteorological Data 123
4.6 Data Acquisition and Control 123
References 123

List of Figures

1.1 Overall System View of the GA-MHTGR RCCS 2
1.2 View of Ex-Cavity RCCS Outer Cold Duct/Inner Hot Duct Run 3
1.3 Cavity Isometric View of Reactor Vessel and RCCS 3
1.4 Cavity Plane View of Reactor Vessel and RCCS 3
2.1 Experiment Cross Section 30
2.2 Two-Group Experiment View Factors with Riser Ducts 31
2.3 One-Group Experiment View Factors with Riser Ducts 32
2.4 Riser Duct Cross Section 34
2.5 Full-Scale Model Cavity and Duct Network 37
2.6 Half-Scale Model Cavity and Duct Network 38
2.7 Experiment 1-Channel System Model Cavity and Duct Network 39
2.8 Experiment 2-Channel System Model Cavity and Duct Network 40
2.9 Full Scale/Medium Flux Reactor Vessel Wall Heat Flux 44
2.10 Full Scale/Medium Flux Riser Duct Air Total Mass Flow 45
2.11 Full Scale/Medium Flux Hot Network Air Mass Flow 45
2.12 Full Scale/Medium Flux Riser Duct Air Velocity 46
2.13 Full Scale/Medium Hot Network Air Velocity 46
2.14 Full Scale/Medium Flux RPV Temperature 47
2.15 Full-Scale/Medium Flux Cavity Back Liner Temperature 48

2.16 Full-Scale/Medium Flux Riser Duct Temperatures 49
2.17 Full Scale/Isothermal Forced-Flow Network Air Mass Flow 50
2.18 Full Sacle/Isothermal Forced-Flow Hot Network Air Velocity 51
2.19 Full Scale/Isothermal Forced-Flow Riser Pressure Drops 52
2.20 Full Scale/High Flux Riser Duct Temperature 54
2.21 Full Scale/Medium Flux Hot Network Air Mass Flow 56
2.22 Half-Scale Isothermal Various Junction Wall Friction and Form Loss Pressure Drops (ΔP) 57
2.23 Half-Scale Isothermal Various Junction Elevation Change Pressure Drops (ΔP) 58
2.24 Half-Scale/High Flux Riser Duct Air Total Mass Flow 60
2.25 Half Scale/High Flux Hot Network Air Mass Flow 60
2.26 Half Scale/High Flux Riser Duct Air Velocity 61
2.27 Half Scale/High Flux Hot Network Air Velocity 61
2.28 Half Scale/High Flux RPV Temperature 62
2.29 Half Scale/High Flux Cavity Back Liner Temperature 62
2.30 Half Scale/High Flux Riser Duct Temperatures 63
2.31 Half Scale Conduction Case of Various Junction Wall Friction and For Loss Pressure Drops (ΔP) 64
2.32 Half Scale Conduction Case of Various Junction Elevation Change Pressure Drops (ΔP) 65
2.33 1 Channel NSTF with Radiation Riser Duct Air Total Mass Flow 69
2.34 1 Channel NSTF with Radiation Riser Duct Air Velocity 69
2.35 1 Channel NSTF with Radiation Chimney Air Velocity 70
2.36 1 Channel NSTF with Radiation Heated Wall Temperature 70
2.37 1 Channel NSTF with Radiation Back Wall Liner Temperature 71
2.38 1 Channel NSTF with Radiation Riser Duct Temperatures 72
2.39 2 Channel NSTF 46″ (116.84 cm) x52″ (132.08 cm) Heated Temperature 74
2.40 2 Channel NSTF 46″ (116.84 cm) x52″ (132.08 cm) Cavity Side Liner Temperature 74
2.41 2 Channel NSTF 46″ (116.84 cm) x52″ (132.08 cm) Cavity Back Liner Temperature 75
2.42 2 Channel NSTF 46″ (116.84 cm) x52″ (132.08 cm) Mass Flow Rates 76
2.43 2 Channel NSTF 46″ (116.84 cm) x52″ (132.08 cm) Velocities 77
2.44 2 Channel NSTF 46″ (116.84 cm) x52″ (132.08 cm) Riser Inner Duct Temperatures 78
2.45 2 Channel NSTF 46″ (116.84 cm) x52″ (132.08 cm) Riser Outer Duct Temperatures 79
2.46 2 Channel NSTF Emissivity Change Cavity Side Wall Temperature 81
2.47 2 Channel NSTF Emissivity Change Cavity Side Liner Temperature 81
2.48 2 Channel NSTF Emissivity Change Cavity Back Liner Temperature 82
2.49 2 Channel NSTF Emissivity Change Riser Inner Duct Temperatures 83
2.50 2 Channel NSTF Emissivity Change Riser Outer Duct Temperatures 84
3.1 Complete RCCS Model 88
3.2 Full RCCS Slide Cut Away View 88
3.3 CAD Image Showing the Simplified CFD Model of the NSTF Air-Cooled RCCS Experiment 89
3.4 Mesh Distribution in Riser Cross-section 90
3.5 Residual Values Monitored over 15,000 Iterations for Baseline NSTF Simulation 91
3.6 Predicted Temperature Profiles at Riser Outlet for Baseline Model 92
3.7 Predicted Velocity Magnitude Profiles in Risers for Baseline Model 93

3.8 Extracted Scalar Profiles along a Line from Front to Back of Each Riser 94
3.9 Velocity Profiles in a Vertical Cross-section of the Outlet Plenum 94
3.10 Out-of-plane Velocity Profiles in a Horizontal Cross-section of the Outlet Plenum and Piping 95
3.11 Chimney Flow Temperature and Velocity Profiles 95
3.12 Out-of-plane Velocity Profiles in a Horizontal Cross-section of the Outlet Plenum and Piping from Simulations using Two Alternate Mesh Sizes 97
3.13 Comparison of Predicted Velocity Profiles at the Outlet of a Central Riser along a Line from the Front Surface to the Back 98
3.14 Comparison of Predicted Velocity Profiles at the Outlet of a Central Riser along a Line from the Front Surface to the Back 98
3.15 Predicted Velocity Profiles 25 cm Downstream of the Inlet along a Line from Front to Back of Each Riser for Simulations using Two Different Turbulence Models 99
3.16 Comparison of Temperature Profiles at the Outlet of the 6th Riser Duct for Simulations using Two Turbulence Models 100
3.17 Comparison of Velocity Magnitude Profiles at the Outlet of the 6th Riser Duct for Simulations using Two Turbulence Models 100
3.18 (a) Perspective view and (b) Detail view images of the Modified NSTF System Geometry with Unheated Riser Extensions Protruding into the Outlet Plenum 100
3.19 Residual Values Monitored over 12,000 Iterations for Alternative NSTF Geometry with Extended Riser Ducts 102
3.20 Predicted Velocity Magnitude Profiles in Risers for Extended Riser Model 103
3.21 Velocity Profiles in a Vertical Cross-section of the Outlet Plenum for the Extended Riser Case 103
3.22 Out-of-plane Velocity Profiles in a Horizontal Cross-section of the Outlet Plenum and Piping for the Extended Riser Case 104
3.23 Comparison of the Two Parametric Models used in Evaluation of Impact of Upper Hot Plenum Design: (a) baseline and (b) raised lower surface of the Upper Hot Plenum, Reducing the Hot Plenum Volume to 0.707 Times the Baseline Height 104
3.24 Residual Values Monitored over 10000 Iterations for Alternative NSTF Geometry with Reduced-height Outlet Plenum 105
3.25 Predicted Velocity Magnitude Profile in Risers for the Reduced-height Outlet Plenum Model 106
3.26 Velocity Profiles in a Vertical Cross-section of the Outlet Plenum for Reduced-height Outlet Plenum Case 106
3.27 Out-of-plane Velocity Profiles in a Horizontal Cross-section of the Outlet Plenum and Piping for the Reduced-height Outlet Plenum Case 107
3.28 Modified Geometry with Extended Vertical Inlet 107
3.29 Residual values Monitored over 8900 Iterations for Alternative NSTF Geometry with an Extended Vertical Inlet 108
3.30 Predicted Velocity Magnitude Profile in the Extended Vertical Inlet Case 109
3.31 Extracted Scalar Profiles along a Line from Front to Back of each Riser for the Extended Vertical Inlet Case 110

3.32 Out-of-plane Velocity Profiles in a Horizontal Cross-section of the Outlet Plenum and Piping for the Reduced-height Outlet Plenum Case 110
4.1 Surface Temperature and Heater Control Thermocouples on Heated Walls....112
4.2 Surface Temperature Thermocouples and Heat Flux Meters on Unheated Walls....113
4.3 Surface Temperature Thermocouple Installation....115
4.4 Estimated Stack Velocity and Temperature at Six Operating Points for Low, Medium, and High Heat Flux....116
4.5 The ΔP-based Rosemount Annubar Flow Meter 117
4.6 Stack Reynolds Number at Six Operating Points for Low, Medium, and High Heat Flux 117
4.7 Layout of Ceramic Heating Elements with Two Central Zones Flanked By Guard Heaters....120
4.8 Heater Control and Monitoring Systems 121
4.9 Self-powered Heat Flux Meter for Temperatures up to 315°C 121
4.10 Tube Instrumentation Detail 122
4.11 Data Acquisition and Control Systems....124

List of Tables

1.1 Non-dimensional Variables 5
1.2 Scaling Ratios 16
2.1 Two Group Experiment View Factors 28″ (71.1 cm) -8″ (20.3 cm) Separation 32
2.2 Two Group Experiment View Areas 28″ (71.1 cm)-8″ (20.3 cm) Separation 32
2.3 Two Group Experiment View Factors 28″ (71.1 cm)-8″ (20.3 cm) Separation Adjusted....33
2.4 Two Group Experiment View Area 28″ (71.1 cm)-8″ (20.3 cm) Separation Adjusted....33
2.5 Two Group Experiment View Factors 28″ (71.1 cm)-8″ (20.3 cm) Separation 33
2.6 Two Group Experiment View Areas 28″ (71.1 cm)-8″ (20.3 cm) Separation 34
2.7 Riser Duct Internal Radiation View Factors....35
2.8 Summary of Full Scale/Half Scale Case Results....43
2.9 Summary of 1 & 2 Channel NSTF Case Results....67
4.1 Instrumentation Overview 112

ACRONYMS

ANL	Argonne National Laboratory
BOP	Balance-of-Plant
CAD	Computer Aided Design
CFD	Computational Fluid Dynamics
DLOFC	Depressurized Loss of Forced Cooling
HTGR	High Temperature Gas Cooled Reactor
LDV	Laser Doppler Velocimetry
NGNP	Next Generation Nuclear Plant
NSTF	Natural Convection Shutdown Heat Removal Test Facility
PBMR	Pebble Bed Modular Reactor
RANS	Reynolds Averaged Navier Stokes Equations
RCCS	Reactor Cavity Cooling System
RPV	Reactor Pressure Vessel
RVACS	Reactor Vessel Auxiliary Cooling System
VHTR	Very High Temperature Reactor
V&V	Verification and Validation

NOMENCLATURE

A = flow area
C_p = fluid specific heat
D = hydraulic diameter
D_{Ip} = diameter of riser duct
E = enthalpy
E_r = reference enthalpy
f = friction factor
g = acceleration of gravity
H = height
h_I = heat transfer coefficient in the riser duct
K = loss coefficient
k = conductivity
L = length
L_a = vertical length of the hot leg above the heated section
L_c = vertical length of the cold leg before it enters the heated section
L_h = length of heated section
δp_f = frictional pressure drop
P_I = perimeter of the riser duct
p_{in} = pressure at the top of inlet chimney
δp_ℓ = other pressure losses
p_{out} = pressure at the top of the hot leg (exit of return line)

Δp = $p_{in} - p_{out}$

ΔP = dimensionless pressure = $\dfrac{\Delta p}{\rho_o U_r^2}$

R = radius

T_c = temperature of the cold wall

T_I = temperature of air in the riser duct

T_h = reactor vessel temperature

T_{sI} = temperature of the riser duct

T_o = reference temperature

T_{out} = air temperature at the outlet of the heated section of the RCCS

t = time

U = velocity

$u^* = \dfrac{\mu}{\rho H}$ = reference velocity in air-cavity

V = velocity component in the horizontal direction (Y)

W = velocity component in the vertical direction (Z)

X_m = jet ceiling height

Y, Z = Cartesian coordinates

Greek Symbols

α^* = thermal diffusivity

β = volumetric coefficient of thermal expansion

δ = structure thickness

ε = emissivity

μ = dynamic viscosity

θ = non-dimensional temperature

θ_I = non-dimensional temperature of air in the riser duct

θ_{sI} = non-dimensional temperature of riser duct (structure)

ρ = air density

ρ_c = air density in the cold leg before it enters the heated section

σ = Stefan-Boltzmann constant

τ = non-dimensional transport time

τ^* = non-dimensional conduction time

Subscripts

c = cold

d = down

g = vapor

h = hot

I	=	inner
j	=	jet
m	=	mean
o	=	outer
p	=	pipe
r	=	reference value
s	=	structure
TP	=	two-phase
x	=	exit

<u>Similarity Groups</u>

$B_i = \dfrac{h\delta}{k}$, Biot number

$N_c = \dfrac{A_c h_{cav}}{A_o \rho C_p U_o}$, Cavity convective number

$N_r = \dfrac{A_{rad} \varepsilon \sigma T_o^4}{U_o A_o \rho_o C_p \left(T_r - T_o\right)}$, Cavity radiation number

$F_r = \dfrac{U_r^2}{g L_r}$, Froude number

$F_j = \dfrac{U_j^2 \rho_j}{\left(\rho_a - \rho_j\right) g D_j}$, jet densimetric Froude number

$F = \dfrac{f \ell}{d} + K$, Friction number

$\Pr = \dfrac{C_p \mu}{k}$, Prandtl number

$R\alpha = \dfrac{C_p \rho^2 g \beta \left(T_h - T_c\right) H^3}{\mu k}$, Rayleigh number

$Ri = \dfrac{g \beta \left(T_r - T_o\right) L_r}{U_r^2}$, Richardson number

$St_I = \dfrac{4 h_I L_r}{\rho C_p U_r D_{ip}}$, Stanton number (riser duct)

$N_t = \frac{T_r - T_o}{T_o}$, Temperature ratio number

$T^* = \frac{\alpha}{\delta^2} \frac{L_r}{U_r}$, Time Ratio number

1.0 Introduction

The work documented in this report is a follow-on to the FY 2010 work reported in [1.1] on the air-cooled reactor cavity cooling system (RCCS) design of the General Atomics (GA) Modular High Temperature Gas-cooled Reactor (MHTGR). This workscope focused on confirming the scaling laws selected to design the scaled experiments in the large-scale Argonne National Laboratory (ANL) Natural Convection Shutdown Heat Removal Test Facility (NSTF) and on sensitifity studies to evaluate the effects of the modeling approximations made in FY 2010 on the RELAP5 models developed for the experiment design supporting analysis.

In FY 2010, the objective for the effort was to update the NSTF feasibility study conducted in FY 2005, but focus on the GA-MHTGR RCCS rather than the gas turbine modular helium reactor RCCS. The objectives of the FY 2010 work were to reconfirm that the NSTF facility can be used to generate experimental data to validate computational fluid dynamics (CFDs) and systems codes for the analysis of the air-cooled RCCS for the very high temperature reactor (VHTR). More specifically, the objectives were to: (a) update the scaling relations to be used in modifying the existing NSTF facility into a scaled model of the GA-MHTGR air-cooled RCCS; and (b) provide an analytical basis for the NSTF modifications needed to conduct scaled experimental simulations of this RCCS.

In summary, the RELAP5 system code evaluation of the air-cooled RCCS system was performed based on available information about the RCCS design of the GA-MHTGR. The evaluation updated the basis that the air-cooled RCCS can be simulated at the ANL NSTF facility at a prototypic scale in the lateral direction and about half scale in the vertical direction. Three groups of RELAP5 models were developed: full-scale GA MHTGR, half-scale GA-MHTGR, and NSTF experiment configuration. It is clear from the nondimensional analyses that all similarity conditions cannot be satisfied. Since, by necessity, the scaling is based on a number of approximations, and because no analytical information is available on the performance of a reference air-cooled RCCS, the scaling laws selected need to be validated by analysis of the steady-state and transient performance of the reference air-cooled RCCS design. The analyses performed with the RELAP5 GA-MHTGR and NSTF models provided information on the magnitude of distortions imposed by the similarity conditions that are not satisfied. More information was developed in the study reported here to evaluate these initial conclusions.

The RCCS is an important system to the passive safety case being incorporated in the overall safety strategy for the NGNP. The RCCS will be one of the new safety systems specifically designed for the next generation of nuclear power plants. In particular, it is being developed and incorporated into the proposed reactor and plant designs for the VHTR— a helium gas-cooled nuclear plant with a thermal-spectrum reactor. The RCCS forms a passive heat sink external to the reactor, and is located within the reactor cavity/silo surrounding the metal vessel. During emergency accident conditions when all ac (alternating current) power is lost, natural convection of the RCCS coolant removes the heat radiated or naturally convected from the metal vessel wall to the inner boundary of the RCCS facing the vessel. This will be a first-of-a-kind (FOAK) passive safety system for core decay heat removal when the FOAK VHTR is built.

1.1 GA-MHTGR RCCS Design [1.2]

In the GA-MHTGR design, the reactor vessel is housed in a cavity located next to the power conversion unit (PCU) cavity. The overview of the entire RCCS system from the chimneys to the hot riser tubes/cold downcomers surrounding the vessel inside the cavity is shown in Figure 1.1. There are two sets of four chimneys. Each set of four chimneys is arranged in two alternating groups of a hot discharge outlet chimney and a cold inlet suction chimney side by side. The alternating groups share a common manifold and the two sets of four chimneys are connected in such a way that no single fault can disable the entire system. The midplane symmetry divides the RCCS in half, each half having one set of four chimneys, and the hot/cold run of ducting through the reactor building to the reactor cavity. Figure 1.2 shows the hot side metal ducting contained within the cold concrete run of the building, forming the cold channel. The bend and turndown into the reactor cavity with the reactor vessel can also be seen. Within the cavity is an isometric of the reactor vessel surrounded by the hot riser ducts as shown in Figure 1.3. The upper cold plenum can be seen feeding the cold downcomers all the way to the bottom cold plenum. The cold air is turned and rises upward through the hot risers removing the reactor vessel wall heat to the upper hot plenum. The upper hot plenum can be seen surrounding the vessel upper head. A plane cross section view of the reactor cavity is show in Figure 1.4. The reactor vessel is shown surrounded by the distributed hot risers with three reactor supports are and the primary cross-vessel. The downcomer channels form the outer cavity wall.

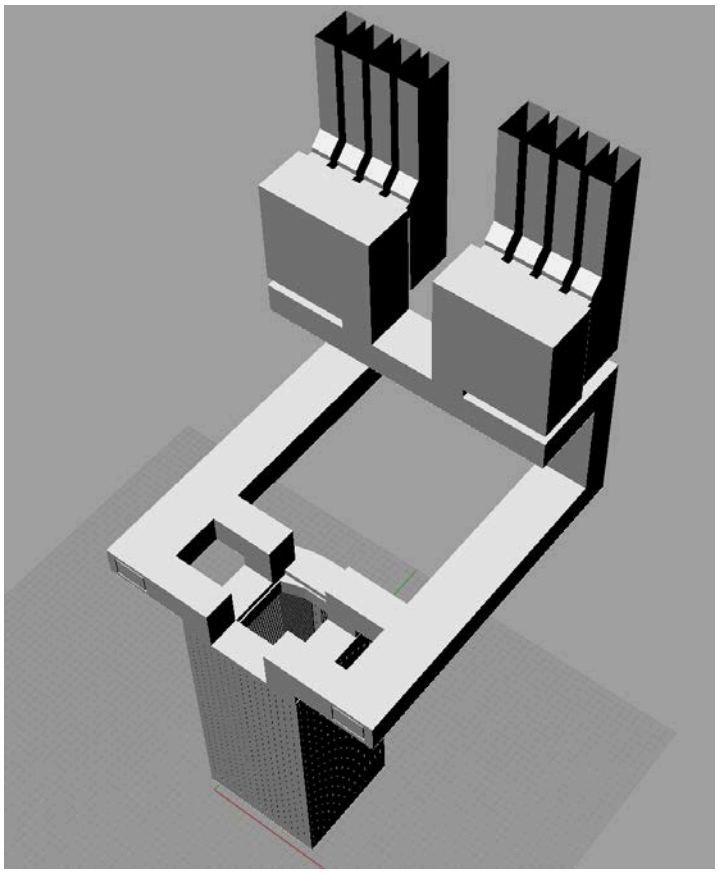

Figure 1.1. Overall System View of the GA-MHTGR RCCS

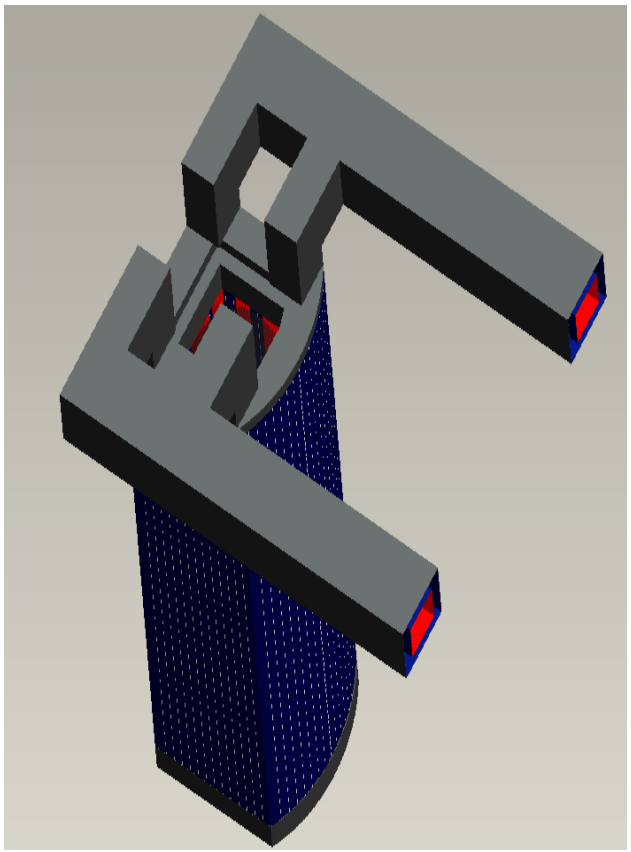

Figure 1.2. View of Ex-Cavity RCCS Outer Cold Duct/Inner Hot Duct Run

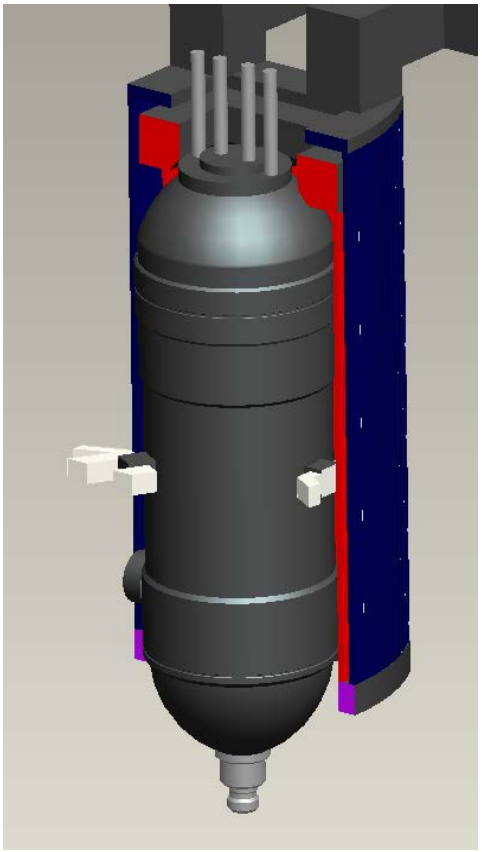

Figure 1.3. Cavity Isometric View of Reactor Vessel and RCCS

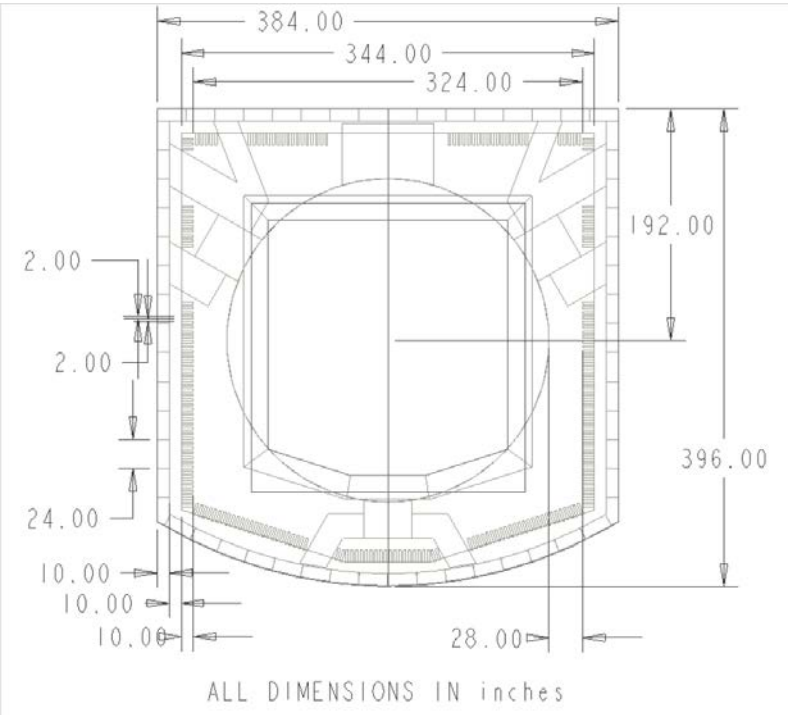

Figure 1.4. Cavity Plane View of Reactor Vessel and RCCS

1.2 NSTF RCCS Experiment Scaling

In summary, a scaling evaluation of an air-cooled RCCS system was performed based on available information on the RCCS design of the GA-MHTGR. Section 1.2 on the top-down scaling approach presents the nondimensional conservation equations describing the response of the air-based RCCS during steady-state and transient operations. These equations are used to develop scaling laws that define a scaling of the NSTF that minimizes distortions between scaled experiments and prototype operation. Section 1.4 presents the bottom-up scaling approach. The focus here is on specific selected phenomena and the mathematical similarity descriptions.

1.2.1 Top-down Scaling

This section presents simplified one-dimensional (1-D) conservation equations dealing with mass, energy, and momentum for the RCCS loop. These equation are properly nondimensionalized to determine the nondimensional groups that govern the similarity between the prototype RCCS and scaled models of the prototype. The assumption is made that the arrangement of the RCCS riser ducts in the reactor cavity is such that the cavity can be approximated by a simple 2-D rectangular cavity with vertical hot and cold walls. For the derivation of scaling ratios, the cavity is represented as a radiating wall (reactor vessel) and a convective boundary condition on the outer surface of the RCCS air riser ducts. This is work based on the scaling evaluation first presented in [1.1] for the air-cooled RCCS design option.

1.2.2 Loop Steady State

The integral momentum equation in the air loop/circuit side of the RCCS can be written

$$p_{in} + \rho_c g L_a + \int_0^{L_h} \left(\rho g dL\right)_d = p_{out} + \int_0^{L_h} \left(\rho g dL\right)_u + \rho_h g L_a + \delta p_f + \delta p_\ell \ . \tag{1}$$

The integral on the left side of Eq. (1) is the gravitational head of the cold leg in the heated section, and the integral on the right side is the gravitational head of the hot leg in the same section. The subscript d is the downcomer region and a is the unheated region above the heated riser u of height L_h. The frictional pressure drop in the i th section is

$$\delta p_{f,i} = \frac{1}{2D_i} f_i \rho_i U_i^2 L_i \tag{2}$$

The form pressure losses in the i th section of the loop are

$$\delta p_{\ell,i} = \frac{1}{2} K_i \rho_i U_i^2 \tag{3}$$

where K_i is the pressure loss coefficient in the i th section. The acceleration term is ignored in the air-cooled RCCS open loop configuration.

In the sections where the density varies with the temperature, the Boussinesq approximation gives

$$\rho = \rho_o \left[1 - \beta \left(T - T_o \right) \right] \tag{4}$$

where:

ρ_o = reference density

β = volumetric coefficient of thermal expansion

T_o = reference temperature.

In the air-cooled RCCS it is logical to pick ρ_o and T_o at the environmental atmospheric condition. It is further assumed that this is same at the NSFT and the full-scale reactor site.

The conservation equations describing the RCCS system are nondimensionalized using nondimensional variables as summarized in Table 1.1.

Table 1.1. Nondimensional Variables

z = Z/H	Vertical Distance
y = Y/H	Horizontal Distance
$\ell = L / L_r$	Length
$d = D / L_r$	Diameter
$u = U \big/ U$	Velocity (1-D Flow)
$\Delta P = \Delta p \big/ \left(\rho U_r^2 \right)$	Pressure Drop
$V = V / u^*$	Horizontal Velocity in Cavity
$W = W / u^*$	Vertical Velocity in Cavity
$\theta = \left(T - T_o \right) \big/ \left(T_r - T_o \right)$	Temperature
$\tau = U_r t / L_r$	Transport Time
$\tau^* = t\alpha^* / \delta^2$	Conduction Time
$\rho_\ell^* = \rho_\ell \big/ \rho$	Fluid Density

A nondimensional temperature θ is defined in terms of a characteristic temperature rise, $T_r - T_o$, as

$$\theta = \frac{T - T_o}{T_r - T_o} \tag{5}$$

Then, Eq. (4) gives

$$\rho = \rho_o - \rho_o \beta \theta \left(T_r - T_o \right) \tag{6}$$

In the air cooled RCCS the inlet and outlet ends are both open to the atmospheric pressure (1 bar nominal). For $p_{in} = p_{out}$ at the same point the chimney, substitution of Eqs. (6), (2), and (3) into Eq. (1) yields for the natural circulation circuit:

$$-\rho_o g\beta\left(T_r - T_o\right)\theta_c L_a - \rho_o g\beta\left(T_r - T_o\right)\int_0^{L_h}\left(\theta dL\right)_d$$
$$= -\rho_o g\beta\left(T_r - T_o\right)\int_0^{L_h}\left(\theta dL\right)_u - \rho_o g\beta\left(T_r - T_o\right)\theta_a L_a + \frac{1}{2}\sum_i \frac{f_i \rho_i U_i^2 L_i}{D_i} + \frac{1}{2}\sum_i K_i \rho_i U_i^2 \tag{7}$$

For generality, θ_a is the temperature of the heated air in the unheated region a above the heated region h.

Using a characteristic velocity U_r and a characteristic length L_r, and noting that the Richardson number Ri is

$$Ri = \frac{g\beta\left(T_r - T_o\right)L_r}{U_r^2}, \tag{8}$$

then division of Eq. (7) by $\rho_0 U_r^2$ gives

$$Ri\left[-\int_0^{\ell_h}\left(\theta d\ell\right)_d + \int_0^{\ell_h}\left(\theta d\ell\right)_u + \ell_a\left(\theta_a - \theta_c\right)\right] - \frac{1}{2\rho_0}\left[\sum_i \frac{f_i \rho_i u_i^2 \ell_i}{d_i} + \sum_i K_i \rho_i u_i^2\right] = 0.0 \tag{9}$$

where

$$\ell_a = \frac{L_a}{L_r},\ d_i = \frac{D_i}{L_r},\ u_i = \frac{U_i}{U_r}$$

In a natural circulation (1-D) circuit, the Richardson number is the more appropriate group to use than the Rayleigh number used in natural convection cavity problems.

There is essentially a hot section of the loop with density ρ_h and a cold section of the loop with density ρ_c. To be general, the continuity equation at the ith section of the loop can be written as

$$U_i A_i = A_o U_o$$

where A_0 is a reference flow area and U_o is the velocity at this flow area. The nondimensional continuity equation is $u_i = \frac{A_o}{A_i} u_o \frac{\rho_o}{\rho_i}$

and Eq. (9) becomes

$$Ri\left[\ell_a\left(\theta_a-\theta_c\right)-\int_0^{\ell_h}\left(\theta d\ell\right)_d+\right]\int_0^{\ell_h}\left(\theta d\ell\right)_u$$

$$-\left[\begin{array}{l}\dfrac{u_o^2}{2}\left[\sum_i\left(\dfrac{f_i\ell_i}{d_i}+K_i\right)\left(\dfrac{A_o}{A_i}\right)^2\right]\dfrac{\rho_c}{\rho_H}=0.0 \text{ for hot sections}\\ \dfrac{u_o^2}{2}\left[\sum_i\left(\dfrac{f_i\ell_i}{d_i}+K_i\right)\left(\dfrac{A_o}{A_i}\right)^2\right]=0.0 \text{ for cold sections}\end{array}\right. \tag{10}$$

In Eq. (9), the heater section where the temperature changes over the length an approximation is made. The reference flow area is picked in the cold section and logically at the open inlet exposed to the environment atmosphere. This means:

$$\frac{\rho_h}{\rho_c}=1-\beta\,\theta_h\left(T_r-T_c\right)$$

If $U_o = U_r$ is selected then u_o=1.

The energy equation for the fluid in the air riser duct is

$$\frac{\pi}{4}D_{Ip}^2U\rho C_p\frac{\partial T_I}{\partial Z}=\pi D_{Ip}h_I\left(T_{sI}-T_I\right)$$

or

$$U\rho C_p\frac{\partial T_i}{\partial Z}=\frac{4h_I}{D_{Ip}}\left(T_{sI}-T_I\right) \tag{11}$$

For

$$U=U_r u,\;\; Z=L_r z,\;\; u=u_o\frac{A_o}{A}$$

the nondimensional energy equation is

$$u_o\frac{A_o}{A}\frac{\partial\theta_I}{\partial z}=\frac{4h_I L_r}{\rho C_p U_r D_{Ip}}\left(\theta_{sI}-\theta_I\right)$$

or

$$u_o\frac{A_o}{A}\frac{\partial\theta_I}{\partial z}=St_I\left(\theta_{sI}-\theta_I\right) \tag{12}$$

and

$$St_I = \frac{4h_I L_r}{\rho C_p U_r D_{Ip}} \tag{13}$$

is the modified Stanton number for the riser duct.

1.2.3 Loop Transient

In the event that the RCCS has to change operating point in the natural circulation mode, the system will operate in a transient mode for a length of time. In this section, analytical equations are presented for system operation in the transient mode of operation.

The integrated momentum equation in the i th section, where the flow is incompressible, ignoring the acceleration term and the transient density terms, is

$$\rho \frac{dU_i}{dt} L_i = \Delta p_i - g \int_0^{L_i} \rho dL - \frac{1}{2D_i} f_i \rho_i U_i^2 L_i \tag{14}$$

With the Boussinesq approximation in the gravitational term, the above equation gives

$$\rho \frac{dU_i L_i}{dt} = \Delta p_i - g \rho_o L_i + \rho_0 g \beta \left(T_r - T_o\right) \int_0^{L_i} \theta dL - \frac{1}{2D_i} \rho f_i U_i^2 L_i \tag{15}$$

For a nondimensional time τ defined as

$$\tau = \frac{U_r t}{L_r} \tag{16}$$

Eq. (15) is written as

$$\rho U_r^2 l_i \frac{du_i}{d\tau} = \Delta p_i - g \rho_0 \ell_i L_r + \rho_0 g \beta \left(T_r - T_o\right) L_r \int_0^{l_i} \theta dL - \frac{1}{2} \frac{\rho}{D_i} f_i U_r^2 u_i^2 L_i$$

and

$$\left(\frac{\rho_i}{\rho_o}\right) \ell_i \frac{du_i}{d\tau} = \Delta P_i - \frac{gL_r}{U_r^2} \ell_i + Ri \int_0^{\ell_i} \theta d\ell - \frac{1}{2} \frac{f_i u_i^2 L_i}{D_i} \left(\frac{\rho_i}{\rho_o}\right) \tag{17}$$

From the nondimensional continuity equation, ignoring the transient density and picking the cold inlet location for the A_o flow area,

$$u_i = \frac{A_o}{A_i} u_o \frac{\rho_o}{\rho_i}$$

the integral momentum equation in the i th section becomes

$$\ell_i \frac{A_0}{A_i} \frac{du_0}{d\tau} = \Delta P_i - \frac{gL_r}{U_r^2} \ell_i + Ri \int_0^{\ell_i} \theta d\ell - \frac{u_0^2 f_i L_i}{2D_i} \left(\frac{A_0}{A_i} \right) \left(\frac{\rho_0}{\rho_i} \right) \tag{18}$$

Summation of the above integral momentum equation over all the sections of the loop where the fluid is compressible (air), and accounting of the other pressure losses (expansions, contractions, bends) gives the overall integral momentum equation as

$$\left[\frac{du_o}{d\tau} \sum_i \ell_i \frac{A_0}{A_i} = R_i \sum_0^{\ell_i} \theta d\ell - \left\{ \begin{array}{l} \left[\frac{u_0^2}{2} \sum_i \left(\frac{f_i L_i}{D_i} + K_i \right) \left(\frac{A_o}{A_i} \right)^2 \right] \frac{\rho_c}{\rho_H} \text{for hot sections} \\ \left[\frac{u_o^2}{2} \sum_i \left(\frac{f_i L_i}{D_i} + K_i \right) \left(\frac{A_o}{A_i} \right)^2 \right] \text{for cold sections} \end{array} \right\} \right. \tag{19}$$

The heated riser section is treated approximately as in Eq. (10).

The energy equation for the fluid in the riser duct is

$$\frac{\pi}{4} D_{Ip}^2 \rho C_p \frac{\partial T_I}{\partial t} + \frac{\pi}{4} D_{Ip}^2 \rho U C_p \frac{\partial T_I}{\partial Z} = \pi D_{Ip} h_I \left(T_{sI} - T_I \right) \tag{20}$$

The nondimensional form of this equation is

$$\frac{\partial \theta_I}{\partial \tau} + u_o \frac{A_o}{A} \frac{\partial \theta_I}{\partial z} = \frac{4 h_I L_r}{\rho C_p U_r D_{Ip}} \left(\theta_{sI} - \theta_I \right)$$

or

$$\frac{\partial \theta_I}{\partial \tau} + u_o \frac{A_o}{A} \frac{\partial \theta_I}{\partial z} = St_I \left(\theta_{sI} - \theta_I \right) \tag{21}$$

The energy equation for the solid structure in the i th section is

$$\frac{\partial T_s}{\partial t} = \frac{k}{\rho C_p} \frac{\partial^2 T_s}{\partial Z^2} = \alpha_i^* \frac{\partial^2 T_s}{\partial Z^2} \tag{22}$$

For

$$\tau^* = t\frac{\alpha^*}{\delta_i^2} \tag{23}$$

Equation (22) gives

$$\frac{\alpha_i^*}{\delta_i^2}\left(T_r - T_0\right)\frac{\partial\theta_s}{\partial\tau^*} = \alpha_i^*\frac{T_r - T_0}{L_r^2}\frac{\partial^2\theta_s}{\partial z^2}$$

or

$$\frac{\partial\theta_s}{\partial\tau^*} = \frac{\delta_i^2}{L_r^2}\frac{\partial^2\theta}{\partial z^2} \tag{24}$$

For

$$\tau = t\frac{U_r}{L_r}$$

Equation (23) gives

$$\tau^* = \tau\frac{L_r}{U_r}\frac{\alpha_i^*}{\delta_i^2}$$

and Eq. (24) becomes

$$\frac{\partial\theta_s}{\partial\tau} = \left(\frac{\alpha_i^*}{\delta_i^2}\frac{L_r}{U_r}\right)\frac{\delta_i^2}{L_r^2}\frac{\partial^2\theta_s}{\partial z^2} \tag{25}$$

For the riser duct of the RCCS, Eq. (25) is written, respectively, as

$$\frac{\partial\theta_{sI}}{\partial\tau} = \left(\frac{\alpha_I^*}{\delta_I^2}\frac{L_r}{U_r}\right)\frac{\delta_I^2}{L_r^2}\frac{\partial^2\theta_{sI}}{\partial z^2} \tag{26}$$

The boundary conditions between the solid and fluid in the ducts of the RCCS are

$$\left.\frac{\partial\theta_{sI}}{\partial r}\right/_{r_1} = \frac{h_I\delta_I}{k_{s,I}}\left(\theta_{sI,I} - \theta_I\right) \tag{27}$$

Where $r = R/\delta$ (nondimensional radius).

Taking into consideration the radiative heat transfer from the reactor vessel to the outer wall of the riser duct, the boundary condition at the outer surface of the duct can be written as

$$A_k k_{se} \frac{\partial T_{se}}{\partial R} = A_c h_c \left(T_h - T_{se,o}\right) + A_r \varepsilon \sigma \left(T_h^4 - T_{se,o}^4\right) \text{ or}$$

$$\frac{\partial \theta_{se}}{\partial r} = \frac{A_c h_c \delta_e}{A_k k_{se}} \left(\theta_h - \theta_{se,o}\right) + \frac{\delta_e A_r \varepsilon \sigma T_0^4}{A_k k_{se} \left(T_r - T_o\right)} \left\{ \left[\theta_h \left(\frac{T_r}{T_0} - 1 \right) + 1 \right]^4 - \left[\theta_{se,o} \left(\frac{T_r}{T_0} - 1 \right) + 1 \right]^4 \right\} \tag{28}$$

Where A_k, A_c and A_r are equivalent areas, and $T_{se,o}$ is the temperature of the outer surface of the riser duct.

1.2.4 Cavity Steady-State

In a rectangular 2-D cavity with one vertical wall heated, the other vertical wall cooled, and the two horizontal walls insulated, the conservation equations for mass, momentum and energy can be written as:

$$\frac{\partial W}{\partial Z} + \frac{\partial V}{\partial Y} = 0 \tag{29}$$

$$\rho \left(W \frac{\partial W}{\partial Z} + V \frac{\partial W}{\partial Y} \right) = -\frac{\partial P}{\partial Z} - \bar{\rho}_o g \left[1 - \beta \left(T - \bar{T}_o \right) \right] + \mu \left(\frac{\partial^2 W}{\partial Z^2} + \frac{\partial^2 W}{\partial Y^2} \right) \tag{30}$$

$$\rho \left(W \frac{\partial V}{\partial Z} + V \frac{\partial V}{\partial Y} \right) = -\frac{\partial P}{\partial Y} + \mu \left(\frac{\partial^2 V}{\partial Z^2} + \frac{\partial^2 V}{\partial Y^2} \right) \tag{31}$$

$$\rho C_p \left(W \frac{\partial T}{\partial Z} + V \frac{\partial T}{\partial Y} \right) = k \left(\frac{\partial^2 T}{\partial Z^2} + \frac{\partial^2 T}{\partial Y^2} \right) \tag{32}$$

where

P	=	pressure
W	=	velocity component in the vertical direction (Z)
V	=	velocity component in the horizontal direction (Y)
$\bar{\rho}$	=	density at the reference temperature $\bar{T}$

and the Boussinesq approximation for the temperature dependence of density has been used in the buoyancy term of Eq. (30).

For $$z = \frac{Z}{H}, \quad y = \frac{Y}{H} \tag{33a}$$

$$w = \frac{W}{u*},\ v = \frac{V}{u*},\ u* = \frac{\mu}{\rho H} \tag{33b}$$

$$p = \frac{P + \rho_o g Z}{\rho u*^2}\ ,\ \theta = \frac{T - \overline{T}_0}{T_h - T_c} \tag{33c}$$

Eqs. (29) to (32) become

$$\frac{\partial w}{\partial z} + \frac{\partial v}{\partial y} = 0 \tag{34}$$

$$w\frac{\partial w}{\partial z} + v\frac{\partial w}{\partial y} = -\frac{\partial p}{\partial z} + \frac{R\alpha}{\Pr}\theta + \frac{\partial^2 w}{\partial z^2} + \frac{\partial^2 v}{\partial y^2} \tag{35}$$

$$w\frac{\partial v}{\partial z} + v\frac{\partial v}{\partial y} = -\frac{\partial p}{\partial y} + \frac{\partial^2 v}{\partial z^2} + \frac{\partial^2 v}{\partial y^2} \tag{36}$$

$$w\frac{\partial \theta}{\partial z} + v\frac{\partial \theta}{\partial y} = \frac{1}{\Pr}\left(\frac{\partial^2 \theta}{\partial z^2} + \frac{\partial^2 \theta}{\partial y^2}\right) \tag{37}$$

where

$R\alpha$ = $\dfrac{C_p \rho^2 g \beta \left(T_h - T_c\right) H^3}{\mu k}$ = Rayleigh number

$\Pr$ = $\dfrac{C_p \mu}{k}$ = Prandtl number

T_h = temperature of the hot wall

T_c = temperature of the cold wall

$\overline{T}$ = $0.5\ \left(T_h + T_c\right)$

The heat, $Q(t)$, transferred from the reactor vessel to the RCCS at time t can be roughly approximated by

$$Q(t) = A_c h_{cav}\left(T_h - T_{se,o}\right) + A_{rad}\varepsilon\sigma\left(T_h^4 - T_{se,o}^4\right) \tag{38}$$

where A_c and A_{rad} are equivalent areas of heat transfer by convection and radiation, h_{cav} is the heat transfer coefficient for heat transfer in the reactor cavity by convection, and T_h is an average temperature of the reactor vessel. At steady state

$$Q(o) = A_o U_o \rho_o C_p \left(T_r - T_o\right)$$

where T_r and T_o are the inlet and outlet temperatures at the heated section of the RCCS. Equation (38) can be nondimensionalized as

$$\frac{Q(o)\, f(t)}{U_o A_o \rho_o C_p \left(T_r - T_o\right)} = f(t) = \frac{A_c h_{cav}}{A_o \rho_o C_p U_o}\left(\theta_h - \theta_{se,o}\right) + \frac{A_{rad}\varepsilon\sigma T_o^4}{U_o A_o \rho_o C_p \left(T_r - T_o\right)}$$
$$\left\{\left[\theta_h\left(\frac{T_r}{T_o} - 1\right) + 1\right]^4 - \left[\theta_{se,o}\left(\frac{T_r}{T_o} - 1\right) + 1\right]^4\right\} \tag{39}$$

where $Q(t)$ has been written as

$$Q(t) = Q(o)\, f(t) \tag{40}$$

Equation (39) introduces the nondimensional groups

$$\frac{A_c h_{cav}}{A_o \rho C_p U_o},\ \frac{A_{rad}\varepsilon\sigma T_o^4}{U_o A_o \rho_o C_p \left(T_r - T_o\right)},\ \text{and}\ \frac{T_r - T_o}{T_o} \tag{41}$$

which are here denoted as the "cavity convective number," Nc, the "cavity radiation" number, Nr, and the "temperature ratio" number, Nt, respectively.

1.3 Top-Down Scaling Laws

The nondimensional groups derived in the previous sections are used in this section to determine approximate similarity relations between the prototype and its simulation at NSTF. For the scaled NSTF model of the RCCS to be similar to the prototype RCCS, the ratio of the value of a similarity group at NSTF conditions to the value of the same group at prototype conditions must be equal to one. In the analysis that follows, the subscript R denotes the ratio of the value of a parameter in the model to the value of the same parameter in the prototype. Thus

$$\psi_R = \frac{\psi(model)}{\psi(prototype)} = \frac{\psi_m}{\psi_p} \tag{42}$$

At NSTF the same materials will be used as in the prototype. Therefore, $\psi_R = 1.0$ for any material property ψ (strictly only at the same temperature).

1.3.1 Baseline Scaling

The key to the air-cooled RCCS scaling is selecting the cold inlet to the hot riser duct as the reference location and that the cold atmosphere air is at the same condition for all scales and

experiments. After the geometric similarity condition is decided, the similarity condition for the friction number

$$\left[\sum_i F_i \left(\frac{A_o}{A_i}\right)^2\right]_R = \left[\sum_i \left(\frac{f_i L_i}{D_i} + K_i\right)\left(\frac{A_o}{A_i}\right)^2 + \sum_i \left(\frac{f_i L_i}{D_i} + K_i\right)\left(\frac{A_o}{A_i}\right)^2 \left(\frac{\rho_o}{p_i}\right)\right] \tag{43}$$

can be easily satisfied by using appropriate orifices but also needs $(\rho_c / \rho_h)_R = 1.0$

To preserve the density ratio, taking the heated section as the reference section, at steady state conditions, the temperature rise, ΔT_o, along the heated section is

$$\Delta T_o = \frac{\dot{Q}}{U_o A_o \rho_o C_p} = T_r - T_o \tag{44}$$

where T_r and T_o are the temperatures at the exit and inlet of the heated section. From the above definition of the reference section, $L_r = L_h$, $U_r = U_o$ (cold inlet velocity to the heated section).

If ΔT_o is preserved at different scales, in addition to $T_o = T_c$, then $T_r = T_h$ and T_h is also preserved. This then automatically preserves the density ratio. Insertion of the above expression for ΔT_o into the steady-state integral momentum equation, Eq. (7) gives

$$U_o = \left\{\frac{g\beta\dot{Q}}{A_o \rho_o C_\rho}\left[\frac{L_c + \frac{1}{2}L_h}{\sum_o F_i \left(\frac{A_o}{A_i}\right)^2}\right]\right\}^{1/3} \tag{45}$$

If

$$\left[\sum_i F_i \left(\frac{A_O}{A_i}\right)^2\right]_R = 1.0$$

then

$$U_{OR} = \left\{\frac{\dot{Q}_R}{A_{OR}}\left(L_c + \tfrac{1}{2}L_h\right)_R\right\}^{1/3} \tag{46}$$

From Eq. (44)

$$\Delta T_{oR} = \frac{\dot{Q}_R}{U_{oR} A_{oR}} \tag{47}$$

and the Richardson number ratio becomes

$$Ri_R = \frac{\dot{Q}_R L_{hR}}{U_{oR}^3 A_{oR}} \tag{48}$$

Use of Eq. (46) gives

$$Ri_R = \frac{L_{hR}}{\left(L_c + \frac{1}{2} L_h\right)_R} \tag{49}$$

From the geometric similarity (same in all directions)

$$\ell_R = L_{hR} = L_{cR}$$

and the similarity condition from the Richardson number gives

$$Ri_R = \frac{\ell_R}{\ell_R} = 1.$$

Thus, with the U_o and ΔT_o scaling given by Eqs. (46) and (47) the similarity requirement $Ri_R = 1$ is automatically satisfied. This setting of the Richardson number plus other choices gives the scaling laws in Table 1.2.

Table 1.2 gives the different scaling ratios as a function of the height scaling ratio ℓ_R and their numerical values for $\ell_R = 0.5$. The scaling ratio T_{oR} and the geometric scaling ratios in the lateral direction (D_R, A_{oR}, δ_{iR}, δ_{yR}) have also been set equal to one. The driver of the table is

$$q_R'' = \frac{1}{\sqrt{\ell_R}}$$

From Eq. (54)

$$q_r'' = \frac{\dot{Q}_R}{\delta_{yR} \ell_R},$$

and for δ_{yR} = 1.0, it gives

$$\dot{Q}_R = \sqrt{\ell_R}$$

For A_{oR} = 1.0, Eq. (47) gives

$$\Delta T_{oR} = \frac{\dot{Q}_R}{U_{oR}\, A_{oR}} = 1.$$

Table 1.2. Scaling Ratios

Scaling Ratios	**Values for** $\ell_R = 0.5$
$(N_{Fr})_R = 1$	1
$\delta_{iR} = 1$	1
$U_{oR} = \sqrt{\ell_R}$	0.707
$T_R^* = \sqrt{\ell_R}$	0.707
$(Ri)_R = 1$	1
$\Delta T_{oR} = 1$	1
$T_{oR} = 1$	1
$D_R = \delta_{yR} = 1$	1
$A_{oR} = 1$	1
$q_R'' = \ell_R^{-0.5}$	1.414
$(Nd)_R = \ell_R^{-0.5}$	1.414
$(\mathrm{Re})_R = \sqrt{\ell_R}$	0.707
$h_R = \ell_R^{0.4}$	0.758
$St_R = \ell_R^{0.9}$	0.536
$(Nr)_R = \sqrt{\ell_R}$	0.707
$(Nt)_R = 1$	1
$(Bi)_R = h_R = \ell_R^{0.4}$	0.758

Since $U_{oR} = \sqrt{\ell_R}$ from $Ri_R = 1.0$ in Eq. (48), there is consistency with the assumed preservation of ΔT_o between the scales. This means that the air exit temperature from NSTF should equal those of the full-scale reactor because the inlet cold air temperature is the same.

It is interesting to note that the similarity condition for the Froude number also requires

$$U_{oR} = \sqrt{\ell_R} \qquad (50)$$

For $\delta_{iR} = 1$ and $U_{oR} = \sqrt{\ell_R}$, the similarity condition for the time number gives

$$T_R^* = \frac{\ell_R}{U_{oR}} = \sqrt{\ell_R} \qquad (51)$$

The above equation indicates that in a reduced-height model, the time-scale of the events is shortened. This summarizes the base-line scaling laws which will be used in the scaling of the NSTF experiments. A number of the implications of the scaling selections made are discussed in the following section.

1.3.2 Time Number Scaling

Time number, T^*, similarity requires

$$T_R^* = \frac{L_{hR}}{U_{oR}\delta_{i\ R}^2} = 1$$

For $\delta_{iR} = \ell_R$, the above equation gives

$$U_{oR}\ell_R = 1, \text{ or } U_{oR} = \frac{1}{\ell_R} \qquad (52)$$

Then, from the Richardson number

$$\frac{\Delta T_{oR}\ell_R}{U_{oR}^2} = 1$$

and

$$\Delta T_{oR} = \frac{U_{oR}^2}{\ell_R} = \frac{1}{\ell_R^3} \qquad (53)$$

$$\Delta T_{o,m} = \frac{\Delta T_{o,p}}{\ell_R^3}$$

If $\ell_R = 0.5$, then

$$\Delta T_{oR} = 8, \text{ and } \Delta T_{o,m} = 8\Delta T_{o,p}$$

Similarly, from Eq. (44) and from $A_{oR} = \ell_R^2$

$$\dot{Q}_R = \frac{1}{\ell_R^2} = 4$$

and

$$\dot{Q}_m = 4Q_p$$

The power $\dot{Q}$ transferred from the reactor vessel to the RCCS is

$$\dot{Q} = q''\delta_y L_{Rv} \tag{54}$$

where δ_y is the width of the RCCS cell (section) simulated at NSTF and L_{Rv} is the height of the reactor vessel.

Then

$$\dot{Q}_R = q''_R \delta y_R \ell_R = q''_R \ell_R^2$$

And from Eq. (54)

$$q''_R = \frac{1}{\ell_R^4} \tag{55}$$

For $\ell_R = 1/2$

$$q''_m = 16 q''_p \tag{56}$$

Equation (56) imposes an excessive requirement on the model (NSTF) heat flux. To overcome this difficulty, the similarity requirements need to be relaxed.

1.3.3 Alternate Time Number Scaling

If $\delta_{iR} = 1$ (similarity requirement for thickness is relaxed), the time ratio T_R^* becomes

$$T_R^* = \frac{L_{hR}}{U_{oR}}$$

for a real time simulation $T_R^* = 1$, and

$$U_{oR} = L_{hR} = \ell_R \tag{57}$$

Then, from $Ri_R = 1$,

$$\frac{\Delta T_{oR}\ell_R}{U_{oR}^2} = \frac{\Delta T_{oR}\ell_R}{\ell_R^2} = \frac{\Delta T_{oR}}{\ell_R} = 1$$

or

$$\Delta T_{oR} = L_{hR} = \ell_R \tag{58}$$

and from the steady state energy balance Eq. (44)

$$\dot{Q}_R = \ell_R^2 A_{oR}$$

The power $\dot{Q}$ transferred from the reactor vessel to the RCCS is

$$\dot{Q} = q''\delta y L_{Rv}$$

and

$$\ell_R^2 A_{oR} = q_R''\delta y_R \ell_R$$

For $D_R = \delta y_R$

$$q_R'' = \ell_R D_R \tag{59}$$

1.3.4 <u>Stanton Number Scaling</u>

The similarity requirement imposed by the Stanton number is

$$St_R = \frac{h_R \ell_R}{U_{oR} D_R} = 1.0$$

where h_R is the ratio of the heat transfer coefficient.

For $U_{oR} = \ell_R$ from (Eq. (57) we have

$$St_R = \frac{h_R}{D_R} = 1.0$$

or

$$h_R = D_R$$

If the flow is turbulent and the heat transfer coefficient is given by a relation of the form (Dittus-Boelter correlation)

$$Nu = 0.023\,\mathrm{Re}^{0.8}\,\mathrm{Pr}^{0.4} = \frac{hD}{k}$$

Then

$$h_R = \frac{\left(U_{oR} D_R\right)^{0.8}}{D_R} = \ell_R^{0.8} D_R^{-0.2}$$

For $h_R = D_R$, the above relation gives

$$D_R^{1.2} = \ell_R^{0.8} \tag{60}$$

For $\ell_R = 0.5$, the above relation gives $D_R = 0.630$, or $D_R \approx \ell_R$. For $D_R = \ell_R$,

$$\mathrm{Re}_R = U_R D_R = \ell_R^2$$

and for $\ell_R = 0.5$, the Re ratio becomes $\mathrm{Re}_R = 0.25$. This means that it needs to be assured that the flow in the scaled model remains turbulent.

The similarity conditions imposed by the boundary condition between the solid and the fluid in the pipes requires

$$Bi_R = h_R \delta_{iR} = 1.0$$

or $h_R = 1.0$ for $\delta_{iR} = 1.0$. This is the same condition imposed by $St_R = 1.0$ for $\delta_{iR} = D_R = 1.0$.

1.3.5 Cavity Scaling

The cavity radiation number, Nr, gives

$$Nr_R = \frac{\ell_R \delta y_R T_{oR}^4}{\ell_R D_R^2 \ell_R} = \frac{T_{oR}^4}{D_R \ell_R} = 1$$

For $D_R = \ell_R = 1/2$

$$T_{oR}^4 = \ell_R^2$$

or

$$T_{oR} = \sqrt{\ell_R} = 0.707$$

From

$$\Delta T_{oR} = T_{oR}\left(\frac{T_r}{T_o} - 1\right)_R = \ell_R$$

The temperature ratio number gives

$$Nt_R = 0.707$$

versus $Nt_R = 1$ that the similarity condition requires.

The cavity convective number, Nc, gives

$$Nc_R = \frac{\ell_R \delta y_R h_{cavR}}{D_R^2 \ell_R} = \frac{h_{cavR}}{D_R}$$

or

$$h_{cavR} = Nc_R D_R = D_R$$

If the heat transfer coefficient in the cavity is given from [1.3]

$$Nu = 0.046 R\alpha^{1/3}$$

then

$$h_{cavR}\ell_R = \left[\left(T_h - T_c\right)_R \ell_R^3\right]^{1/3}$$

and

$$h_{cavR} = \left(T_h - T_c\right)_R^{1/3}$$

Some analysis is needed to evaluate how close the above value is to

$$h_{cavR} = Nc_R D_R = D_R$$

If scaling in the lateral direction is modified and D_R is set equal to one, i.e.,

$$D_R = \delta_{iR} = \delta_{yR} = 1.0$$

then the process described above gives

$$q''_R = \ell_R$$
$$St_R = h_R = 1.0$$

but $h_R = \ell_R^{0.8}$ from the heat transfer correlation (Dittus-Boelter), and for $\ell_R = 0.5$: $h_R = 0.57$, and $\mathrm{Re}_R = 0.5$. From $Nc_R = 1$, we get $T_{oR} = \ell_R^{1/4}$, and $Nt_R = \ell_R^{3/4}$, or $T_{oR} = 0.84$, and $Nt_R = 0.59$ (for $\ell_R = 0.5$) . The similarity condition for the cavity convective number requires $Nc_R = h_{cavR} = 1.0$, but the heat transfer correlation in the cavity gives

$$h_{cavR} = \left(T_h - T_c\right)_R^{1/3}$$

1.4 Bottom-Up Scaling

The standard top-down scaling methodology as applied to the scaling of the NSTF air-cooled RCCS experiments is detailed in Section 1.2. It can be seen from the quantitative development in Section 1.2 that the top-down scaling is the standard nondimensionalization analysis applied to the 1-D conservation equations to obtain the important similarity parameters. It is essentially focused on a 1-D loop/circuit incorporating one average hot riser duct where the important variables are the natural convection air velocity in the riser, the corresponding gas mass flow rate, and the riser outlet temperature as a function of the imposed heat flux or equivalently the core power. This is the core power, most importantly during the decay heat production accident phase, being conducted or radiated to the metal vessel wall boundary.

However it can be seen that the top-down scaling methodology as applied here does encompass 3-D thermofluid phenomena in the plenums, either hot or cold. Furthermore, it is not focused on the phenomena involving multiple hot riser ducts such as parallel channel flow stability. In the case of the GA-MHTGR hot plenum, thermal stratification could occur through incomplete mixing of the jet flow from multiple parallel ducts of varying temperature or, perhaps less likely, from boundary heat losses. The parallel channel flow stability phenomena from the multiple ducts with varying outlet temperature could perhaps lead to recirculation flow patterns between neighboring ducts. The implications of all these phenomena for the heat transfer and heat removal of the core decay heat production to the ultimate heat sink, the atmosphere, may need to be considered. Instead of the heated air flow from the hot risers discharging from the top hot plenum into the hot duct network of the building and exiting from the hot outlet chimney to the atmosphere, it could be that the air flow patterns recirculate and stratify within these volumes and ducts. This would reduce the heat removal by the natural convection flow from the values commensurate with the total natural convection densimetric gravity head. Natural convection phenomena, particularly at low flow rates for air systems with the low gas driving heads, are known to be complex to predict. In addition, the viscosities of gases as opposed to those for liquids are noted for increasing with temperature. This leads to the potential for positive feedback and flow stagnation/instability in heated gas systems.

To start the work on the bottoms-up scaling, the focus in this report is on jet behavior in the top hot plenum of the RCCS. The penetration of the hot jet exiting the hot riser ducts into hot plenum should influence the thermal stratification patterns in the hot plenum. It also, to a degree,

determines the conditions for potential recirculation flows between the different hot riser ducts. To this extent then, the initial concentration of the bottom-up scaling is on the maximum ceiling height X_m for jet penetration. Implicit in this are the phenomena of jet entrainment, laminar-to-turbulent transition and ambient stratification, which will be treated at future stages of the scaling analysis. Turner [1.4] conducted experiments on a negative buoyant jet for the axisymmetric case. This is a considerable simplification over a hot riser jet, which is initially positive buoyant until it reaches neutral buoyancy and perhaps negative buoyancy. But as a first step it is instructive to note that the Turner data shows

$$\frac{X_m}{D_j} \ \alpha \ F_j^{1/2} \tag{61}$$

so

$$X_m \ \alpha \ D_j^{1/2} U_j \tag{62}$$

So using the notation of Table 2.

$$X_{mR} = D_{jR}^{1/2} \ \ell_R^{1/2} \tag{63}$$

For the selected NSTF RCCS experiment scaling $D_{jR} = 1$ and $\ell_R = 0.5$ giving

$$X_{mR} = 0.707 \tag{64}$$

This should be useful in the scaling of the hot plenum height for the NSTF experiments.

1.5 Study Approach

In preparation for the integral RCCS experiments in the NSTF, a parallel track effort on two main project tasks is reported here:

1. Analysis support for the scaling study and the experiment design
2. Instrumentation support for the experiments.

Analysis support for the scaling study and the experiment design consists of (a) ultimate air heat sink 1-D system analyses with the RELAP5 system code and (b) reactor air plenum multidimensional CFD analyses with the STARCCM+ CFD code. The in-vessel region and ex-vessel cavity are coupled only through a heat flux boundary condition for the group of events where the integrity of the primary system is maintained and no mass transfer coupling occurs between in-vessel and ex-vessel regions. For reactor cavity phenomena, this is the heat-transfer-only focus, which, for these analyses, further divides the RCCS and its response to the initiating events into the air transport/heat sink system and cavity with its air circulation and heat transport. For the STARCCM+ analyses reported here the cavity system is treated as a heat-flux boundary

condition. For the RELAP5 air transport/heat sink system analyses, the cavity is treated with a natural convection heat transfer correlation and radiation view factors.

Instrumentation support for the experiments includes bulk flow and temperature instrumentation. The Laser Doppler Velocimetry (LDV) is the only measurement technique with the possibility of measuring gas velocities within the cavity. However, LDV requires seeding particles to reflect the laser light that generates signals. Particles are usually kept suspended by forced circulation. The cavity will be a closed natural circulation system. This is a configuration of low velocities and stagnant regions where the potential exists for the seed particles to deposit out off the flow stream, thereby impacting the laser measurement signals of the velocity. The FY 2010 LDV study [1.1] determined the feasibility of using LDV for air velocity measurements in the cavity under RCCS conditions.

(a) RELAP5 Air Heat Sink System Analyses

To provide confirmation analysis support for the up-dated scaling laws, effort was focused on utilizing the input deck for RELAP5, which models the RCCS at full-scale for the GA-MHTGR design. The full-scale RELAP5 model starts from the vessel wall where a heat flux boundary condition is imposed with a one volume cavity treatment using natural convection correlations and focuses on the 1-hot riser model for the air-cooled RCCS all the way from the cold chimney inlet to the hot chimney outlet. A half-scale RELAP5 model was constructed from this full-scale model by applying geometric similarity and the selected scaling laws of half-scale axial height and full-scale lateral dimension.

The corresponding NSTF model does not include a downcomer, cold ducting, or manifolding. The hot plenum is part of the NSTF chimney. Both top and bottom cold plenums are not represented. Riser, vessel and cavity heat structure surfaces are included for the in-cavity radiation and natural convection heat transfer. Based on the test cavity symmetry, the experiment design has been modeled in RELAP5 as a one channel grouping or a two channel grouping of all the hot riser ducts. For the two channel grouping in one-half of the test cavity, half of the test cavity risers are represented by two RELAP5 channels. The outermost riser closest to the test cavity side and its neighbor form one channel. Included in the second channel are the remaining four central ducts which form that half of the symmetric system, connected to the common chimney. It is assumed that the effect on the two RELAP5 channels is representative of the effect on both halves and that the heat load is therefore mirror- symmetric.

The full-scale model was used as a baseline to test the response of the system to varying heat fluxes and confirm the scaling laws. Cases at 10 and 5-kW/m^2 full-scale heat fluxes were run. The heat flux of 5.0 kW/m^2 represents the reference reactor case of medium heat flux. The high heat flux case corresponds to the system model with l0 kW/m^2. Note that these are uniform heat fluxes, applied at the reactor vessel outer surface over the heated height.

A series of cases were run with a half-scale model at heat fluxes proportionally scaled to the full size. This half-scale deck was used to verify the scaling analysis. The system was scaled down to half scale according to the scaling in Section 1.2. Essentially the lengths and heights were halved but the widths, depths, diameters, and thicknesses in the plane cross-section were

kept unaltered. The radial dimensions of the cavity were maintained at full scale. System power was reduced by a factor of the square root of 2, and the scaled heat flux was increased by the same factor to maintain the scaled heat added per unit volume over the standpipes. The half-scale system was converted directly from the full-scale model. An orifice coefficient was then implemented in the inlet to the hot riser. The orifice value was adjusted to match the hot riser air outlet temperature for the full-scale model given by the high heat flux case. With this coefficient fixed, the medium flux case was run and the hot riser air outlet temperature was compared with the corresponding value from the full-scale model. In line with the scaling laws, the air outlet temperature was preserved, confirming that the approximations made in the derivation of the scaling laws have minimal effect. But while the NSTF test section is also 50% height scale with full lateral scale hot risers, there are differences in the rectangular test cavity geometry. Ambient heat losses from the NSTF test section need to be also included in the baseline cases. Therefore to support the Argonne NSTF heat transfer experiment, the RELAP5 model of the NSTF experimental system was also used.

NSTF cases were run at various internal power generation levels. These power levels produce the proportionally scaled heat fluxes previously used. A number of experiment cross section configurations are under discussion, but in this report, the analyses mainly involve varying the separation distance between the heated surface of the box and the hot risers from 8 in. (20.3 cm) to 28 in. (71.1 cm). The test cavity box depth is of variable design. Conduction and radiation models have been studied to evaluate the relative modeling importance.

These verification scaling analyses and the NSTF experiment design sensitivity analyses allows for extrapolation of results from the NSTF experimental system to the full-scale GA-MHTGR response.

This work is detailed in Chapter 2.

(b) STARCCM+ RCCS CFD Analyses

A series of solution verification studies have been completed for simulations using the baseline NSTF STAR-CCM+ CFD geometry. In order to evaluate the sensitivity of the predicted flow fields to the mesh size, two alternate computational meshes describing the baseline geometry were developed using the same process. In these cases, the sizes of the nominal cells are increased by 20 and 40% above the baseline size. In both cases, the thickness of the first three cell layers near the wall of the test section structures is maintained at the same value. This reduces the number of computational cells used by these models to 8.3 million and 6.3 million respectively.

In both alternate mesh cases, predicted flow behaviors are very similar to the baseline case. The primary impact of the coarsening of the mesh is the loss of resolution in the prediction of peak velocities and temperatures. Since the primary focus of the experiment is the heat transfer performance within the riser ducts themselves, the extracted profiles at the outlet of the 6th riser duct were used for a more quantitative comparison. For the three different mesh cases, the average axial component of the velocity along the selected line is 6.2 m/s and the average temperature along the same line is 356.7 K. The average standard deviation between the three

cases in the predicted values at each sampling point along the selected line is 0.022 m/s for velocity and 0.81 K for temperature. The maximum standard deviation at any single position is 0.10 m/s for velocity and 4.3 K for temperature. Based on these results, the baseline mesh size selection is expected to provide an adequate representation of the flow and heat transport physics for the current series of analyses.

In a separate study, the thickness of the prismatic layer was also increased by 20% over the baseline value. Similarly, no significant differences in predicted flow behaviors were observed. In a subsequent study, the meshes in the inlet and outlet plena were isolated and refined to the same fine scale as the riser ducts. Again, no significant deviations in predicted flow behavior were observed.

In order to evaluate the sensitivity of the predicted flow fields to the selected turbulence model, an alternate simulation was completed using the Menter k-omega SST model with the baseline geometry and computational mesh. The SST model should be expected to be more sensitive to flow separations and predict increased turbulence in the wake fields downstream from such flow structures. As a result, the model is often used in aerodynamic analyses when accurate prediction of base drag is desirable. The predicted riser flow fields using the SST model are much less uniform, in spite of very similar flow field predictions in the lower inlet plenum. In comparisons of predicted temperature profiles within the duct, the SST model consistently predicts more turbulent diffusion than the realizable k-epsilon model, resulting in higher riser flow temperatures and flatter temperature distributions. The increase in the energy tied up in turbulence also results in reduced riser velocities. In the absence of experimental data to validate the selection of turbulence model, the realizable k-epsilon model, which predicts more conservative RCCS duct performance, was used for remaining design analyses.

Upon completion of this minimal solution study a series of design studies were completed using the baseline modelling study. For the present studies, uniform heat flux conditions are applied on all riser surfaces to evaluate bulk flow behavior; radiation heat transport through the cavity is not evaluated. A uniform 1.24 kW/m^2 heat flux is applied to all the risers, which is consistent with a loss of flow accident in which the risers transport all of the heat from the reactor vessel out of the system at a uniform heat flux of 10 kW/m^2. Additional planned analyses will evaluate the effect of realistic nonuniform heat flux conditions using the final selected geometry.

The four design cases considered are:

- Nominal geometry
- Extension of the risers through the floor of the outlet plenum by 25 cm to allow for instrumentation access
- Raised outlet plenum floor and the addition of an unheated extension of the risers between the cavity and the outlet plenum to allow for instrumentation access and better agreement with jet penetration scaling parameters
- A modification of the raised outlet plenum model with a substantially extended inlet pipe length for improved inlet flow stability and instrumentation access

All four cases retain the primary flow features of the anticipated RCCS design. The introduction of extended risers to support instrumentation access does not dramatically alter the parallel riser flows. The use of a reduced-height outlet plenum does impact the riser jet penetration and the rotational flow that develops in the plenum volume and may be an attractive option for better representing the outlet plenum flow, if desired. The extended inlet provides better inlet flow conditioning and improves the rate of simulation convergence.

This work is detailed in Chapter 3.

(c) Bulk Instrumentation

A characterization of bulk velocities and temperatures within the cavity and hot risers and chimney are desired for comparison with code simulations. The FY 2010 evaluation of instrumentation alternatives identified LDV as the most feasible candidate for local flow measurements. This is in view of the facility's high operating temperature and the expectation of rather low flow velocities within the cavity.

The facility is heavily instrumented to evaluate heat removal performance and help guide experiment operations. There are instruments to measure air and surface temperatures, bulk air flow rate and local velocity, total normal radiation heat flux, and electrical power supplied to the duct wall heaters.

All thermocouples are type-K with an accuracy of ±2.2°C or 0.75% of measured temperature. The vast majority of these sensors, roughly 200, are located on the upper and lower plates of the test section. Sensors are flush-mounted for accurate measurement of surface temperatures without disruption of the flow field. A high-temperature thermal cement is used to bond junctions to the plate. Note that the wires are not joined at the junction and so the electrical circuit is completed through the steel plate. This allows detachment of the wire from the plate to be detected as an open circuit, which is not the case if the wires are bonded together at the junction as in conventional configurations.

Measurements of fluid flow can be divided into two categories. The first is bulk flow rate through pipes and ducts, which is needed for energy balances and determination of flow partitioning across the twelve ducts. The second category is local gas velocity measurements, which are intended to support CFD analysis.

There are two types of bulk flow measurement: one is flow through the twelve 5 × 25 cm ducts and the other is through the two 61 cm diameter stacks. Both the duct and stack measurements will be made with instruments positioned downstream and closer to their outlets than inlets. It is not possible, unfortunately, to make reliable flow measurements near the test section inlet because entrance lengths are far too short. Sensors near the inlet might be able to provide indications of relative flow, such as balance between the two main inlets, but local flow patterns are likely to be unstable and so even that may not be reliable. Refraining from inlet measurements means sensors much operate at elevated rather than ambient temperature, which is more difficult and generally less accurate, but it is necessary in order to provide the instruments adequate entrance length.

Stack measurements will be made with an averaging pitot tube such as the Rosemount 485 Annubar flow meter. The flow element acts as a collection of pitot tubes by effectively averaging the stagnation pressure across a pipe chord. The width of the Annubar sensing element is 49 mm and it operates at process temperatures up to 260°C. The pressure losses associated with this device are much lower than that of an orifice flow meter.

Duct flow conditions pose the same problems described for the stacks so a pitot-tube type instrument is again recommended. But the ducts are smaller than the stacks so probes will block a larger percentage of the flow area, ~10 to 30% for the typical 10 to 15 mm diameter probes used in small pipes and ducts. Pressure losses will be small, only a fraction of the measured ΔP and on the order of several Pascals, but probes will certainly alter the distribution of flow as it enters the upper plenum. If this degree of outlet blockage is acceptable, all duct sensors could be calibrated along with the stack sensors. If these probes are too large, it is possible to use light gauge conventional pitot tubes having a diameter of ~2 to 3 mm.

While measurements of bulk flow are required for energy balances and assessments of overall system behavior, CFD requires data on localized velocity, preferably at many locations. LDV is normally used in open systems and forced circulation loops with either naturally suspended particles or flows that are easily seeded artificially. Without such particles to reflect light, there is no signal for the LDV to process. Measurements in the closed cavity would be problematic since they require periodic seeding injections followed by a waiting period for reestablishment of natural circulation patterns. Particles may not remain suspended long enough for high quality measurements. Perhaps more critical is the change in surface emissivity that is likely to accompany the use of seeding particles. Oils are the most promising seeding candidates as they generate strong signals, but extensive use is likely to result in a thin coating of oil over all of the cavity surfaces.

LDV is more feasible for measurements within the upper plenum. Seeding can be added at the bottom end of the ducts to be swept along up towards the upper plenum, where windows allow access for the laser beams. The inner surfaces of the ducts, upper plenum, and eventually the stacks will be coated with oil, but their emissivities should have less influence on heat transfer, which is also conductive and convective.

This work is detailed in Chapter 4.

References

1.1 S. Lomperski, W. D. Pointer, C. P. Tzanos, T.Y.C Wei, C. M. Crooks, and O. A. Rodriguez, “RCCS Studies and NSTF Preparation Air-Cooled Option,” ANL-GenIV-142, Sept. 30. 2010.

1.2 DOE/HTGR -86-024, Preliminary Safety Information Document for the Standard MHTGR, Vol. 1: Sections 5.5.1–5.5.16.

1.3 J. G. Collier, “Convective Boiling and Condensation,” McGraw-Hill, NY (1972).

1.4 J. S. Turner, “Jets and Plumes with Negative or Reversing Buoyancy,” J. Fluid, Mech. 26, 779-792 (1966).

2.0 Air Heat Sink System Analyses

Cavity phenomena determine the passive transfer of the heat produced by the reactor core within the primary vessel from the outer vessel metal wall surface to the air ducts of the RCCS, to the air within the cavity and eventually to the liner/insulation/concrete of the cavity boundary. The experience is that this heat transfer is dominated by radiation heat transfer mechanisms for this air-cooled RCCS design but that some natural convection air heat transfer also occurs driven by the natural convective air flow patterns. Radiant heat transfer rates are established by the predefined geometry, operating history surface emissivities and the presence or absence of gray gas factors such as graphite dust particles, water vapor and other impurities. The geometry of the cavity establishes the radiation view factors between the metal vessel wall and the RCCS hot riser ducts. A nonsymmetric/nonuniform reactor cavity geometry leads to nonuniform heating of the riser ducts, which could lead to thermal-fluid (T-F) nonuniformities in the T-F phenomena within the air duct network. There is also the potential for intraduct radiation between the inner surfaces of the hot riser walls. This leads to more uniform circumferential duct wall temperature distributions.

2.1 RCCS Design View Factors

2.1.1 Experiment Geometry: Cavity

All the subsequent view factors presented in this section were obtained using the Net Energy Verification and Determination Analyzer (NEVADA) methodology; NEVADA 97 is a thermal radiation analysis software package. The package is equipped with both radiation analysis tools and a special CAD tool for the radiation analysis. The NEVADA software package consists of several radiation analysis tool, one of which is RENO. The RENO computer code is used for radiation interchange factors calculations using Monte-Carlo mathematical techniques. It uses statistical ray tracing to compute view factors for complex geometry problems. The number of rays can be changed to improve program accuracy level and account for time constraints.

The experimental geometry is based on the planned experiment at the Argonne NSTF [2.1]. The NSTF was originally designed to simulate a Reactor Vessel Auxiliary Cooling System (RVACS) for the Advanced Liquid Metal Reactor Program. The NSTF test section essentially consists of a metal box, 7.7 m high and 1.32 × 1.16 m in cross section, surrounded on the outside by insulation. One side of the box contains a ceramic heater to simulate heating from the active core height (6.7 m maximum) in a reactor that can be adjusted to various distances from the riser ducts. There is a small air gap between this heater and a steel plate simulating the RPV. The opposite unheated side of the box is meant to represent the insulated metal shield and concrete structure around the reactor. The other two sides consist of two steel brackets each, to support the structure, with insulation between and behind the brackets, as shown in Figure 2.1.

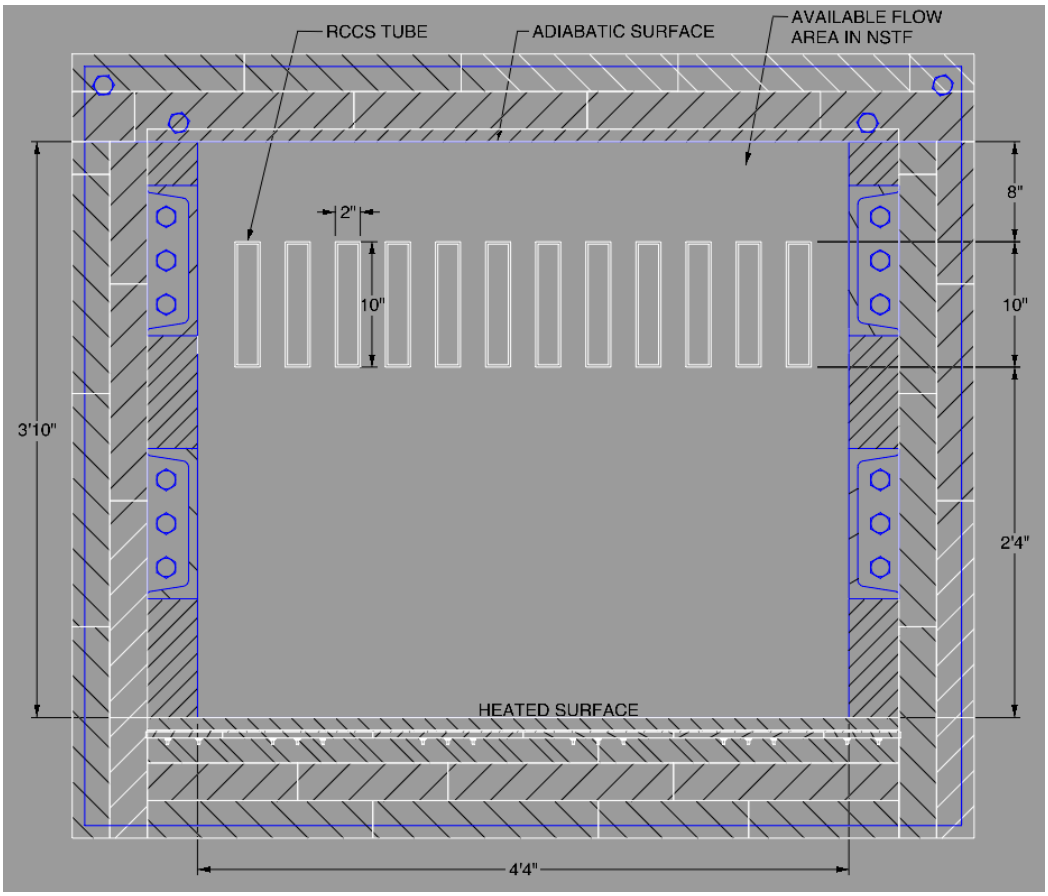

Figure 2.1. Experiment Cross Section

Twelve 10″ (25.4 cm) by 2″ (5.0 cm) riser ducts are located near the back wall, with the same shape and radial dimensions as the full-scale model. The bottom ends are located above the bottom of the box, to provide flow area for the natural circulation of air in the cavity. The riser ducts 22′ (6.7 m), which means that they occupy the entire heated length of the box, and are flush with the top cover of the box. This configuration exists because the cover is necessary to support the riser. Furthermore, the cover forms the bottom of the hot plenum into which the hot risers discharge the heated natural convection air, which is removing the core residual heat. One approach to simulate this variation in the experiments is to vary the depth of the box, thereby changing the distance between the heated box surface simulating the reactor vessel wall and the riser ducts. The two separation distance cases discussed here for the NEVADA simulations are 25″ (63.5 cm) and 28" (71.1 cm). The minimum gap distance between the GA-MHTGR reactor vessel wall and the front surface of the RCCS riser ducts is 28″ (71.1 cm). In the FY 2010 work [2.2], the separation distance of 25″ (63.5 cm) was a baseline for the parametric calculations and provides a comparison point for this FY 2011 work. It was also decided to change the distance between the back of the riser ducts and the reflective NSTF test section box back plate from 4″ (10.1 cm) to 8″ (20.3 cm). This is in accordance with the scaling approach that dictates full-scale in the radial direction for the experiment. The distance from the back surface of the GA-MHTGR hot riser ducts to the metal front surface of the downcomer walls is 10″ (25.4 cm). But there is a layer of 2″ (5.0 cm) thick insulation on the front surface of the downcomer wall which

determines the need for this 8″ (20.3 cm) gap. The effect of this variation on the view factors from the heated box wall to the other surfaces in the test cross section is displayed in Figures 2.2 and 2.3. There is a 2-Group lumping of the riser ducts incorporated in the Figure 2.2 results. The Inner Group ducts are the eight central ducts and the Outer Group is the subset of the two outer ducts on each side of the Inner Group flanking the two side walls of the box. In this fashion the temperature gradient induced by the heat loss through the side wall insulation can be modeled by the corresponding RELAP5 calculations. The Figure 2.3 results are the corresponding results for a one-group lumping of the riser ducts. Both figures use a heated side of an infinite height (9999″ [25397.4 cm]). The purpose of this is to minimize the heat loss from the top and bottom. It essentially redistributes those view factors to the other surfaces. It was decided that the initial NSTF experiment use the separation distances of 28″ (71.1 cm) and 8″ (20.3 cm). Table 2.1 and Table 2.2 present the details of the raw view factor data for this experiment and the corresponding surface area used for Figure 2.2. However, when the view factors are used in the base RELAP5 models, heat losses to space through the top and bottom (up & down) of the NSTF test box cannot be taken into account. The corresponding adjusted view factors and areas for those calculations are tabulated in Tables 2.3 and 2.4 respectively. It can be seen that the up & down view factors have been deleted. These are the view factor numbers used in the RELAP5 calculations presented later in Section 2.3, since the RELAP5 models do not treat the axial radiation heat transfer.

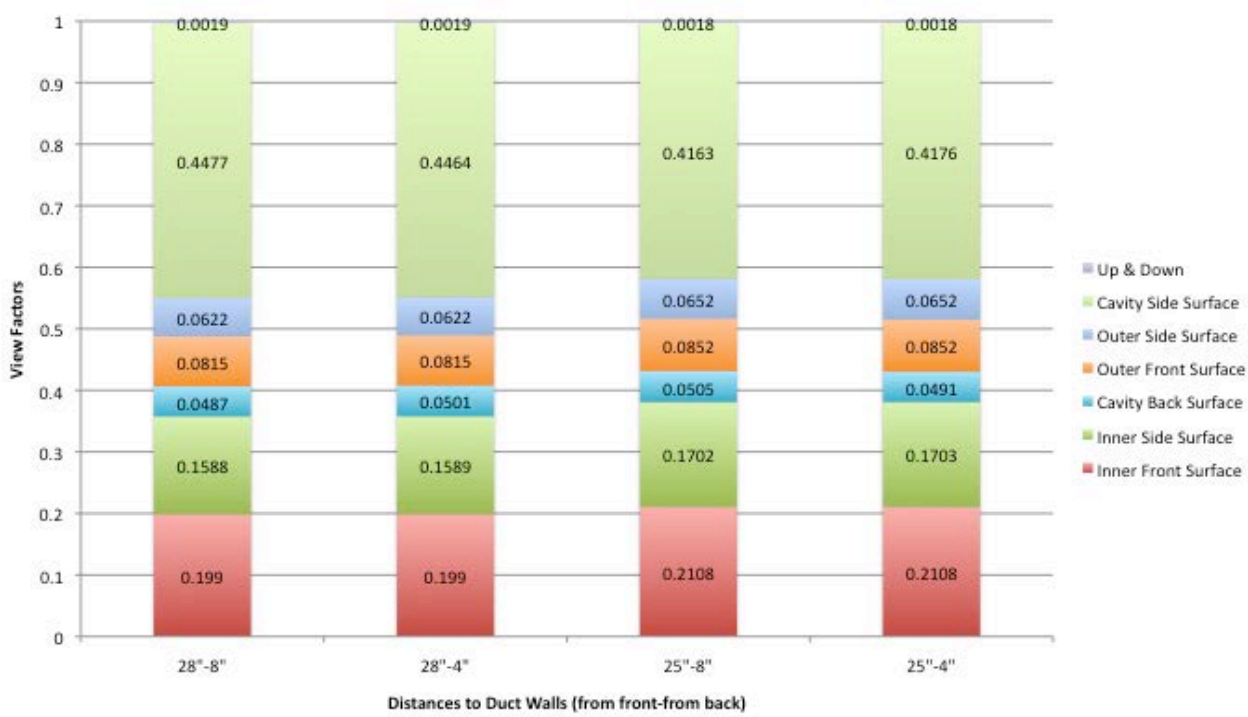

Figure 2.2. Two-Group Experiment View Factors with Riser Ducts (9999′ [25397.4 cm] Height)

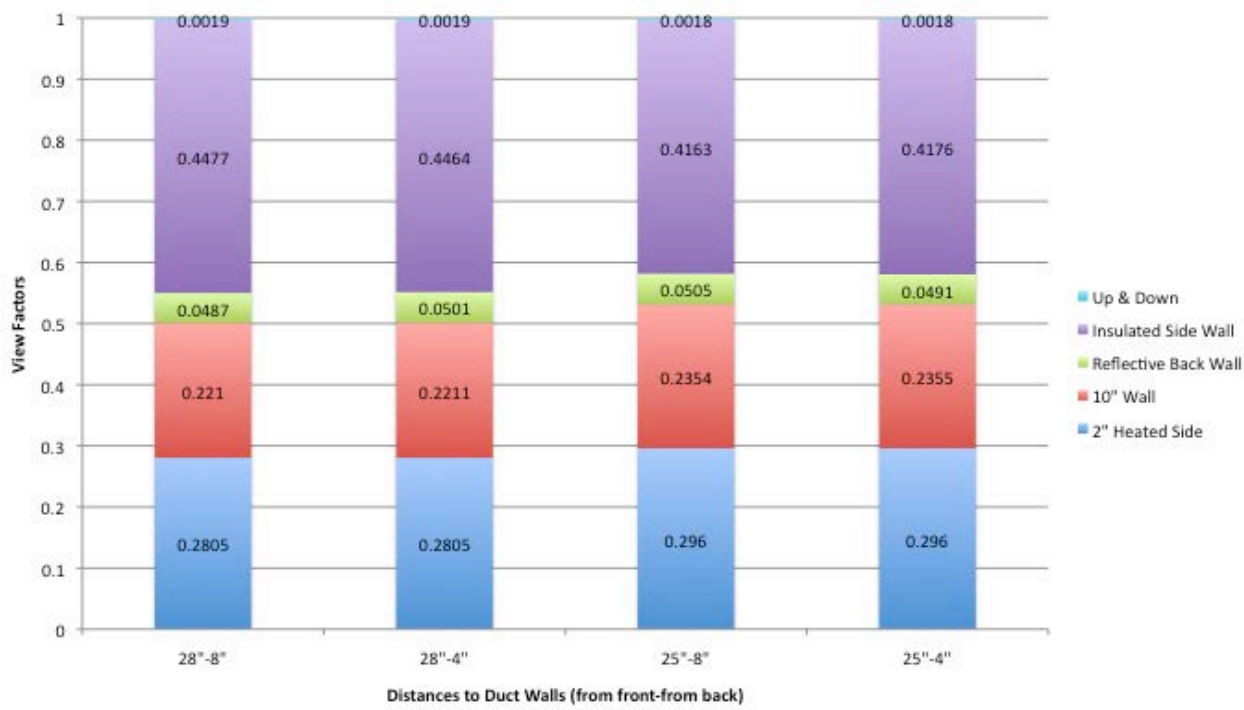

Figure 2.3. One-Group Experiment View Factors With Riser Ducts (9999″ [25397.4 cm] Height)

Table 2.1. Two Group Experiment View Factors 28″ (71.1 cm) -8″ (20.3 cm) Separation (9999″ [25397.4 cm])

				Inner Group				Outer Group				
			Reactor	2" Riser Surface Facing Reactor	10 " Side Riser Surface	2" Riser Surface Facing Cavity Wall	Cavity Back Surface	2" Riser Surface Facing Reactor	10 " Side Riser Surface	2" Riser Surface Facing Cavity Wall	Cavity Side Surface	Up & Down
			Heated	FW2	SW3	WTB3	UH3	FW1	SW1	WTB	UH1	Space
			1	2	3	4	5	6	7	8	9	
	Heated	1	0.0	0.1990	0.1588	0.0	0.0487	0.0815	0.0622	0.0	0.4477	0.0019
Inner Group	FW2	2	0.6472	0.0	0.0001	0.0	0.0	0.0	0.0	0.0	0.3508	0.0019
	SW3	3	0.0516	0.0	0.7174	0.0	0.0824	0.0	0.1022	0.0	0.0461	0.0004
	WTB3	4	0.0	0.0	0.0	0.0	0.9356	0.0	0.0	0.0	0.0637	0.0007
	UH3	5	0.0488	0.0	0.2529	0.2879	0.0	0.0	0.0927	0.1201	0.1967	0.0009
Outer Group	FW1	6	0.5294	0.0	0.0	0.0	0.0	0.0	0.0001	0.0	0.4689	0.0016
	SW1	7	0.0404	0.0	0.2050	0.0	0.0604	0.0	0.4098	0.0	0.2840	0.0004
	WTB	8	0.0	0.0	0.0	0.0	0.7794	0.0	0.0	0.0	0.2200	0.0006
	UH1	9	0.2530	0.0610	0.0802	0.0110	0.1111	0.0409	0.2471	0.0191	0.1751	0.0015

Table 2.2. Two Group Experiment View Areas 28″ (71.1 cm) -8″ (20.3 cm) Separation NEVADA (9999″ [25397.4 m])

		Inner Group				Outer Group			
	Reactor	2" Riser Surface Facing Reactor	10 " Side Riser Surface	2" Riser Surface Facing Cavity Wall	Cavity Back Surface	2" Riser Surface Facing Reactor	10 " Side Riser Surface	2" Riser Surface Facing Cavity Wall	Cavity Side Surface
Area in^2	3610.750	1111.000	11110.000	1111.000	3610.750	555.500	5555.000	555.500	6388.250

Table 2.3. Two Group Experiment View Factors 28″ (71.1 cm) -8″ (20.3 cm) Separation Adjusted (9999″ [25397.46 cm])

				Inner Group				Outer Group			
			Reactor	2" Riser Surface Facing Reactor	10 " Side Riser Surface	2" Riser Surface Facing Cavity Wall	Cavity Back Surface	2" Riser Surface Facing Reactor	10 " Side Riser Surface	2" Riser Surface Facing Cavity Wall	Cavity Side Surface
			Heated	FW2	SW3	WTB3	UH3	FW1	SW1	WTB	UH1
			1	2	3	4	5	6	7	8	9
	Heated	1	0.0	0.1994	0.1587	0.0	0.0487	0.0817	0.0617	0.0	0.4497
Inner Group	FW2	2	0.6485	0.0	0.0	0.0	0.0	0.0	0.0	0.0	0.3515
	SW3	3	0.0516	0.0	0.7173	0.0	0.0823	0.0	0.1022	0.0	0.0046
	WTB3	4	0.0	0.0	0.0	0.0	0.9363	0.0	0.0	0.0	0.0637
	UH3	5	0.0489	0.0	0.2532	0.2881	0.0	0.0	0.0928	0.1200	0.1970
Outer Group	FW1	6	0.5303	0.0	0.0	0.0	0.0	0.0	0.0	0.0	0.4693
	SW1	7	0.0401	0.0	0.2044	0.0	0.0603	0.0	0.4100	0.0	0.2852
	WTB	8	0.0	0.0	0.0	0.0	0.7799	0.0	0.0	0.0	0.2201
	UH1	9	0.2537	0.0610	0.0804	0.0111	0.1112	0.0408	0.2475	0.0191	0.1754

Table 2.4. Two Group Experiment View Areas 28″ (71.1 cm)-8″ (20.3 cm) Separation Adjusted (9999″ [25397.46 cm])

		Inner Group				Outer Group			
	Reactor	2" Riser Surface Facing Reactor	10 " Side Riser Surface	2" Riser Surface Facing Cavity Wall	Cavity Back Surface	2" Riser Surface Facing Reactor	10 " Side Riser Surface	2" Riser Surface Facing Cavity Wall	Cavity Side Surface
Area in^2	3610.750	1111.000	11110.000	1111.000	3610.750	555.500	5555.000	555.500	6388.250

One special parameteric case has been performed where the RELAP5 base model has been modified to include a lumped top/bottom heat structure slab. The model therefore accounts for the radiation to the top and bottom of the NSTF section box. These losses require the view factors for the 22′ (6.7 m) height NSTF test section with the top and bottom included. Table 2.5 shows the required view factors while Table 2.6 give the corresponding areas.

Table 2.5. Two Group Experiment View Factors 28″ (71.1 cm) -8″ (20.3 cm) Separation (22′ [6.7 m])

				Inner Group				Outer Group				
			Reactor	2" Riser Surface Facing Reactor	10 " Side Riser Surface	2" Riser Surface Facing Cavity Wall	Cavity Back Surface	2" Riser Surface Facing Reactor	10 " Side Riser Surface	2" Riser Surface Facing Cavity Wall	Cavity Side Surface	Up & Down
			Heated	FW2	SW3	WTB3	UH3	FW1	SW1	WTB	UH1	Space
			1	2	3	4	5	6	7	8	9	
	Heated	1	0.0	0.1846	0.1846	0.0	0.0435	0.0754	0.0569	0.0	0.4225	0.0709
Inner Group	FW2	2	0.6006	0.0	0.0	0.0	0.0	0.0	0.0	0.0	0.3274	0.0720
	SW3	3	0.0476	0.0	0.7128	0.0	0.0798	0.0	0.1017	0.0	0.0433	0.0148
	WTB3	4	0.0	0.0	0.0	0.0	0.9356	0.0	0.0	0.0	0.0604	0.0007
	UH3	5	0.0435	0.0	0.2451	0.2809	0.0	0.0	0.0899	0.1170	0.1911	0.0325
Outer Group	FW1	6	0.4894	0.0	0.0	0.0	0.0	0.0	0.0	0.0	0.4497	0.0610
	SW1	7	0.0370	0.0	0.2036	0.0	0.0585	0.0	0.4076	0.0	0.2796	0.0136
	WTB	8	0.0	0.0	0.0	0.0	0.7609	0.0	0.0	0.0	0.2153	0.0238
	UH1	9	0.2387	0.0572	0.0752	0.0105	0.1081	0.0392	0.2434	0.0187	0.1534	0.0556

Table 2.6. Two Group Experiment View Areas 28″ (71.1 cm) -8″ (20.3 cm) Separation (22′ [6.7 m])

		Inner Group				Outer Group			
	Reactor	2" Riser Surface Facing Reactor	10 " Side Riser Surface	2" Riser Surface Facing Cavity Wall	Cavity Back Surface	2" Riser Surface Facing Reactor	10 " Side Riser Surface	2" Riser Surface Facing Cavity Wall	Cavity Side Surface
Area in^2	95.333	29.3333	293.333	29.3333	95.333	14.66667	146.6667	14.66667	168.666

2.1.2 Experiment Geometry: Intraduct

As mentioned in Section 2.1.1, the risers consist of metal plates making up the 10″ (25.4 cm) by 2″ (5.0 cm) ducts. Given the temperature difference across the cavity box, there is heat transfer between these metal plates that comprise the surface of the riser ducts. Duct wall conduction is clearly one possible heat transfer model, but given the elevated temperatures, there is also the potential for intraduct radiation heat transfer inside the hot riser. In the T-F sensitivity analyses documented in this report, most models for all the four base RELAP5 models compared the difference between setting the heat transfer method of the duct walls interacting with each other from conduction to radiation. Given the drastic difference between the cross-sectional areas, as seen in Figure 2.4 and the height of the risers, the intraduct radiation heat transfer is treated as 2-D exchange between surfaces in an enclosure. Using this concept, the view factors were calculated using the reciprocity rule

$$A_A F_{A \to B} = A_B F_{B \to A} \tag{65}$$

and the summation rule

$$\sum_{j=1}^{n} F_{S_i \to S_j} = 1 \tag{66}$$

where F is the view factor and A is the surface area.

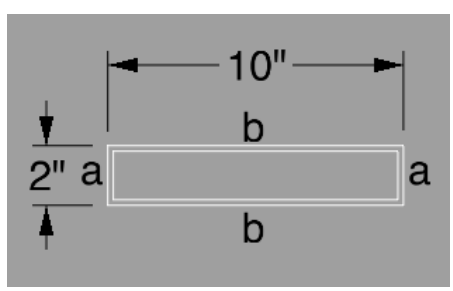

Figure 2.4. Riser Duct Cross Section

Applying Eq. (65) to the a sides

$$A_{a1} = A_{a2} = A_a \tag{67}$$

$$A_{a1} F_{a1 \to a2} = A_{a2} F_{a2 \to a1} \Rightarrow F_{a1 \to a2} = F_{a2 \to a1}. \tag{68}$$

With the b sides merged together,

$$2A_b = A_B \tag{69}$$

and Eq. (65) gives

$$F_{B\to a1} = F_{B\to a2} \tag{70}$$

$$F_{B\to a1} = F_{a1\to B}\frac{A_a}{A_b}. \tag{71}$$

Applying Eq. (66) to side B makes

$$F_{B\to B} + F_{B\to a1} + F_{B\to a2} = 1 \tag{72}$$

and Eq. (70) makes it

$$F_{B\to B} = 1 - 2F_{B\to a1}. \tag{73}$$

A solution was generated with the use of a iterative method based on Eq. (68), Eq. (70), Eq. (71), and Eq. (72). The results are presented in Table 2.7. These are the view factor values used in the RELAP5 calculations presented later in Section 2.3.

Table 2.7. Riser Duct Internal Radiation View Factors

		2" Riser Surface Facing Reactor	10 " Side Riser Surface	2" Riser Surface Facing Cavity Wall
		1	2	3
2" Riser Surface Facing Reactor	1	0	0.9162	0.0838
10 " Side Riser Surface	2	0.0916	0.8168	0.0916
2" Riser Surface Facing Cavity Wall	3	0.0838	0.9162	0

2.2 RELAP5 Modeling

The focus of the modeling work during FY 2011 was on the NSTF experiment RELAP5 model. The RELAP5 full-scale model and the RELAP5 half-scale model were not the focus of the modeling work during FY 2011, so an expanded description of the NSTF experiment RELAP5 model is provided here.

2.2.1 Full-Scale Model

Details of the RELAP5 full-scale model are available in [2.2]. For convenience Figure 2.5 showing the nodalization of the RELAP5 full-scale model is provided here. This is reproduced from the reference.

2.2.2 Half-Scale Model

The half-scale system was converted directly from the full-scale model. The design layout and nodalization is identical, and all assumptions made in the full scale were carried forward to the half-scale. The system was scaled down to half scale according to the scaling reported in Section 1.3. Essentially, the lengths and heights were halved but the widths, depths, diameters and thicknesses in the plane cross-section were kept unaltered. Since the half-scale deck was built by converting the full-scale deck it is the same set of modeling issues discussed in [2.2]. Figure 2.6 shows the RELAP5 nodalization for the half-scale model. Additional details regarding the half-scale RELAP5 model are available in Ref. [2.2].

2.2.3 1 Channel NSTF Model

Figure 2.7 shows the experimental system RELAP5 model, which is based on the NSTF experiment cross section shown in Figure 2.1. The 12 hot risers in the test cavity box section are grouped together into pipe P970. The riser lengths are selected to be 22′ (6.7m). The heat structure HS9000, which simulates the heated wall of the box, represents the hot reactor vessel wall. The height is equivalent to the 22′ (6.7m) of the risers. Heat structure HS8000 and branch B800 are the NSTF ceramic heaters and the one-eight inch air gap between these heaters and the heated box wall. The cavity box back wall is given by HS9001. All the box walls are externally insulated. The branch B900 is connected to the volume TD905 to represent the box cavity air. TD905 is a large volume of air that creates an isothermal heat sink to absorb the parasitic heat losses and to smooth out any volume expansion by temperature changes in the branch B900. HS9700, HS9701, and HS9702 simulate the front wall, two lumped side walls, and back wall of the inner group of riser ducts. The external ducting and hot manifold for the heated air from the test box hot risers is represented by pipe P978. It also includes the chimney discharging to the atmosphere. HS9780 is the metal structure around this flow path. The bottom suction inlet to the test box cavity is represented by junction J952 which takes its suction from the atmospheric air in volume TD950. TD980 is the corresponding air volume on the discharge side.

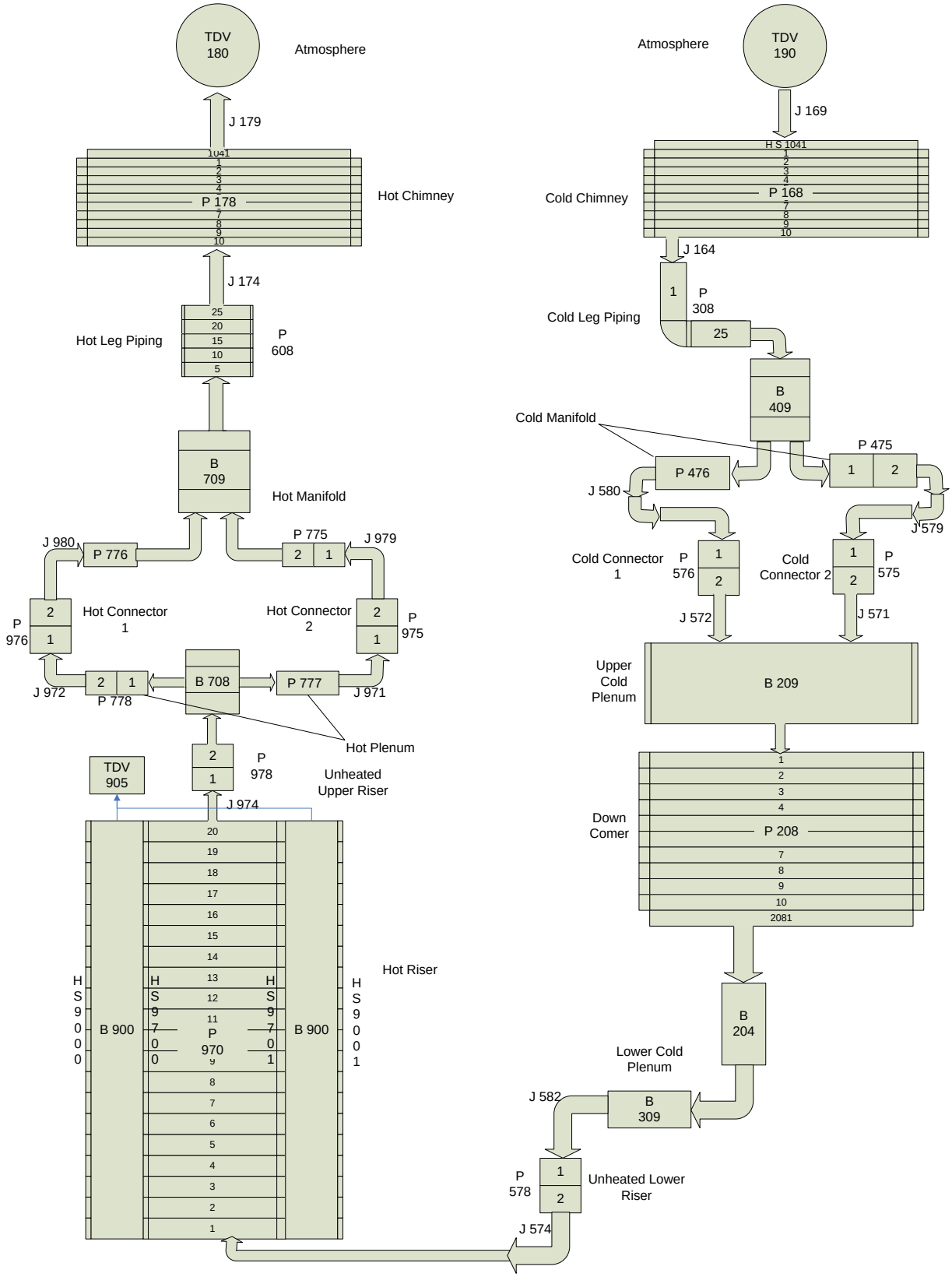

Figure 2.5. Full-Scale Model Cavity and Duct Network

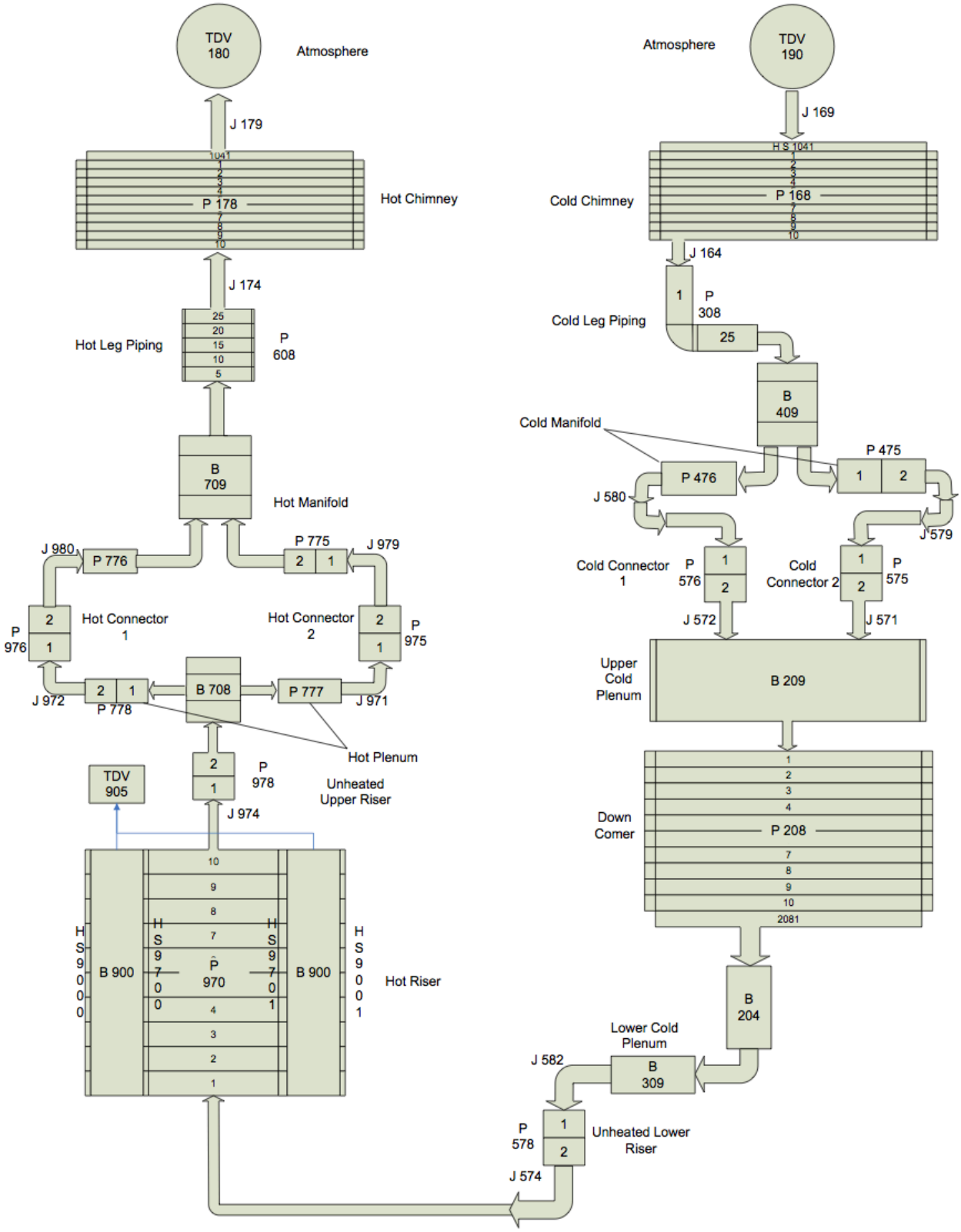

Figure 2.6. Half-Scale Model Cavity and Duct Network

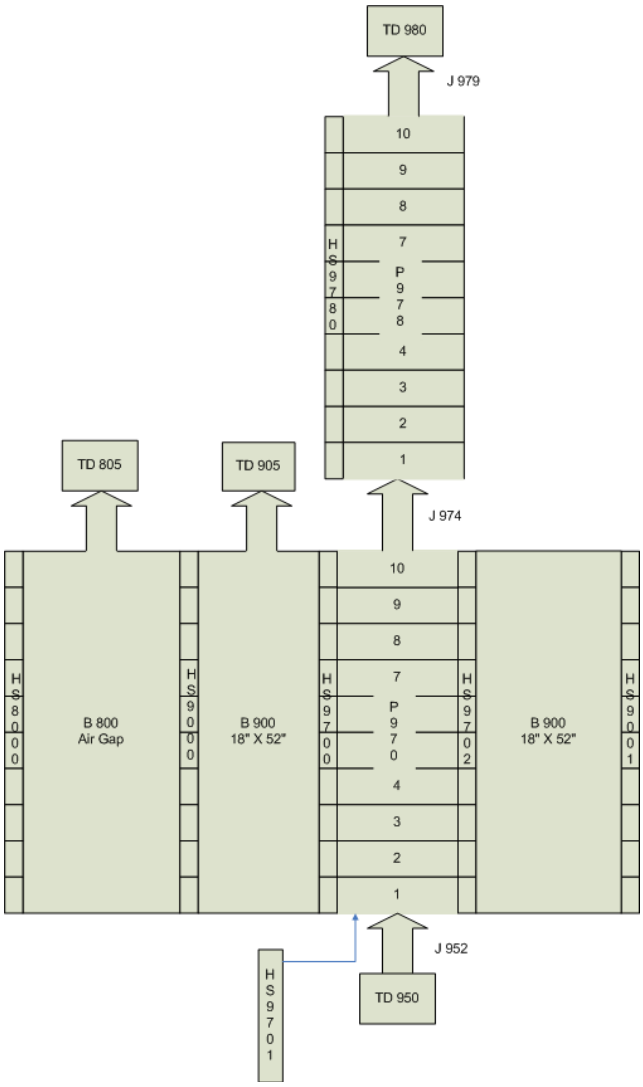

Figure 2.7. Experiment 1—Channel System Model Cavity and Duct Network

2.2.4 2-Channel NSTF Model

Figure 2.8 shows the 2 channel experimental system RELAP5 model. This is based on the NSTF experiment cross section shown in Figure 2.1. A number of experiment cross section configurations are under discussion but they mainly involve varying the separation distance between the heated surface of the box and the hot risers. The test cavity box depth will be of variable design. There may be experiment configurations where the array of hot riser ducts is offset by a yet-to-be-determined angle to simulate corners of the cavity. Figure 2.8 will be the starting basis for modifying RELAP5 models as the experiment matrix is defined.

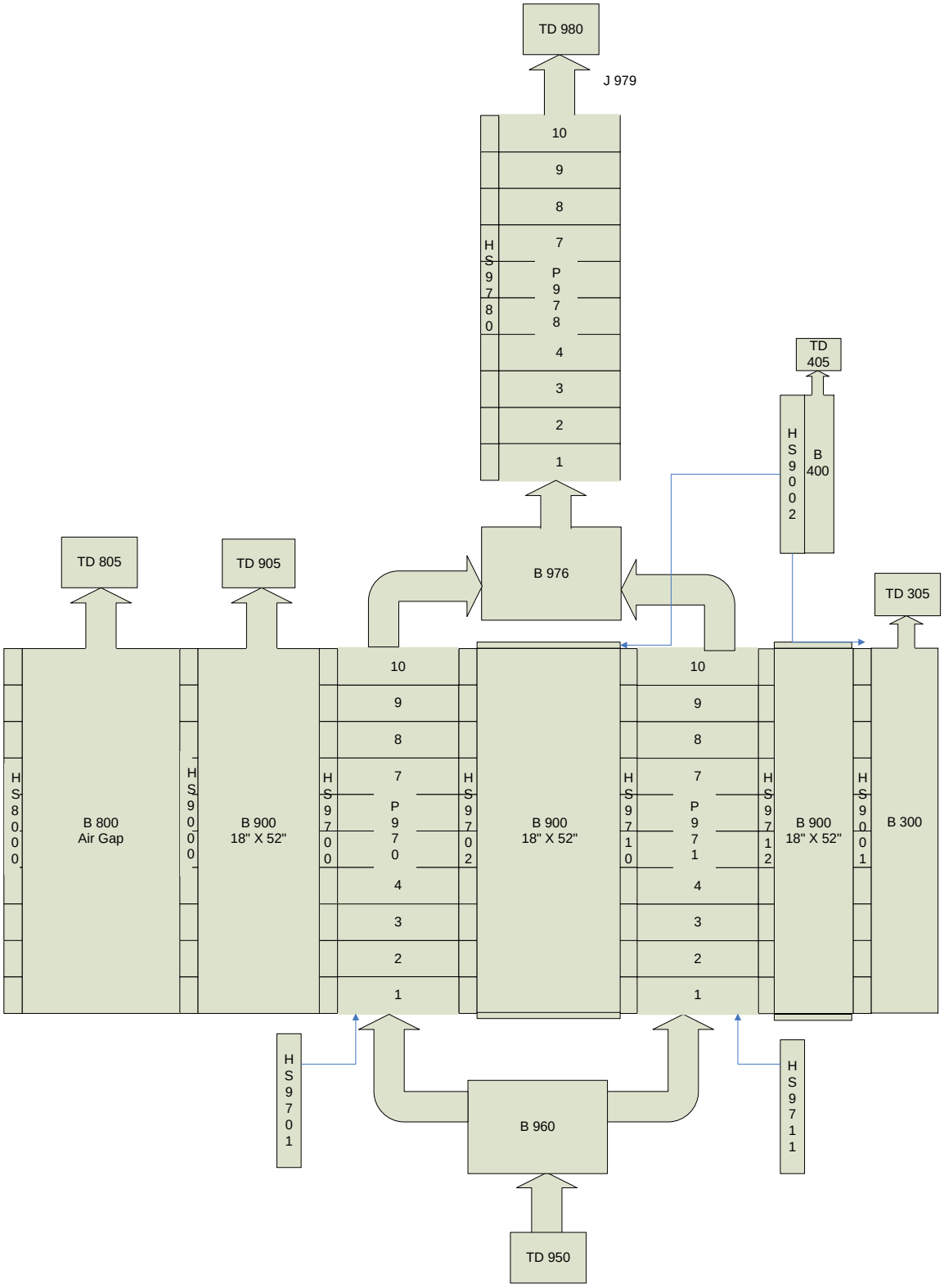

Figure 2.8. Experiment 2-Channel System Model Cavity and Duct Network

The 12 hot risers in the test cavity box section are grouped into two separate RELAP5 channels. These two channels are pipes P970 and P971. This is a two group lumping of the riser ducts incorporated in this model. The inner group consists of the eight inner central ducts and the outer group is the subset of the two outer ducts on each side of the inner group flanking the two side walls of the test section box. In this fashion the temperature gradient induced by the heat loss through the side wall insulation can be modeled by the corresponding RELAP5 calculations. The riser lengths are selected to be 22′ (6.7 m). This is the heated surface height/length of heat structure HS9000, which simulates the heated wall of the box. This heated wall represents the hot vessel wall. Heat structure HS8000 and branch B800 are the NSTF ceramic heaters and the one-eighth inch air gap between these heaters and the heated box wall. The cavity box back wall is given by HS9001. The side wall is HS9002. All the box walls are externally insulated. Heat losses to the surrounding air from the insulation are also accounted for by the inclusion of the branches B300 and B400 on the outside to represent the surrounding air. Volumes TD405 and TD305 are arbitrary large volumes of air that form isothermal heat sinks to absorb the parasitic heat losses and to smooth out any volume expansion caused by temperature changes in the branches. A similar arrangement of branch and connected volume B900/TD905 is used to represent the box cavity air. HS9700, HS9701, and HS9702 simulate the front wall, two lumped side walls and back wall of the inner group of riser ducts. HS9710, HS9711, and HS9712 are the walls for the other group of riser ducts. The external ducting and hot manifold for the heated air from the test box hot risers is represented by pipe P978. It also includes the chimney discharging to the atmosphere. HS9780 is the metal structure around this flow path. The bottom suction inlet to the test box cavity is represented by branch B960, which takes its suction from the atmospheric air in volume TD950. TD980 is the corresponding air volume on the discharge side.

Both natural convection heat transfer and radiation heat transfer are simulated in the model. However, the radiant heat transfer is only in the plane cross section as specified by the view factors. Axial radiation heat transfer, in particular to the top and bottom of the test cavity box, is not simulated. Included in this iteration on RELAP5 modeling is the effect of intrariser duct radiation between the four internal surfaces of the hot riser ducts. Previously the circumferential conduction around the duct walls of the hot riser ducts was simulated but this has been replaced by the simulation of the intraduct radiant heat transfer. Ambient heat losses from the insulated chimney system to the building environment will be included in the next iteration.

2.3 Full/Half RCCS Model RELAP5 Results

The results presented herein are a follow-on to the initial analysis work supporting the experiment design documented in the FY 2010 report [2.2]. The primary goal of this follow-on work is to confirm the scaling laws being utilized to design the half-scale NSTF experiments. The secondary goal is to perform sensitivity parametrics to evaluate the importance of the modeling assumptions made in the supporting analysis.

To confirm the validity of the scaling laws, the FY 2010 one-hot riser model deck was used as the baseline for the full-scale GA-MHTGR air heat sink system analysis. The model was used to confirm the scaling laws and sensitivities to heat flux profiles, thus testing system response. Modifications will be made in the next iteration to better model heat losses such as those between cold and hot ducting. In addition to the full-reactor-scale cases, a series of cases

were run with a half-scale model at heat fluxes proportionally scaled to the full size. This half-scale deck is also used to verify the scaling analysis. The duct flow areas and the radial dimensions of the cavity are maintained at full scale. Duct length, height, and the cavity height are halved. The system power is reduced by a factor of the square root of 2, and the scaled heat flux is increased by the same factor to maintain the scaled heat added per unit volume over the riser ducts. There are also three corresponding heat flux cases (high, medium, and low), but with different numerical values from the full-scale cases. The friction drop dimensionless number will have to be preserved in the scaling. Discussions are ongoing with the experimenters about calibration procedures for the system pressure flow drop at selected forced flow rates.

With the extremely low pressure drops under natural circulation at atmospheric conditions, experimental experience shows that it will be difficult to determine the friction drop dimensionless number from the experiment measurements. An alternative is to preserve the air outlet temperature at the exit of the hot riser ducts by introducing the requisite orifice. This is one of the consequences of preserving the friction drop number under the scaling laws derived for these NSTF experiments, since the chimney air inlet temperatures, by definition, are the same as for the full-scale GA-MHTGR case. By implication, the pressure drops should then be preserved with this orificing under isothermal conditions for the forced flow case, between the half-scale configuration and the full-scale configuration when the air velocities are the same. Since the isothermal densities should be the same, the mass flow should be set at half the full-scale value. Another method to confirm the validity of the scaling law is to vary the driving metal vessel heat flux and determine if the hot riser air outlet temperature is still preserved for the same orificing between the two scaled configurations at the different power levels.

Table 2.8 shows the important T-F parameters for the various RELAP5 cases conducted to confirm the scaling laws. Results from the various sensitivity analyses performed to evaluate the effect of different modeling assumptions are also included. Details of each of these cases are outlined in the following sections.

Table 2.8. Summary of Full-Scale/Half-Scale Case Results

Model	Heat Flux	J574 energy loss coefficient	Duct Heat-Transfer Type Radiation / Conduction	Transient Length[s]	Peak Front Duct Wall Heat Flux [kW/m^2]	Peak Air Mass Flow Rate [kg/s]	Peak Duct Air Flow Velocity [m/s]	Peak Temperatures [K]			Peak Duct Temperatures [K]		
								RPV	Cavity Wall	Air Duct Outlet	Front Wall	Side Wall	Back Wall
Full Scale	High	X	Conduction	24000	4.51	7.5	8.43	739	471	471	593	505	519
Full Scale	Med	X	Conduction	24000	2.20	6.62	6.28	602	389	393	467	411	420
Full Scale	Med (Axial)	X	Conduction	24000	2.20	6.66	6.50	729	417	396	533	438	419
Full Scale	Isothermal	X	X	24000	0.00	53.74	40.05	295	295	296	295	295	295
Full Scale	High	X	Radiation	24000	4.51	7.50	8.43	735	469	471	566	517	508
Full Scale	Med (Axial)	X	Radiation	24000	2.20	6.66	6.50	726	416	396	503	435	422
Half Scale	High	0.5	Conduction	24000	5.84	6.02	6.71	807	514	451	642	544	519
Half Scale	High	2.2	Conduction	24000	5.84	5.89	6.41	809	517	455	653	548	523
Half Scale	High	4.4	Conduction	24000	5.84	5.40	6.24	816	528	468	669	555	541
Half Scale	High	8.8	Conduction	24000	5.84	4.74	5.55	828	546	491	693	594	571
Half Scale	High	8.8	Radiation	24000	5.84	4.75	5.55	820	542	491	648	588	577
Half Scale	Isothermal	8.8	X	24000	0.00	53.75	41.55	294	294	294	294	294	294
Half Scale	Med	4.4	Conduction	24000	2.88	4.72	4.48	662	420	393	520	447	432

2.3.1 Full-Scale Axial Power Variation

This case with the vessel wall axial heat flux variations is compared to the results of the spatially uniform Medium Heat Flux model previously obtained in [2.2]. The heat flux profile applied to the reactor vessel was given a chopped cosine distribution as shown in Figure 2.9. The axial locations included in the figures start from the bottom of the riser and proceed to the top. The average heat flux on the pressure vessel wall was 4.97 kW/m^2, which is equivalent to 0.715 MW of total heat from half the system. This average surface heat flux is taken over the cylindrical part of the reactor vessel. Driven by this incident heat flux, the heat transferred from the outer surface of the pressure vessel wall is partitioned into an average radiation heat flux of 4.0 kW/m^2 and an average convective heat flux of 0.95 kW/m^2. This leads to a heat flux incident upon the front wall of the hot riser duct of 2.20 kW/m^2. The transient duration was 24,000 seconds.

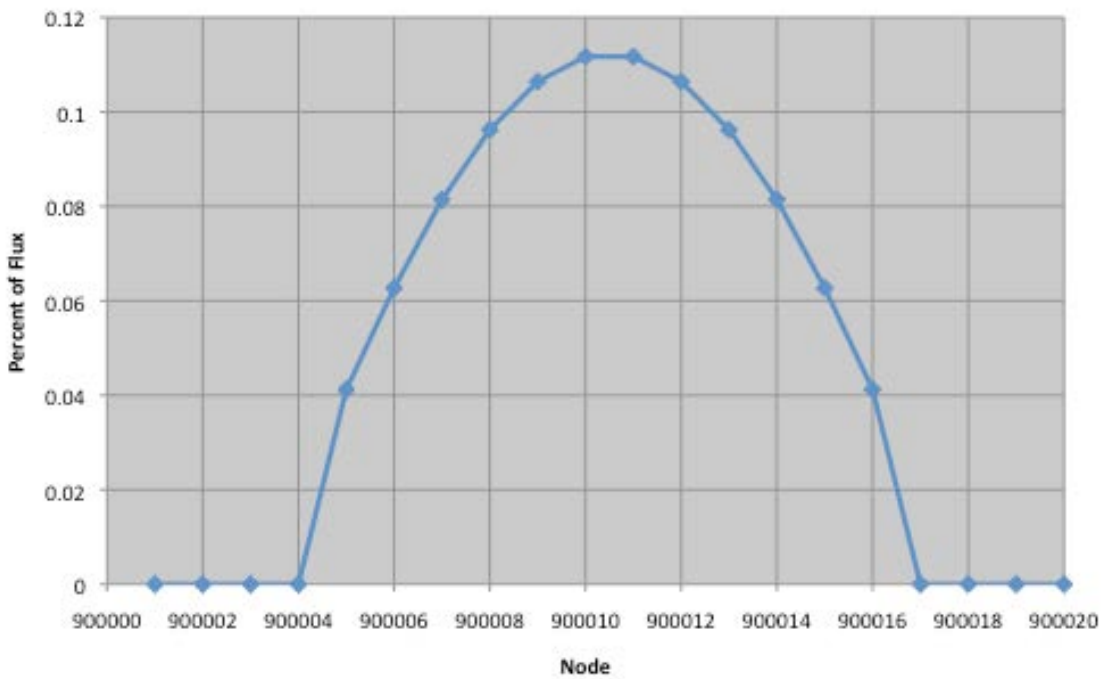

Figure 2.9. Full-Scale/Medium Flux Reactor Vessel Wall Heat Flux

Table 2.8 shows the peak air mass flow rate as 6.66 kg/s and the peak duct airflow velocity as 6.50 m/s. The peak reactor pressure vessel wall temperature is 729 K and the peak cavity wall temperature is 417 K. The air temperature exiting the duct outlet is 396 K. The peak temperatures of the front wall, side wall, and back wall of the riser ducts are 533 K, 438 K, and 419 K respectively. Figure 2.10 shows the time history of the riser duct air mass flow rate while Figure 2.11 shows the air mass flow rate at several various locations after it has passed through the hot risers. Figures 2.12 and 2.13 show the corresponding airflow velocities.

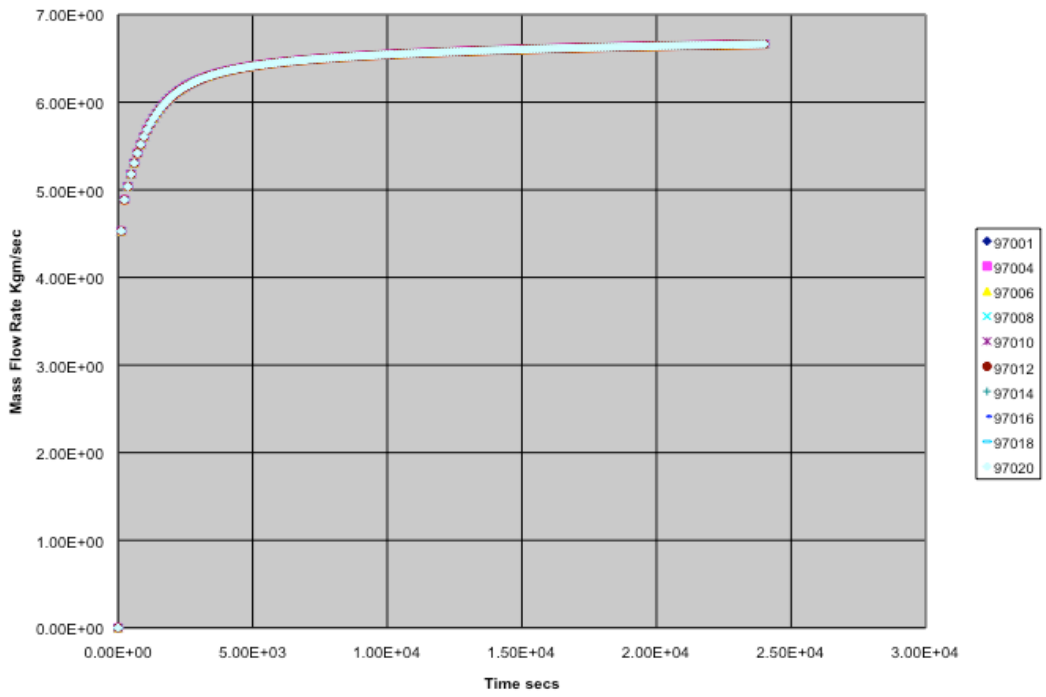

Figure 2.10. Full-Scale/Medium Flux Riser Duct Air Total Mass Flow

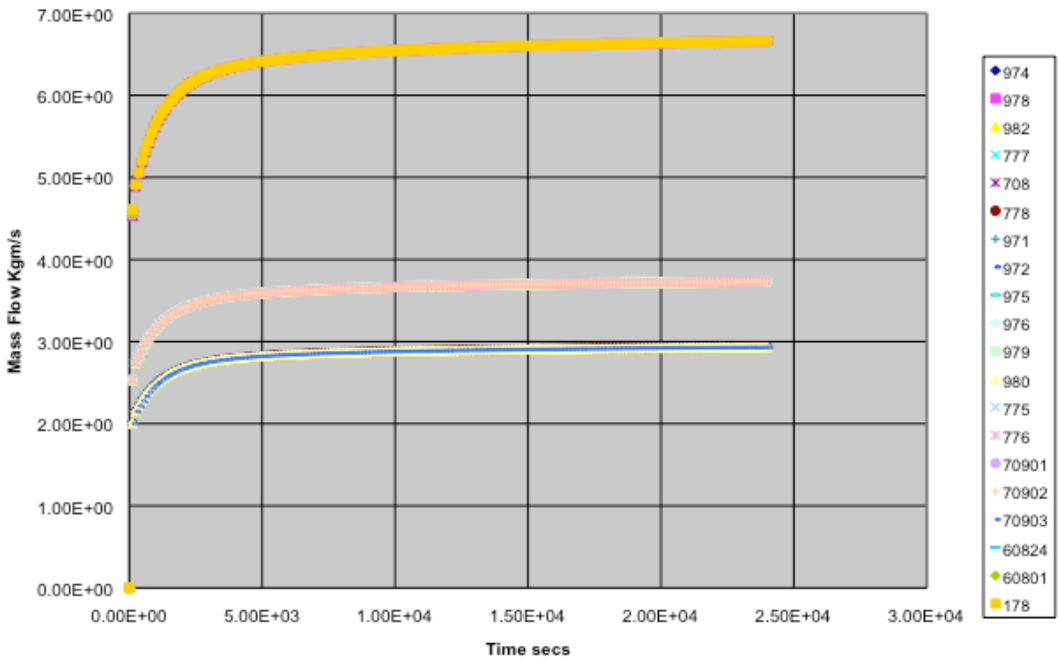

Figure 2.11. Full-Scale/Medium Flux Hot Network Air Mass Flow

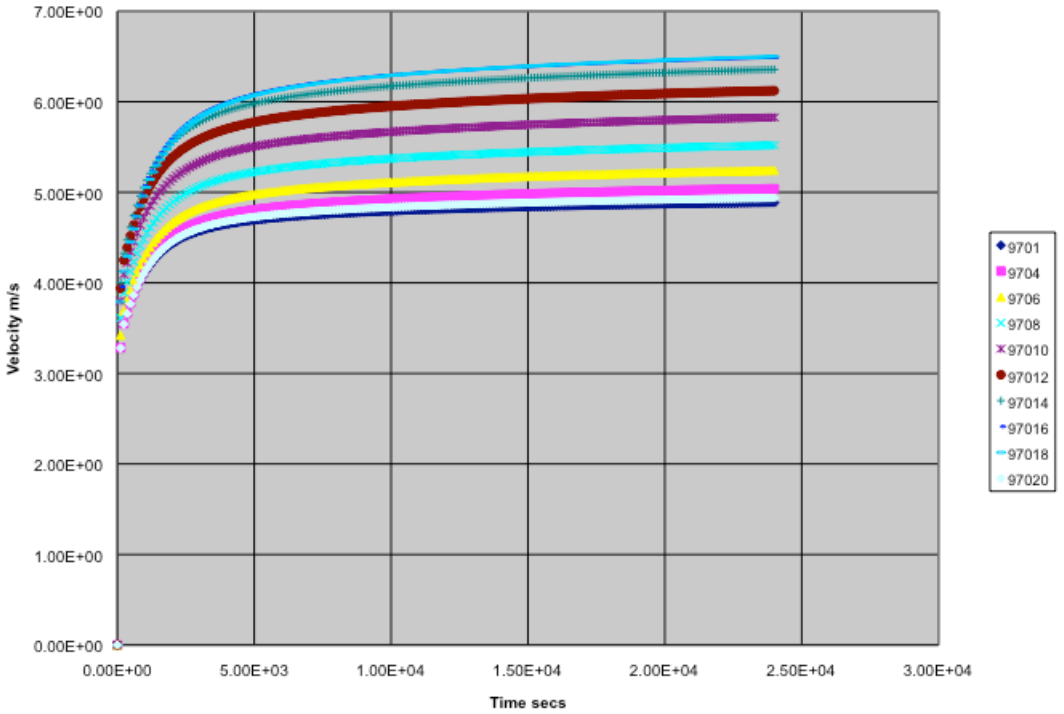

Figure 2.12. Full-Scale/Medium Flux Riser Duct Air Velocity

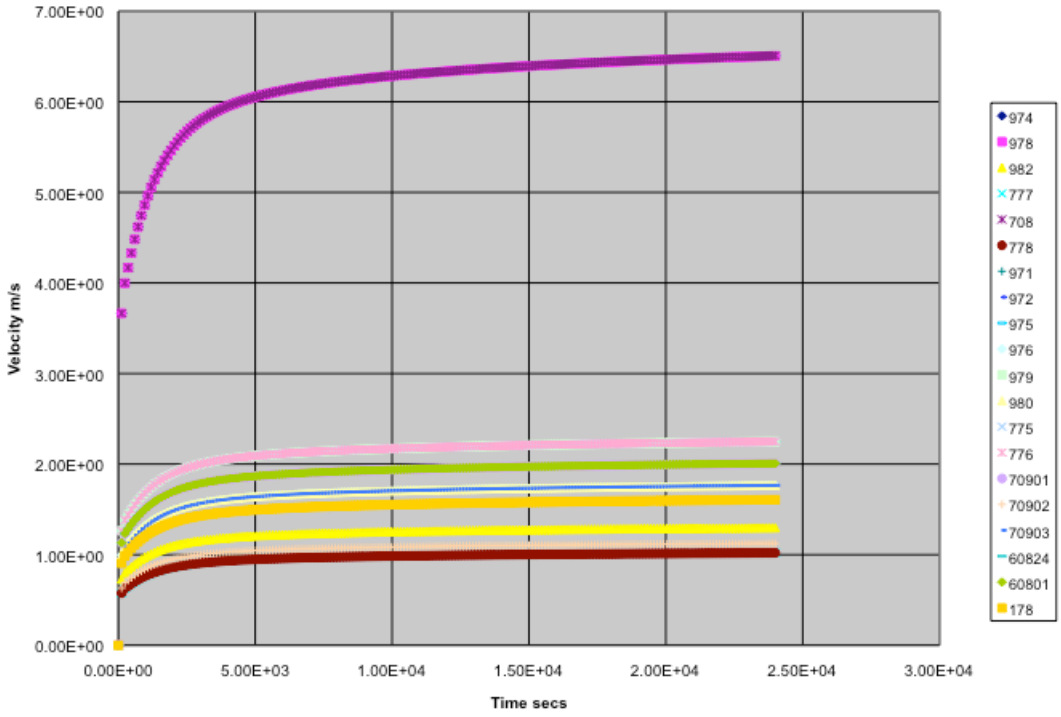

Figure 2.13. Full-Scale/Medium Hot Network Air Velocity

The transient history of the pressure vessel outer wall temperature is given at the surface nodes starting from the bottom and proceeding to the top of the heated segment in Figure 2.14 while Figure 2.15 shows the corresponding liner (insulation) temperature at the corresponding axial locations on the back wall of the cavity. More details on the temperatures of the hot riser duct can be found in Figure 2.16. The transient behavior of the temperatures of the hot riser duct front wall, side wall, back wall, and air coolant can be observed. The metal temperatures in these figures are axial profiles starting with the bottom node and proceed to the outlet end. In the case of the air temperature, temperatures ex-hot riser duct can also be found in Figure 2.16d. The locations start with the cold chimney inlet and transport through the cold suction ducting and manifolds down through the top and bottom cold plenums by way of the downcomer. Hot side locations can also be found in Figure 2.16d where the air heated by the transferred core residual heat rises out off the outlet of the hot riser into the hot plenum and thereon to the hot discharge ducting and manifolds into the hot chimney for ultimate discharge into the atmosphere.

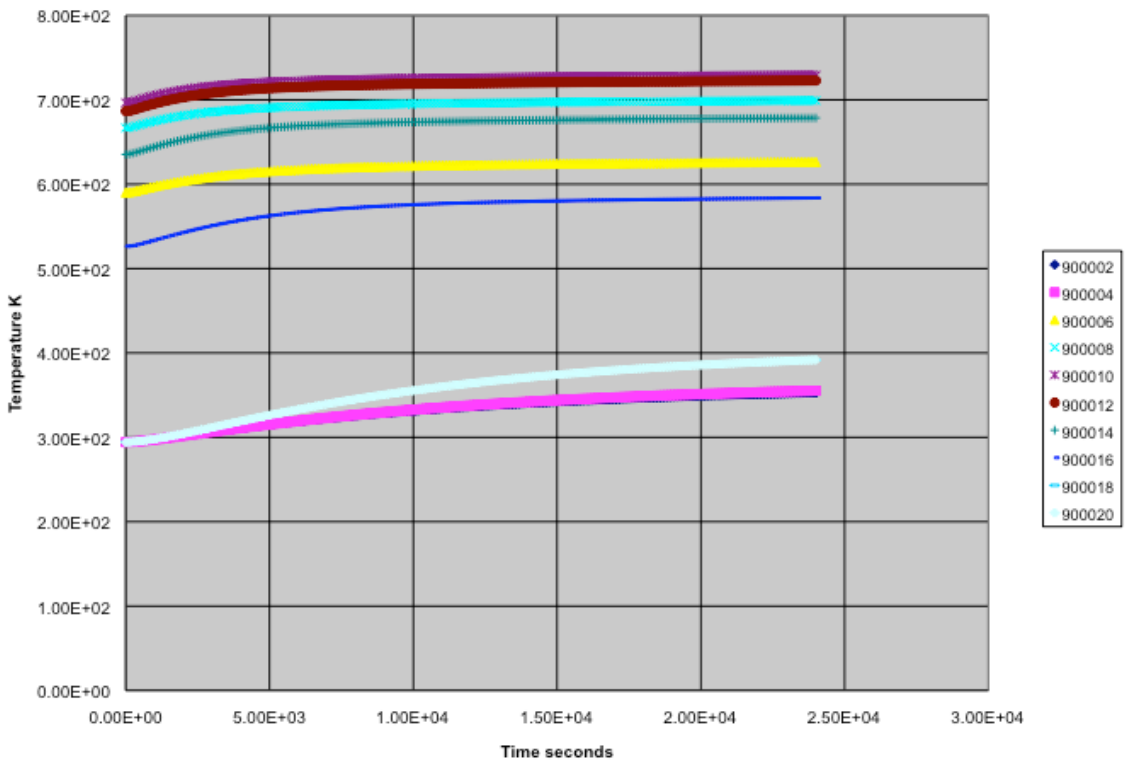

Figure 2.14. Full-Scale/Medium Flux Rpv Temperature

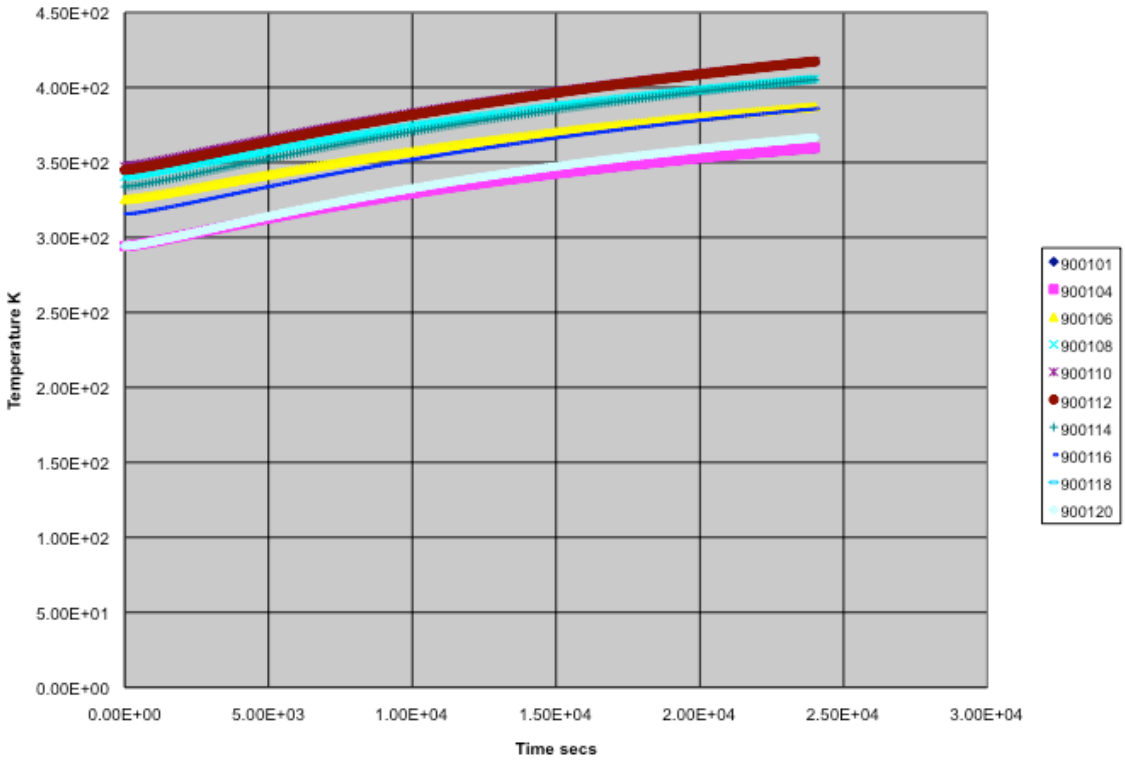

Figure 2.15. Full-Scale/Medium Flux Cavity Back Liner Temperature

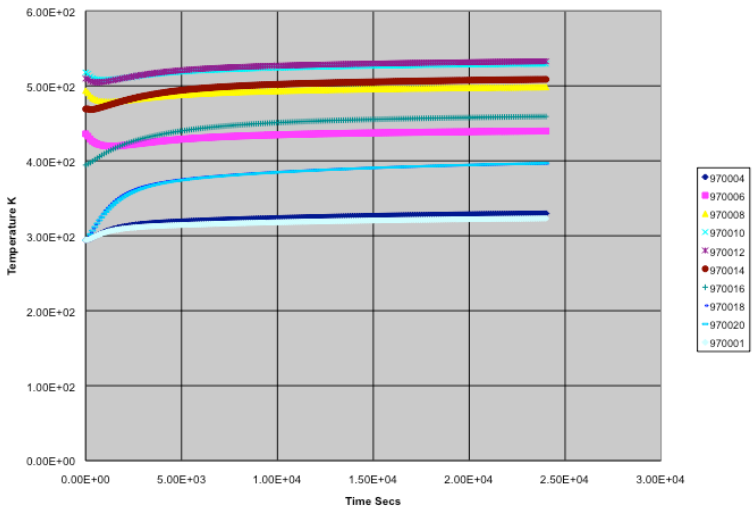

Figure 2.16a. Front wall temperatures

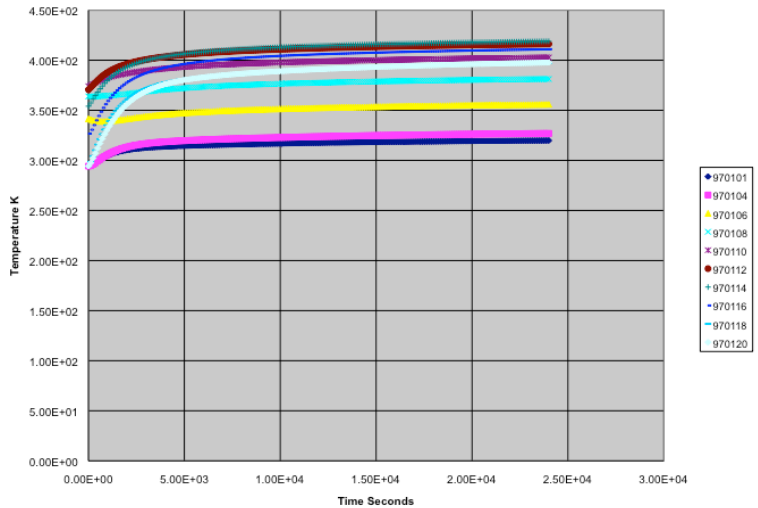

Figure 2.16b. Side Wall Temperatures

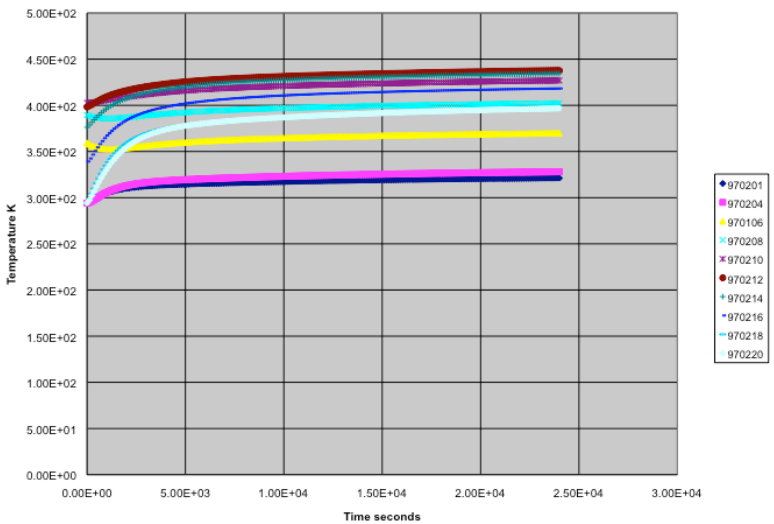

Figure 2.16c. Back Wall Temperatures

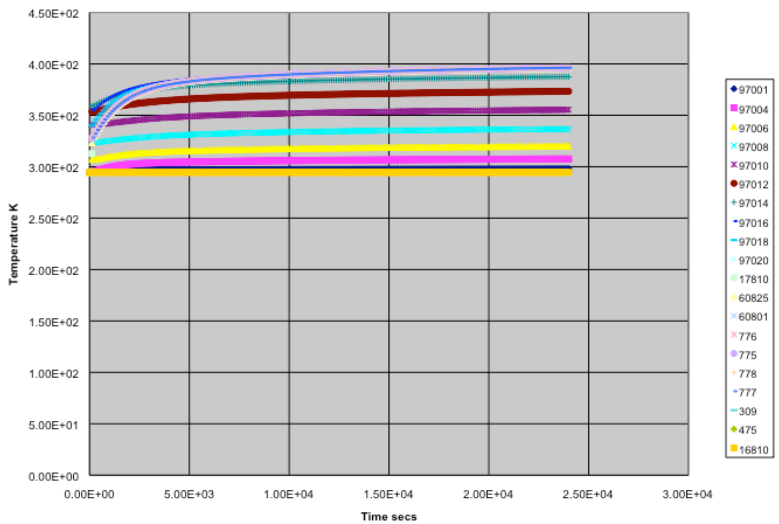

Figure 2.16d. Air System Temperature Profile

Figure 2.16. Full-Scale/Medium Flux Riser Duct Temperatures

2.3.2 Full-Scale Isothermal Forced-Flow

This model is considered the baseline for the comparison of the pressure drops in the system. The heat flux on the pressure vessel was 0 kW/m^2, making the model isothermal. The mass flow at junction J169 was set to 53.74 kg/s to create a 10^4 ft^3/min volumetric flow through the risers. The transient duration was 24,000 seconds.

The air traveling through the ducts had a constant velocity and mass flow rate of 53.74 kg/s and 40.05 m/s through all of the nodes. Figure 2.17 shows the air mass flow rate at several various locations after it has passed through the hot risers. Figure 2.18 shows the corresponding velocities. The nodal pressure loss because of wall friction and form loss is shown in Figure 2.19a. This is the pressure drop that relates to the friction drop number in the scaling analysis. It shows that the hot riser nodes dominate. For each hot riser (20 nodes), this pressure drop totals 140 Pa. Figures 2.19b–d show the model pressure drops because of elevation change. The transient behavior of the model pressure losses of the risers and various locations are described in Figure 2.19.

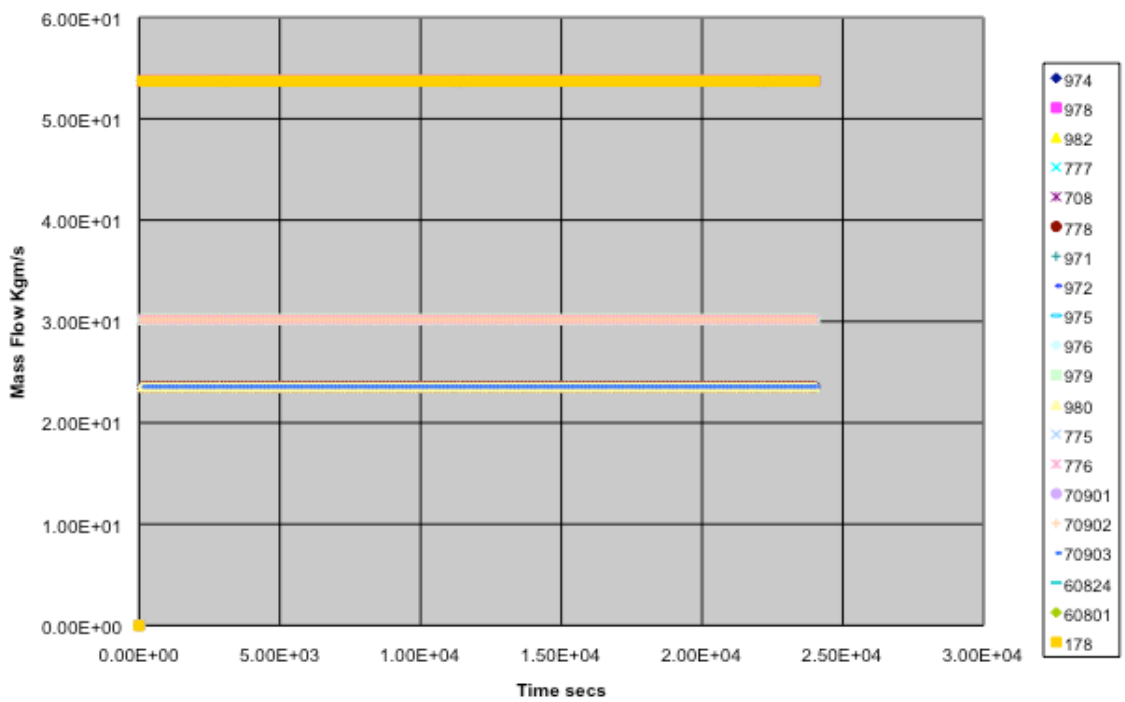

Figure 2.17. Full-Scale/Isothermal Forced-Flow Network Air Mass Flow

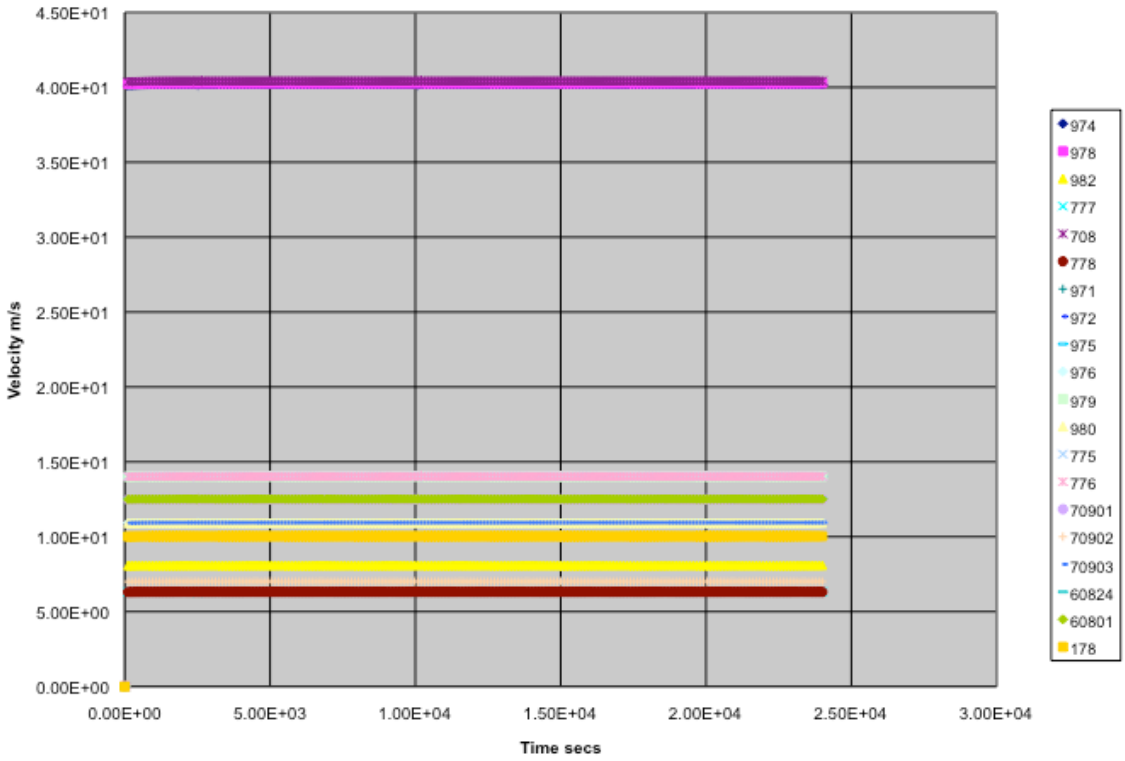

Figure 2.18. Full-Scale/Isothermal Forced-Flow Hot Network Air Velocity

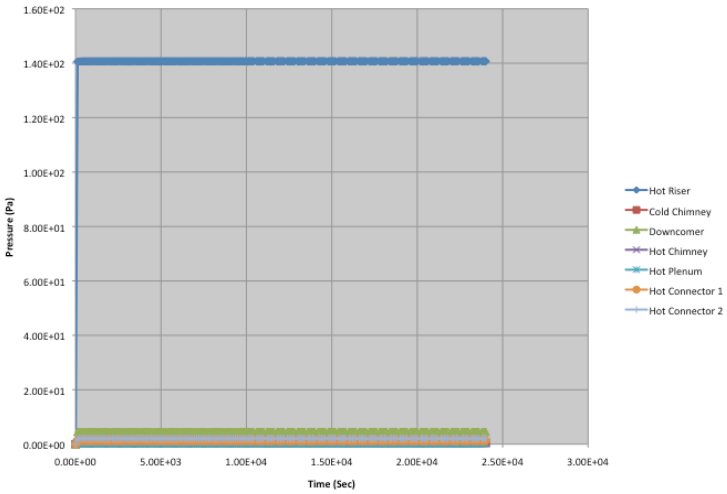

Figure 2.19a. Junction wall friction and form loss pressure drop (total)

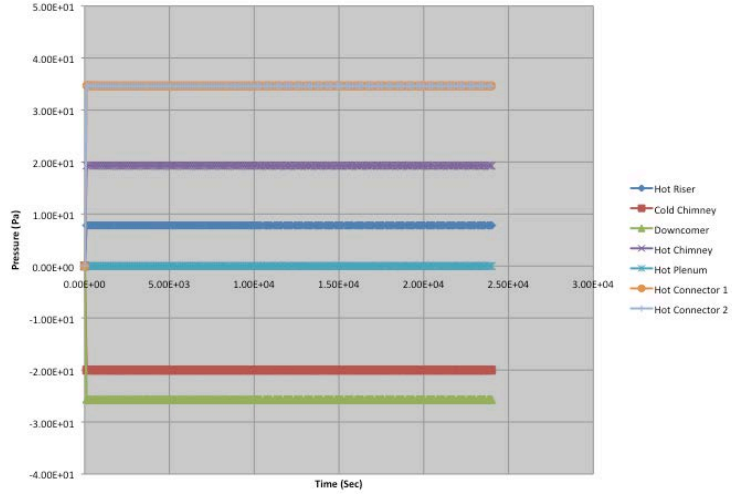

Figure 2.19b. Junction elevation change pressure drop (total)

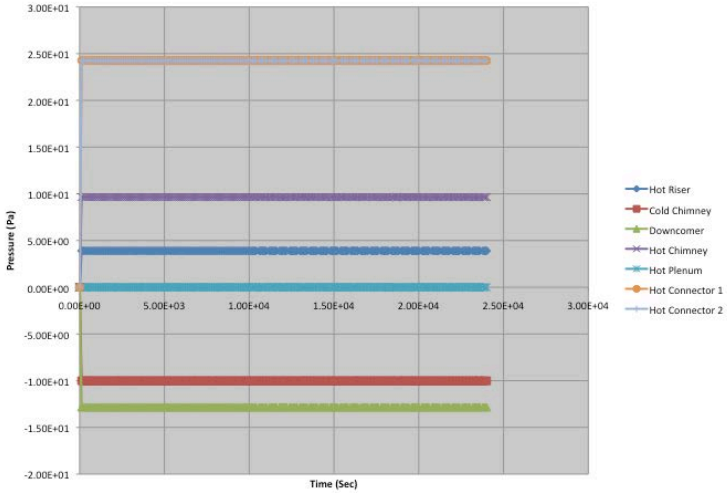

Figure 2.19c. Junction elevation change pressure drop (from side)

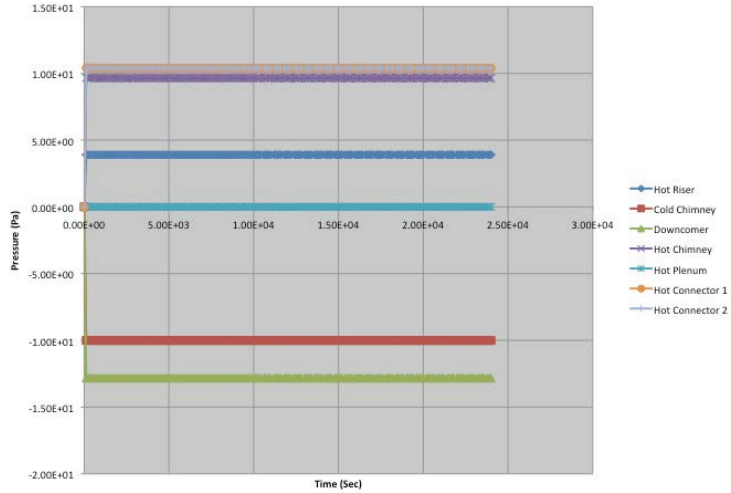

Figure 2.19d. Junction elevation change pressure drop (to side)

Figure 2.19. Full-Scale/Isothermal Forced-Flow Riser Pressure Drops

2.3.3 Full-Scale Duct-Radiation

This case was used to compare the difference in setting the internal heat transfer between the walls of the hot riser ducts from conduction to radiation. In this spatially uniform heating case, the heat flux on the pressure vessel wall was 9.95 kW/m^2, which is equivalent to 1.43 MW of total heat from half the system. This is the high heat flux case. Driven by this incident heat flux, the heat transferred from the outer surface of the pressure vessel wall is partitioned into a radiation heat flux of 8.76 kW/m^2 and a convective heat flux of 1.18 kW/m^2 off the vessel wall. This leads to a heat flux incident upon the front wall of the hot riser duct of 4.51 kW/m^2. The case was run from cold shutdown conditions with a step-up to the driving power level. The transient duration was 24,000 seconds.

With the different mode of heat transfer, the only major difference from the previous conduction model case is that the temperatures of the hot riser duct walls are more uniform. Table 2.8 shows that the peak temperatures of the front wall, side wall, and back wall of the riser ducts are 566, 517, and 508 K respectively. More details on the temperatures of the hot riser duct can be found in Figure 2.20. The transient behavior of the temperatures of the hot riser duct front wall, side wall, back wall, and air coolant can be observed. The metal temperatures in these Figures are axial profiles starting with the bottom node and proceeding to the outlet end. The air temperatures of the ex-hot riser duct can also be found in Figure 2.20d. The locations start with the cold chimney inlet and transport through the cold suction ducting and manifolds down through the top and bottom cold plenums by way of the downcomer. Hot side locations can also be found in Figure 2.20d where the air heated by the transferred core residual heat rises out off the outlet of the hot riser into the hot plenum and thereon to the hot discharge ducting and manifolds into the hot chimney for ultimate discharge into the atmosphere.

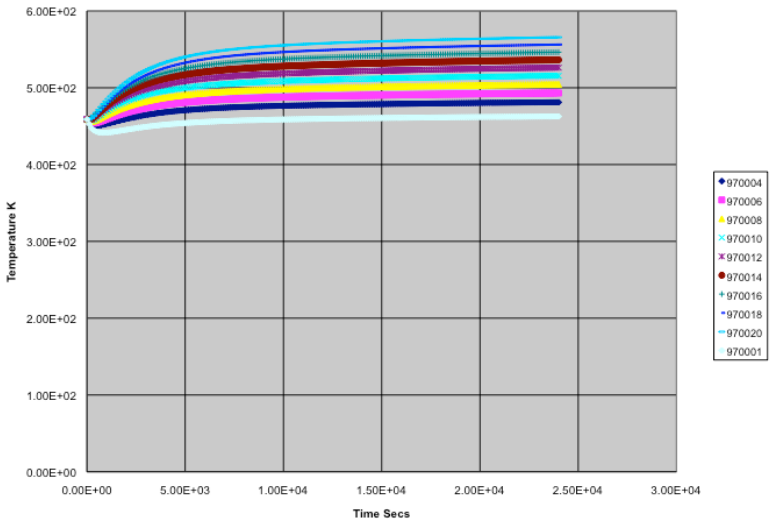

Figure 2.20a. Front Wall Temperatures

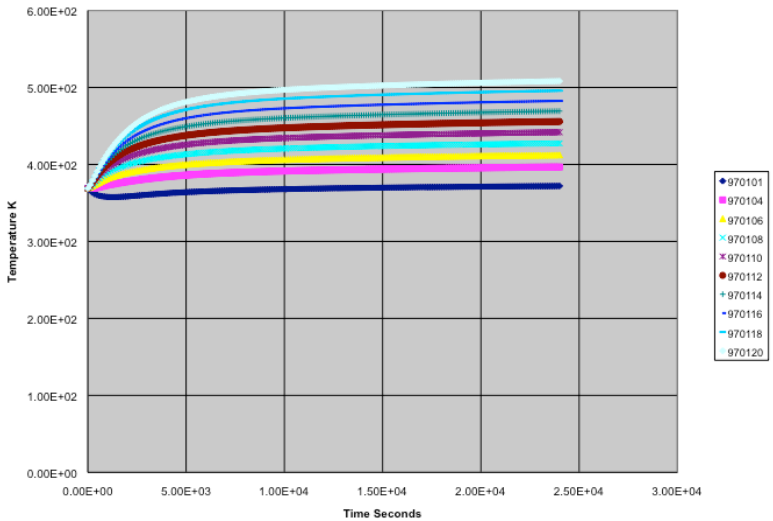

Figure 2.20b. Side Wall Temperatures

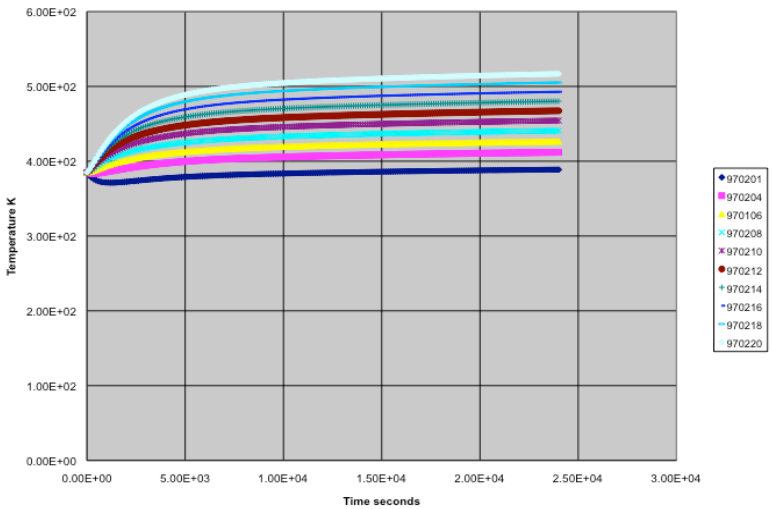

Figure 2.20c. Back Wall Temperatures

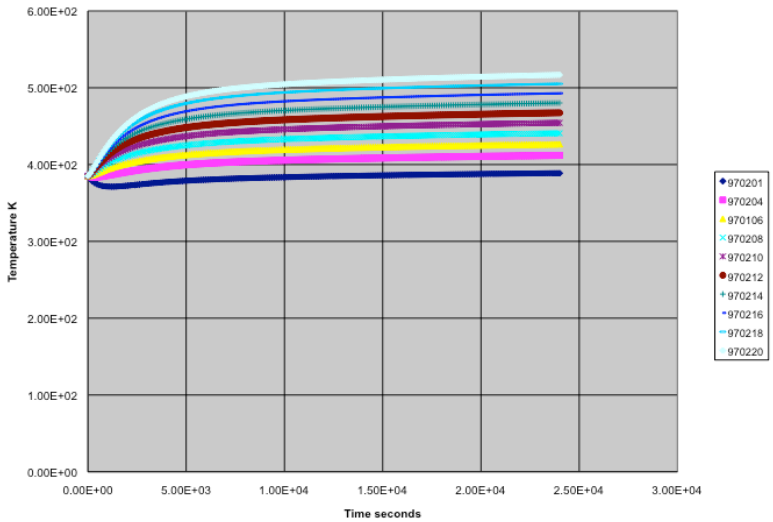

Figure 2.20d. Air System Temperature Profile

Figure 2.20. Full-Scale/High Flux Riser Duct Temperatures

2.3.4 Full-Scale Axial Power-Variation/Duct-Radiation

This case is compared to the results of the of the Full-Scale Axial Power-Variation case to compare the difference in setting the heat transfer between the walls of the hot ducts from conduction to radiation. The heat profile applied to the reactor vessel was given the same chopped cosine distribution as the previous axial power variation case discussed in Section 2.3.1. As in that case, the average heat flux on the pressure vessel wall was 4.97 kW/m^2, which is equivalent to 0.715 MW of total heat from half the system. This is the medium heat flux case. Driven by this incident heat flux, the heat transferred from the outer surface of the pressure vessel wall is partitioned into an average radiation heat flux of 4.0 kW/m^2 and an average convective heat flux of 0.95 kW/m^2. This leads to an average heat flux incident upon the front wall of the hot riser duct of 2.20 kW/m^2. The transient duration was 24,000 seconds.

With the different mode of heat transfer, the only major difference from the previous model is that the temperatures of the duct walls are more uniform. Table 2.8 shows that the peak temperatures of the front wall, side wall, and back wall of the riser ducts are 503, 435, and 422 K respectively.

2.3.5 Half-Scale Isothermal Forced-Flow 8.8-J574

This case was run to verify the scaling analysis to predict the needed orifice to match the friction drop number through the risers and the rest of the RCCS system. The heat flux on the pressure vessel was zero kW/m^2, making the model isothermal. The mass flow at junction 169 was set to 53.74 kg/s to create a 10^4 ft^3/min volumetric flow through the risers. The Reynolds number independent forward flow energy loss coefficient in J574 was set to 8.8 in an attempt to match the pressure drop in the system to the full scale. This in turn will provide the amount of orifice that will need to be applied to the bottom of the risers in the NSTF experiment. The transient duration was 24,000 seconds.

The air mass flow rate at several locations after it has passed through the hot risers can be seen in Figure 2.21. Figures 2.22 and 2.23 display the nodal pressure loss from wall friction and form loss and the model pressure drops caused by elevation change of each major junction of the Half-Scale network. Each node of the riser tubes has on average pressure loss of 146.07 Pa because of wall friction and 7.50 Pa caused by elevation change. This makes the total loss for each 1460.7 P and 750 Pa respectively. This closely matches half the pressure drops shown in the Full-Scale Isothermal model. The energy loss coefficient has to compensate for this to make it acceptable.

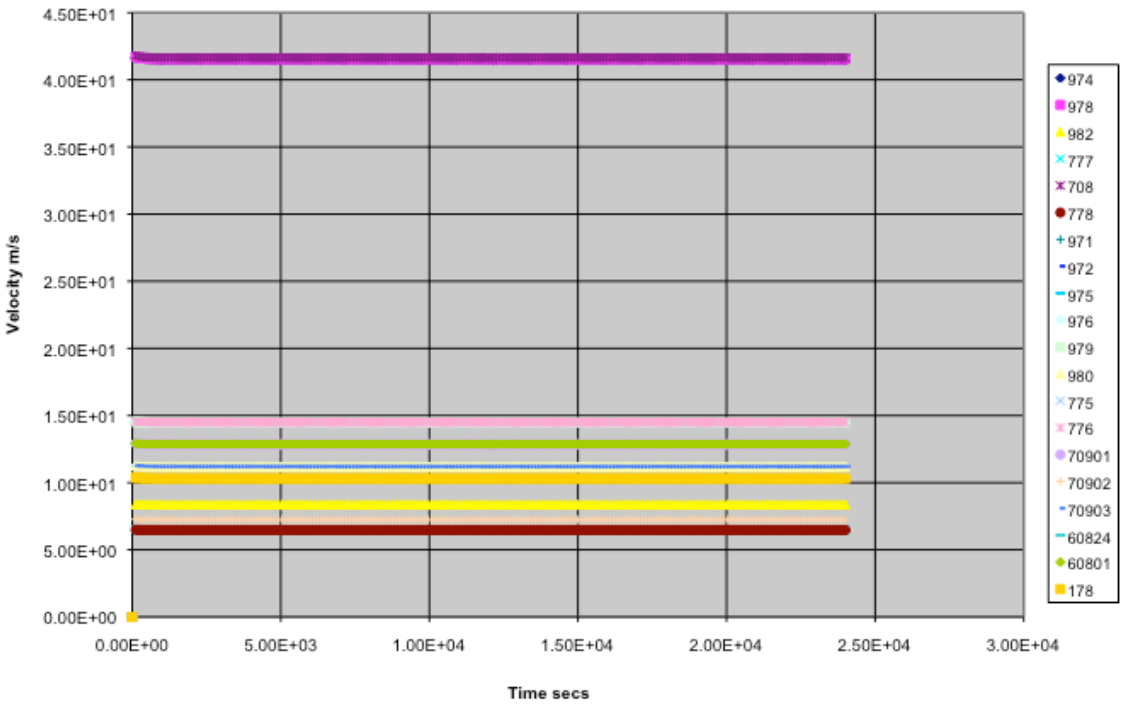

Figure 2.21. Half-Scale/Medium Flux Hot Network Air Mass Flow

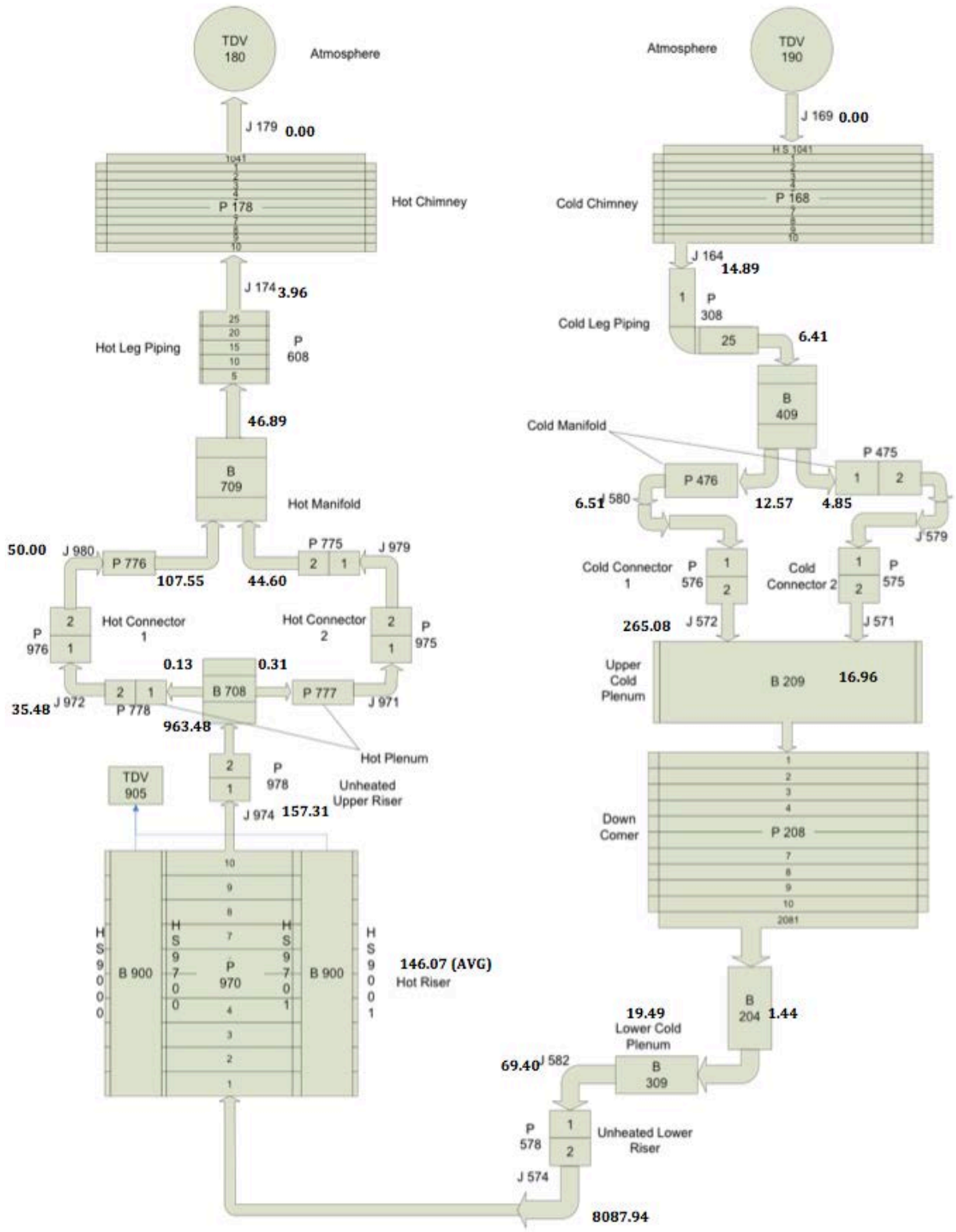

Figure 2.22. Half-Scale Isothermal Various Junction Wall Friction and Form Loss Pressure Drops (ΔP)

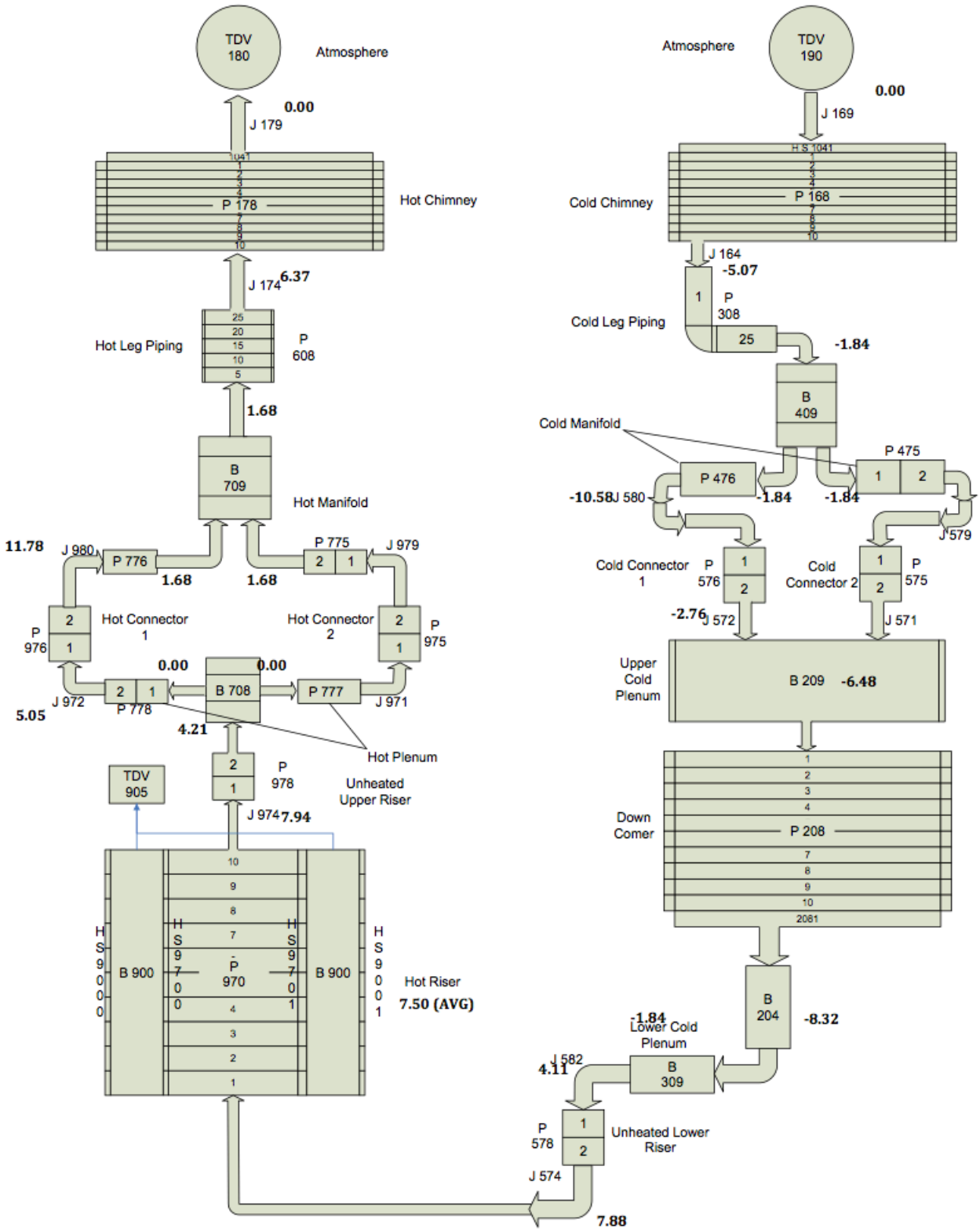

Figure 2.23. Half-Scale Isothermal Various Junction Elevation Change Pressure Drops (ΔP)

2.3.6 Half-Scale 8.8-J574 Duct-Conduction

This case was used to apply a heat flux to the half-scale model with the Reynolds number independent energy loss coefficient of 8.8. The heat flux was scaled from the full-scale case to 14.0 kW/m^2. This is the high heat flux case and is equivalent to 1.01 MW of total heat from half the system. Driven by this incident heat flux, the heat transferred from the outer surface of the pressure vessel wall is partitioned into a radiation heat flux of 12.58 kW/m^2 and a convective heat flux of 1.46 kW/m^2 off the vessel wall. This leads to a heat flux incident upon the front wall of the hot riser duct of 5.84 kW/m^2. The transient duration was 24,000 seconds.

Table 2.8 (above) shows the peak air mass flow rate as 4.75 kg/s and the peak duct airflow velocity as 5.55 m/s. The peak reactor pressure vessel wall temperature is 828 K and the peak cavity wall temperature is 546 K. The air temperature exiting the duct outlet is 491 K. The peak temperatures of the front wall, side wall, and back wall of the riser ducts are 693, 594, and 571 K respectively. Figure 2.24 shows the time history of the riser duct air mass flow rate while Figure 2.25 shows the air mass flow rate at several various locations after it has passed through the hot risers. Figures 2.26 and 2.27 show the corresponding airflow velocities.

The transient history of the pressure vessel outer wall temperature is given at the surface nodes starting from the bottom and proceeding to the top of the heated segment in Figure 2.28, while Figure 2.29 shows the corresponding liner (insulation) temperature at the corresponding axial locations on the back wall of the cavity. More details on the temperatures of the hot riser duct can be found in Figure 2.30. The transient behavior of the temperatures of the hot riser duct front wall, side wall, back wall, and air coolant can be observed. The metal temperatures in these Figures are axial profiles starting with the bottom node and proceeding to the outlet end. In the case of the air temperature, temperatures of the ex-hot riser duct can also be found in Figure 2.30d. The locations start with the cold chimney inlet and transport through the cold suction ducting and manifolds down through the top and bottom cold plenums by way of the downcomer. Hot side locations can also be found in Figure 2.30d where the air heated by the transferred core residual heat rises out off the outlet of the hot riser into the hot plenum and thereon to the hot discharge ducting and manifolds into the hot chimney for ultimate discharge into the atmosphere.

The air mass flow rate at several various locations after it has passed through the hot risers can be seen in Figure 2.25. Figures 2.31 and 2.32 display the pressure loss from wall friction, form loss, and the pressure drops caused by the elevation change of each major junction of the Half-Scale network. Each node of the riser tubes has an average pressure loss of 2.49 Pa from wall friction and 5.66 Pa from elevation change. This makes the total loss for each 24.9 Pa and 56.6 Pa respectively.

Table 2.8 shows the important T-F parameter results for these corresponding cases where the J576 orifice coefficient varies from a value of 8.8 to 0.5.

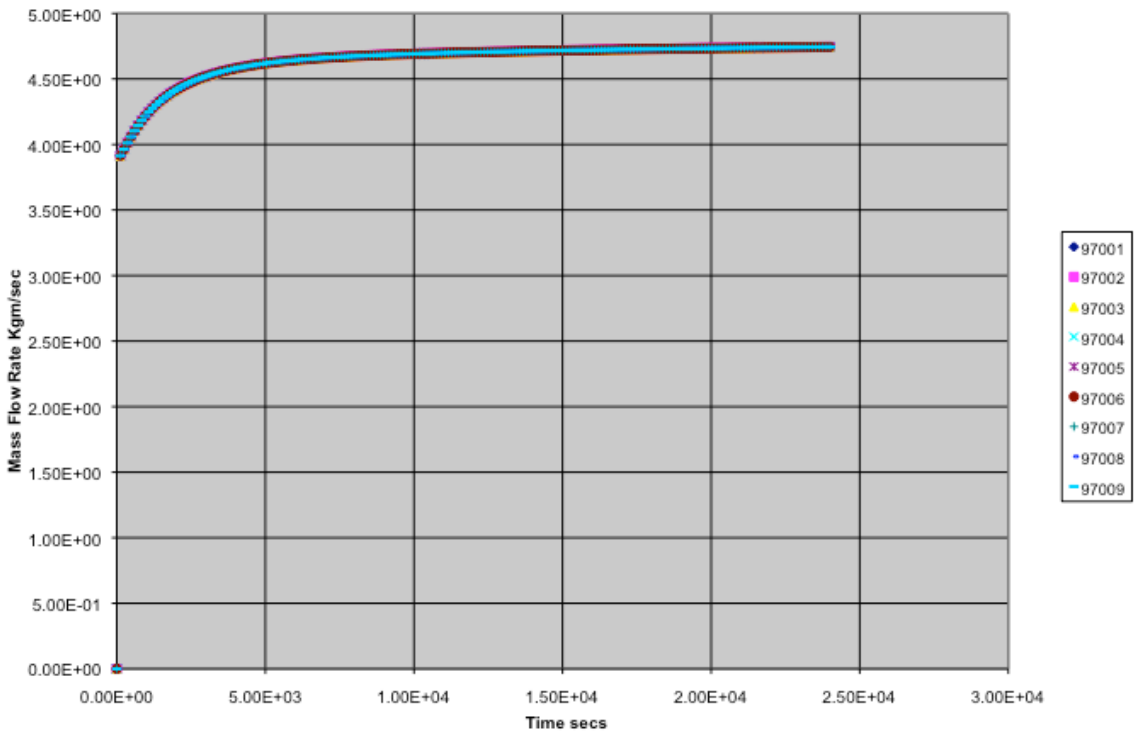

Figure 2.24. Half-Scale/High Flux Riser Duct Air Total Mass Flow

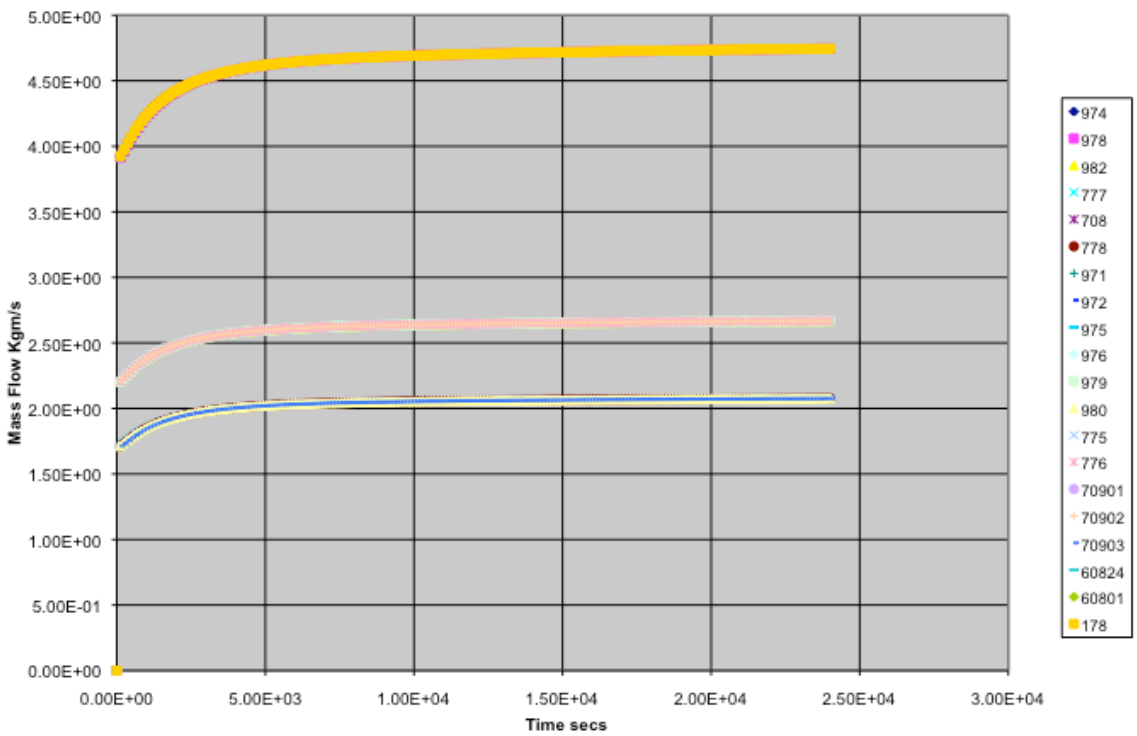

Figure 2.25. Half-Scale/High Flux Hot Network Air Mass Flow

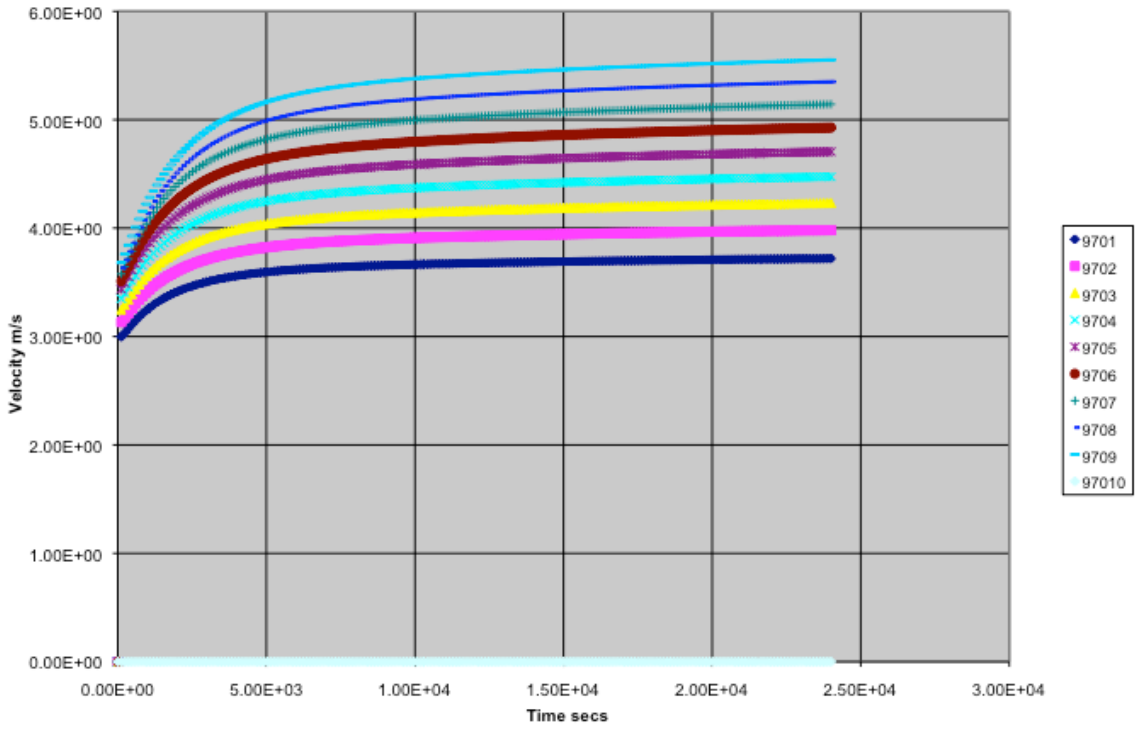

Figure 2.26. Half-Scale/High Flux Riser Duct Air Velocity

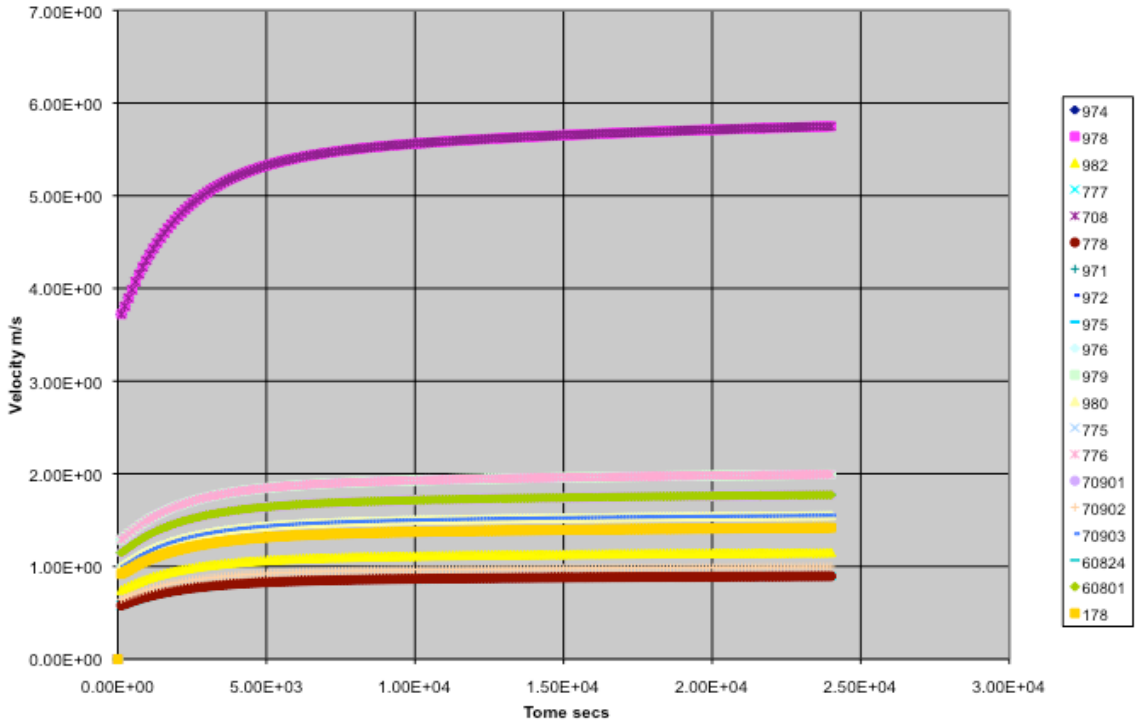

Figure 2.27. Half-Scale/High Flux Hot Network Air Velocity

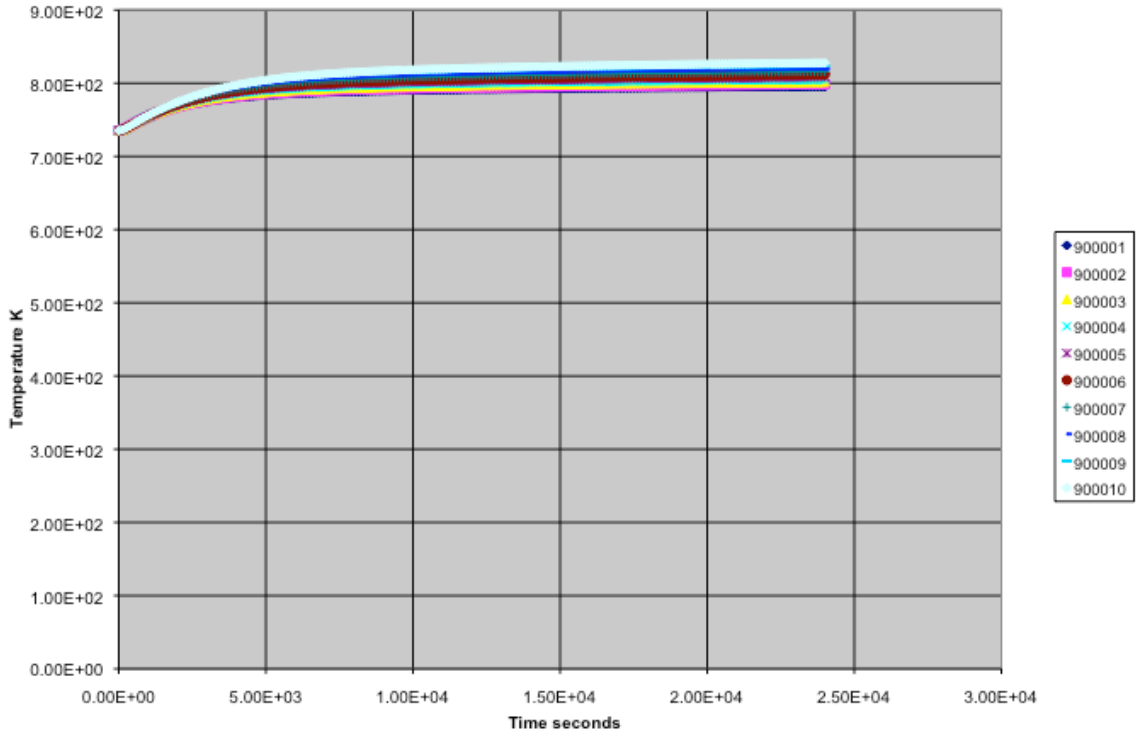

Figure 2.28. Half-Scale/High Flux RPV Temperature

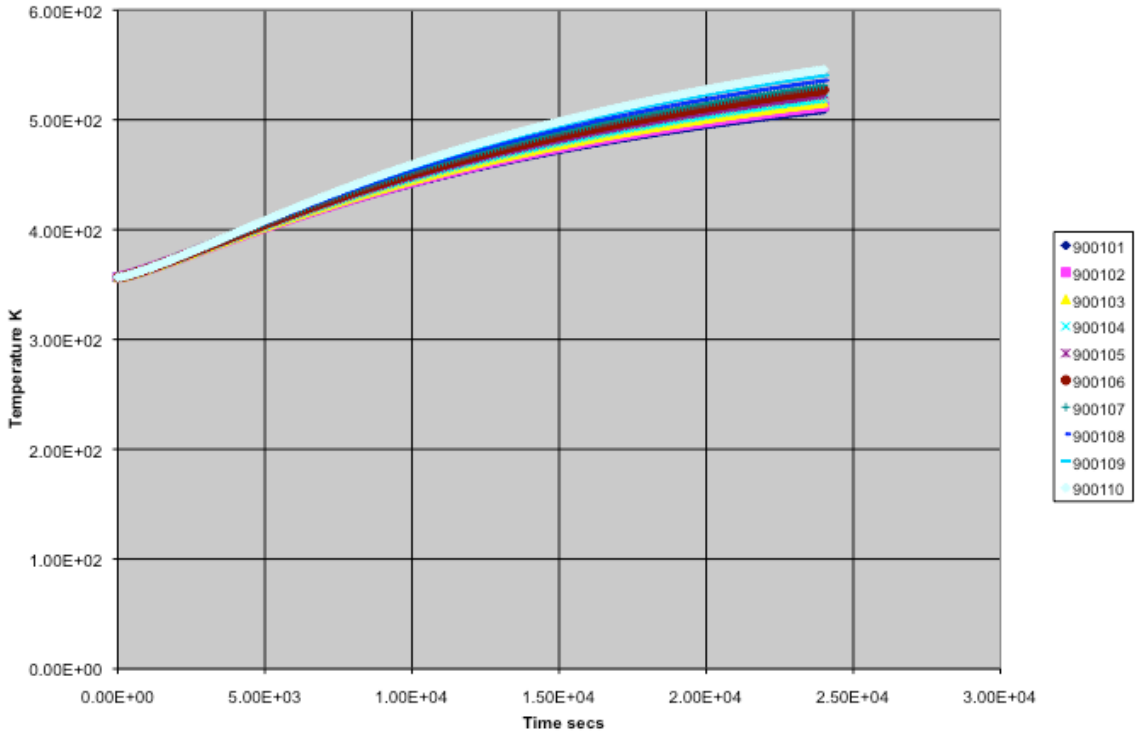

Figure 2.29. Half-Scale/High Flux Cavity Back Liner Temperature

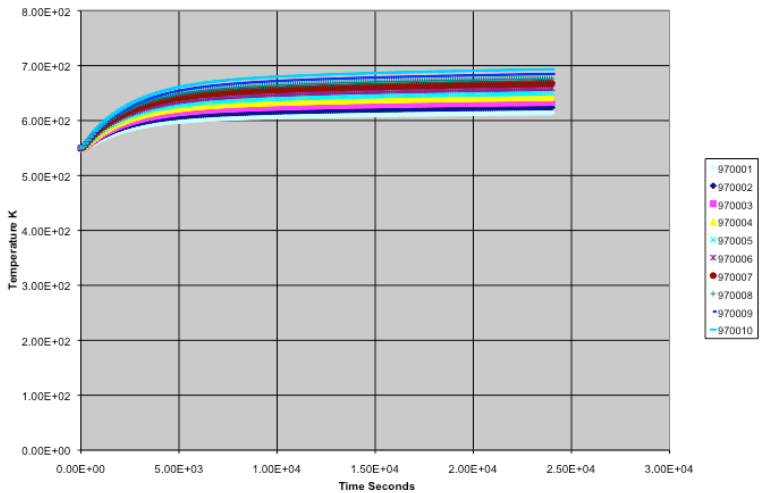

Figure 2.30a. Front Wall Temperatures

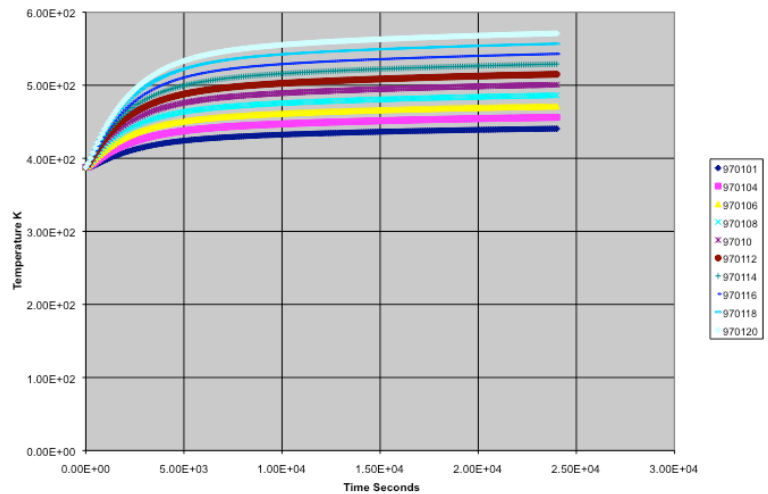

Figure 2.30b. Side Wall Temperatures

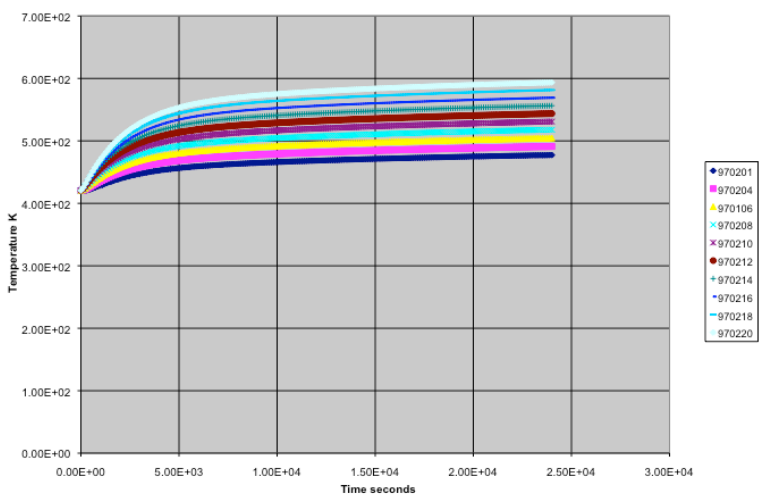

Figure 2.30c. Back Wall Temperatures

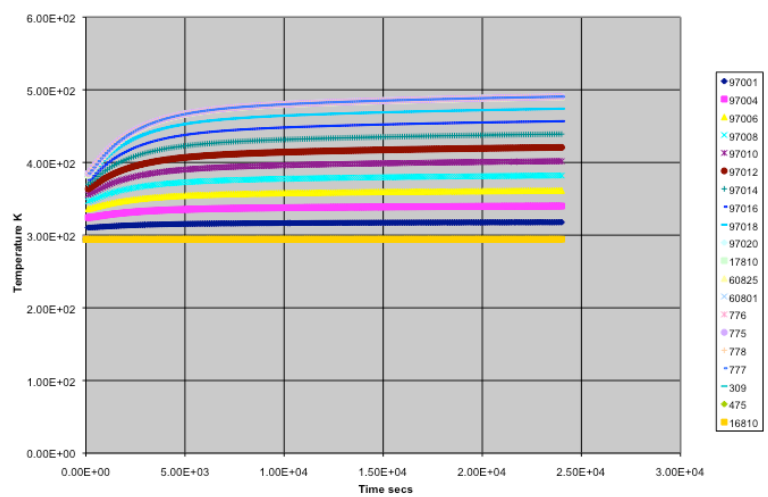

Figure 2.30d. Air System Temperature Profile

Figure 2.30. Half-Scale/High Flux Riser Duct Temperatures

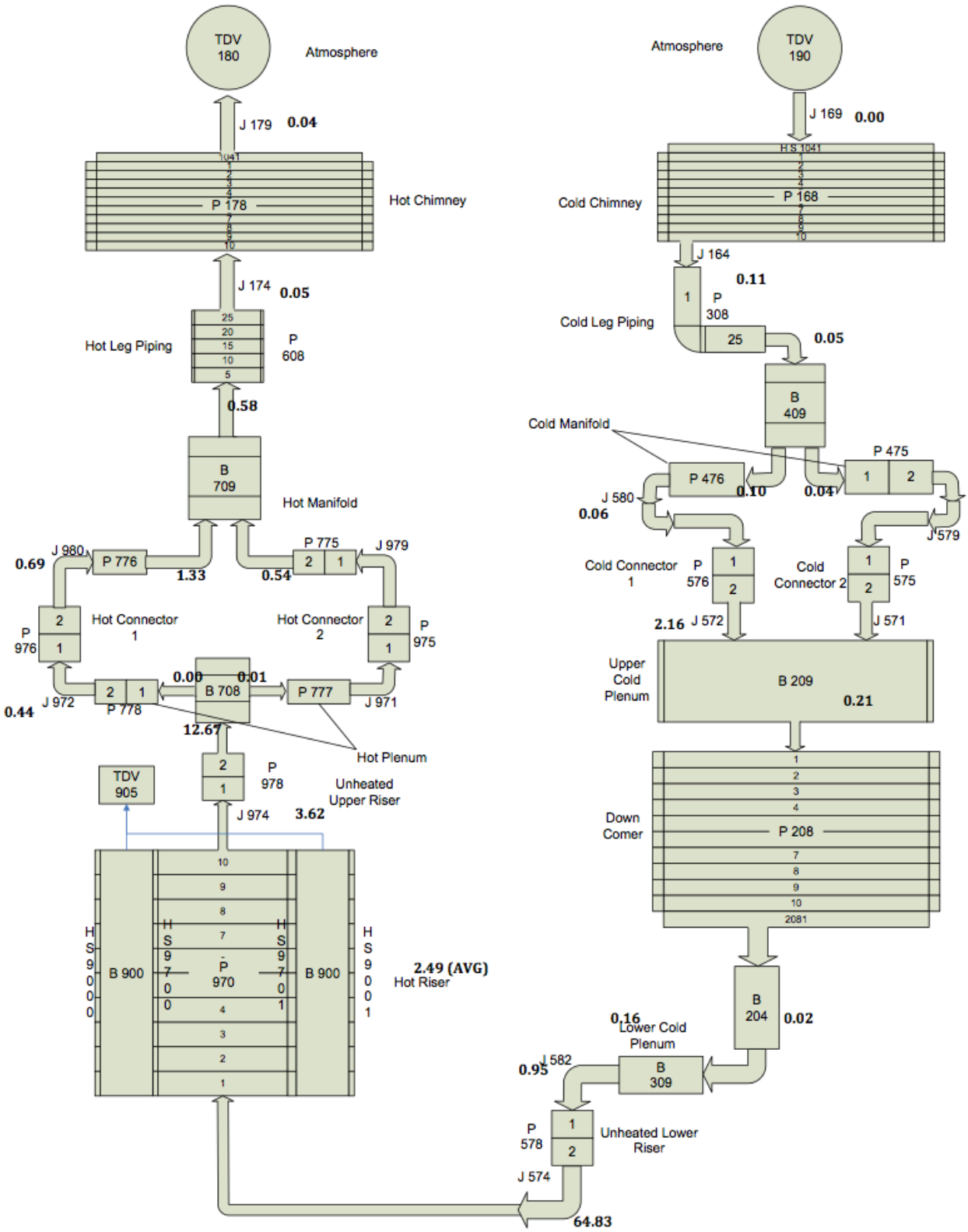

Figure 2.31. Half-Scale Conduction Case of Various Junction Wall Friction and Form Loss Pressure Drops (ΔP)

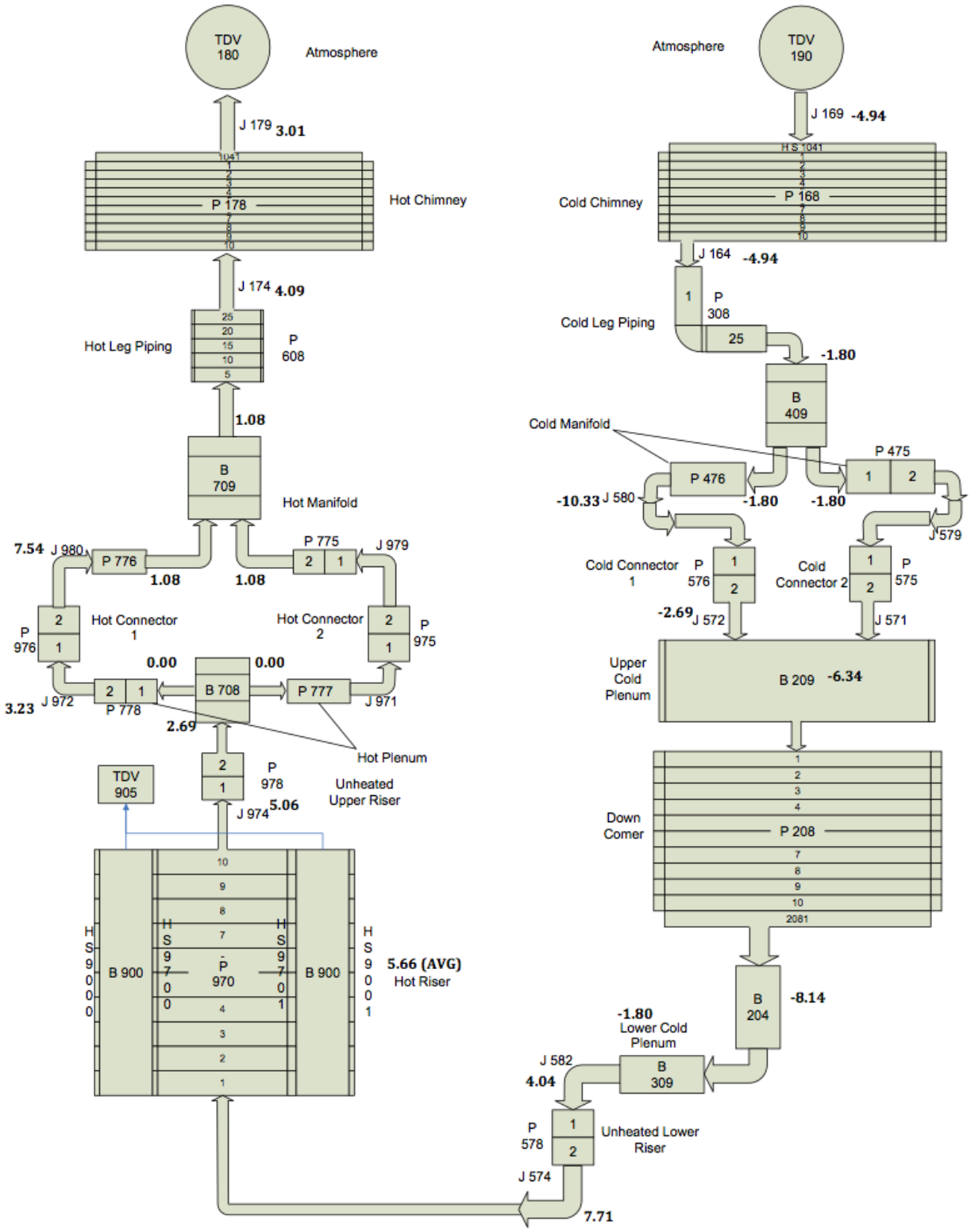

Figure 2.32. Half Scale Conduction Case of Various Junction Elevation Change PressureDrops (ΔP)

2.3.7 Half-Scale 8.8-J574 Duct-Radiation

This case is compared to the results of the case with the Half-Scale 8.8-J574 Duct-Radiation model to compare the difference in setting the internal heat transfer between the walls of the riser ducts from conduction to radiation. The heat flux was scaled from the full-scale case to 14.0 kW/m^2. This is equivalent to 1.01 MW of total heat from half the system. This is the high heat flux case. Driven by this incident heat flux, the heat transferred from the outer surface of the pressure vessel wall is partitioned into a radiation heat flux of 12.58 kW/m^2 and a convective heat flux of 1.46 kW/m^2 off the vessel wall. This leads to a heat flux incident upon the front wall of the hot riser duct of 5.84 kW/m^2. The transient duration was 24,000 seconds.

With the different mode of heat transfer, the only major difference from the previous model is that the temperatures of the duct walls are more uniform. Table 2.8 shows that the peak temperatures of the front wall, side wall, and back wall of the riser ducts are 648, 588, and 577 K respectively.

2.4 NSTF Experiment RELAP5 Results

To support the Argonne NSTF heat transfer experiments, cases modeling the experiment configuration were also run. The baseline model of the experimental system is a two-hot riser channel model. This grouping of two risers is to allow transverse temperature gradients driven by the parasitic heat losses to be evaluated. The scaling allows for comparisons between the experimental system and the full-scale model. The system is currently assumed to be 50% scale, with the same changes made as in the half-scale model. As to be expected, the major difference with the half-scale model is in the external duct runs, manifolds, connectors and the chimneys. Environmental parasitic heat loss from the NSTF test section box is included in the baseline cases. Cases were run at three internal power generation levels. These power levels produce the three proportionally scaled heat fluxes equivalent to the full scale cases. Sensitivity cases modeling wall emissivity changes, intraduct thermal radiation, separation distance between the box heated surface and the riser ducts, and box top and bottom radiation effects were performed. One-hot riser approaches were also evaluated, and the pressure drop through the test section was examined. The results are shown in Table 2.9.

2.4.1 1 Channel NSTF Isothermal Forced-Flow

This case was performed for the comparison to the Isothermal Half-Scale 8.8-J574 case. This comparison is made with regard to the pressure losses. Based on this comparison, an effective orifice for the Argonne NSTF heat transfer experiments can be determined to create an equivalent pressure loss in the heated experiment as with the full-scale GA-MHTGR RCCS. The heat flux on the pressure vessel was 0 kW/m^2, making the model isothermal. The mass flow at junction J952 was set to 38.99 kg/s to create a 10^4 ft^3/min volumetric flow through the risers. The transient duration was 24,000 seconds.

Table 2.9 Summary of 1 and 2 Channel NSTF Case Results

Model	Heat Flux [kW/m²]	Cavity Dimensions	Duct Heat-Transfer Type Radiation/ Conduction	Transient Length[s]	Peak Chimney Mass Flow Rate [kg/s]	Peak Air Mass Flow Rate [kg/s] Inner/Outer	Peak Duct Air Flow Velocity [m/s] Inner/Outer	Peak Temperatures [K]			Peak Inner Duct Temperatures [K]			Peak Outer Duct Temperatures [K]		
								RPV	Cavity Wall	Air Duct Outlet	Front Wall	Side Wall	Back Wall	Front Wall	Side Wall	Back Wall
1 Channel	9.24	18" x 52"	Conduction	24000	0.80	0.80	8.50	872	610	473	741	553	553	X	X	X
1 Channel	0.00	18" x 52"	X	24000	5.69	5.68	38.99	295	295	295	295	295	295	X	X	X
1 Channel	9.24	18" x 52"	Radiation	24000	0.80	0.80	8.50	858	608	473	676	560	559	X	X	X
2 Channel	12.22	18" x 52"	Conduction	24000	0.80	0.53 / 0.25	7.29 / 7.42	783	516	432	645	483	472	637	494	478
2 Channel	12.22	46" x 52"	Conduction	24000	0.75	0.50 / 0.25	7.05 / 7.36	780	605	434	607	470	477	599	497	494
2 Channel (Emissivity)	12.22	46" x 52"	Conduction	24000	0.74	0.49 / 0.25	6.97 / 7.09	784	488	432	604	466	478	597	496	495
2 Channel (Emissivity)	12.22	46" x 52"	Radiation	24000	0.74	0.49 / 0.25	6.99 / 7.29	774	485	431	565	472	479	565	488	497

The air traveling through the riser ducts had a constant velocity and mass flow rate of 38.99 kg/s and 40.05 m/s through all of the nodes as shown in Table 2.9. Because of the simple model nodalization geometry and constant flow, the pressure losses in the various parts of the system were constant through the nodes. Each node of the riser tubes has an average pressure loss of 138.12 Pa from wall friction and 7.95 Pa from elevation change. This makes the total loss for each hot riser 1381.2 and 79.5 Pa respectively. This closely matches the pressure drops shown in the Half-Scale Isothermal model for the hot riser part of the system.

In the case of the NSTF chimney, the corresponding junction wall friction and form loss pressure drop per node is 1.38 Pa and the junction elevation change pressure drop per node is 21.12 Pa.

2.4.2 1 Channel NSTF Duct-Radiation

This case was used to compare the difference in changing the heat transfer between the walls of the riser ducts from conduction to radiation. The internal heat flux from heated surface of the NSTF box was 9.24kW/m^2, which is equivalent to 150 kW of total heat from half the system. Driven by this incident heat flux, the heat transferred from the outer surface of the heated wall is partitioned into a radiation heat flux of 8.76 kW/m^2 and a convective heat flux of 1.18 kW/m^2 off the heated wall. This leads to a heat flux incident upon the front wall of the hot riser duct of 4.51 kW/m^2 .The case was run from cold shutdown conditions with a step-up to the driving power level. The transient duration was 24,000 seconds. The NSTF test box dimensions remain at 18" (45.7 cm) x 52" (132.0 cm) which were the dimensions set in the FY 2010 work [2.2]. The 18" (45.7 cm) corresponded to a separation distance of 4″ (10.1 cm) between the twelve duct hot riser array from both the heated wall and the back wall of the NSTF box.

Table 2.9 shows the peak air mass flow rate as 0.80 kg/s and the peak duct airflow velocity as 8.50 m/s. The peak heated wall temperature is 858ºK and the peak cavity wall temperature is 608ºK. The air temperature exiting the duct outlet is 473ºK. The peak temperatures of the front wall, side wall, and back wall of the riser ducts are 676ºK, 560ºK, and 559ºK respectively. Figure 2.33 shows the time history of the riser duct air mass flow rate. Figures 2.34 and 2.35 show the corresponding airflow velocities in the hot riser ducts and the NSTF chimney. The table results show the major effect of the intraduct radiation is to make the riser duct wall temperatures more uniform in comparison to the conduction model case.

The transient history of the NSTF heated surface wall temperature is given at the surface nodes starting from the bottom and proceeding to the top of the heated segment in Figure 2.36 while Figure 2.37 shows the corresponding liner (insulation) temperature at the corresponding axial locations on the back wall of the cavity. More details on the temperatures of the hot riser duct can be found in Figure 2.38. The transient behavior of the temperatures of the hot riser duct front wall, side wall, back wall and air coolant can be observed. The metal temperatures in these Figures are axial profiles starting with the bottom node and proceed to the outlet end.

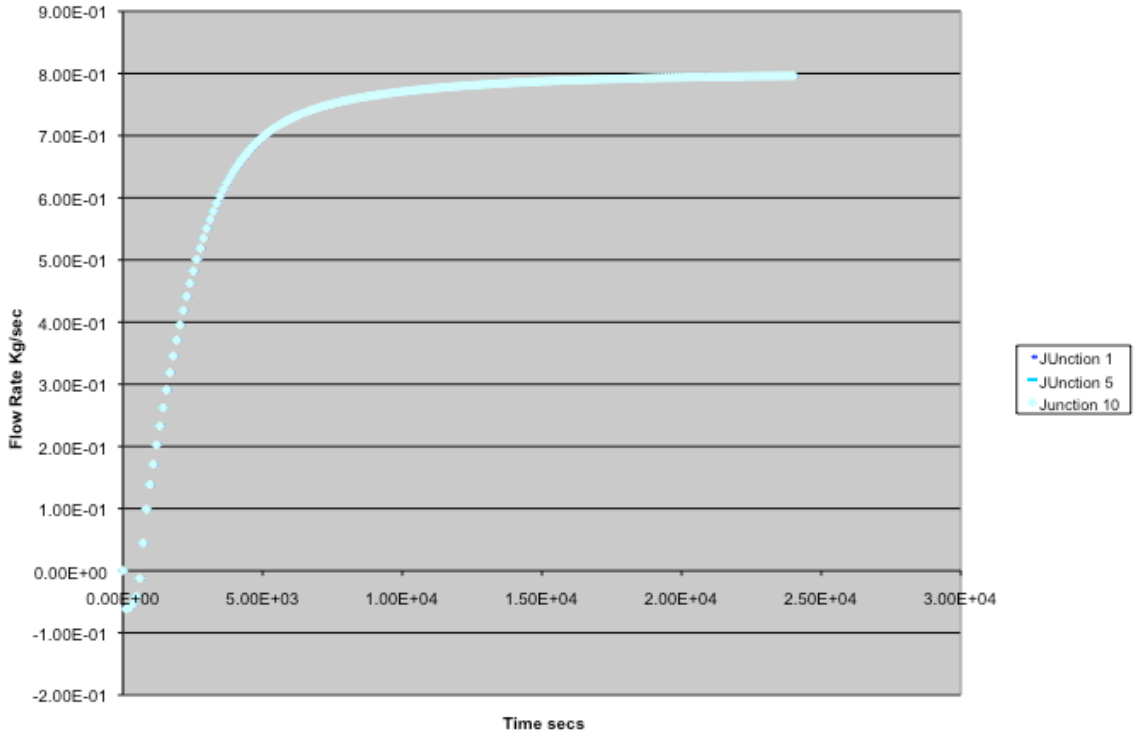

Figure 2.33. 1 Channel NSTF with Radiation Riser Duct Air Total Mass Flow

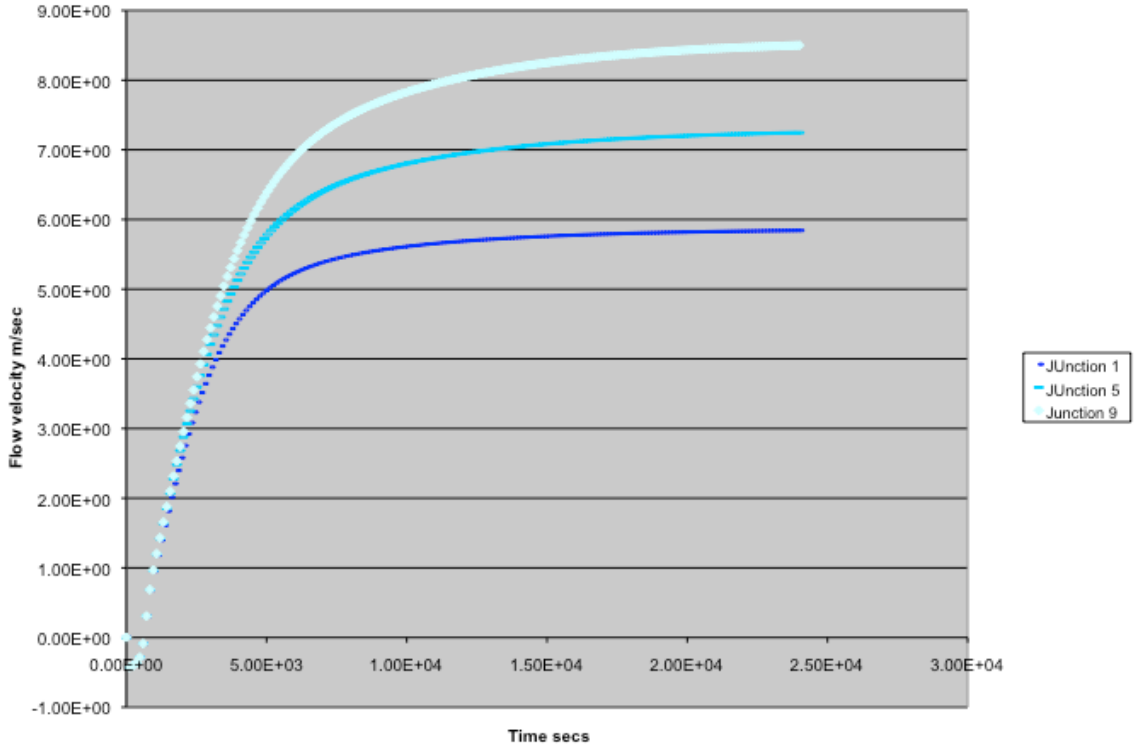

Figure 2.34. 1 Channel NSTF with Radiation Riser Duct Air Velocity

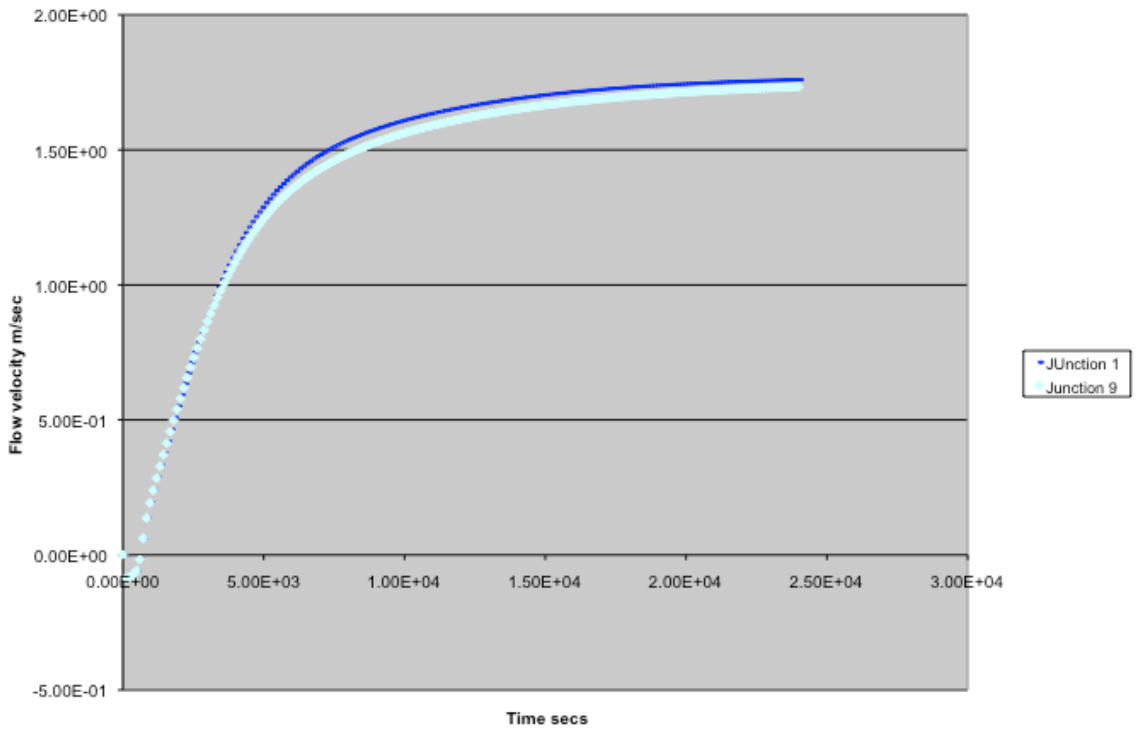

Figure 2.35. 1 Channel NSTF with Radiation Chimney Air Velocity

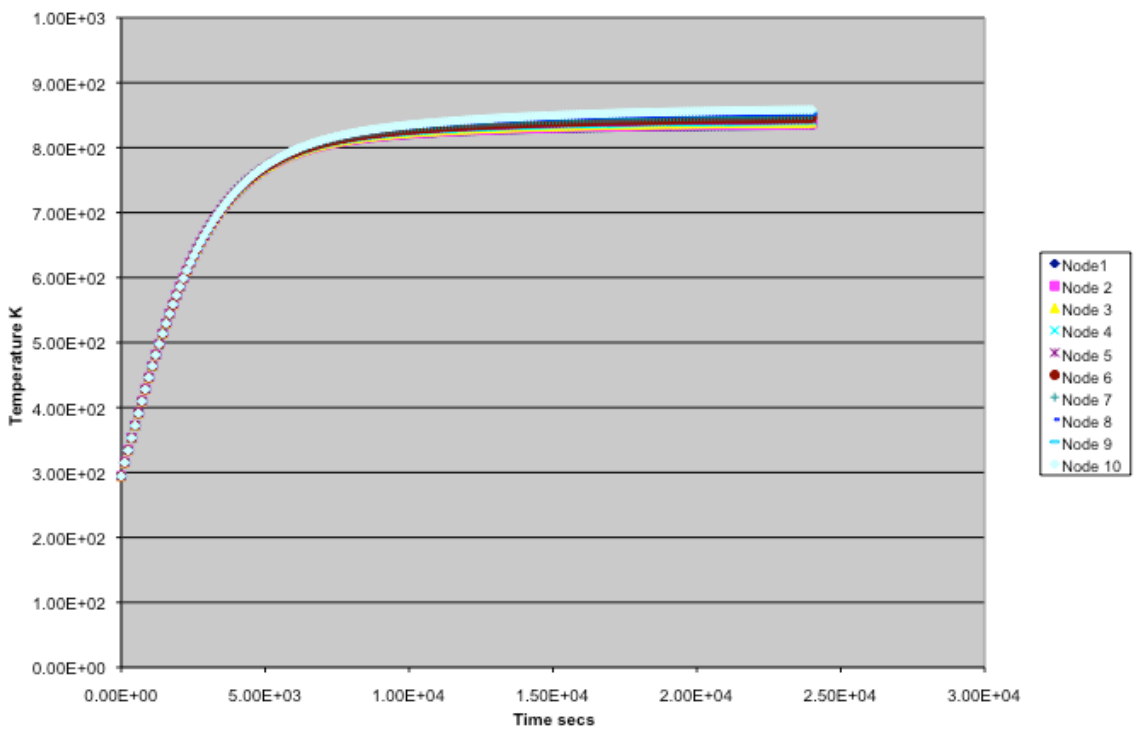

Figure 2.36. 1 Channel NSTF with Radiation Heated Wall Temperature

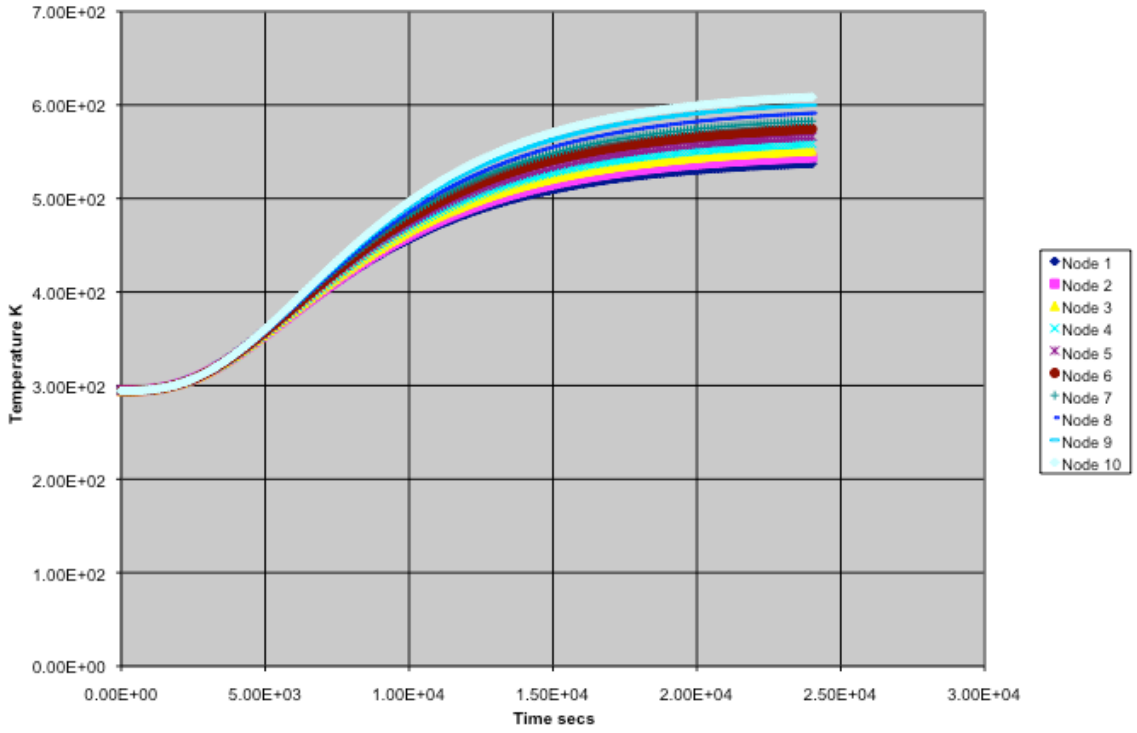

Figure 2.37. 1 Channel NSTF with Radiation Back Wall Liner Temperature

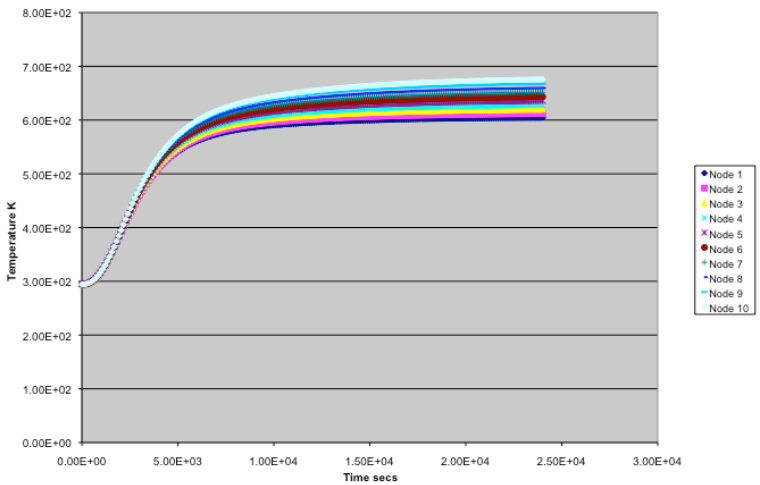

Figure 2.38a. Front Wall Temperatures

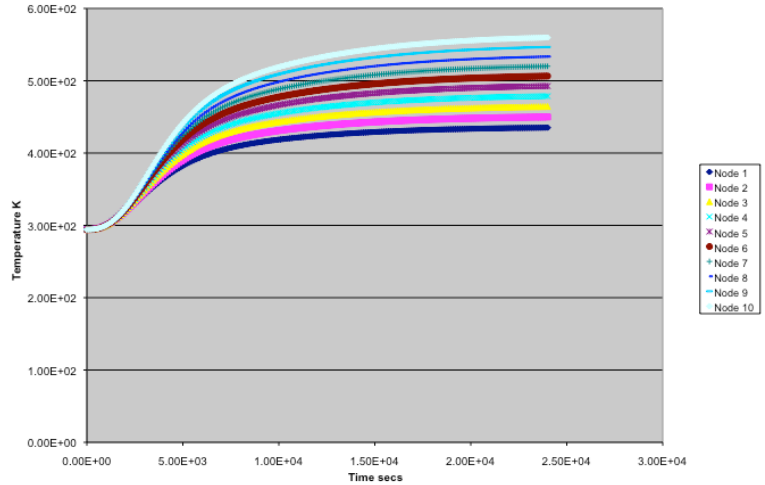

Figure 2.38b. Side Wall Temperatures

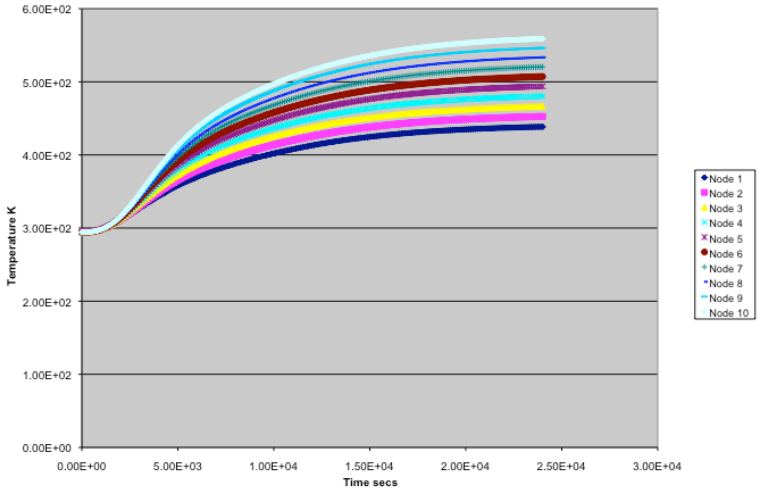

Figure 2.38c. Back Wall Temperatures

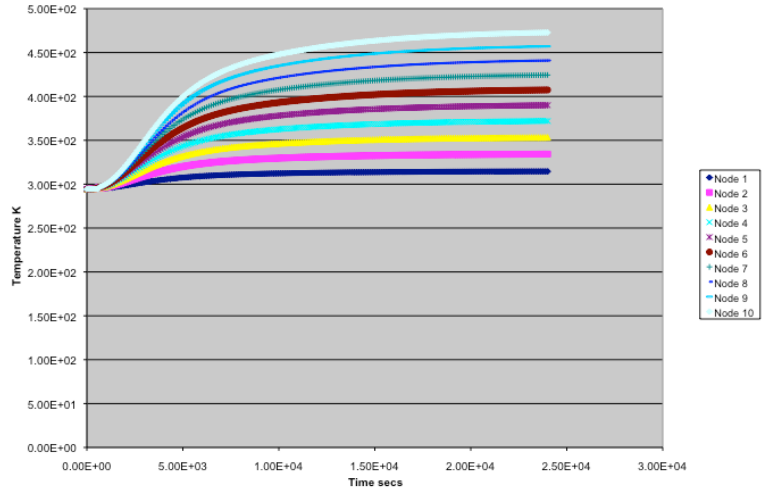

Figure 2.38d. Duct Air Temperature Profile

Figure 2.38. 1 Channel NSTF with Radiation Riser Duct Temperatures

2.4.3 2 Channel NSTF 46" (116.84 cm) x52" (132.08 cm)

This case is considered the baseline for the comparison of all the NSTF experiments with the same cavity dimensions. The total internal power generation in the heater remains at the high heat flux case of 108.3 kW. The heat flux incident on the heated surface of the NSTF box therefore remains 12.2 kW/m^2. The heat transferred from the outer surface of the heated box wall is still partitioned into a radiation heat flux of 10.78 kW/m^2 and a convective heat flux of 1.19 kW/m^2 off the vessel wall. The transient duration was 24,000 seconds. The 46″ (116.84 cm) × 52″ (132.08 cm) dimensions of the NSTF test box correspond to the use of the 28″ (71.1 cm) to 8″ (20.3 cm) NEVADA view factors. The front surface of the 12 duct hot riser array is separated by 28" from the heated wall of the box. The unheated back wall of the box is located 8″ (20.3 cm) away from the rear surface of the hot riser array. The intraduct wall heat transfer modeled using conduction. The emissivity of the inner surfaces of the NSTF box walls remains at 0.8 consistent with the FY 2010 work [2.2].

The model performed as expected as the T-F conditions monotonically increase to reach a stable steady condition in the asymptote. Table 2.9 shows that the peak air mass flow rate in the chimney is 0.745 kg/s. Table 2.9 shows that the peak air mass flow rate for the group of eight inner central riser ducts is 0.50 kg/s and the peak air velocity in the duct is 7.05 m/s. Table 2.9 also shows that the peak air mass flow rate for the four outer boundary riser ducts is 0.25 kg/s and the peak air velocity in the duct is 7.36 m/s. The corresponding values for the peak air riser outlet temperatures are 434 and 443 K. The peak heated box wall temperature is 780 K while the peak box back wall surface temperature is 605 K. Focusing on the central inner riser ducts, the peak front wall temperature is 607 K; the peak side wall temperature is 470 K and the peak duct back wall temperature is 477 K. The peak front wall temperature for the outer boundary riser ducts is 599 K, the peak side wall temperature is 497 K, and the peak duct back wall temperature is 494 K.

The transient history of the heated wall temperature is given at the surface nodes starting from the bottom and proceeding to the top of the heated segment in Figure 2.39. Figure 2.40 shows the corresponding liner (insulation) temperature at the corresponding axial locations on the side wall of the cavity while Figure 2.41 shows the same for the back wall. Figure 2.42 shows the time histories of both the inner and outer riser duct air mass flow rate along with the air mass flow rate of the chimney system. Figure 2.43 shows the corresponding airflow velocities.

More details on the temperatures of the inner hot riser ducts can be found in Figure 2.44, while the temperatures of the outer hot riser ducts are displayed in Figure 2.45. The transient behavior of the temperatures of the hot riser duct front walls, side walls, back walls, and air coolants can be observed. The metal temperatures in these Figures are axial profiles starting with the bottom node and proceeding to the outlet end.

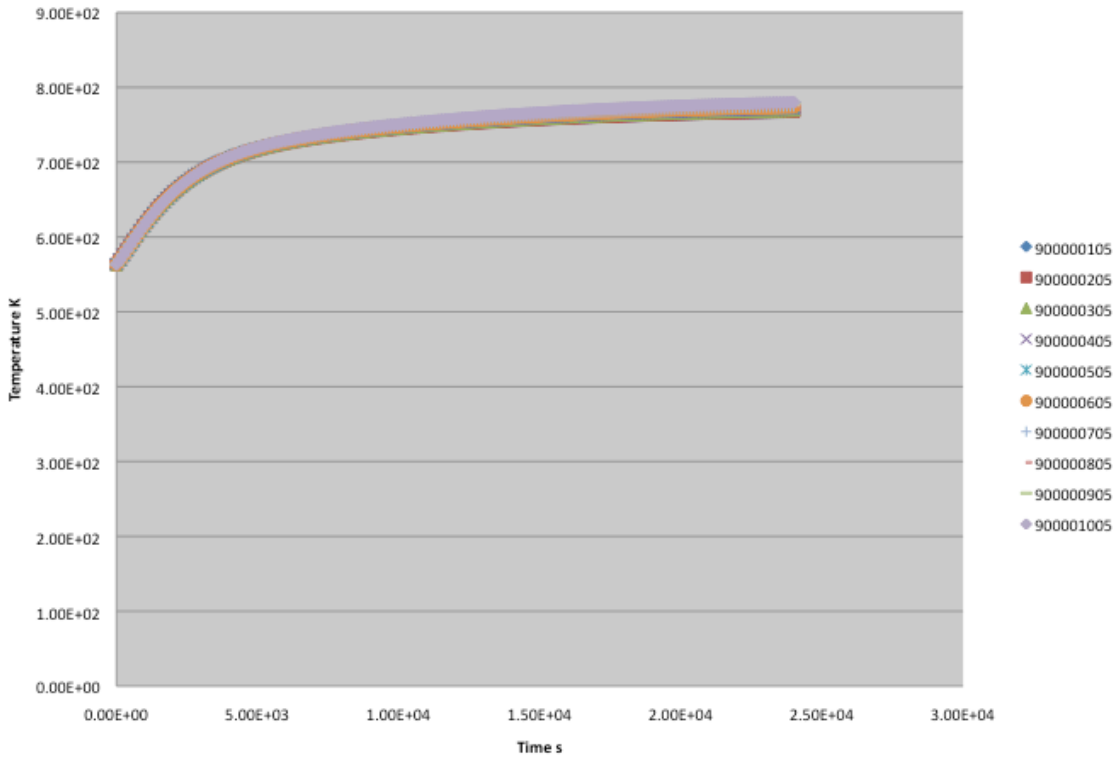

Figure 2.39. 2 Channel NSTF 46″ (116.84 cm) × 52″ (132.08 cm) Heater Temperature

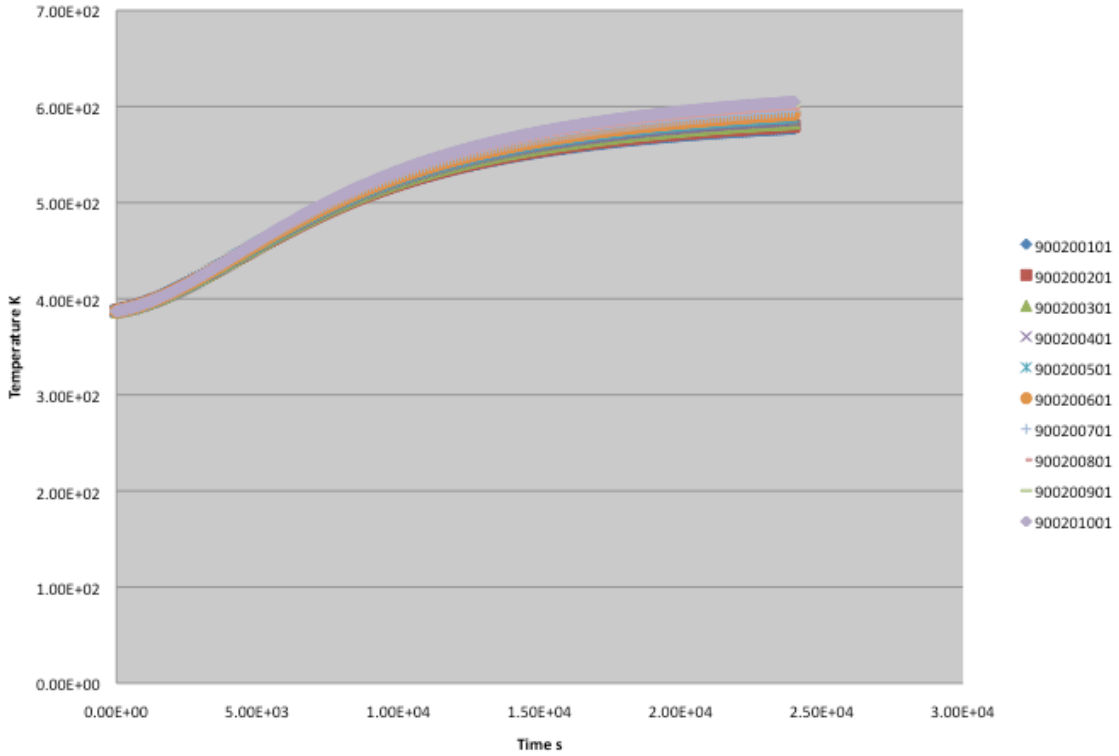

Figure 2.40. 2 Channel NSTF 46″ (116.84 cm) × 52″ (132.08 cm) Cavity Side Liner Temperature

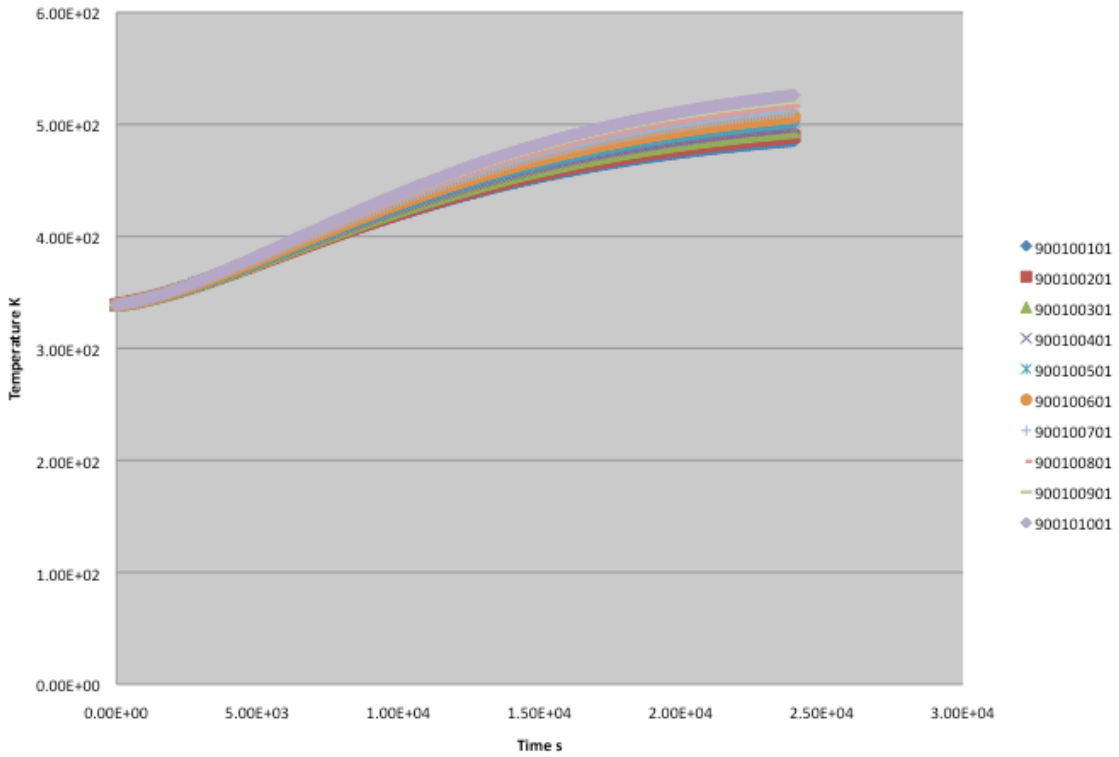

Figure 2.41. 2 Channel NSTF 46″ (116.84 cm) × 52″ (132.08 cm) Cavity Back Liner Temperature

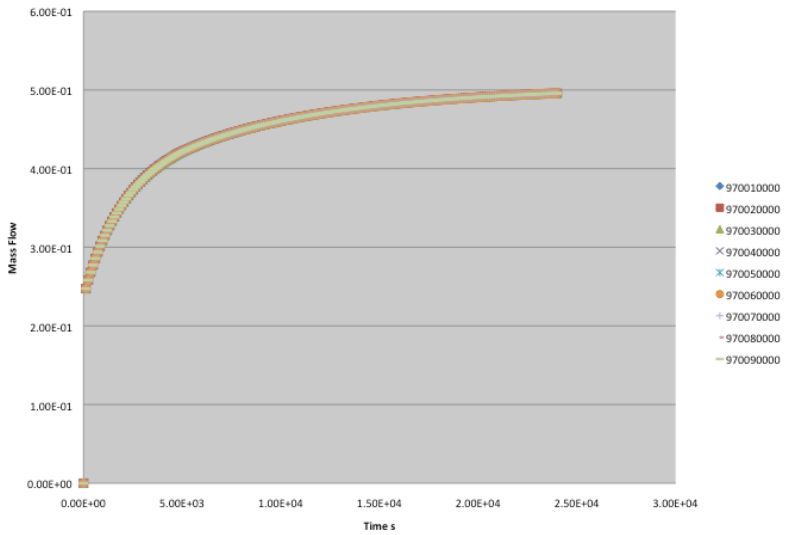

Figure 2.42a. Inner Riser Duct Air Mass Flow Rates

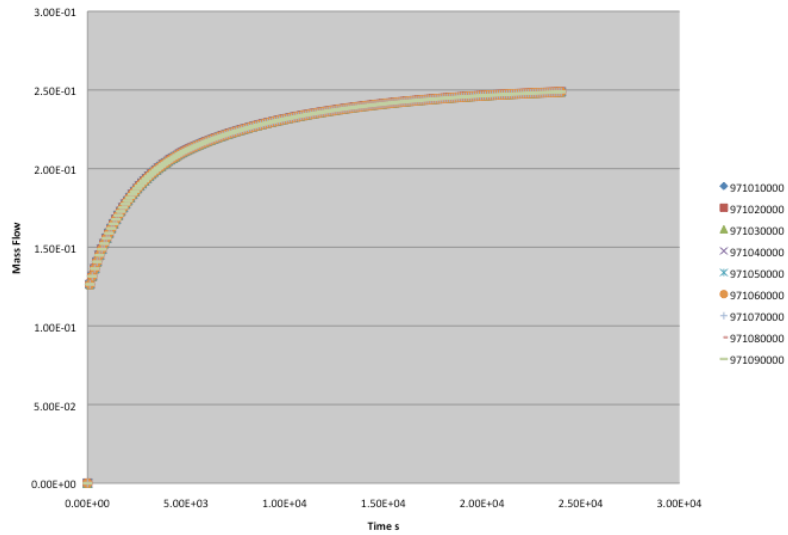

Figure 2.42b. Outer Riser Duct Air Mass Flow Rates

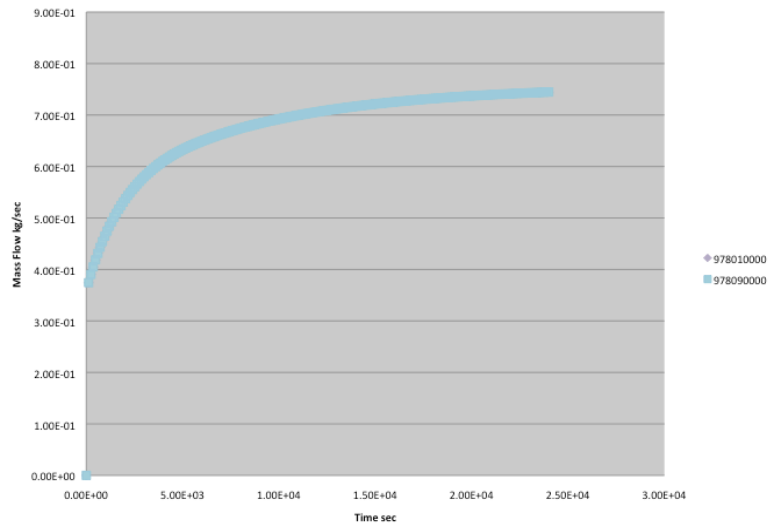

Figure 2.42c. Inner Riser Chimney Air Mass Flow Rates

Figure 2.42 2 Channel NSTF 46″ (71.1 cm) × 52″ 9 (132.0 cm) Mass Flow Rates

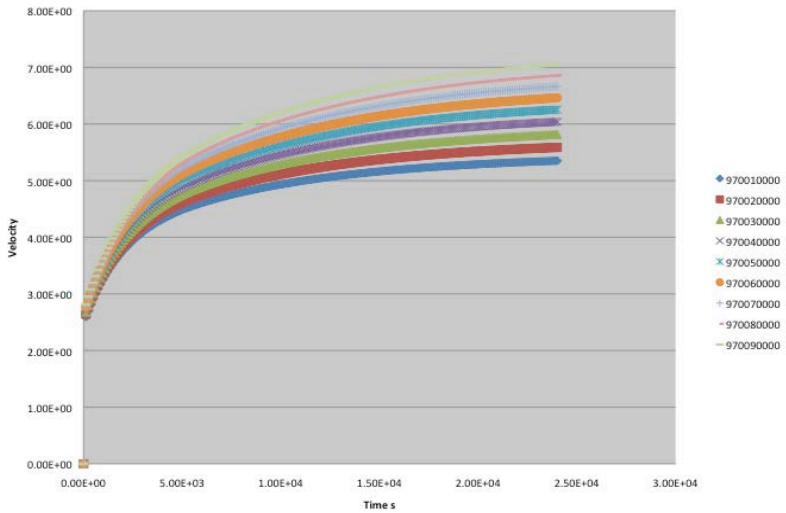

Figure 2.43a. Inner Riser Duct Air Velocity

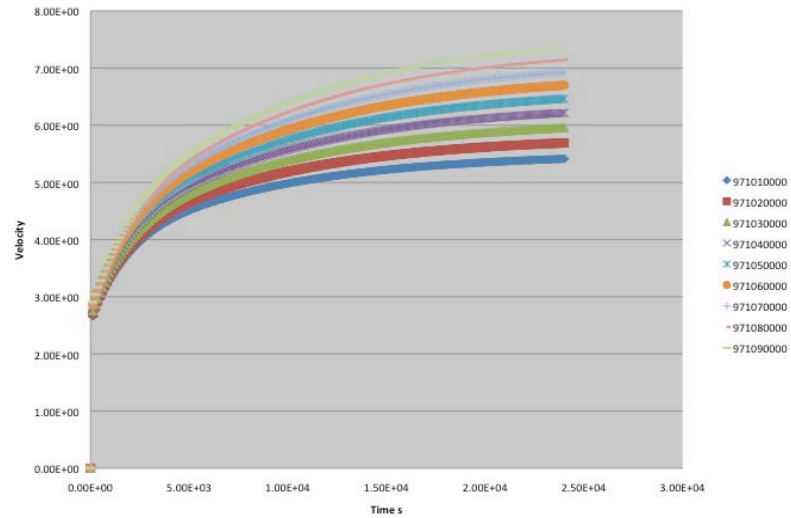

Figure 2.43b. Outer Riser Duct Air Velocity

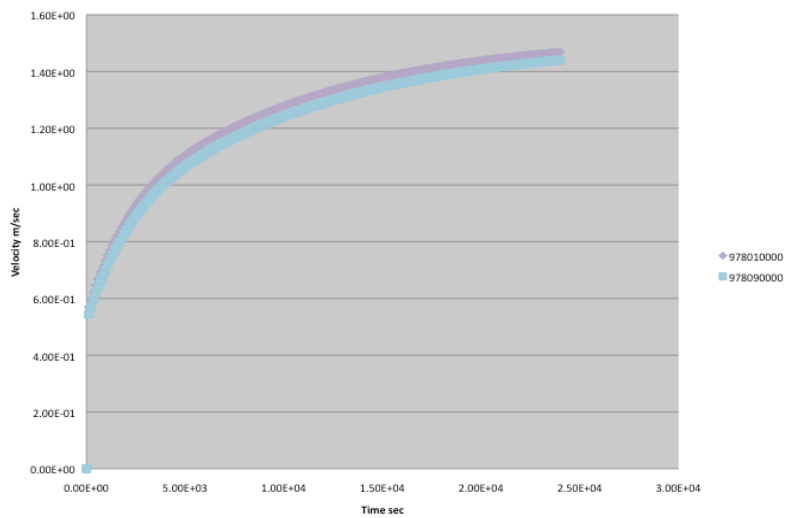

Figure 2.43c. Inner Riser Chimney Air Velocity

Figure 2.43. 2 Channel NSTF 46″ (116.84 cm) × 52″ (132.08 cm) Velocities

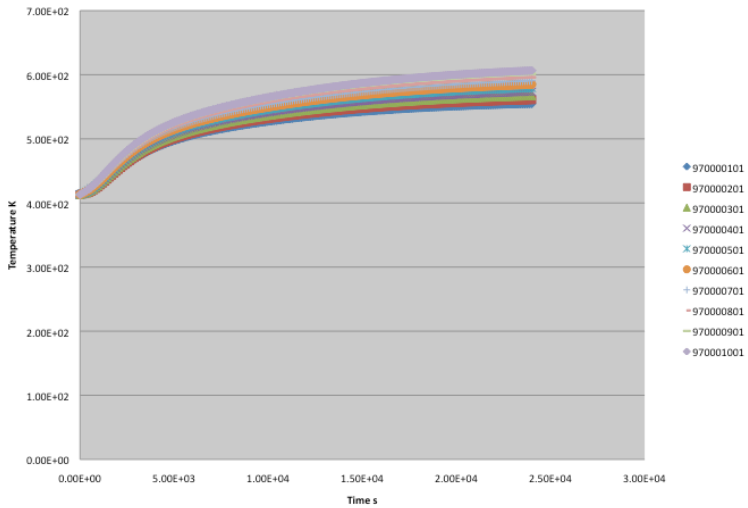

Figure 2.44a. Front Wall Temperatures

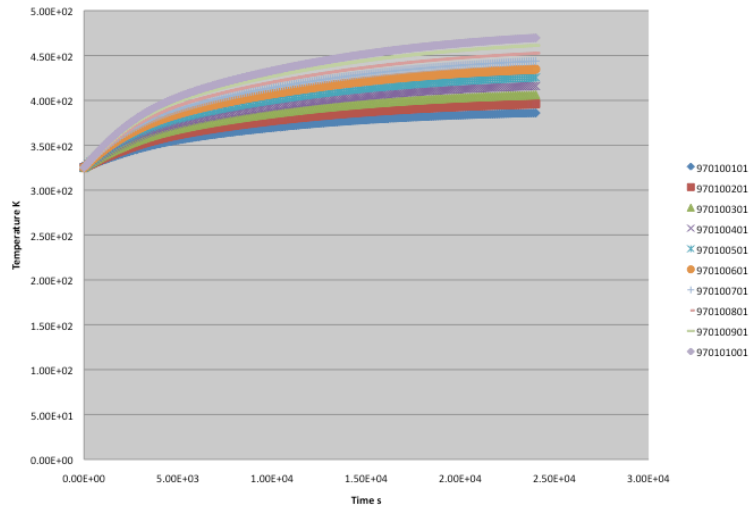

Figure 2.44b. Side Wall Temperatures

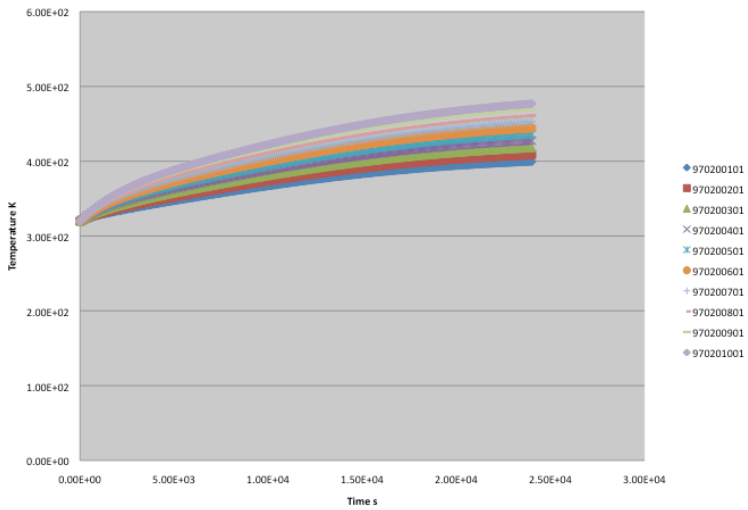

Figure 2.44c. Back Wall Temperatures

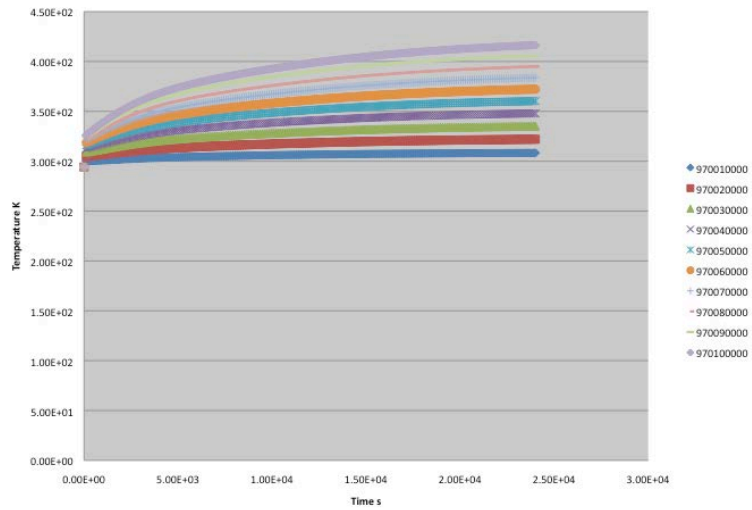

Figure 2.44d. Duct Gas Temperature Profile

Figure 2.44. 2 Channel NSTF 46″ (116.84 cm) × 52″ (132.08 cm) Riser Inner Duct Temperatures

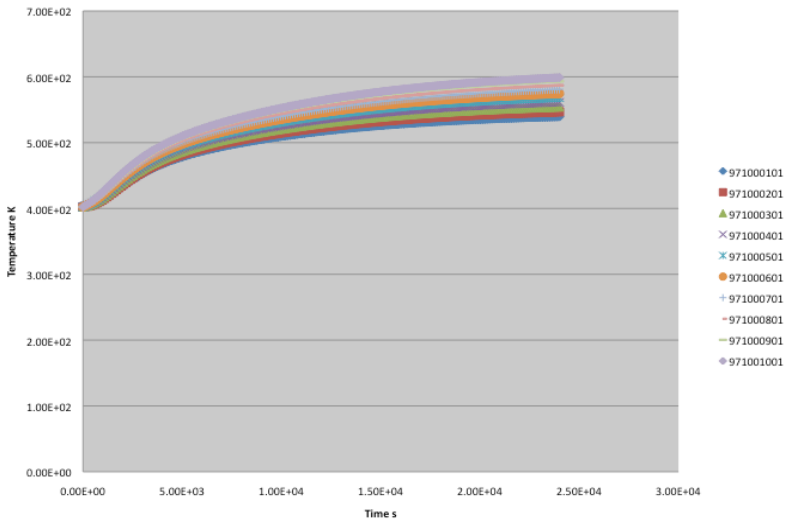

Figure 2.45a. Front Wall Temperatures

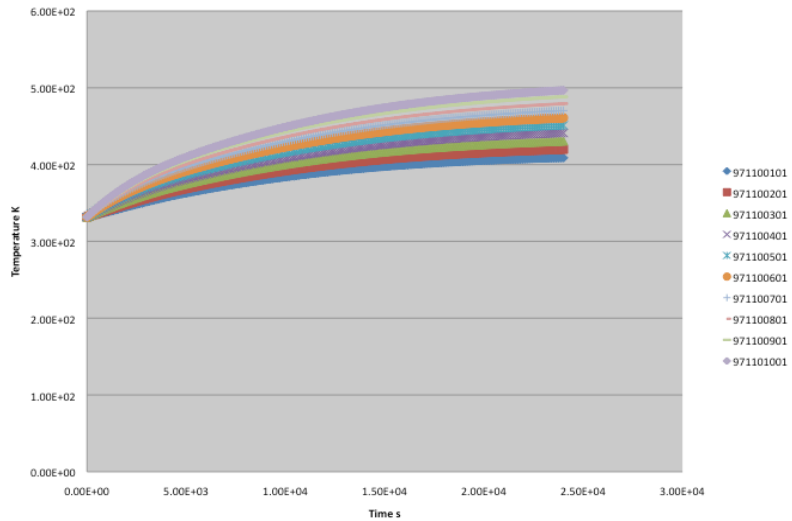

Figure 2.45b. Side Wall Temperatures

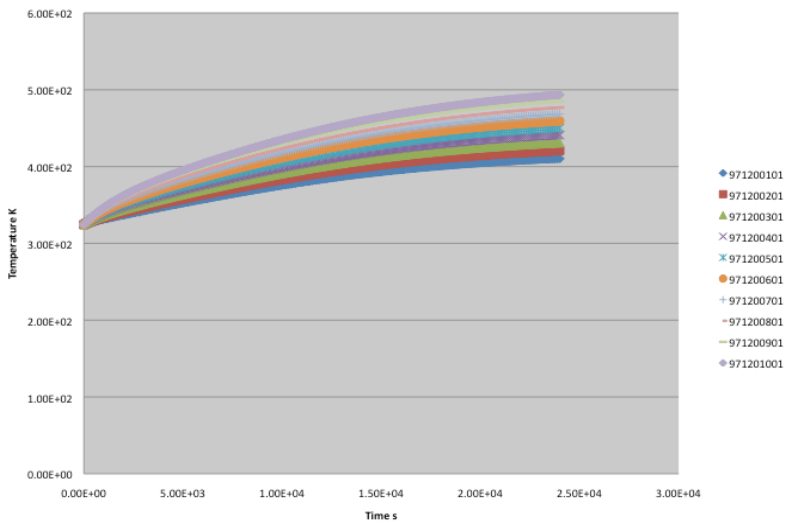

Figure 2.45c. Back Wall Temperatures

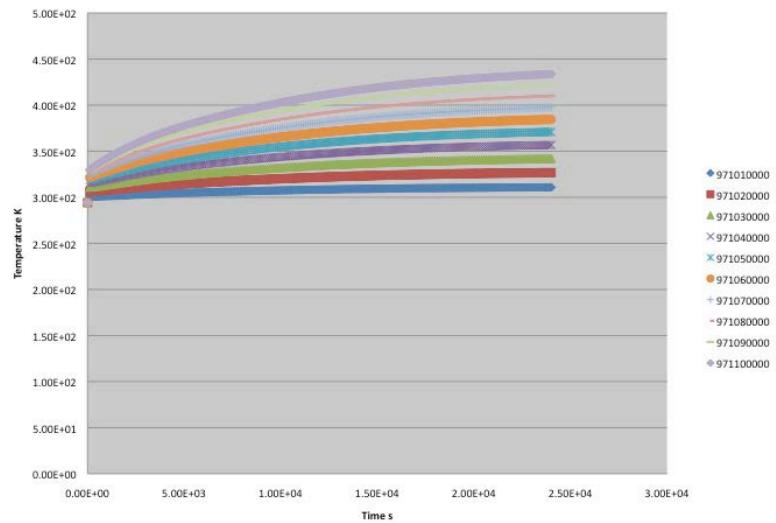

Figure 2.45d. Duct Gas Temperature Profile

Figure 2.45. 2 Channel NSTF 46″ (116.84 cm) × 52″ (132.08 cm) Riser Outer Duct Temperatures

2.4.4 2 Channel NSTF 46″ (116.84) × 52″ (132.08) Emissivity Change

This case simulates the use of reflective surfaces on the sides and back wall of the air cavity to lower the emissivity of the surfaces from 0.8 to 0.1 to match the surfaces from the Full-Scale RCCS Model. The intention was to help create a more uniform heat flux across the cross-section. The total internal power generation in the heater remains at 108.3 kW. The heat flux incident on the heated surface of the NSTF box therefore remains 12.2 kW/m^2. The heat transferred from the outer surface of the heated box wall is still partitioned into a radiation heat flux of 10.78 kW/m^2 and a convective heat flux of 1.19 kW/m^2 off the vessel wall. The transient duration was 24,000 seconds.

The model performed as expected as the T-F conditions monotonically increased to reach a stable steady condition in the asymptote. Table 2.9 shows that the chimney peak air mass flow rate is 0.742 kg/s, the peak air mass flow rate for the group of eight inner central riser ducts is 0.49 kg/s, and the peak air velocity in the duct is 6.97 m/s. Table 2.20 also shows that the peak air mass flow rate for the four outer boundary riser ducts is 0.25 kg/s and the peak air velocity in the duct is 7.09 m/s. The corresponding values for the peak air riser outlet temperatures are 432 and 441 K. The peak heated box wall temperature is 784 K while the peak box back wall surface temperature is 488 K. Focusing on the central inner riser ducts the peak front wall temperature is 604 K; the peak side wall temperature is 466 K, and the peak duct back wall temperature is 478 K. The peak front wall temperature of the outer boundary riser ducts is 597 K, the peak side wall temperature is 496 K and the peak duct back wall temperature is 495 K.

The transient history of the heated wall temperature is given at the surface nodes starting from the bottom and proceeding to the top of the heated segment in Figure 2.46. Figure 2.47 shows the corresponding liner (insulation) temperature at the corresponding axial locations on the side wall of the cavity while Figure 2.48 shows the same for the back wall. More details on the temperatures of the inner hot riser ducts can be found in Figure 2.49 while the temperatures of the outer hot riser ducts are displayed in Figure 2.50. The transient behavior of the temperatures of the hot riser duct front walls, side walls, back walls and air coolants can be observed. The metal temperatures in these Figures are axial profiles starting with the bottom node and proceed to the outlet end. The effect of the emissivity change is best seen in the differences in the back wall temperature of the cavity box.

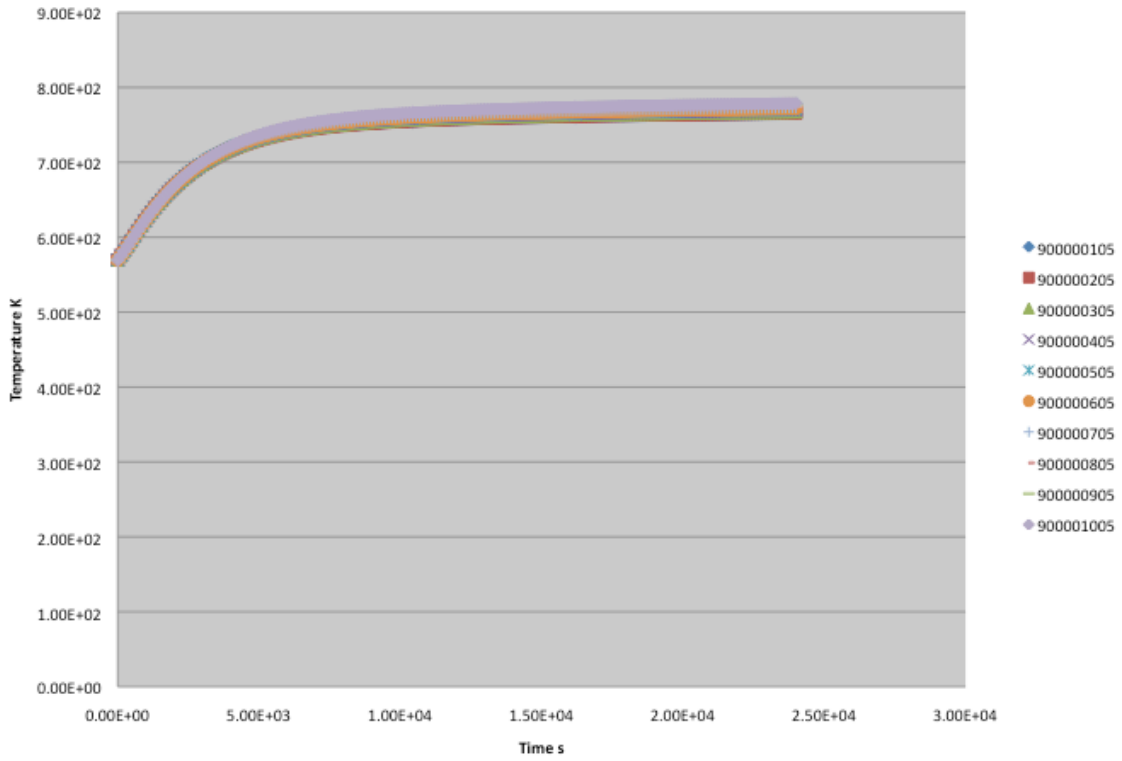

Figure 2.46. 2 Channel NSTF Emissivity Change Heated Wall Temperature

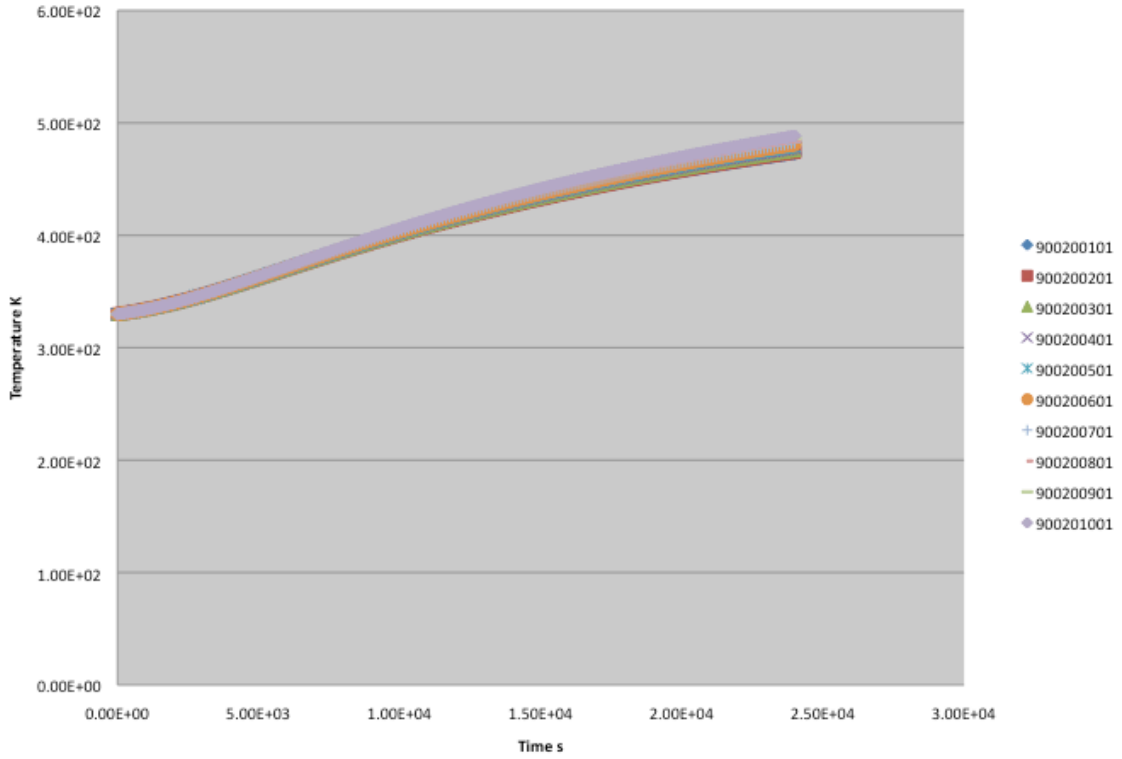

Figure 2.47. 2 Channel NSTF Emissivity Change Cavity Side Liner Temperature

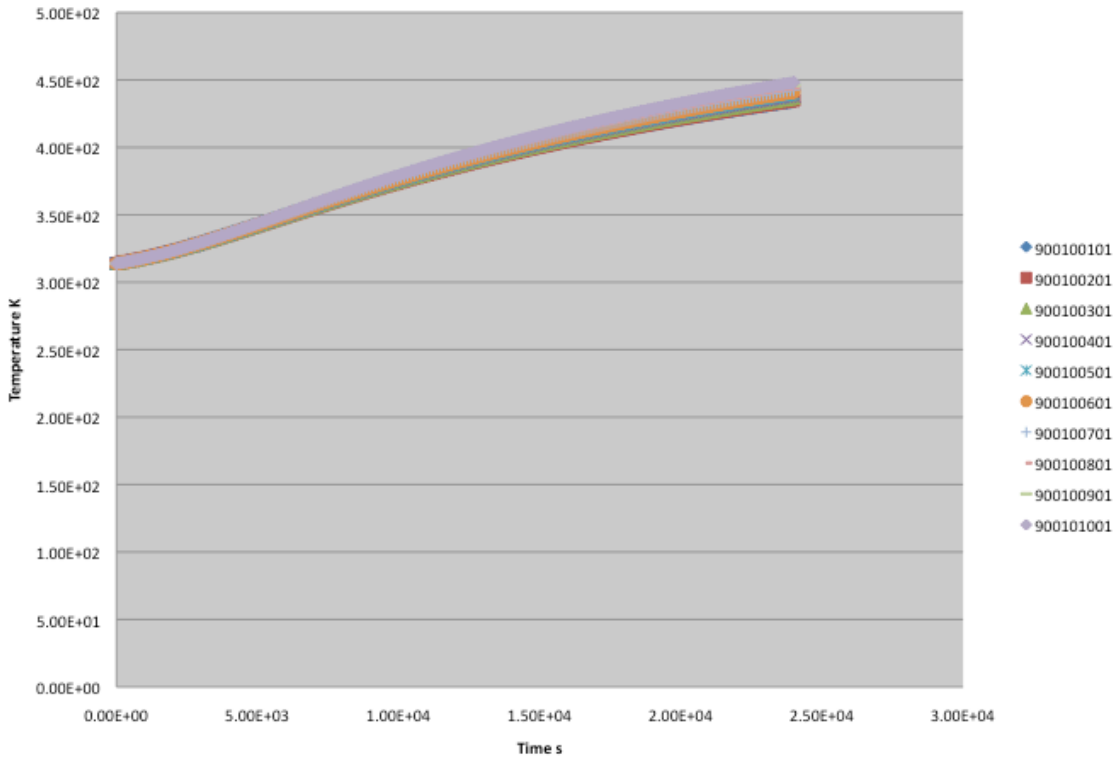

Figure 2.48. 2 Channel NSTF Emissivity Change Cavity Back Liner Temperature

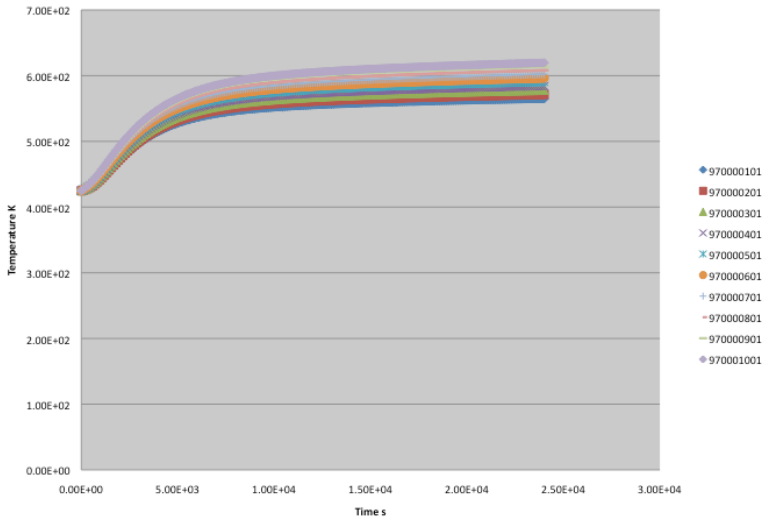

Figure 2.49a. Front Wall Temperatures

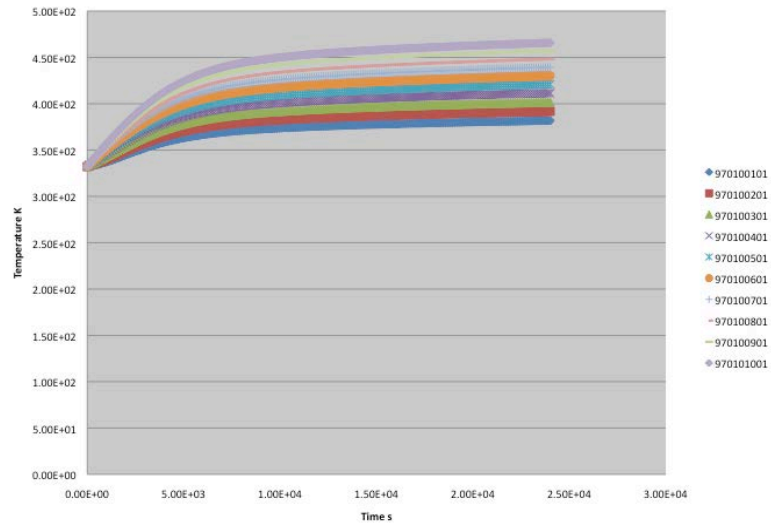

Figure 2.49b. Side Wall Temperatures

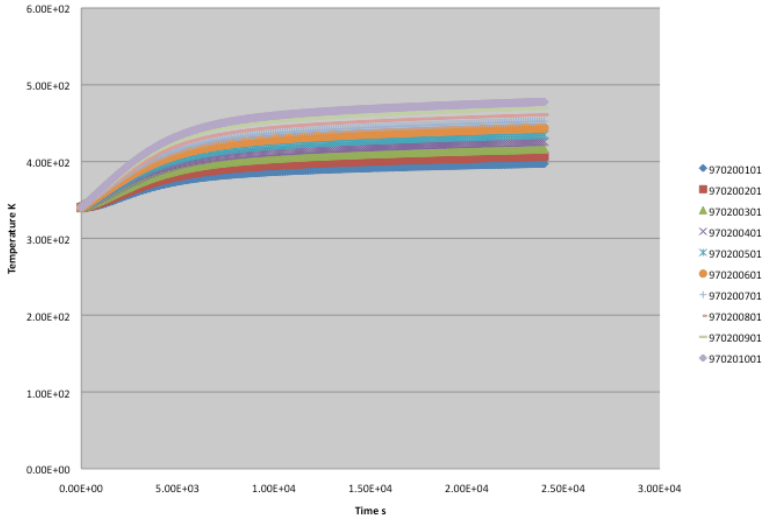

Figure 2.49c. Back Wall Temperatures

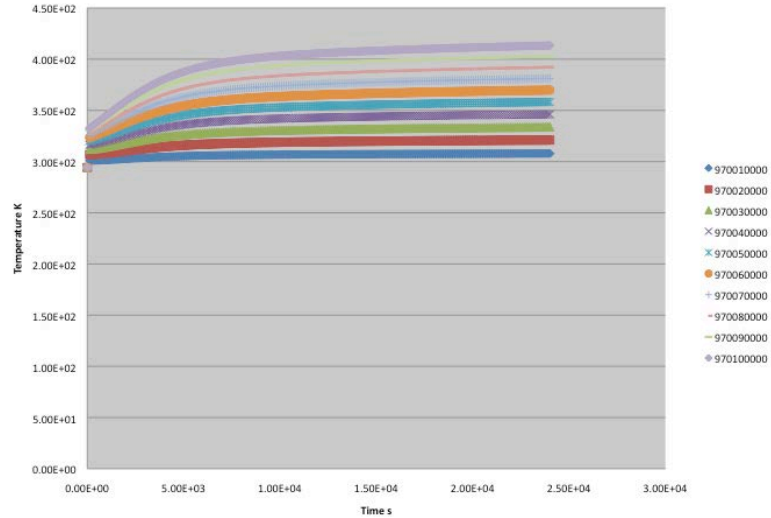

Figure 2.49d. Duct Gas Temperature Profile

Figure 2.49. 2 Channel NSTF Emissivity Change Riser Inner Duct Temperatures

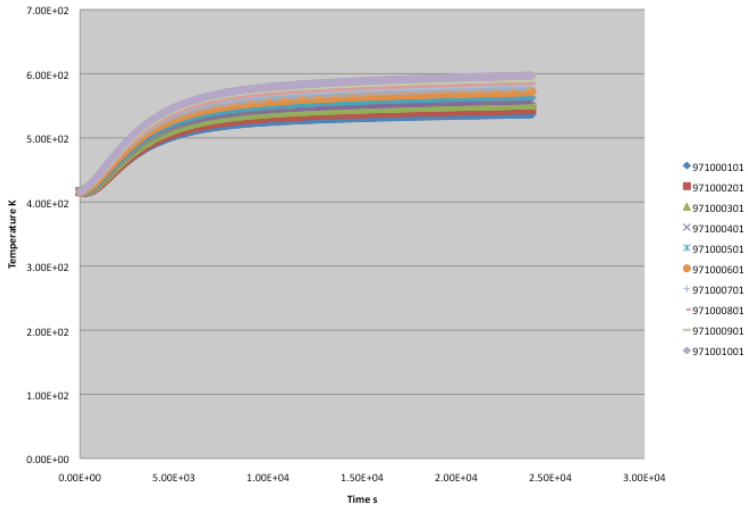

Figure 2.50a. Front Wall Temperatures

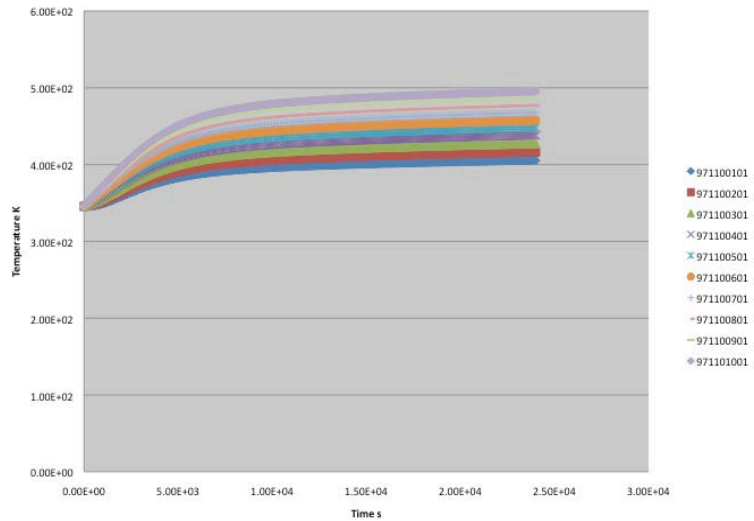

Figure 2.50b. Side Wall Temperatures

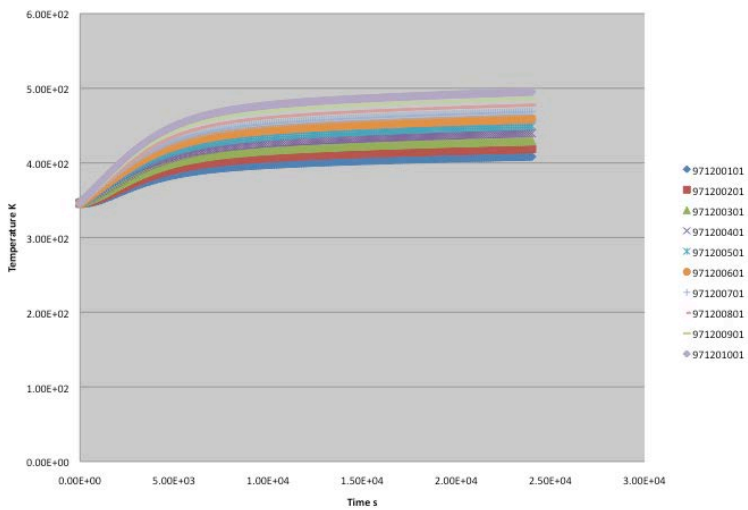

Figure 2.50c. Back Wall Temperatures

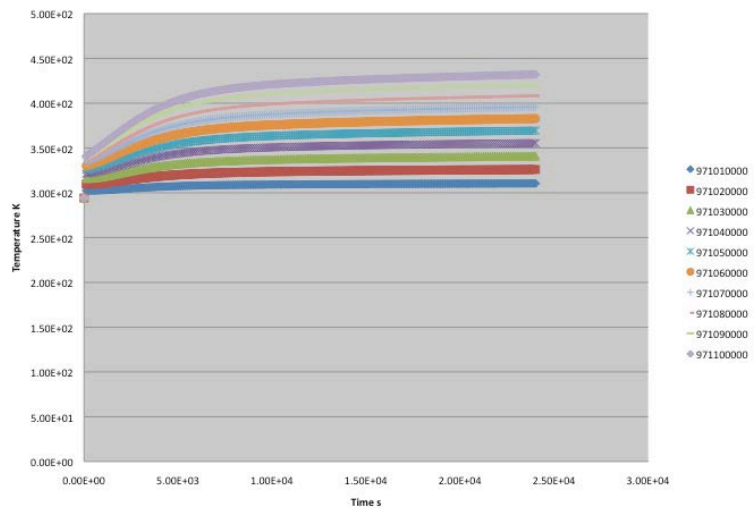

Figure 2.50d. Duct Gas Temperature Profile

Figure 2.50. 2 Channel NSTF Emissivity Change Riser Outer Duct Temperatures

2.4.5 2 Channel NSTF 46″ (116.84 cm) × 52″ (132.08 cm) Duct-Radiation

This case is compared to the results of the 2 Channel NSTF 46″ (117.84 cm) × 52″ (132.08 cm) Emissivity Change model to compare the difference in setting the heat transfer between the walls of the ducts from conduction to radiation. The total internal power generation in the heater remains at 108.3 kW. The heat flux incident on the heated surface of the NSTF box therefore remains 12.2 kW/m^2. The heat transferred from the outer surface of the heated box wall is still partitioned into a radiation heat flux of 10.78 kW/m^2 and a convective heat flux of 1.19 kW/m^2 off the vessel wall. The transient duration was 24,000 seconds.

With the different mode of heat transfer, the only major difference from the previous model is that the temperatures of the duct walls are more uniform. Table 2.9 shows that the peak temperatures of the front wall, side wall, and back wall of the inner riser ducts are 565, 472, and 479 K respectively. The corresponding inner riser duct peak temperatures are 565, 488, and 497 K respectively.

2.5 Conclusions

Based on these RELAP5 models and results, a test of the derived scaling laws was carried out. These scaling laws are detailed in Chapter 1 and used in the design of the proposed NSTF experiments for the GA MHTGR air-cooled RCCS version and the plan is to continue to use them in the experiment design. The fundamental approach is to preserve the air-outlet temperature at the ends of hot riser ducts by adjusting orifices at the inlets of the hot riser ducts simulated in the experiments. In this way, the RCCS riser outlet temperatures from the NSTF experiments will match those from the hot riser outlets in the full-scale GA-MHTGR RCCS. To justify this approach it can be seen from Table 2.8 presenting the full scale/half scale RELAP5 results that the value of 4.4 for the J574 energy loss coefficient gives an air duct outlet temperature of 468 K for the half-scale/high heat flux/conduction case. This is close to the corresponding value of 471 K for the corresponding full-scale/high heat flux/conduction case. Junction J574 is the RELAP5 junction at the inlet to the hot riser as shown in Figure 2.6. Additional details regarding the pressure profiles are available in Figures 2.22 and 2.23. The value of 4.4 for the J547 energy loss coefficient was then used again in the half-scale/med flux/conduction RELAP5 case. Table 2.8 shows that for this case the air outlet temperature is 393°K. In comparison Table 2.8 shows that the air outlet temperature for the corresponding full-scale/med flux/conduction RELAP5 case is also 393°K. This means that the air outlet temperatures for the full-scale cases match those from the half-scale case for two different power level parametrics using the same half-scale riser inlet orifice coefficient. This shows that the scaling approach taken in Chapter 1 is reasonably valid, even with the approximations made for the other nondimensional groups while preserving the Richardson number and the Friction Drop number.

Furthermore, the comparison made in Table 2.8 of the intraduct radiation modeling option made with the intraduct conduction model for the half-scale case shows that the air outlet temperatures are not much affected by the differences in the two modeling options. The major effect is the change in the uniformity of the temperature distribution azimuthally around the metal riser duct wall.

References

2.1 M. T. Farmer, et.al., "Natural Convection Shutdown Heat Removal Test Facility (NSTF) Evaluation for Generating Additional Reactor Cavity Cooling System (RCCS) Data", ANL-GenIV-058, Argonne National Laboratory Report, September 2005.

2.2 S. Lomperski, W. D. Pointer, C. P. Tzanos, T.Y.C. Wei, C. M. Crooks, and O. A. Rodriguez, "RCCS Studies and NSTF Preparation Air-Cooled Option," ANL-GenIV-142, Sept. 30, 2010.

3.0 Air-Cooled RCCS CFD Analyses

3.1 Motivation and Objective

The proposed improvements to the NSTF will enable the completion of a series of experiments that will evaluate the performance of an air-cooled Reactor Cavity Cooling System. The proposed baseline design of the modified NSTF test section has been shown to maintain key scaling parameters related to natural convective flow and thermal mixing. [3.1, 3.2, 3.3] Preliminary CFD studies have shown that large-scale flow structures in mixing plena and chimney structures are also preserved in the NSTF baseline design.**[**3.4**]** The additional CFD analyses described in this section provide a preliminary solution verification study to assess the uncertainty in the baseline simulations and evaluations of the impact of alternative design options that may be considered to simplify instrumentation access or to better represent anticipated RCCS system design.

3.2 Air-Cooled RCCS System Geometry

The air-cooled RCCS uses natural convection to drive the flow of air from outside the power plant to remove residual heat during operational and emergency transients. Air enters the system through an external vent and travels through the outer annulus of a coaxial duct to the upper region of the reactor cavity where it fills a cold upper plenum. Cold outside air from the plenum flows down through insulated downcomers lining the cavity walls to a lower cold plenum and then rises through the heated RCCS ducts. The heated air is collected in an upper hot plenum and then exits through the central region of the coaxial duct to an external chimney. A perspective view of the full system geometry and a cutaway view showing the cross-sections of the plena are shown in Figures 3.1 and 3.2.

3.3 NSTF Baseline Geometry

The baseline modified NSTF geometry replicates the primary features of the air-cooled RCCS. Air from the external environment enters the test section through a lower plenum, accelerates upward through a set of parallel riser channels, and mixes in an outlet plenum before exiting to the environment through one of two chimneys. The baseline NSTF CFD model, shown in Figure 3.3, retains these primary features, but the surrounding environment is simplified to a single large volume rather than explicitly representing building features and the protrusion of the chimney outlets above the building roofline. Since the common air volume used in the model is very large in comparison to the heated region of the experiment, a constant temperature surface condition is sufficient to ensure that air drawn into the test section is at the bulk environmental conditions.

For the present studies, uniform heat flux conditions are applied on all riser surfaces to evaluate bulk flow behavior; radiation heat transport through the cavity is not evaluated. A uniform 1.24 kW/m^2 heat flux applied to all the risers, which is consistent with a loss of flow accident in which the risers expel all of the heat from the reactor vessel radiating at a uniform heat flux of 10 kW/m^2, out of the system. Additional planned analyses will evaluate the effect of realistic nonuniform heat flux conditions using the final selected geometry.

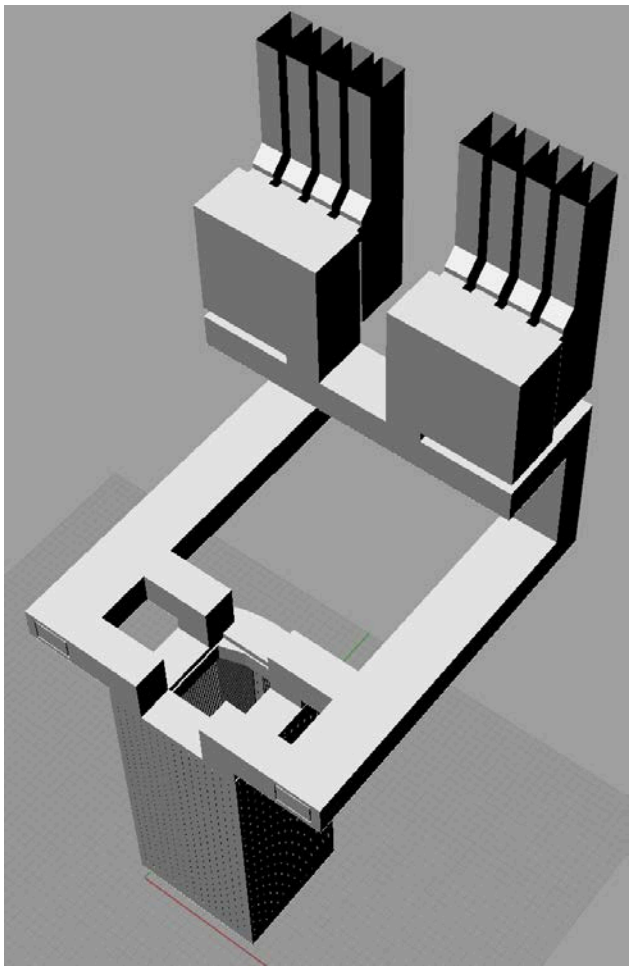

Figure 3.1. Complete RCCS Model

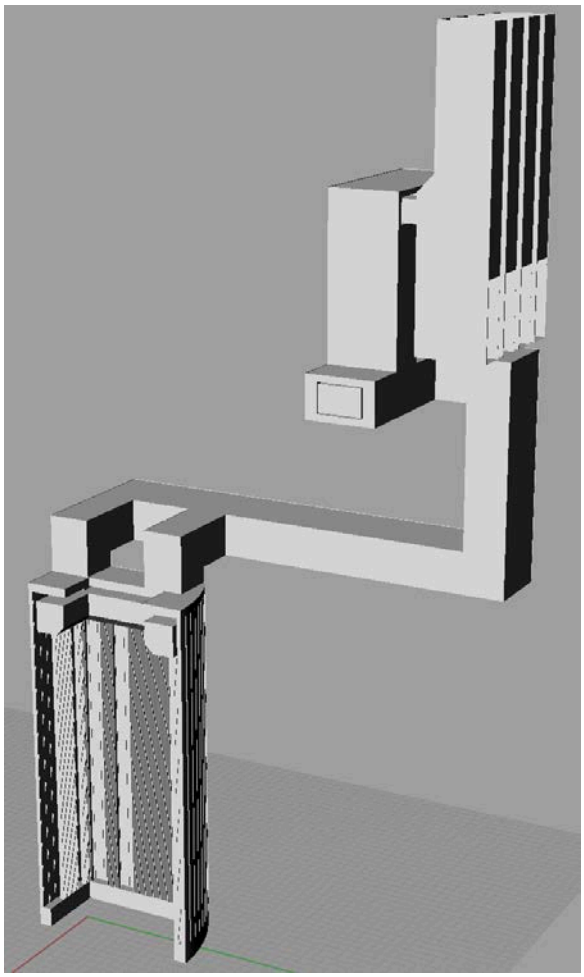

Figure 3.2. Full RCCS Side Cut Away View

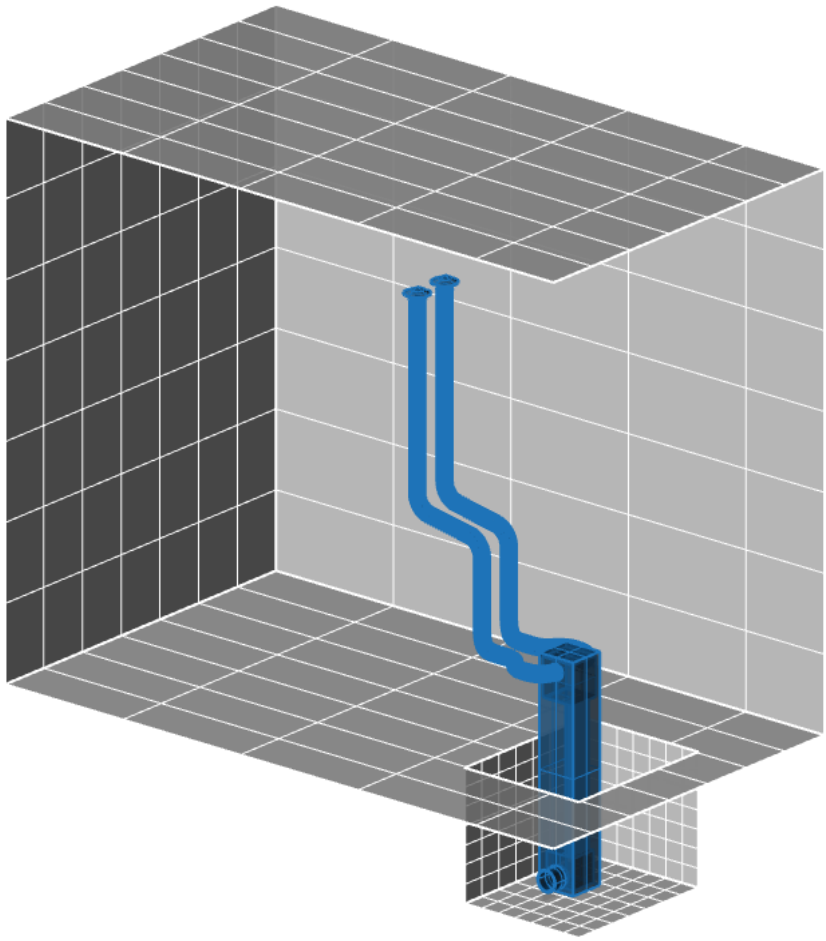

Figure 3.3. CAD Image Showing the Simplified CFD Model of the NSTF Air-cooled RCCS Experiment

3.4 Simulation Methodology

RANS-based simulations of natural convection and radiation heat transport have been completed using the commercial CFD code STAR-CCM+. The general-purpose commercial CFD code STAR-CCM+ is a finite volume formulation code for the analysis of compressible and incompressible flows and heat transfer. STAR-CCM+ supports the use of generic polyhedral mesh elements, greatly simplifying the generation of computational meshes for complex geometries.

The SIMPLE algorithm is used with Rhie-Chow interpolation for pressure-velocity coupling and algebraic multigrid preconditioning. A 2nd-order central differencing scheme and the realizable k-epsilon turbulence model with a two-layer all y+ wall treatment (Norris & Reynolds) were applied. The convergence criteria was defined as the reduction of all equation residuals by four orders of magnitude, i.e., reducing the normalized residuals below 10^{-4}.

3.5 NSTF Baseline CFD Model

The baseline computational mesh was constructed based on CAD data describing the NSTF baseline geometry. Using the CAD surfaces, a well-defined triangulated surface mesh was generated using the default STAR-CCM+ meshing tools. Based on this triangulated surface, a polyhedral volumetric mesh was generated. A polygonal prismatic wall extrusion layer is used to improve the applicability of the wall treatment employed by the turbulence model used in these simulations.

The final optimized mesh consists of more than 15 million polyhedral and prismatic polygonal cells, with local refinements applied in the test section, especially in the riser ducts. The mesh distribution in the riser ducts is shown in Figure 3.4. The baseline simulation was completed using 32 cores of a commercial grade Linux cluster and was allowed to run well beyond the convergence criteria to 15,000 iterations to ensure that a converged steady-state was reached. Prior analyses [3.4] have shown that tighter residual-based convergence criteria do not guarantee uniformity of flow through the 12 parallel riser ducts in steady-state simulations of the NSTF test section. Convergence is determined through a combination of reported residual values and monitoring point values. The evolution of residual values for the baseline simulation is shown in Figure 3.5.

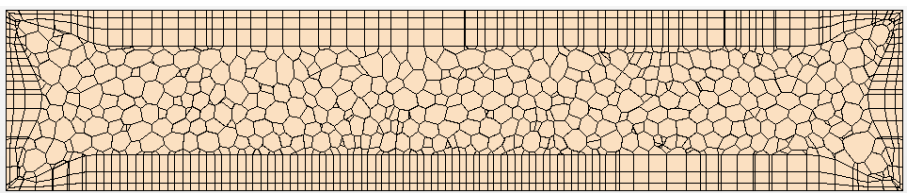

(a) Riser cross-section

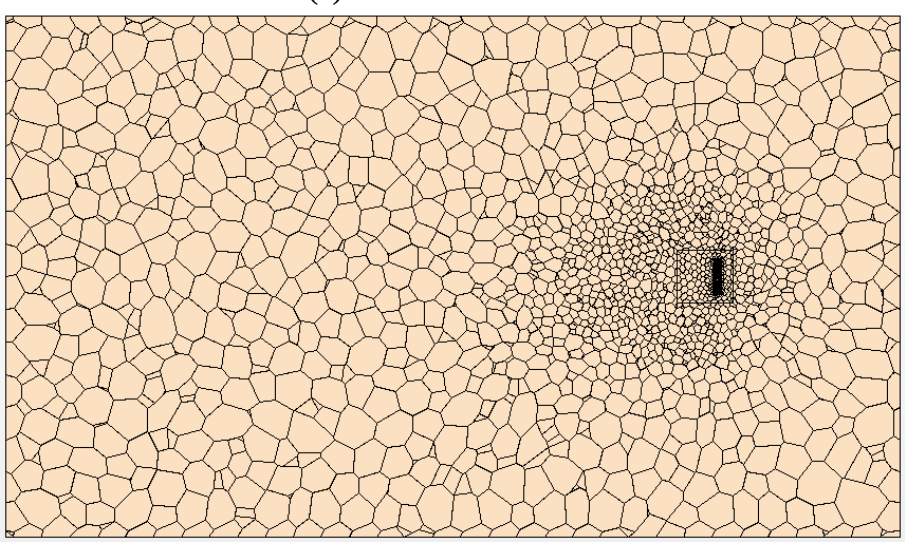

(b) Full model cross-section with concentrated mesh regions indicating riser positions

Figure 3.4. Mesh Distribution in Riser Cross-section

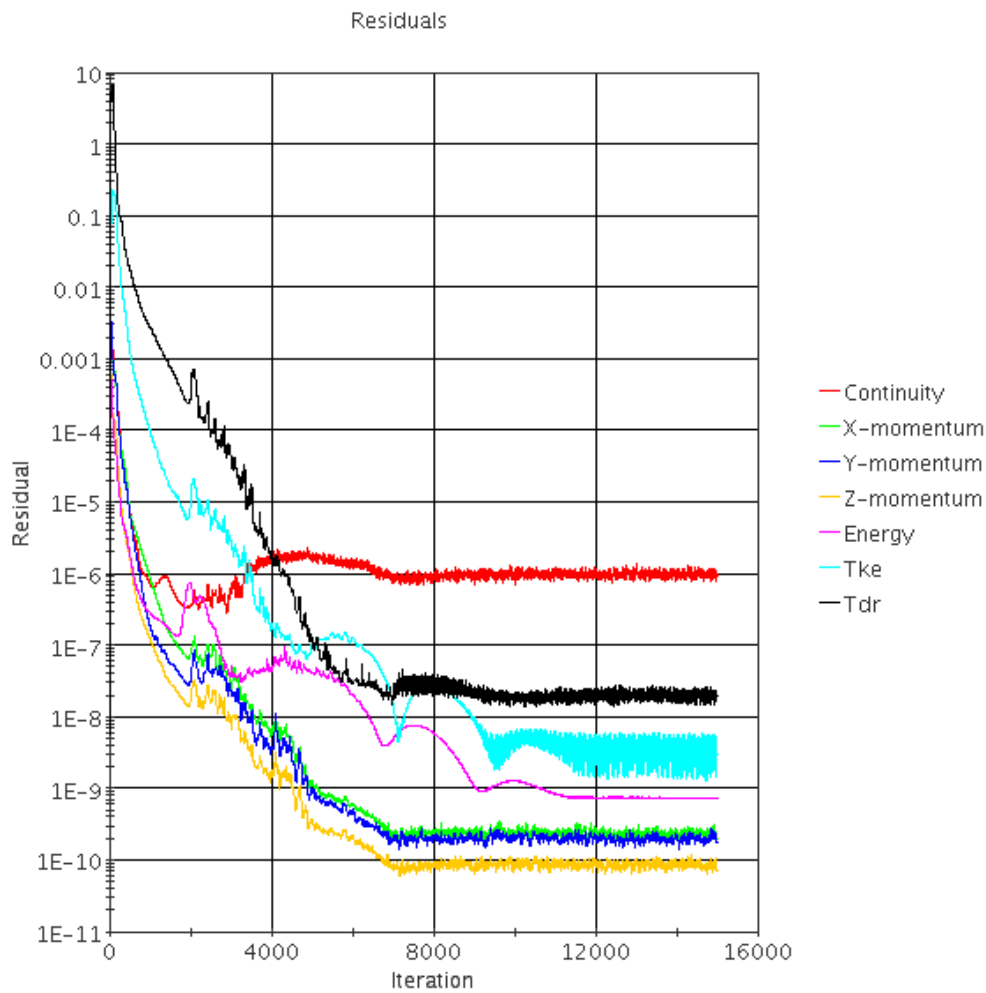

Figure 3.5. Residual Values Monitored over 15000 Iterations for Baseline NSTF Simulation

3.6 NSTF Baseline Results

Predicted temperature profiles in the riser ducts are shown for three different cross sections in Figure 3.6. Although significant nonuniformity in temperatures resulting from the asymmetry of the inlet can be seen in the lower regions of the risers, the temperature profiles are very uniform by the time the flowing air reaches the outlet plenum. This temperature recovery suggests that acceleration rates may not be uniform in the parallel heated channels, and indeed a small nonuniformity in the outlet velocities does appear in the velocity profiles shown in Figure 3.7. The differences in the profiles of each riser at the outlet can be more easily seen in Figure 3.8, where the scalar value is plotted as a function of position along a line from the front surface of the riser duct to the back.

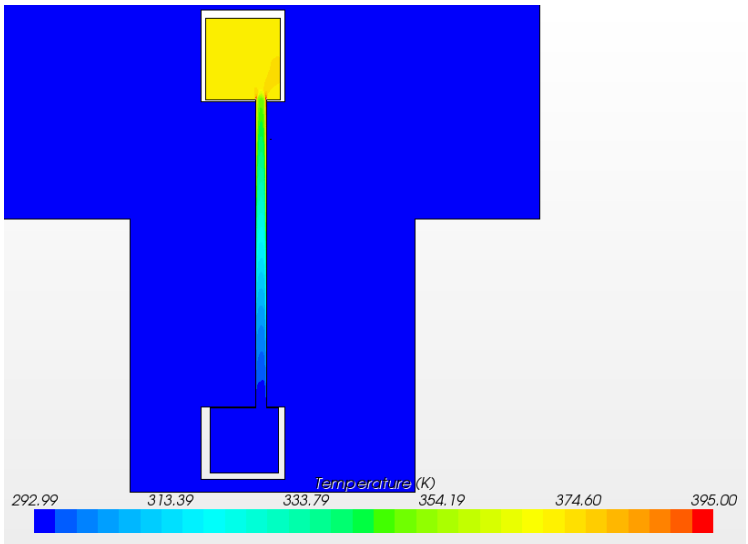

(a) Left vertical cross-section

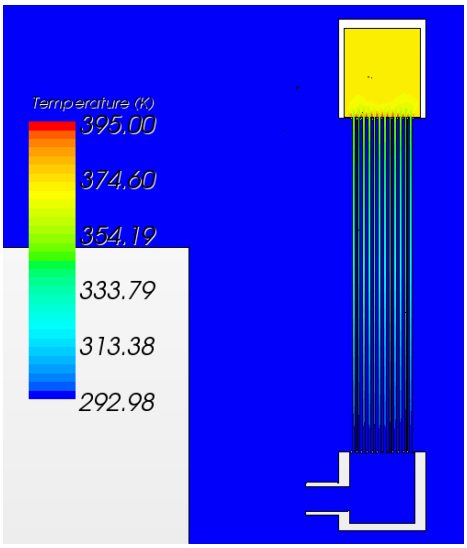

(b) Front vertical cross-section

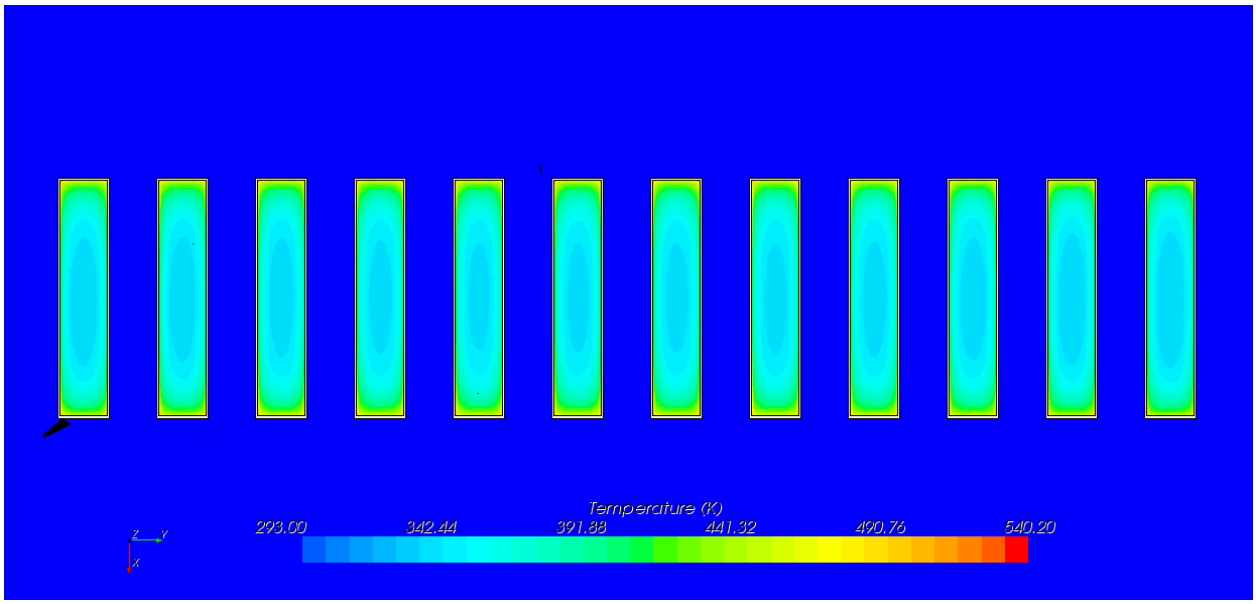

(c) Horizontal cross-section near riser outlet

Figure 3.6. Predicted Temperature Profiles at Riser Outlet for Baseline Model

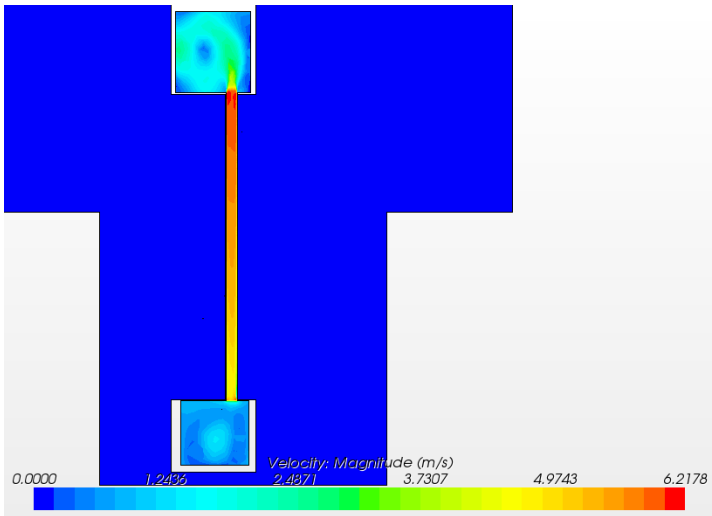

(a) Left vertical cross-section

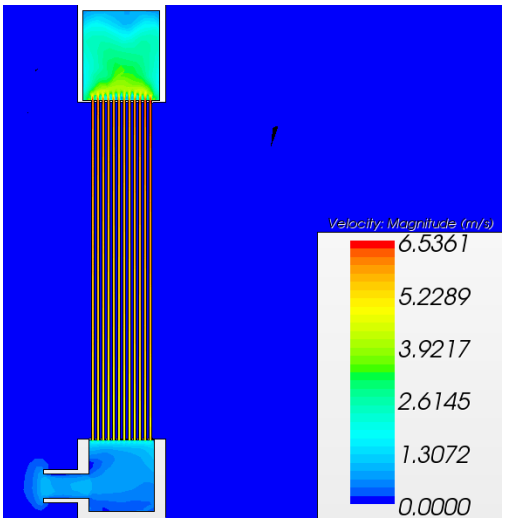

(b) Front vertical cross-section

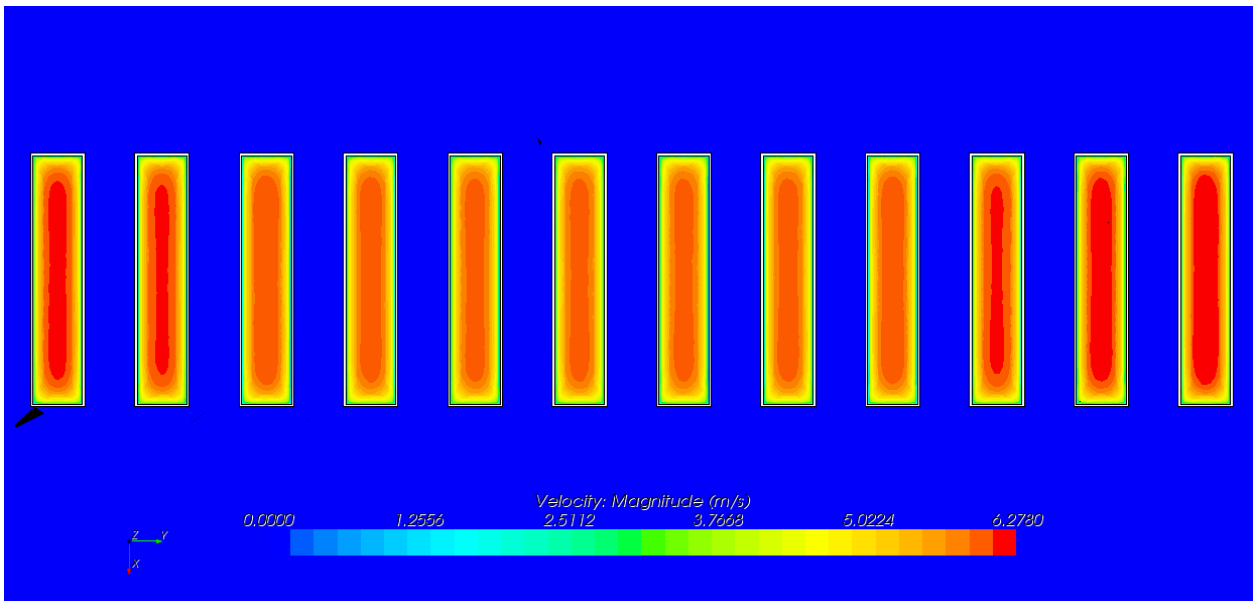

(c) Horizontal cross-section near riser outlet

Figure 3.7. Predicted Velocity Magnitude Profiles in Risers for Baseline Model

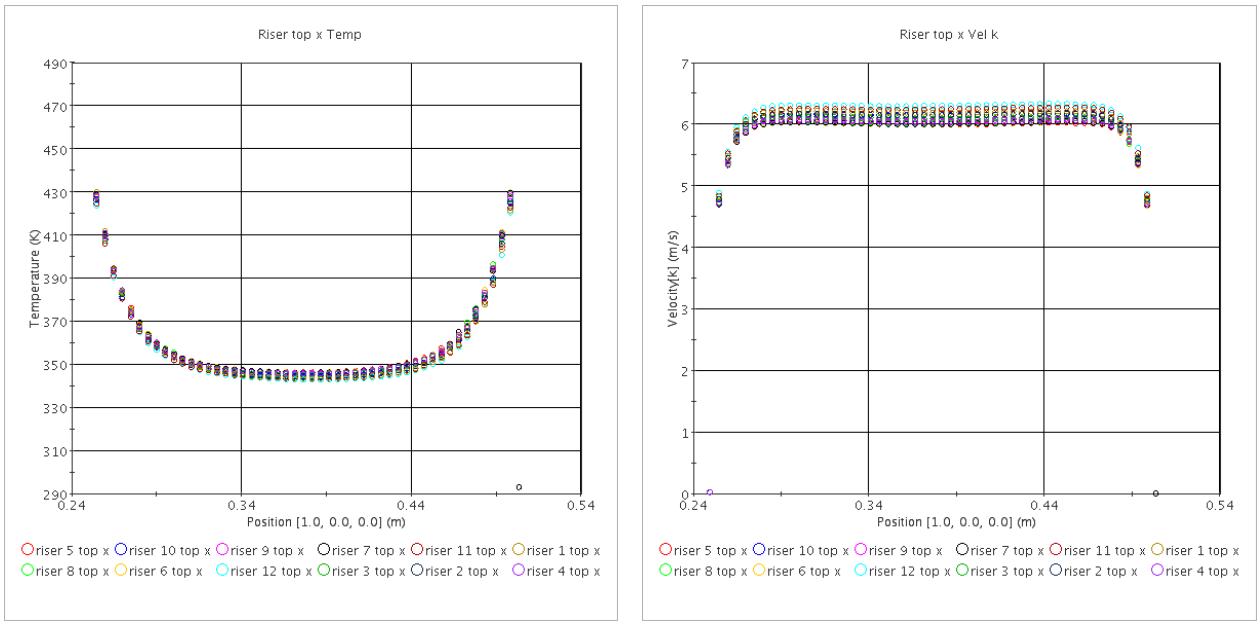

(a) Temperature (b) Vertical Velocity Vector Component

Figure3.8. Extracted Scalar Profiles along a Line from Front to Back of Each Riser

Figure 3.7a, clearly shows the formation of a strong recirculation zone in the outlet plenum, much like those seen in prior analyses of the anticipated RCCS design. This recirculation pattern is seen with greater resolution in Figure 3.9, where the out-of-plane component of velocity is shown in Figure 3.9b to emphasize the strong rotational flow into the page on the top of the outlet plenum and out of the page at the bottom of the lower plenum. The extension of these recirculation cells into the outlet piping shown in Figure 3.10 is again very similar to the behaviors observed in prior RCCS analyses. Some asymmetry is observed in the outlet plenum, possibly resulting from the asymmetry of the inlet configuration. As a result, the two outlet flows are not matched, and slightly different velocity profiles are seen at the chimney outlets as shown in Figure 3.11.

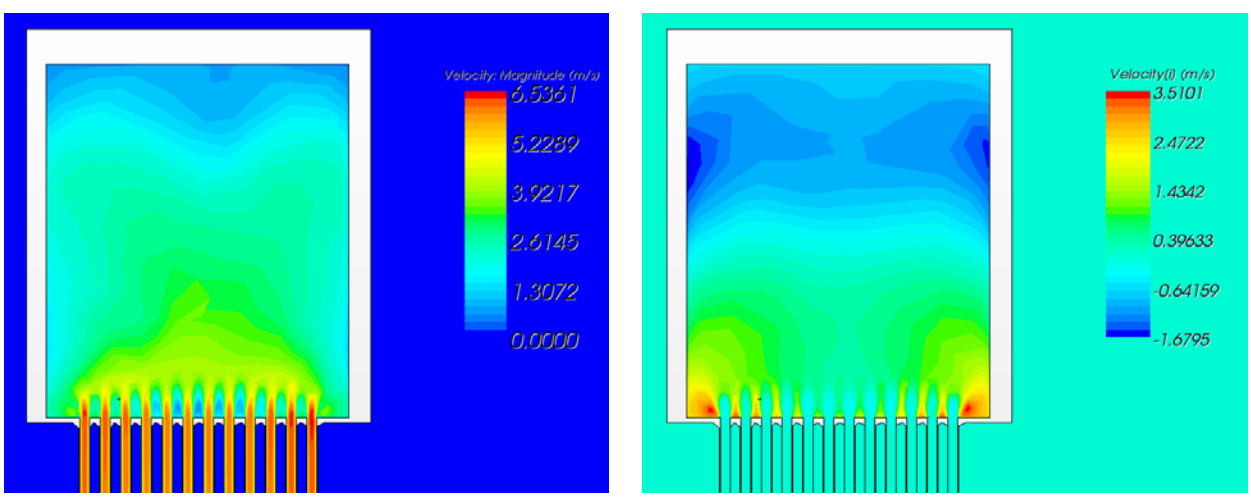

(a) Velocity magnitude (b) Out-of-plane velocity

Figure 3.9. Velocity Profiles in a Vertical Cross-section of the Outlet Plenum

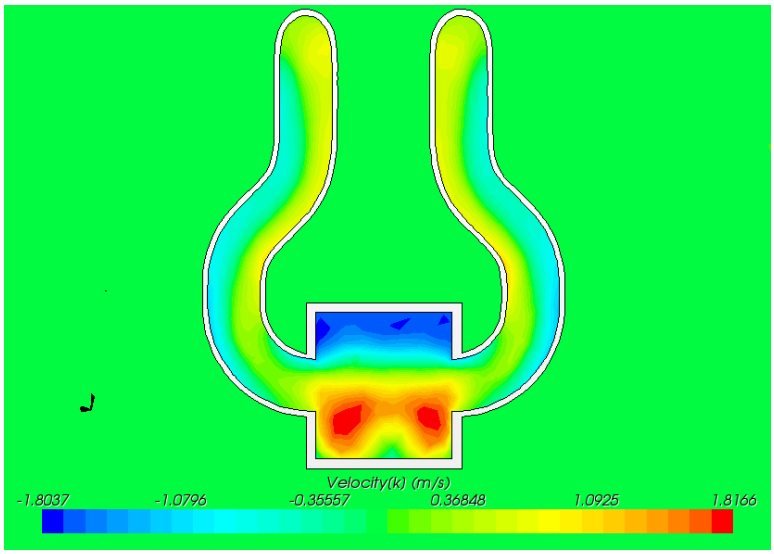

Figure 3.10. Out-of-plane Velocity Profiles in a Horizontal Cross-section of the Outlet Plenum and Piping

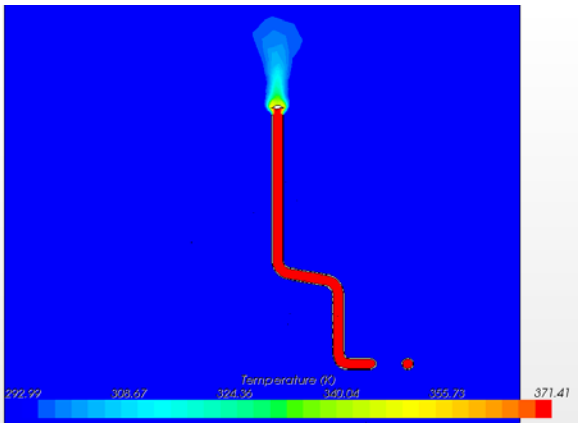

(a) Temperature

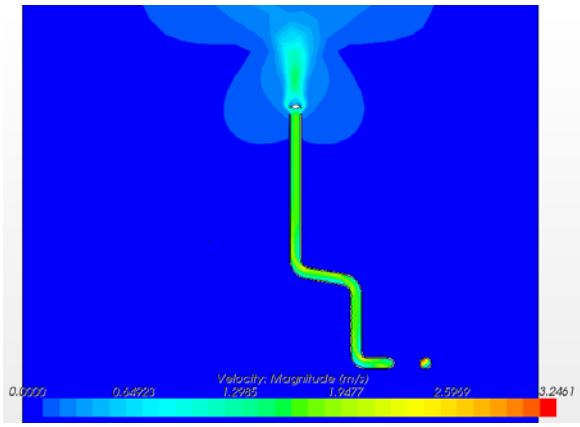

(b) Velocity magnitude

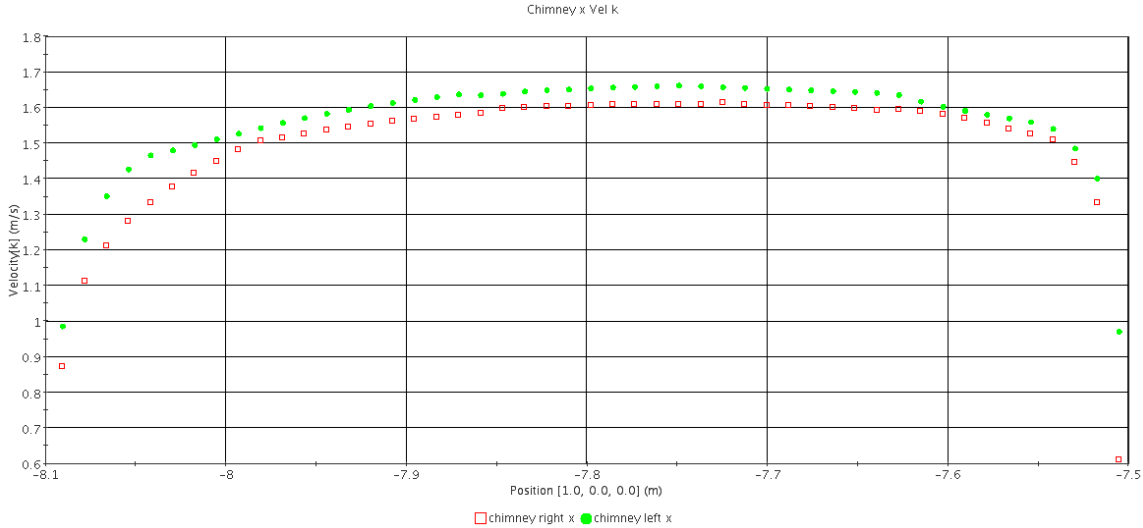

(c) Velocity profile in both chimneys

Figure 3.11. Chimney Flow Temperature and Velocity Profiles

3.7 Mesh Sensitivity Study Results

In order to evaluate the sensitivity of the predicted flow fields to the mesh size, two alternate computational meshes describing the baseline geometry were developed using the same process. In these cases, the sizes of the nominal cells are increased 20 and 40% above the baseline size. In both cases, the thickness of the first three cell layers near the wall of the test section structures is maintained at the same value. This reduces the number of computational cells used by these models to 8.3 million and 6.3 million, respectively.

In both alternate mesh cases, predicted flow behaviors are very similar to the baseline case. The primary impact of the coarsening of the mesh is the loss of resolution in the prediction of peak velocities and temperatures, as illustrated by Figure 3.12 when compared with Figure 3.10. Since the primary focus of the experiment is the heat transfer performance within the riser ducts themselves, the extracted profiles at the outlet of the sixth riser duct were used for a more quantitative comparison as shown in Figures 3.13 and 3.14. For the three different mesh cases, the average axial component of the velocity along the selected line is 6.2 m/s and the average temperature along the same line is 356.76 K. The average standard deviation between the three cases in the predicted values at each sampling point along the selected line is a velocity of 0.022 m/s a temperature of 0.81 K. The maximum standard deviation at any single position is a velocity of 0.10 m/s and a temperature of 4.3 K. Based on these results, the baseline mesh size selection is expected to provide an adequate representation of the flow and heat transport physics for the current series of analyses.

A separate study increased the thickness of the prismatic layer by 20% over the baseline value. Similarly, no significant differences in predicted flow behaviors were observed.

3.8 Turbulence Model Sensitivity Results

In order to evaluate the sensitivity of the predicted flow fields to the selected turbulence model, an alternate simulation was completed using the Menter k-omega SST model with the baseline geometry and computational mesh. The SST model should be expected to be more sensitive to flow separations and predict increased turbulence in the wake fields downstream from such flow structures. As a result, the model is often used in aerodynamic analyses when accurate prediction of base drag is desirable.

As shown in Figure 3.15, the predicted riser flow fields using the SST model are much less uniform, in spite of very similar flow field predictions in the lower inlet plenum. In comparisons of predicted temperature profiles within the duct, the SST model consistently predicts more turbulent diffusion that the realizable k-epsilon model, resulting in higher riser flow temperatures and a flatter temperature distributions, as shown in Figure 3.16. The increase in the energy tied up in turbulence also results in reduced riser velocities as shown in Fig 3.17. In the absence of experimental data to validate the selection of turbulence model, the realizable k-epsilon model, which predicts more conservative RCCS duct performance, was used for remaining design analyses.

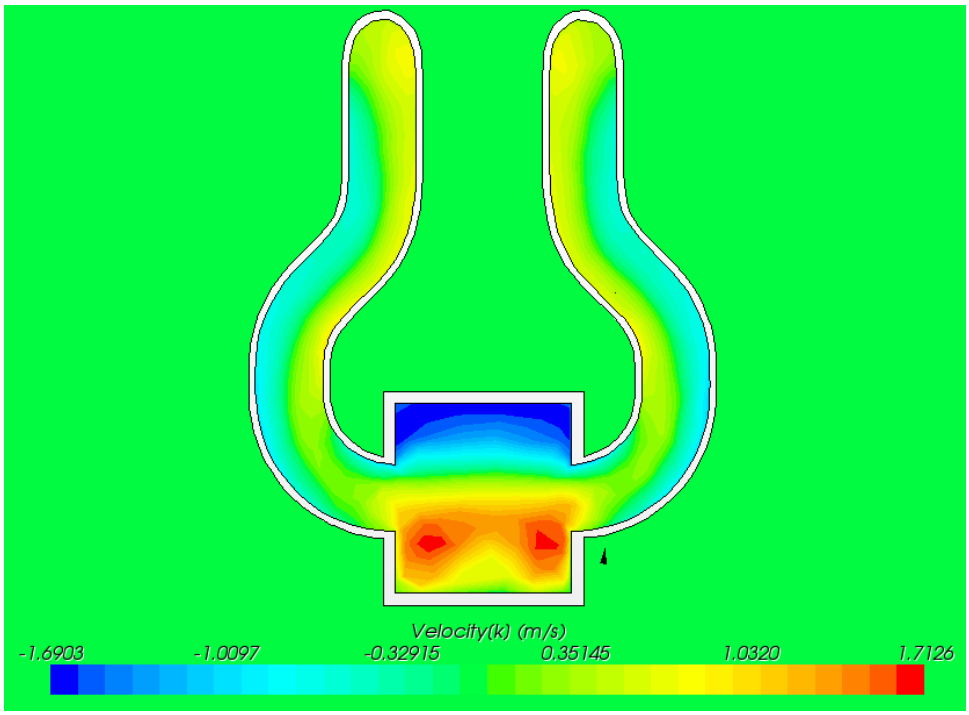

(a) 20% increase in base cell size

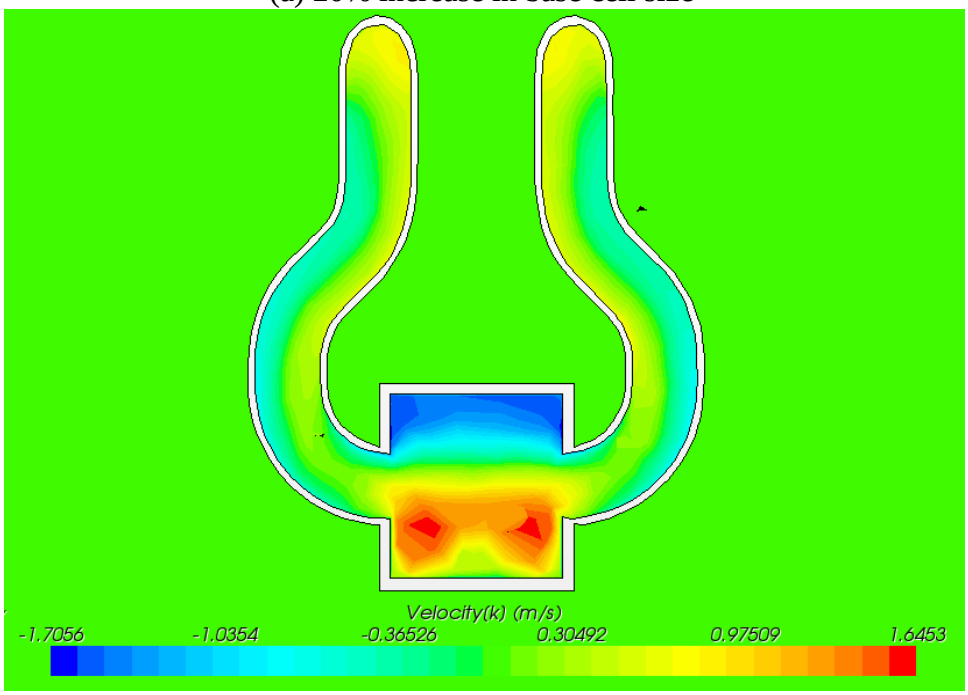

(b) 40% increase in base cell size

Fig 3.12. Out-of-plane Velocity Profiles in a Horizontal Cross-section of the Outlet Plenum and Piping from Simulations using Two Alternate Mesh Sizes

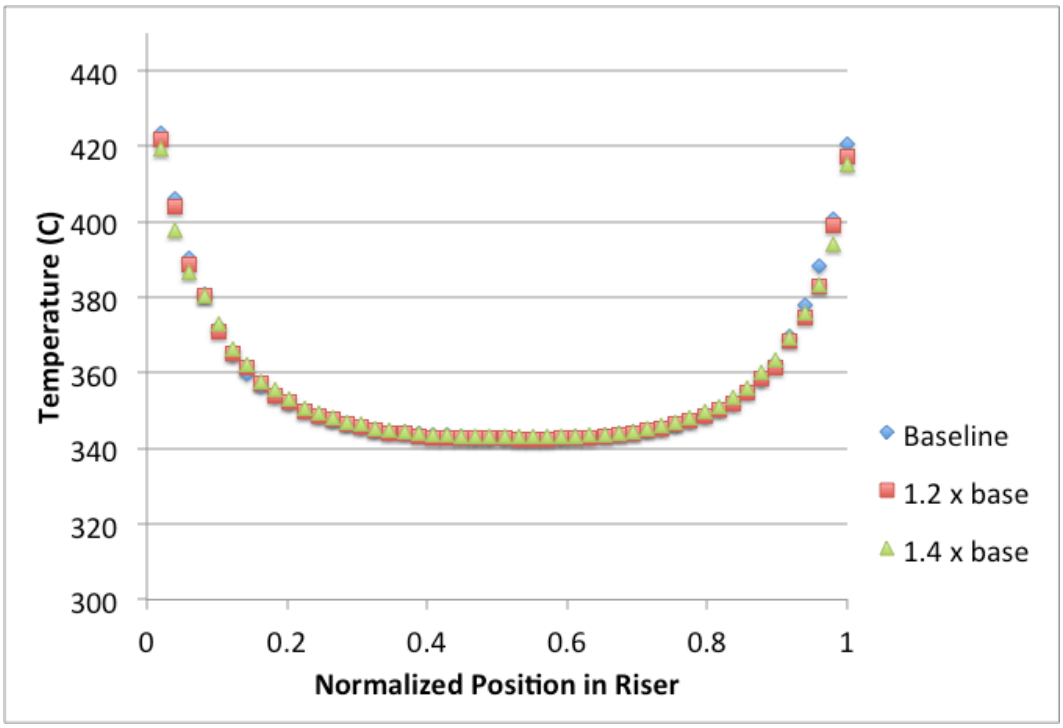

Figure 3.13. Comparison of Predicted Temperature Profiles at the Outlet of a Central Riser along a Line from the Front Surface to the Back

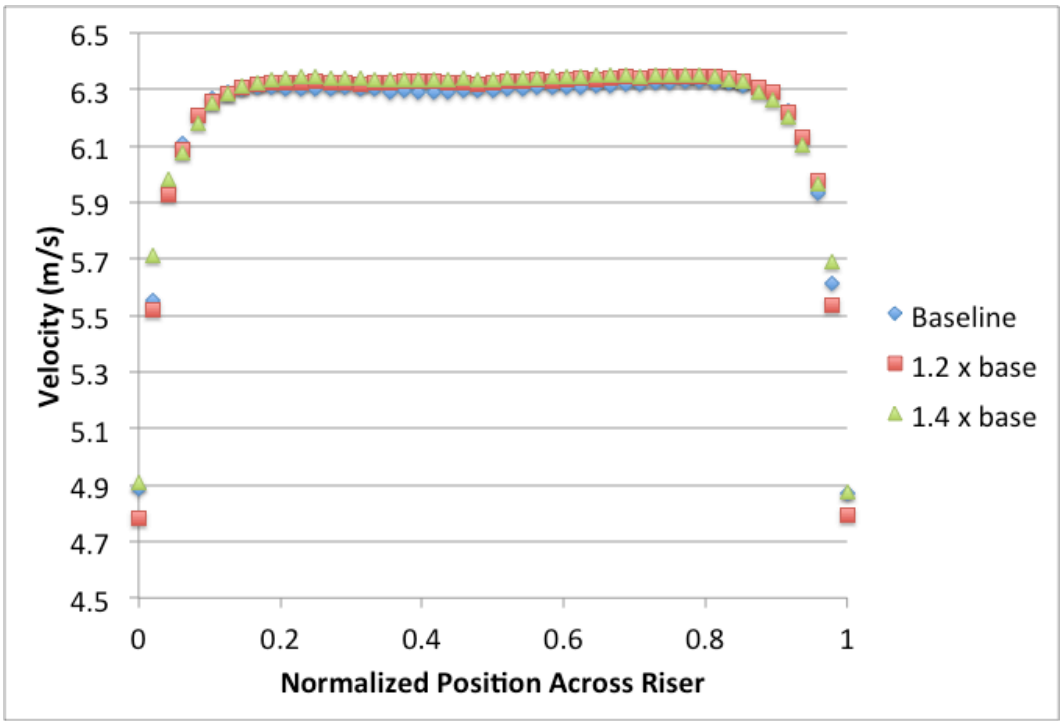

Figure 3.14. Comparison of Predicted Velocity Profiles at the Outlet of a Central Riser Along a Line from the Front Surface to the Back

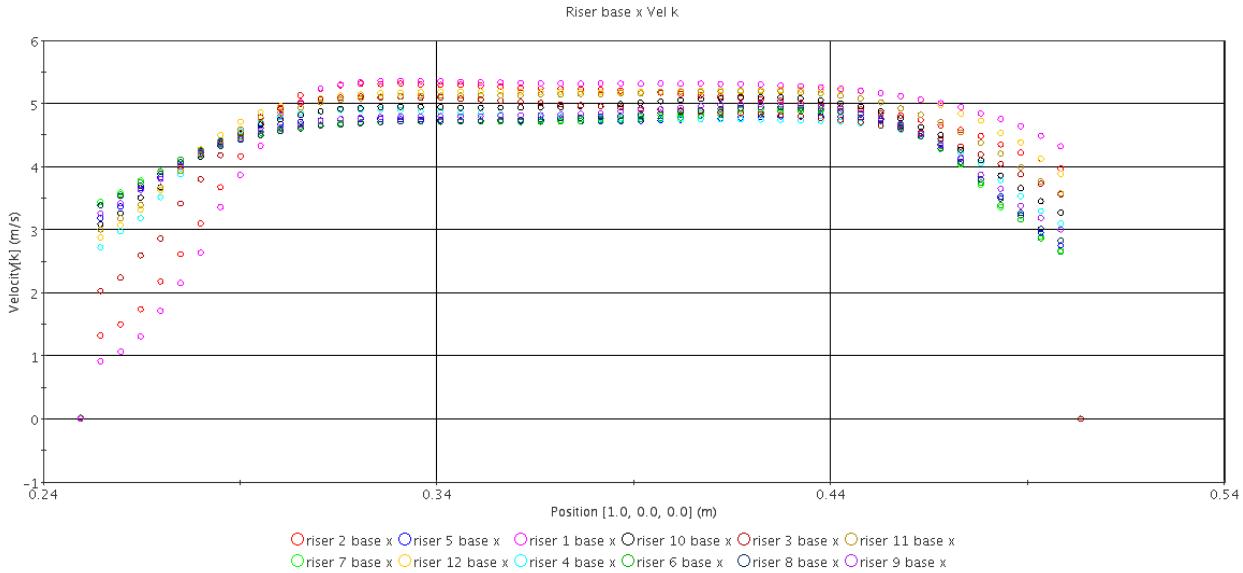

a. Realizable k-epsilon model

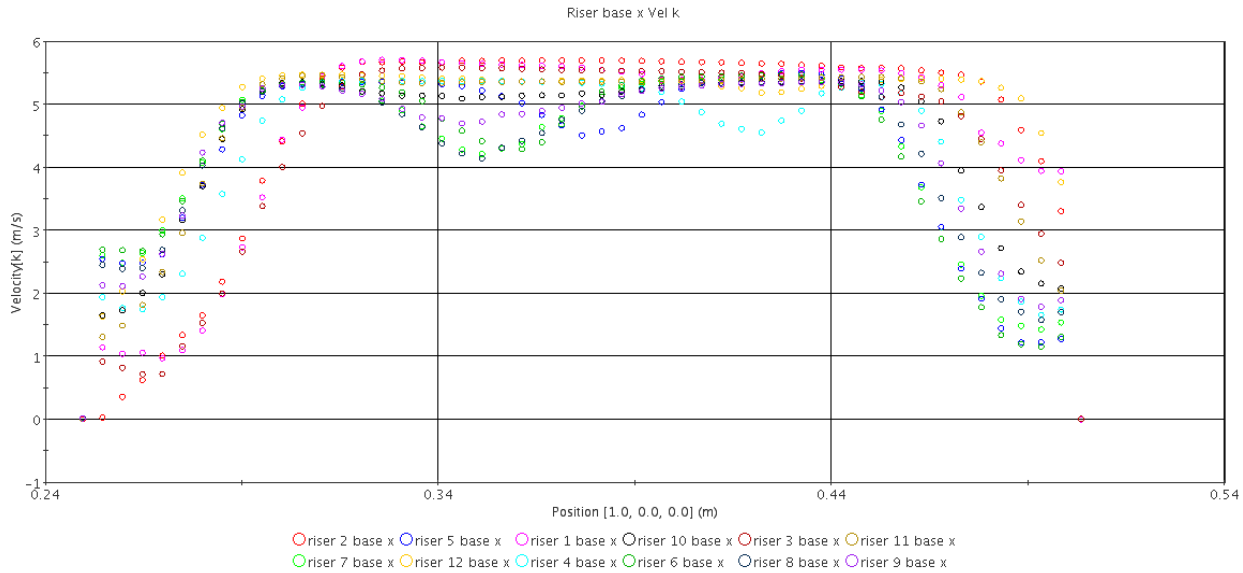

b. Menter k-omega SST model

Figure3.15. Predicted Velocity Profiles 25 cm Downstream of the Inlet Along a Line from Front to Back of Each Riser for Simulations using Two Different Turbulence Models

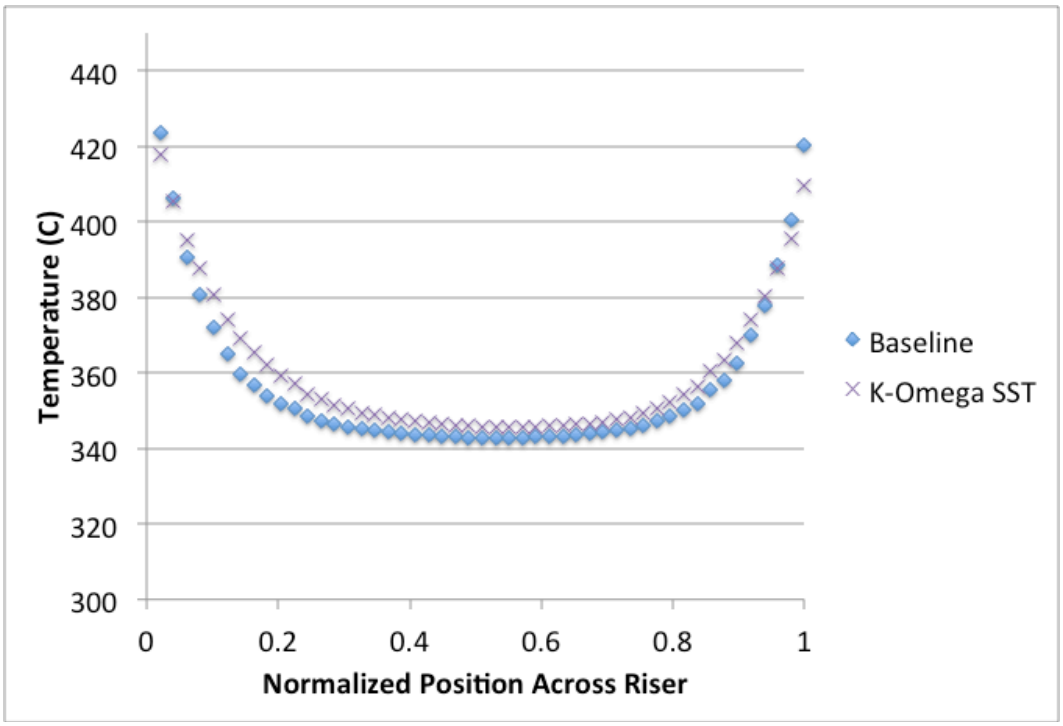

Figure3.16. Comparison of Temperature Profiles at the Outlet of the Sixth Riser Duct for Simulations using Two Turbulence Models

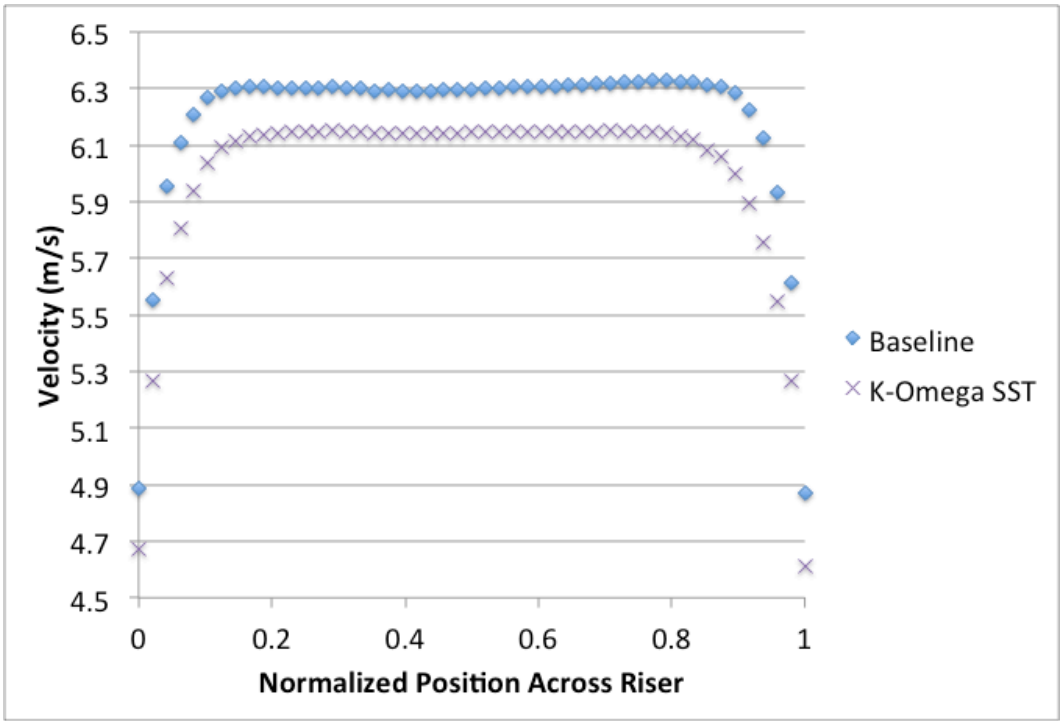

Figure3.17. Comparison of Velocity Magnitude Profiles at the Outlet of the Sixth Riser Duct for Simulations using Two Turbulence Models

3.9 NSTF Design Studies

As more detailed instrumentation plans for the facility have evolved, several design adaptations have been suggested to simplify placement and maintenance of instrumentation. These modifications include the addition of unheated extensions at the outlet of the riser ducts and the extension of the length of the test section inlet by several diameters. Design variations have also been suggested as a consequence of additional scaling studies examining the physical phenomena associated with the outlet plenum and piping. Three alternate designs that address these concerns are considered in this section.

3.9.1 Extended Riser Length

The outlet of each riser duct will be instrumented to measure air flow velocities and temperatures for validation of system and CFD simulation tools. The availability of an unheated section of the riser duct outside the heated cavity would significantly simplify the placement and maintenance of this instrumentation. In the first alternate geometry considered, the riser ducts are extended through the floor of the outlet plenum by one riser width (25 cm), as shown in Figure 3.18.

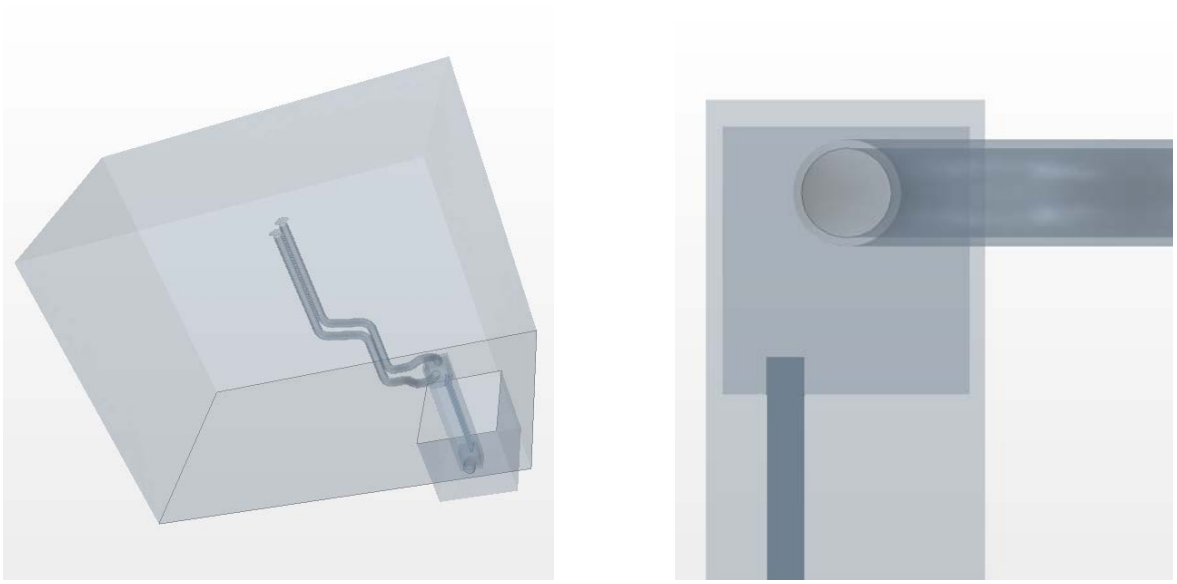

(a) (b)

Figure 3.18. (a) Perspective view and (b) Detail view images of the Modified NSTF System Geometry with Unheated Riser Extensions Protruding into the Outlet Plenum

The first notable impact of the change in geometry is observed while the simulation is in progress. The reported residual values, shown in Figure 3.19, exhibit a strong oscillatory behavior and a slower rate of convergence than is observed in the baseline case. While this behavior is often an indication of unsteadiness in the flow field, the origin of this behavior has not been investigated at this time.

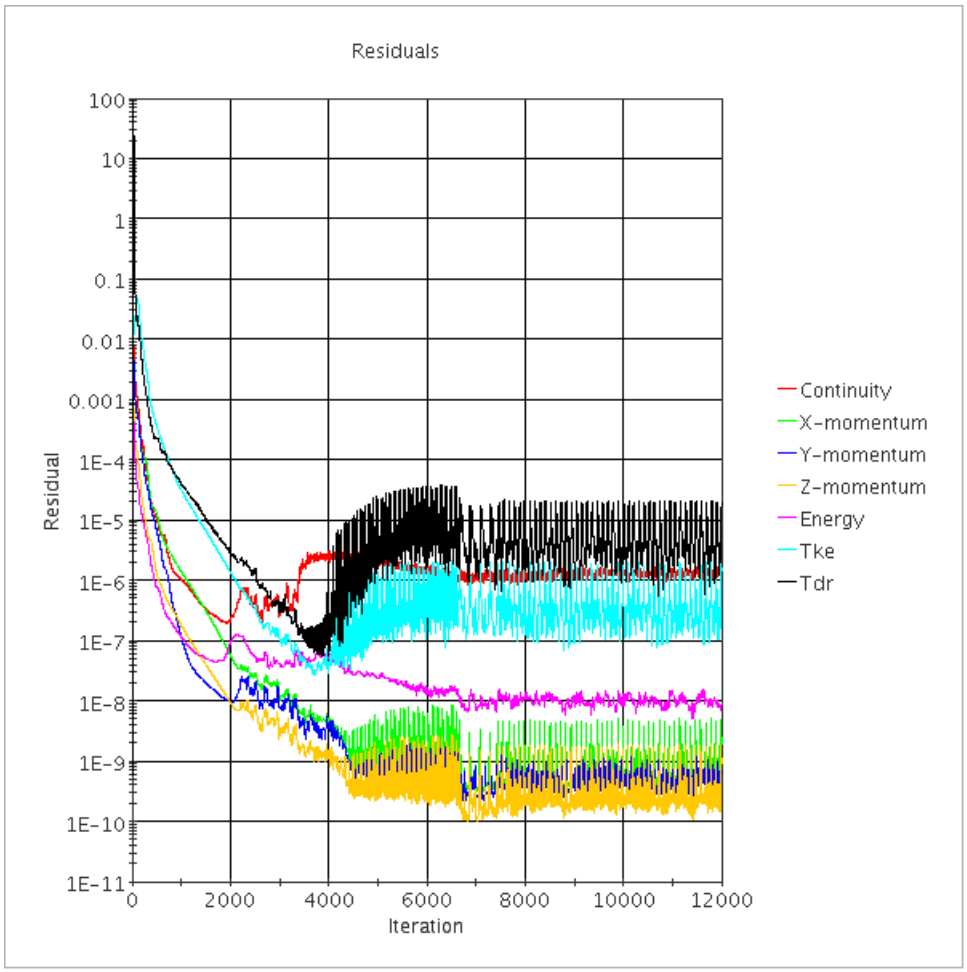

Figure3.19. Residual Values Monitored over 12000 Iterations for Alternative NSTF Geometry with Extended Riser Ducts

The predicted riser velocity profiles for the extended riser case are shown in Figure 3.20. The predicted peak velocities at the riser duct outlet are slightly reduced as a result of the extended length of the risers and the altered outlet plenum geometry. The protruding ducts provide some resistance to the rotational flow feature that forms in the outlet plenum and the predicted lateral velocities are reduced as shown in Figure 3.21. In spite of the interference of the extended ducts, the rotational flow continues to extend into the two outlet ducts, as shown in Figure 3.22.

Although these analyses indicate that the modified geometry continues to produce the major flow features associated with the full-scale RCCS, the clear deviation from the RCCS design may raise questions about the validity of the scaled experiment and such modifications may be less desirable than other options.

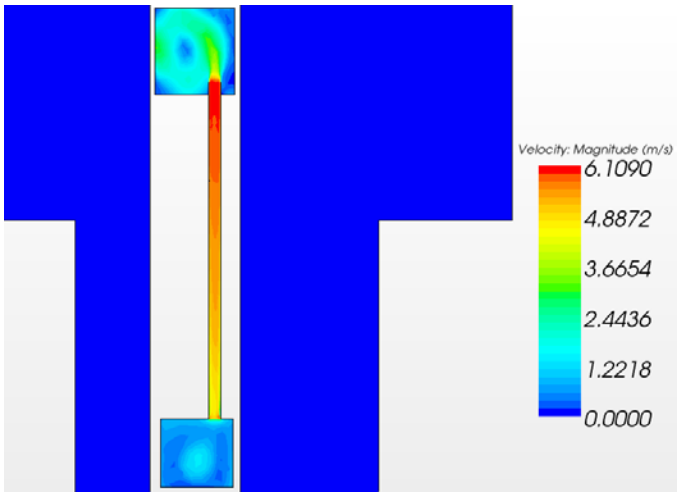

(a) Left vertical cross-section

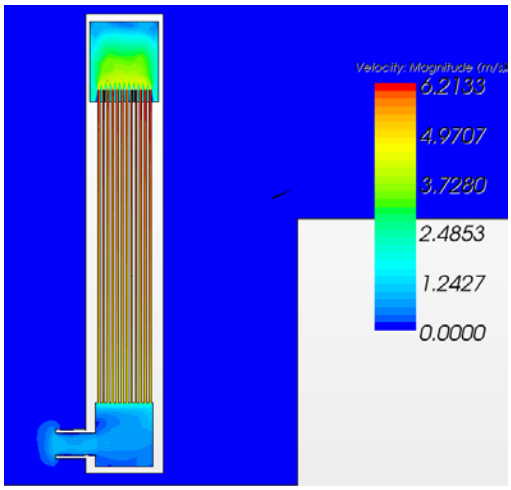

(b) Front vertical cross-section

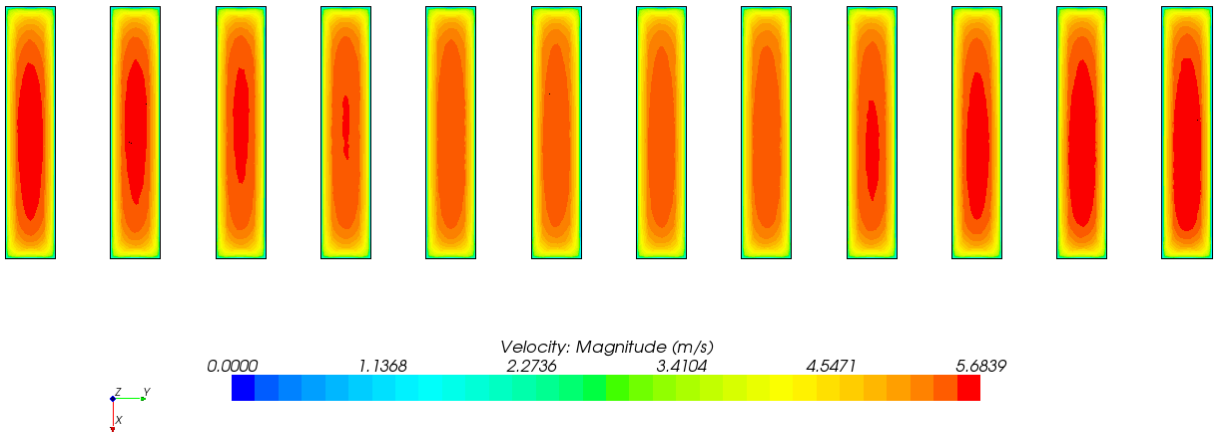

(c) Horizontal cross-section near riser outlet

Figure 3.20. Predicted Velocity Magnitude Profiles in Risers for Extended Riser Model

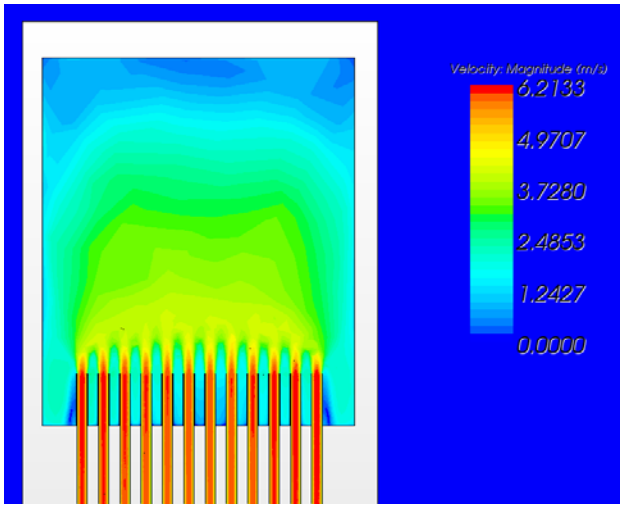

(a) Velocity magnitude

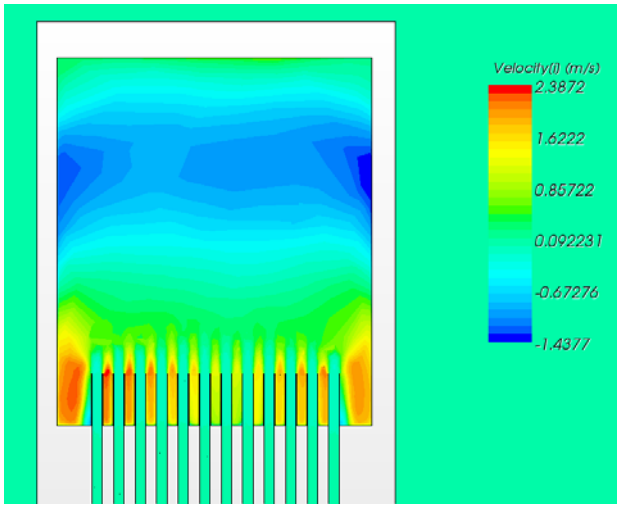

(b) Out-of-plane velocity component

Figure 3.21. Velocity Profiles in a Vertical Cross-section of the Outlet Plenum for the Extended Riser Case

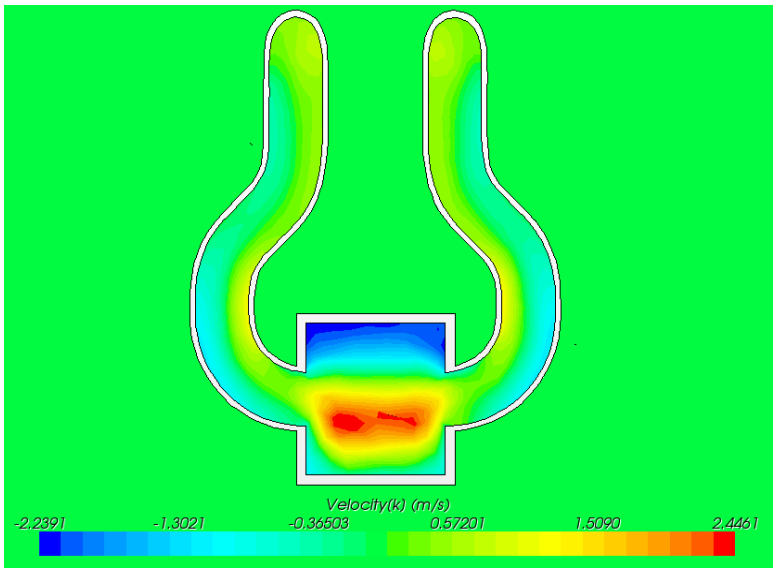

Figure 3.22. Out-of-plane Velocity Profiles in a Horizontal Cross-section of the Outlet Plenum and Piping for the Extended Riser Case

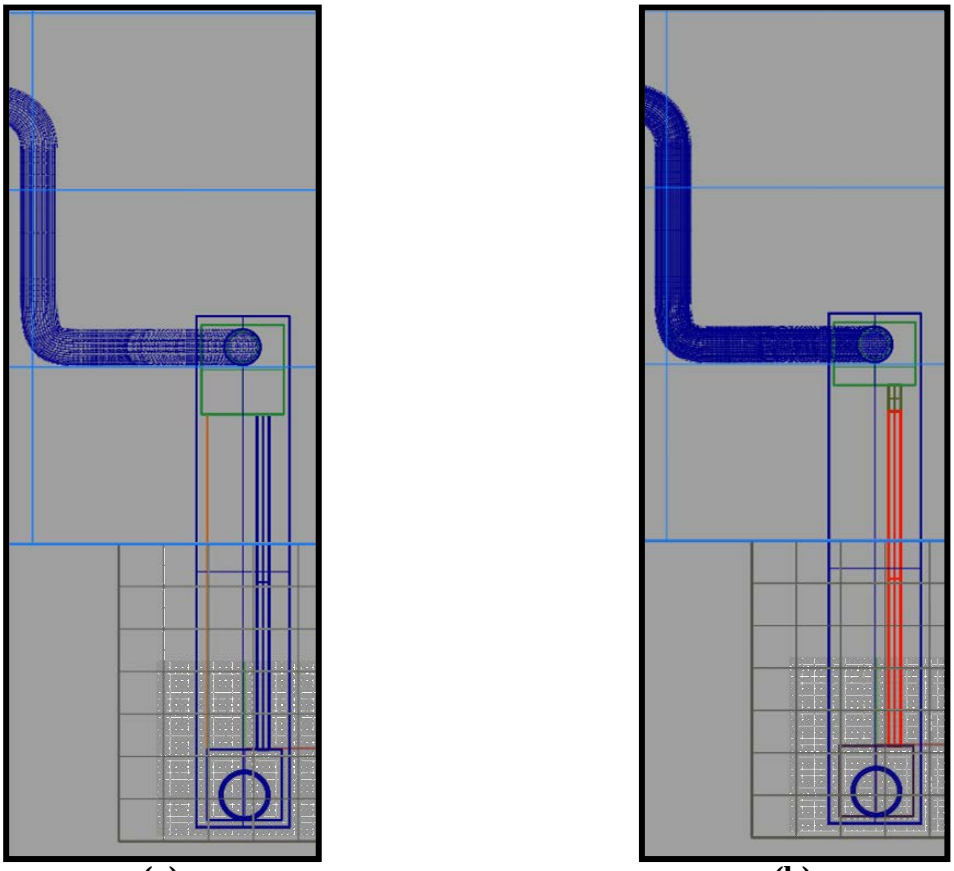

(a) **(b)**

Figure 3.23. Comparison of the Two Parametric Models used in Evaluation of Impact of Upper Hot Plenum Design: (a) baseline and (b) raised lower surface of the Upper Hot Plenum, Reducing the Hot Plenum Volume to 0.707 Times the Baseline Height

3.9.2 Extended Riser with Reduced-Height Outlet Plenum

An alternative design that still addresses the need to extend the risers for instrumentation access but does not modify the outlet plenum geometry has been proposed. In this case, the riser ducts are extended and the outlet plenum is raised to the top of the extended risers. Based on jet penetration scaling analyses completed in the previous year, the height of the outlet plenum is reduced to 70.7% of the baseline height. The modifications to the NSTF geometry are shown in Figure 3.23.

The numerical convergence of the simulation, shown in Figure 3.24, is similar to the baseline case and does not exhibit the oscillations observed in the extended riser case. The predicted riser velocity profiles for this reduced-height outlet plenum case are shown in Figure 3.25. As a strong recirculation pattern continues to form in the outlet plenum, additional secondary flows result in a less symmetric flow field as shown in Figure 3.26. In spite of this asymmetry, the rotational flows continue to extend into the outlet ducts, as shown in Figure 3.27, and the difference in flow rates between the two chimneys is not discernably higher than the baseline case.

The observed asymmetry in the reduced-height outlet plenum warrants either further investigation or the placement of instrumentation in that region to capture the predicted effects.

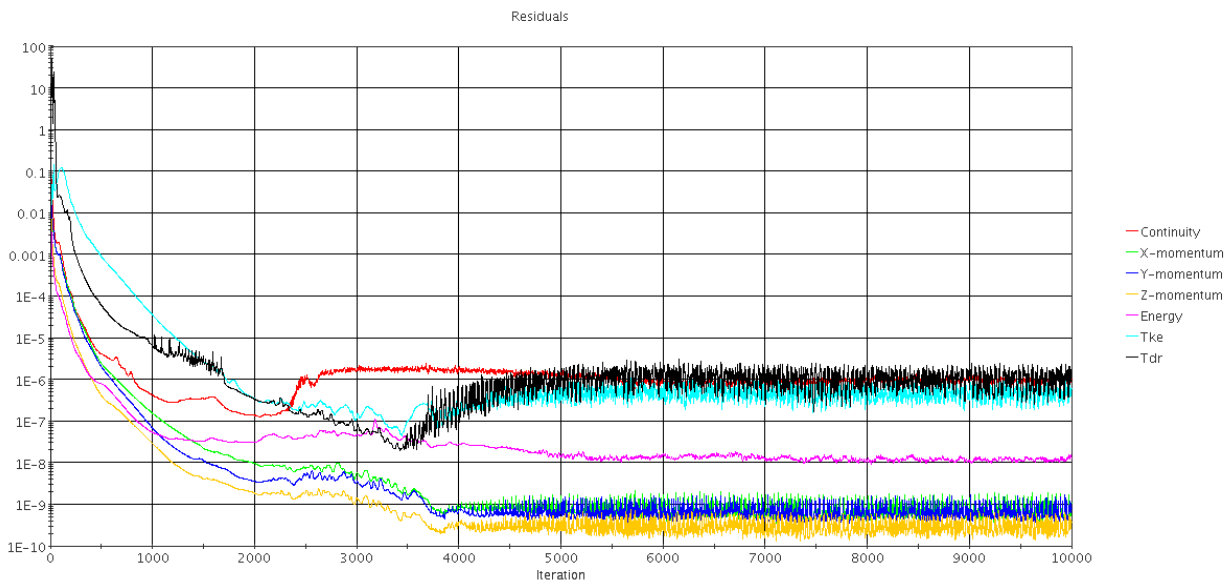

Figure 3.24. Residual Values Monitored over 10000 Iterations for Alternative NSTF Geometry with Reduced-height Outlet Plenum

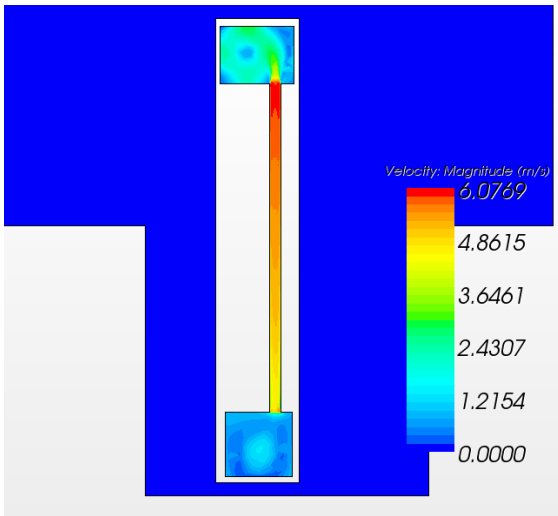

(a) Left vertical cross-section

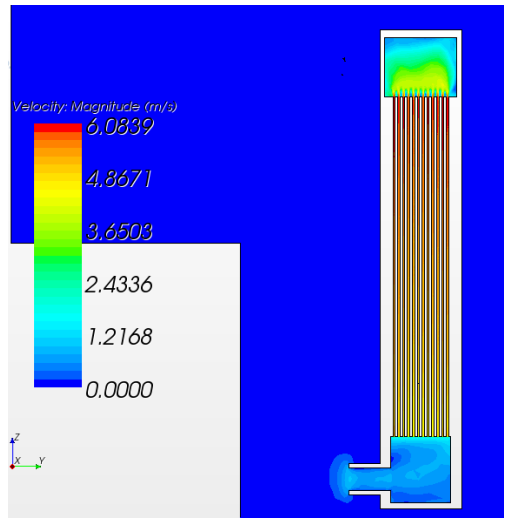

(b) Front vertical cross-section

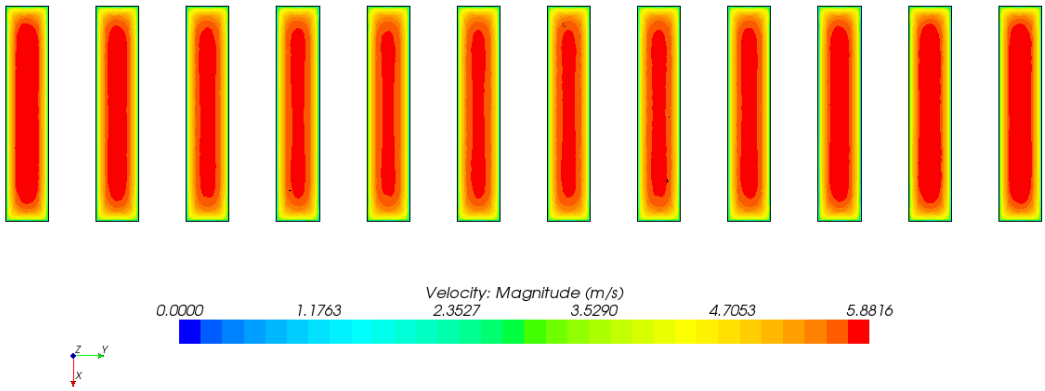

(c) Horizontal cross-section near riser outlet

Figure 3-25. Predicted Velocity Magnitude Profiles in Risers for the Reduced-height Outlet Plenum Model

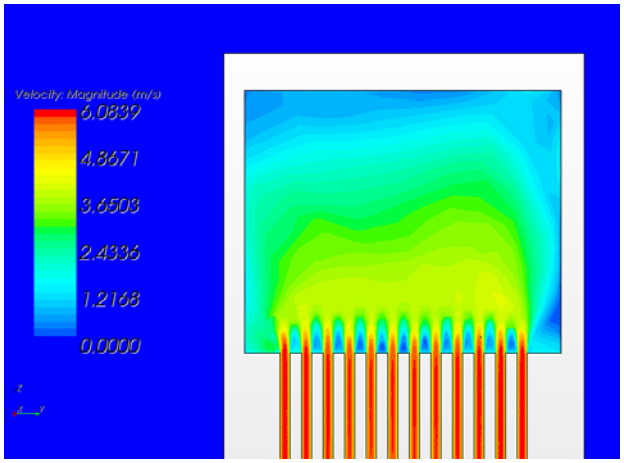

(a) Velocity magnitude

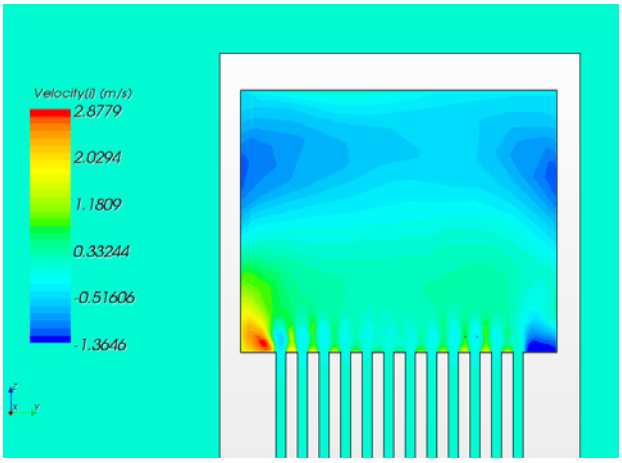

(b) Out-of-plane velocity component

Figure 3.26. Velocity Profiles in a Vertical Cross-section of the Outlet Plenum for Reduced-height Outlet Plenum Case

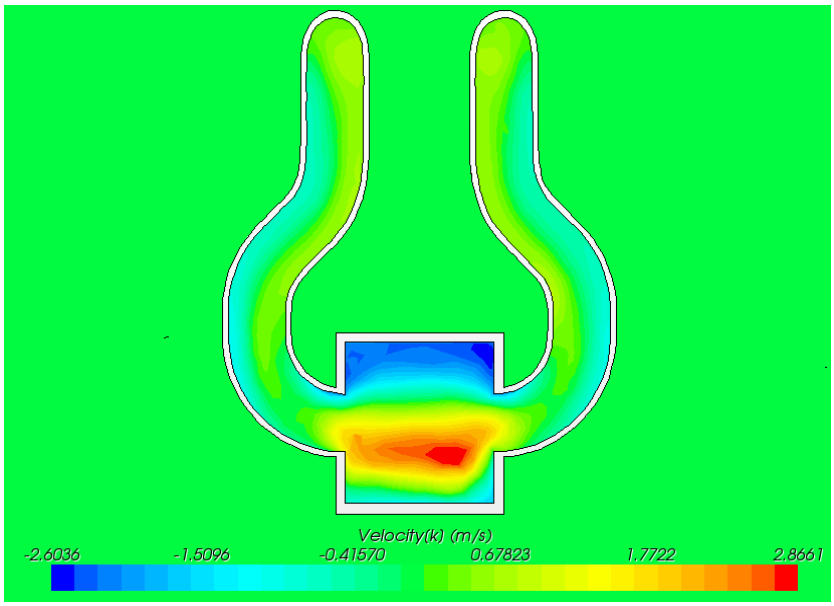

Figure 3.27. Out-of-plane Velocity Profiles in a Horizontal Cross-section of the Outlet Plenum and Piping for the Reduced-height Outlet Plenum Case

3.9.3 Extended Vertical Inlet

The inlet of the test section will be instrumented to measure flow velocities and temperatures. In order to provide well-conditioned flow for this measurement, an extended inlet duct with a length equivalent to more than 10 diameters is highly desirable. An alternative concept being considered that accomplishes this goal is shown in Figure 3.28. This modified geometry also includes the reduced-height outlet plenum from the previous case.

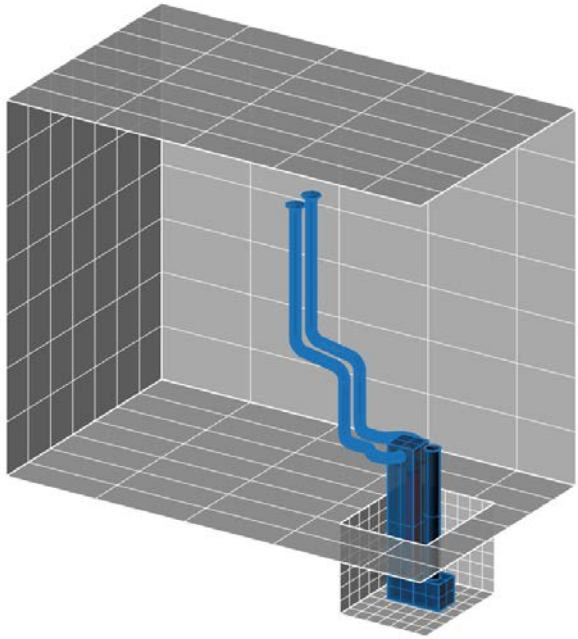

Figure 3.28. Modified Geometry with Extended Vertical Inlet

The extension of the inlet duct clearly has an impact on the numerical convergence of the simulation, reducing the oscillation in reported residuals as shown in Figure 3.29. Predicted riser velocity fields shown in Figure 3.30 have a much more uniform velocity distribution across all bundles. This uniformity is more apparent when considering the extracted line data at the outlet of each riser as shown in Figure 3.31, where the individual risers show no distinguishing characteristics. The uniformity in the riser flows results in the formation of a symmetric recirculation pattern in the outlet plenum, as shown in Figure 3.32.

Although predicted symmetry in steady-state CFD simulations can often be misleading and should generally not be used as motivation for design changes, the increased uniformity of the riser flows and the improved numerical stability of the simulation suggest that this alternate geometry with a better conditioned inlet flow may have some attractive features in addition to allowing for better placement of instrumentation. Planned future analyses that include the effects of nonuniform heating of the riser ducts should continue to consider this design option.

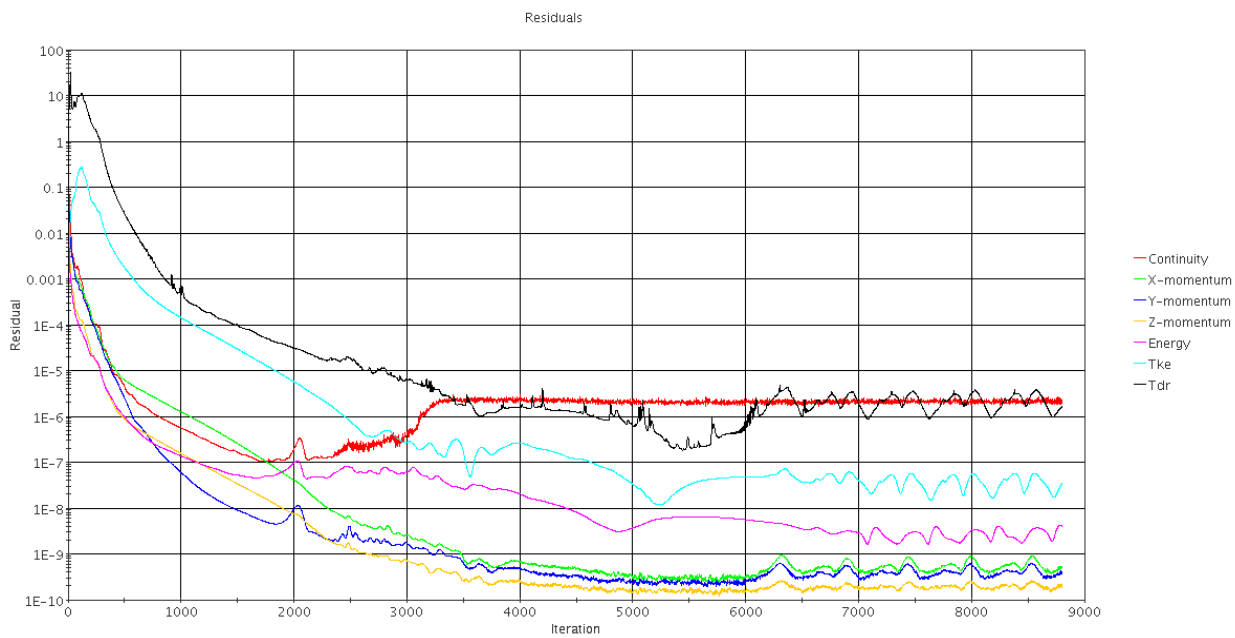

Figure 3.29. Residual Values Monitored over 8900 Iterations for Alternative NSTF Geometry with an Extended Vertical Inlet

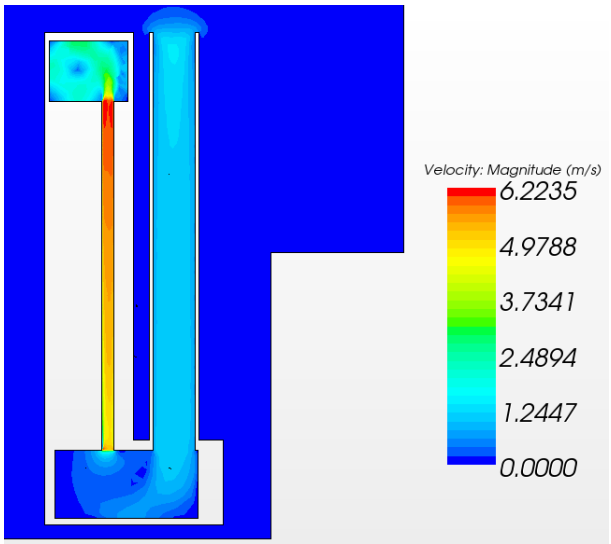

(a) Left vertical cross-section

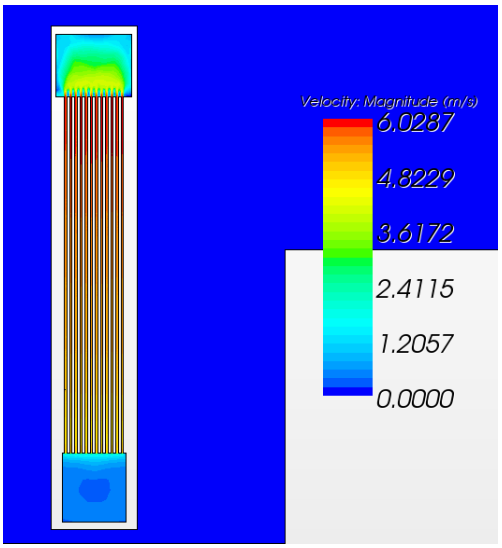

(b) Front vertical cross-section

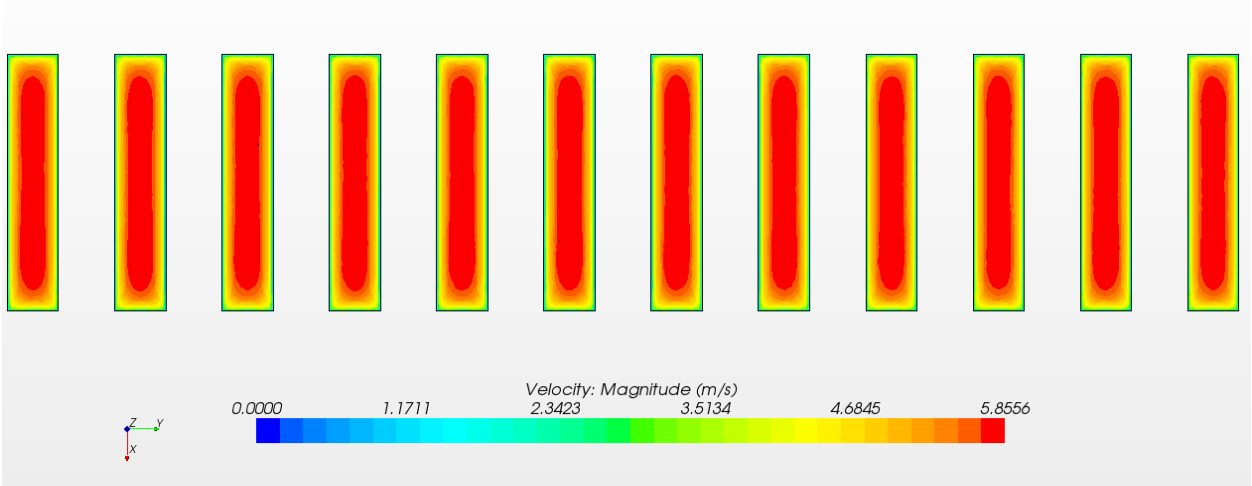

(c) Horizontal cross-section near riser outlet

Figure 3.30. Predicted Velocity Magnitude Profile in the Extended Vertical Inlet Case

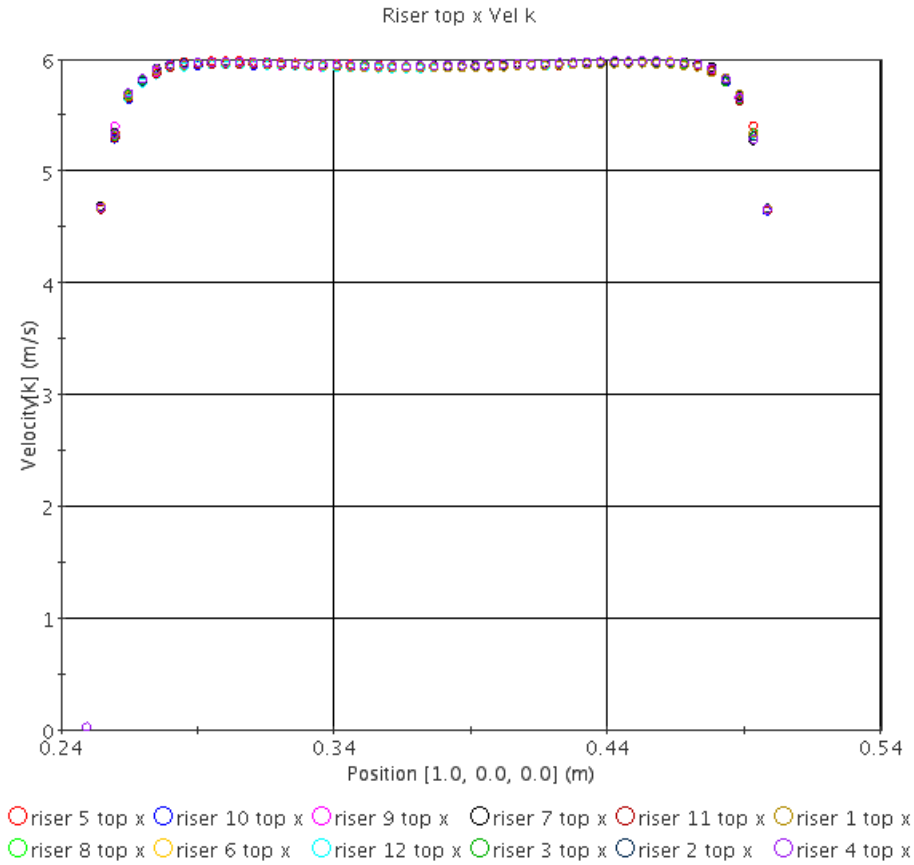

Figure 3.31. Extracted Scalar Profiles along a Line from Front to Back of each Riser for the Extended Vertical Inlet Case

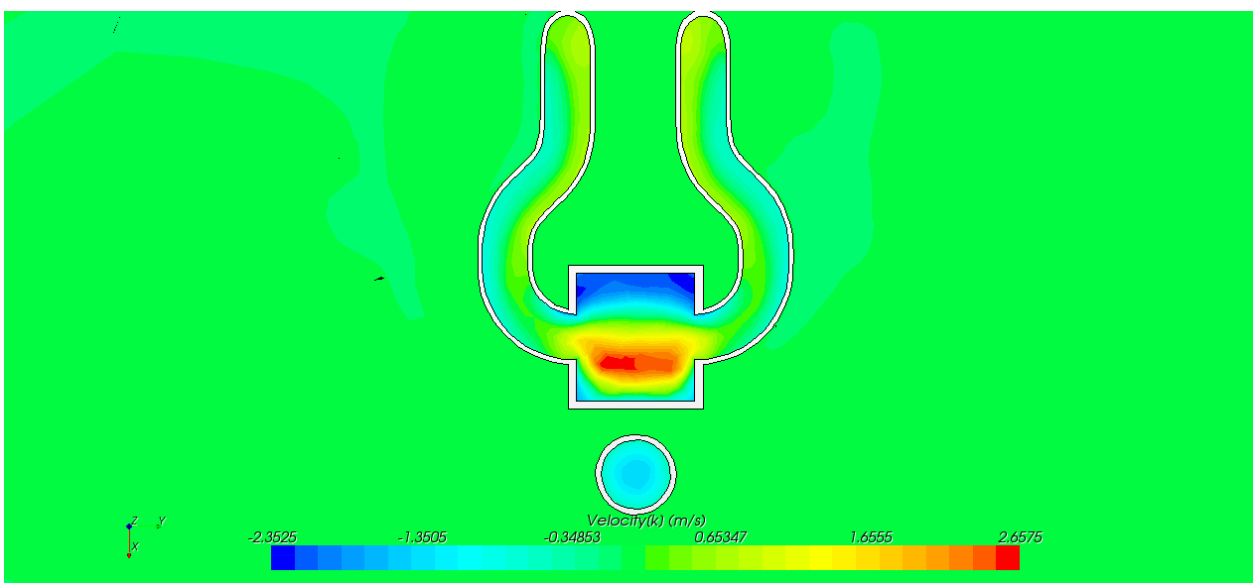

Figure 3.32. Out-of-plane Velocity Profiles in a Horizontal Cross-section of the Outlet Plenum and Piping for the Reduced-height Outlet Plenum Case

3.10. Summary and Future Work

Initial baseline CFD simulations for the air-cooled RCCS and the related NSTF experiments previously showed that the proposed NSTF design duplicates the major flow features of the anticipated RCCS design. An initial series of solution verification studies have been completed for the NSTF analyses in order to begin to quantify the uncertainty in predicted quantities of interest as a result of mesh size and modeling options. Building on this foundational work, a series of design studies have been completed to evaluate potential design options, the most promising of which have been presented. Future work will focus on the application of more realistic thermal boundary conditions for selected cases and on unsteady simulations to evaluate the stability of the natural convection flow field.

References

3.1 M.T. Farmer, et al., "Natural Convection Shutdown Heat Removal Test Facility (NSTF) Evaluation for Generating Additional Reactor Cavity Cooling System (RCCS) Data," ANL-GenIV-058, September 2005.

3.2 R.B. Vilim and E. E. Feldman, "Scalability of the Natural Convection Shutdown Heat Removal Test Facility (NSTF) Data for VHTR RCCS Designs," ANL-Gen IV-049, June 2005.

3.3 C. P. Tzanos, "CFD Analysis for the Applicability of the Natural Convection Shutdown Heat Removal Test Facility (NSTF) for the Simulation of the VHTR RCCS," ANL-Gen IV-055, September 2005.

3.4 S. Lomperski, W. D. Pointer, C. P. Tzanos, T. Y. C. Wei, C. M. Crooks, and O. A. Rodriguez, "RCCS Studies and NSTF Preparation Air-Cooled Option," ANL-GenIV-142, Sept 30, 2010.

4.0 Instrumentation

The facility is heavily instrumented to evaluate heat removal performance and help guide experiment operations. A summary of the instrumentation is provided in Table 4.1. There are instruments to measure air and surface temperatures, bulk air flow rate and local velocity, total normal radiation heat flux, and electrical power supplied to the duct wall heaters. The following sections provide additional detail on each instrument category.

4.1 Temperature

All thermocouples are type-K with an accuracy of ±2.2°C or 0.75% of measured temperature. The vast majority of these sensors, roughly 200, are located on the upper and lower plates of the test section. Figures 4.1 and 4.2 show the thermocouple layouts for both heated and unheated walls. Sensors are flush-mounted for accurate measurement of surface temperatures without disruption of the flow field. Figure 4.3 illustrates the installation configuration. A high-temperature thermal cement is used to bond junctions to the plate. Note that the wires are not joined at the junction so the electrical circuit is completed through the steel plate. This allows detachment of the wire from the plate to be detected as an open circuit, which is not the case if the wires are bonded together at the junction as in conventional configurations.

Table 4.1. Instrumentation Overview

Measurement	Instrument	Purpose/Location
Temperature	Thermocouples	40 for heater temperature control ~75 on lower section heated wall; ~50 on lower section unheated wall; ~ 50 on upper section heated wall; ~25 on upper section unheated wall 24 at tube inlets and outlets 96 in each of the center 3 tubes
Bulk flow rate	Averaging pitot tube	1 in each stack for total flow rate calculations and energy balances
Local velocity	Miniature pitot tube	4 near the exit of each tube to indicate flow distribution among the twelve tubes
Pressure	Strain-gauge transducers	1 inlet static 4 test section differentials
Heat flux	Thermopile	17 on the adiabatic walls of the test section 11 on each of the three center tubes
Heater AC Power Distribution	Power controller	40 to measure power input for energy balances

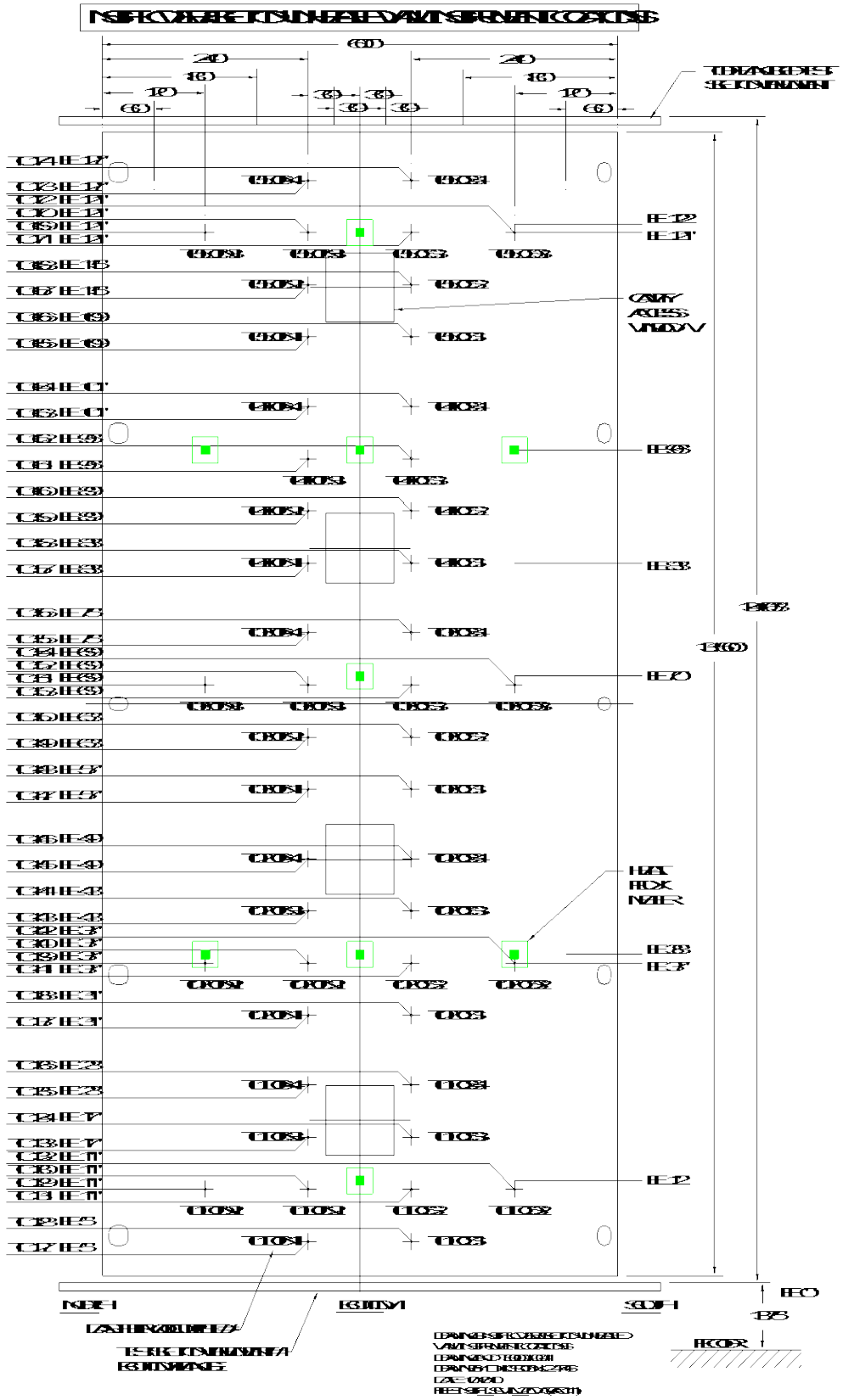

Figure 4.2. Surface Temperature Thermocouples and Heat Flux Meters on Unheated Walls

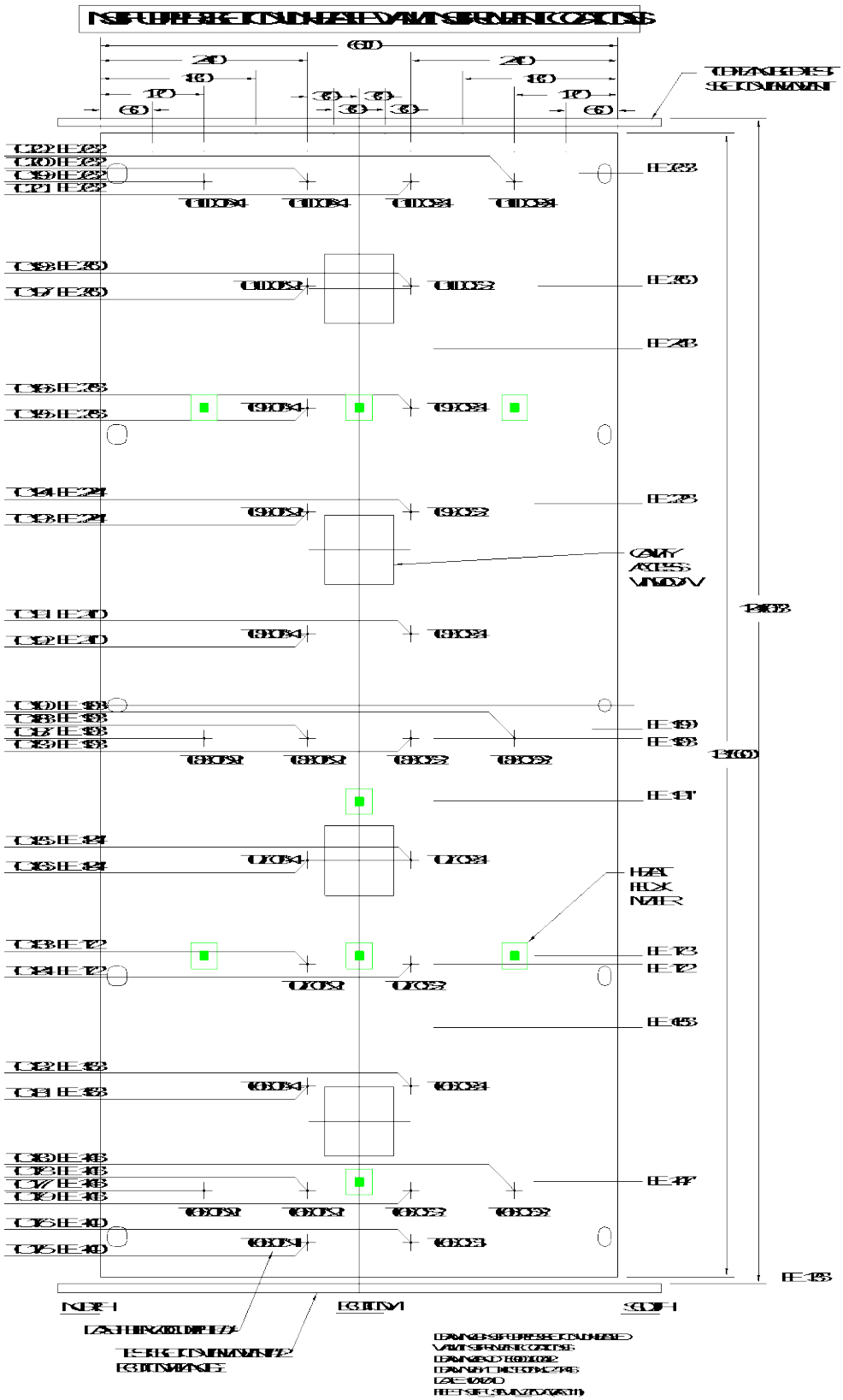

Figure 4.2. (continued)

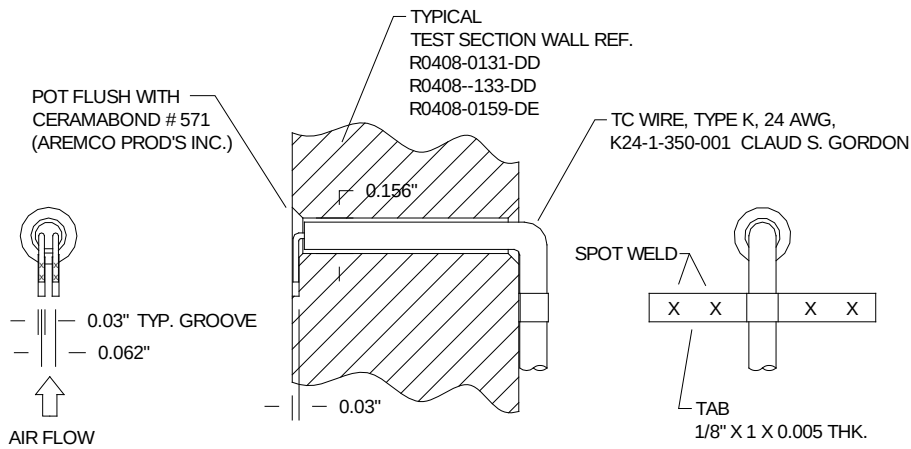

Figure 4.3. Surface Temperature thermocouple Installation

4.2 Flow Rate

Measurements of fluid flow can be divided into two categories. The first is bulk flow rate through pipes and ducts, which is needed to balance energy and determine flow partitioning across the 12 ducts. The second category is local gas velocity measurements, which are intended to support CFD analysis. The former category is discussed here and the latter in the next section.

There are two types of bulk flow measurement: one is flow through the twelve 5 × 25 cm ducts and the other is through the two 61 cm diameter stacks. These will be referred to as duct and stack measurements respectively.

Both the duct and stack measurements will be made with instruments positioned downstream and closer to their outlets than inlets. It is not possible to make reliable flow measurements near the test section inlet because entrance lengths are far too short. Sensors near the inlet might be able to provide indications of relative flow, such as balance between the two main inlets, but local flow patterns are likely to be unstable so even that may not be reliable. Refraining from inlet measurements means sensors must operate at elevated rather than ambient temperature, which is more difficult and generally less accurate, but it is necessary in order to provide the instruments adequate entrance length.

Stack Flow

Figure 4.4 shows stack conditions predicted by a RELAP5 model for two different enclosure geometries at low, medium and high heat flux levels. The symbols represent steady state operating points, and the range they span is taken to be the required operating range for the stack flow meters. Conventional flow meters, such as vortex and coriolis, would be preferred, but they are not practical for large ducts. Hot wire anemometers are often used in ducts, but process temperatures are far above ambient and vary by at least 100°C, which is a difficult operating environment for such sensors. Still, some hot wire anemometers can operate at these high temperatures and there are devices with temperature compensation windows as large as 50°C. The RVACS operating space could be divided into three 50°C stack temperature windows, which if done, allowing the anemometers to be used within one window. Subsequent use in

another window would require recalibration before use. Though feasible, this solution would be cumbersome as well as expensive, since accurate flow measurements require several anemometers in each stack. In this difficult environment, it is preferred to use an instrument based on measurements of differential pressure.

Orifice flow meters are based on differential pressure, but one cannot be used here because its pressure drop would dominate system losses. Instead, stack measurements will be made with an averaging pitot tube such as the Rosemount 485 Annubar flow meter shown in Figure 4.5. The flow element acts as a collection of pitot tubes by effectively averaging the stagnation pressure across a pipe chord. The width of the Annubar sensing element is 49 mm and it operates at process temperatures up to 260°C. The pressure losses associated with this device are much lower than that of an orifice flow meter.

Though an averaging pitot tube is the best instrument for the stack, flow rates are quite low, likely making the measurement difficult. Signal levels will be only ~1 Pa at the highest flow rates, and the pipe Reynolds number will not be more than 40,000 as shown in Figure 4.6. The flow patterns around these sensors are less stable at Reynolds numbers below roughly 100,000, so it is necessary to perform our own in situ calibration.

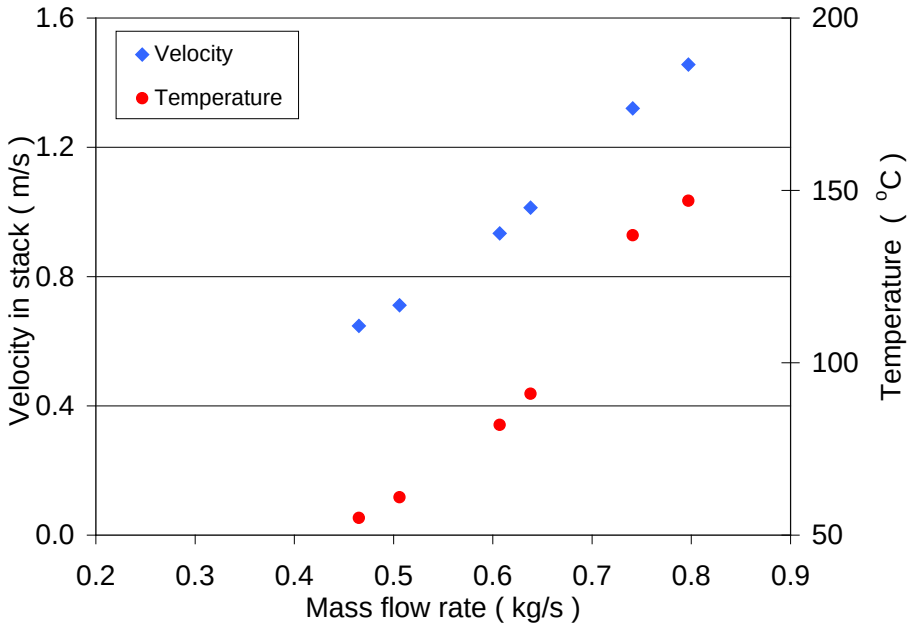

Figure 4.4. Estimated Stack Velocity and Temperature at Six Operating Points for Low, Medium, and High Heat Flux [4.1]

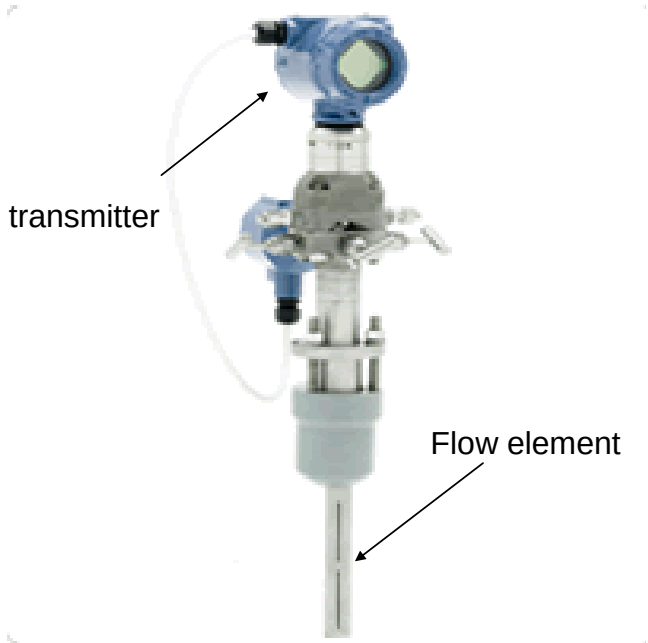

Figure 4.5. The ΔP-based Rosemount Annubar Flow Meter (Emerson Process Management)

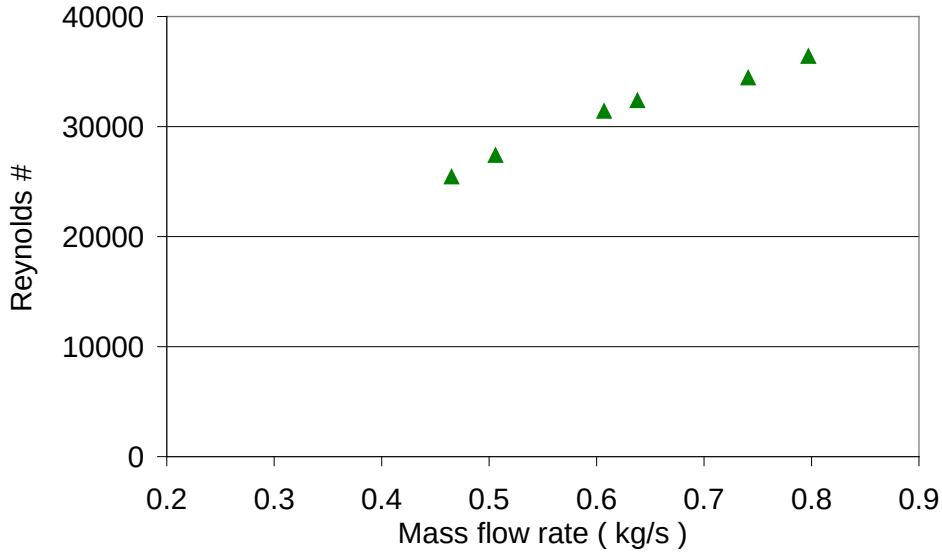

Figure 4.6. Stack Reynolds Number at Six Operating Points for Low, Medium, and High Heat Flux [4.1]

Calibration will be performed against a multipoint hot wire anemometer that is calibrated for ambient temperature flows. A room temperature calibration of the stack sensors will provide calibration coefficients for low Reynolds numbers that can also be used at the higher temperatures existing during natural circulation operation. The hot wire anemometer registers mass flow rate while the stack sensors measure velocity and volumetric flow rate. The averaging pitot tubes will be accompanied by multijunction thermocouples, which are used to calculate the mean gas density. Together, they will provide stack mass flow rates.

The stack flow meters will be calibrated using the two fans on the upper level to force air into the test section inlet and up through the stacks. A temporary duct reconfiguration will allow the fans to draw air from the upper deck region of the hi-bay, forcing it down through a long hose and into one of the two inlets. The other will be blocked off. The hot-wire anemometer will be located in a straight stretch of the temporary hose while the stack flow meters are permanently located above the roof to satisfy entrance length requirements.

Duct Flow

Since duct flow conditions pose the same problems described for the stacks, a pitot-tube type instrument is again recommended. But the ducts are smaller than the stacks and so probes will block a larger percentage of the flow area, ~20 to 30% for the typical 10 to 15 mm diameter probes used in small pipes and ducts. Pressure losses will be small, only a fraction of the measured ΔP and on the order of several Pascals, but probes will certainly alter the distribution of flow as it enters the upper plenum. If this degree of outlet blockage is acceptable, all duct sensors could be calibrated along with the stack sensors.

If these probes are too large, it is possible to use light gauge conventional pitot tubes having a diameter of ~2 to 3 mm. A pitot tube at the center of a duct will read local velocity, but it is insufficient to establish the total duct flow rate since the velocity profiles are unknown. Still, flow rates could be determined with a single sensor per duct using the assumption that duct velocity profiles are all the same at any one time. This implies that the ratio of one duct velocity to another is equal to the volumetric flow ratio as in

$$\frac{v_1}{v_2} = \frac{\dot{V}_1}{\dot{V}_2}$$

This allows one to use the total stack mass flow measurement to determine the mass flow rate through each duct:

$$\dot{M}_{total} = \dot{m}_1 + \dot{m}_2 + ...\dot{m}_{12} \quad = \quad \overline{\rho}_1 \dot{V}_1 + \overline{\rho}_2 \dot{V}_2 + ...\overline{\rho}_{12} \dot{V}_{12}$$

The velocity ratios are used to eliminate all but one of the unknown volumetric flow rates and solve for one duct flow rate, which is then used to calculate the remaining eleven. This approach requires that each pitot tube be positioned precisely the same way and that temperature gradients are not large, enabling a good estimate of average temperature. Also, flow rates at any one time should not differ too much among the ducts to ensure that velocity profiles are indeed the same.

Local Velocity

While measurements of bulk flow are required for energy balances and assessments of overall system behavior, CFD requires data on localized velocity, preferably at many locations. Pitot tubes and hot-wire anemometers are the best sensor candidates, with hot-wires offering superior bandwidth and directional resolution. But as with the bulk flow measurements, hot-

wires are again unsuitable on account of process temperatures: air in the ducts may reach 200°C and cavity temperatures are expected to fall between 200°C and 500°C; hot-wires are generally limited to ~150°C. Even special purpose high-temperature hot-wire probes would be difficult to use because calibrations cannot cover our broad range of process temperatures.

Pitot tubes are again the more rugged alternative, so local velocity measurements will be made with light-gauge, stainless steel pitot tubes. The upper plenum will be instrumented with a rake holding several pitot tubes. The rake can be moved to different positions of interest. The cavity will not be instrumented because velocities are too low to measure with conventional pressure transmitters.

The pitot tubes will be supplemented with a Laser Doppler velocimeter (LDV) if permitted by budget and staffing levels. It offers the high dynamic range and spatial resolution of the hot-wire anemometer while sidestepping difficulties associated with temperature, as it is an optically-based measurement. The instrument operates by crossing two or more laser beams at a desired measurement location so that light is reflected from particles suspended in the flow. The reflected light is collected for photodetectors whose signals are used to determine local gas velocity.

LDV is normally used in open systems and forced circulation loops with either naturally suspended particles or flows that are easily seeded artificially. Without such particles to reflect light, there is no signal for the LDV to process. Measurements in the closed cavity would be problematic because they require periodic seeding injections followed by a waiting period for reestablishment of natural circulation patterns. Particles may not remain suspended long enough for high quality measurements. Perhaps more critical, is the change in surface emissivity that is likely to accompany the use of seeding particles. Oils are the most promising seeding candidates as they generate strong signals, but extensive use is likely to result in a thin coating of oil over all of the cavity surfaces.

LDV is more feasible for measurements within the upper plenum. Seeding can be added at the bottom end of the ducts to be swept along up towards the upper plenum, where windows allow access for the laser beams. The inner surfaces of the ducts, upper plenum and, eventually, the stacks, will be coated with oil, but their emissivities should have less influence on heat transfer, which is also conductive and convective.

4.3 Heater Power

The plate heating system is divided into banks of ceramic heaters that are grouped either along the outside edges of the plate or adjacent to its centerline (Figure 4.7). The facility has a total of 40 such heater banks, each independently monitored and regulated. The main control units are Eurotherm *Epower* single-phase controllers rated for 50 A. The units maintain target power within ±1% of full-scale during any moderate variations in line voltage, load impedance, and ambient temperature. Controllers perform real time measurements of actual delivered power via internal measurements of supply voltage and current, which are both accurate to within ±1%.

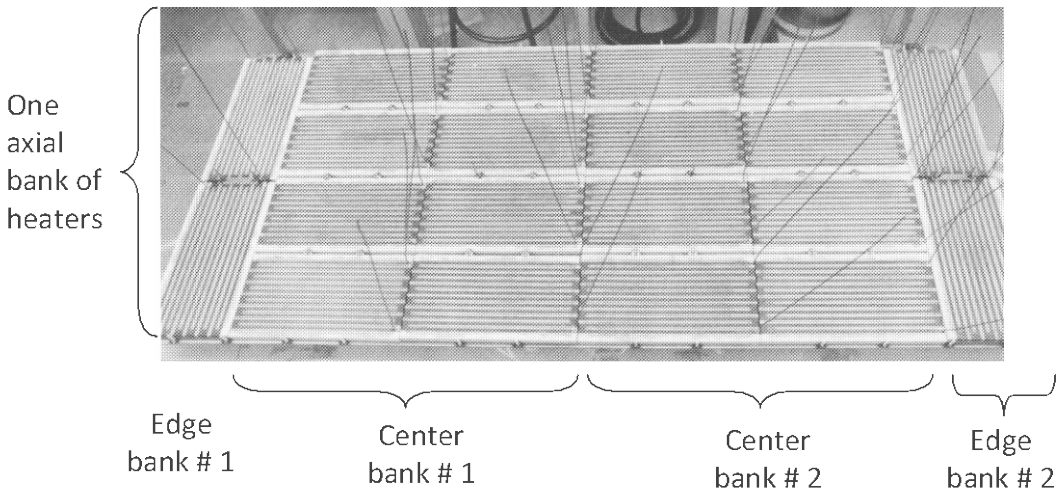

Figure 4.7. Layout of Ceramic Heating Elements with Two Central Zones Flanked by Guard Heaters. The heated section of the facility contains 10 of the above units.

Temperature control of each bank is achieved with Eurotherm model Mini8 PID (proportional, integral, derivative) process controllers (Figure 4.8). The heat of the device is a microprocessor that is programmed for temperature setpoints and PID parameters through a PC. Plate temperature is measured via a thermocouple wired directly to the Mini8 that is independent of the rest of the data acquisition system. The PC communicates with the unit via a TCP/IP connection and *iTools* software.

4.4 Heat Flux

Heat flux meters are used to measure heat losses through the adiabatic walls of the test section at selected locations, which are shown in green in Figure 4.2. The solid state sensors, manufactured by International Thermal Instrument Company, Inc., are made of polyimide and can withstand process temperatures of up to 315°C. A closeup photo of a typical heat flux meter is shown in Figure 4.9. The principle of the measurement is the same as that for a pair of thermocouples measuring the temperature difference across a conductor with a known thermal conductivity. Instead of thermocouples, the heat flux sensor uses a pair of thermopiles, which greatly amplifies the signal generated by the temperature difference. The relationship between the signal and heat flux is obtained through NIST traceable calibration. Sensors are accurate to within 5% of the measured heat flux. Heat flux meters are also used on the three central tubes located as shown in Figure 4.10.

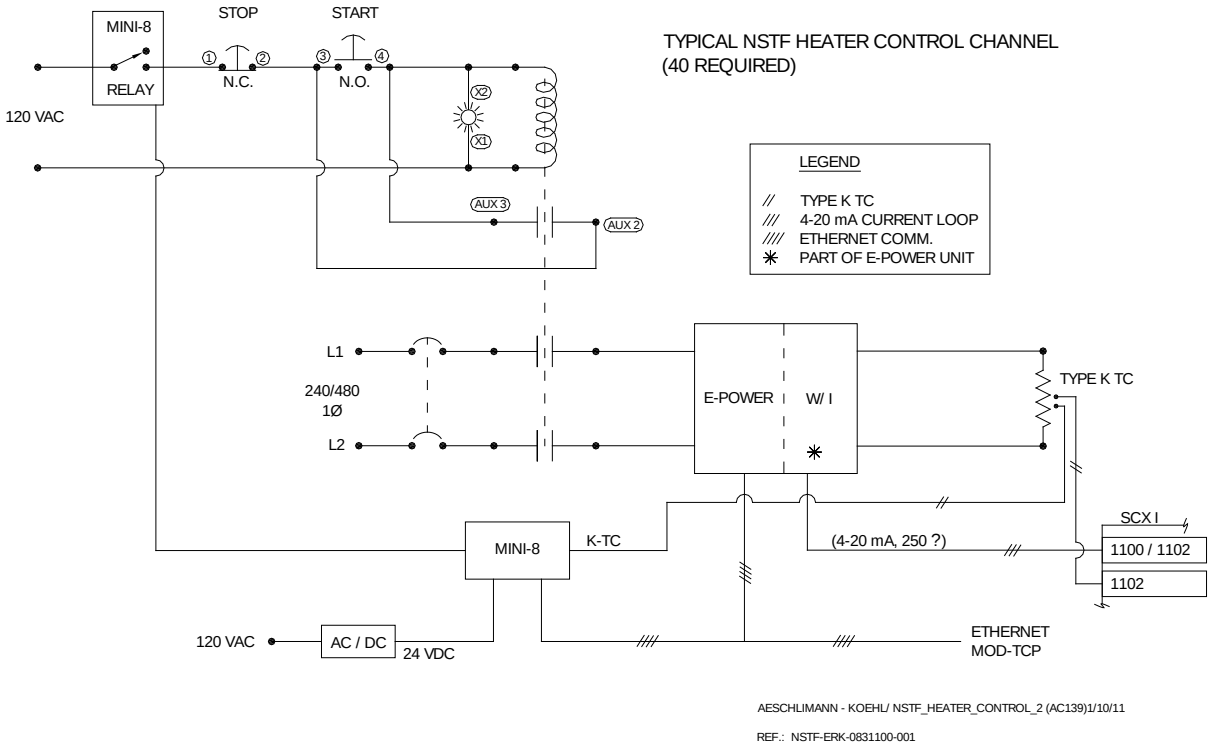

Figure 4.8. Heater Control and Monitoring Systems

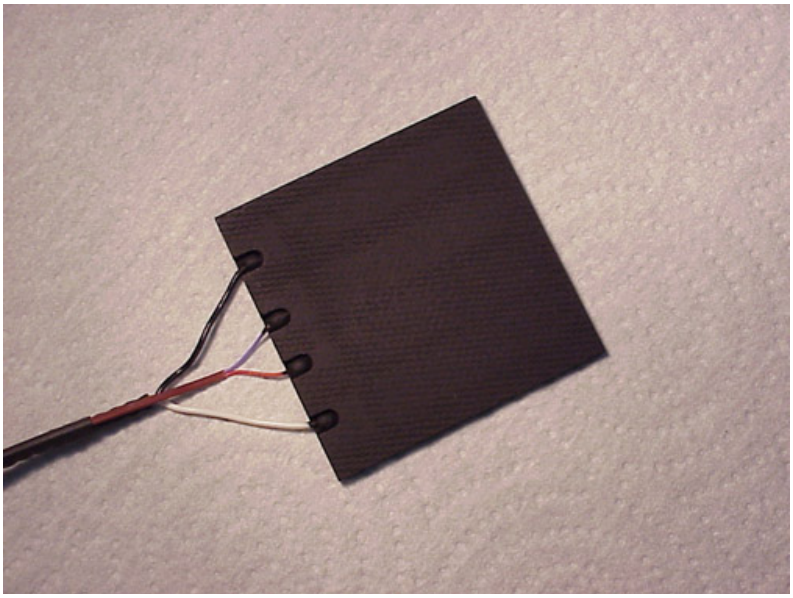

Figure 4.9. Self-powered Heat Flux Meter for Temperatures up to 315°C (ITI, Inc)

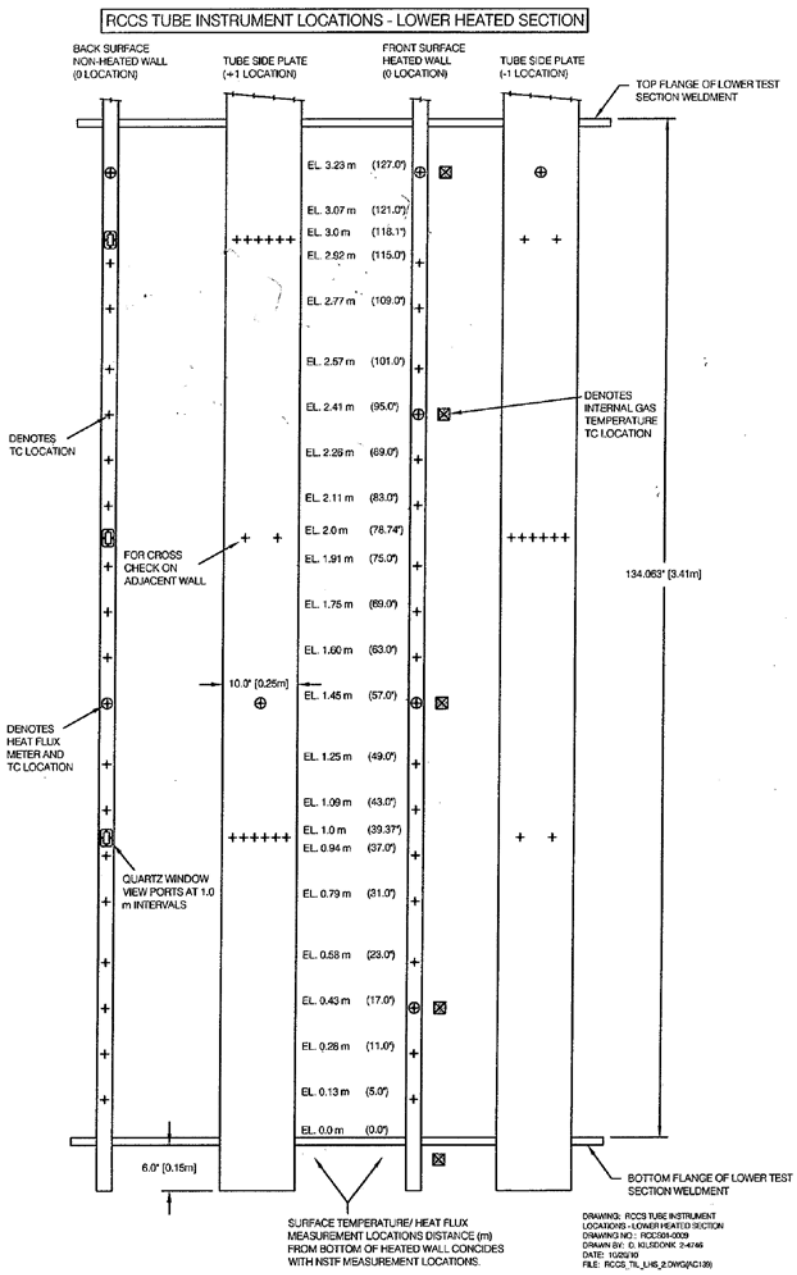

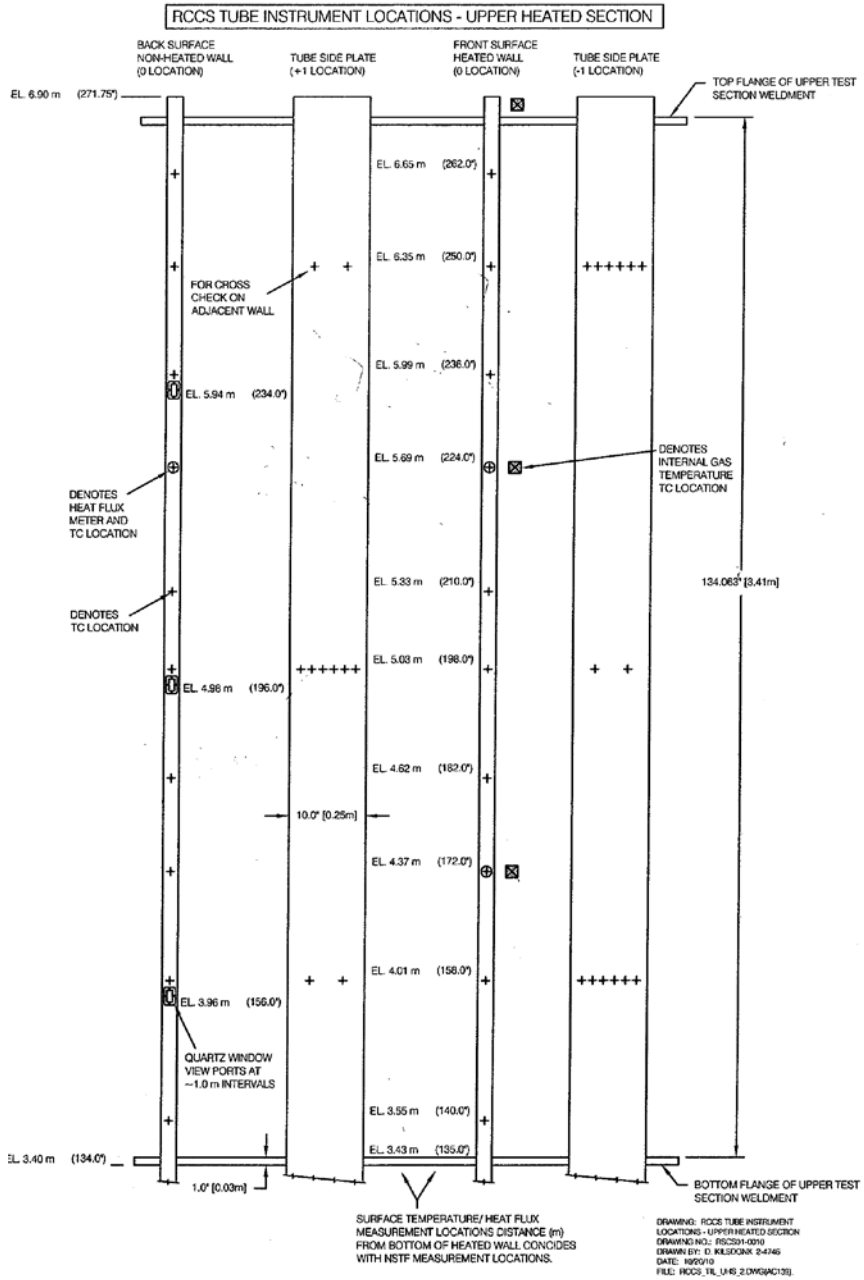

Figure 4.10. Tube Instrumentation Detail

4.5 Meteorological Data

Ambient conditions can have a significant effect on RCCS performance and so it is necessary to monitor conditions outdoors near the stack outlet. A weather station will be used for this purpose, providing barometric pressure, temperature, humidity, wind speed, and wind direction. All measurements except wind direction will be NIST traceable. The weather station will be mounted on the roof of the building and linked to the main data acquisition system via wireless transmissions.

4.6. Data Acquisition and Control

All data acquisition and process control tasks will be managed by a PC executing LabVIEW under a Windows operating environment. The computer is linked to an SCXI chassis (National Instruments) that holds modules for signal conditioning, analogue to digital conversion, and switching. The chassis holds a 16-bit analogue to digital converter (ADC) with a maximum sampling rate of 200 kS/s and ability to multiplex up to 352 input channels. The unit has an input signal range of ±10 V. The ADC module controls the signal conditioning and switching modules within the chassis. The chassis will be located near the test section to minimize the length of instrument cabling and control signal noise. A USB port on the ADC module provides a digital link between the chassis and the computer within the control room. Figure 4.11 provides a schematic of the layout for the data acquisition hardware. Instrument output signals are connected to one of ten SCXI-1102C signal conditioning modules. Each module has 32 input channels and provides cold-junction compensation for thermocouples. Each channel has a programmable gain amplifier and low-pass filter with a cutoff frequency of 10 kHz. For 4 to 20 mA signals, load resistors across the terminal block inputs are used to convert the current output to a voltage signal for the ADC. The input signal range for the SCXI-1102C is ±10 V. These modules are used for signal outputs from flow meters, pressure transmitters, heat flux meters, and emissivity sensors.

A selected number of electrical devices will be controlled from the console using relay switches operated by LabVIEW. The relay modules have 16 SPDT electromechanical relays that can switch up to 2 A at 250 VAC. They are controlled by clicking on switches located on the LabVIEW process diagram. The relays are latched so they maintain their state when the SCXI chassis is switched off or if there is loss of power in the control room. This system is used to control fan motors and the positions of valves on the stack bypass lines.

References

4.1 S. Lomperski, W. D. Pointer, C. P. Tzanos, T. Y. C. Wei, C. M. Crooks, and O. A. Rodriguez, “RCCS Studies and NSTF Preparation Air-Cooled Option,” ANL-GenIV-142, Sept 30. 2010.

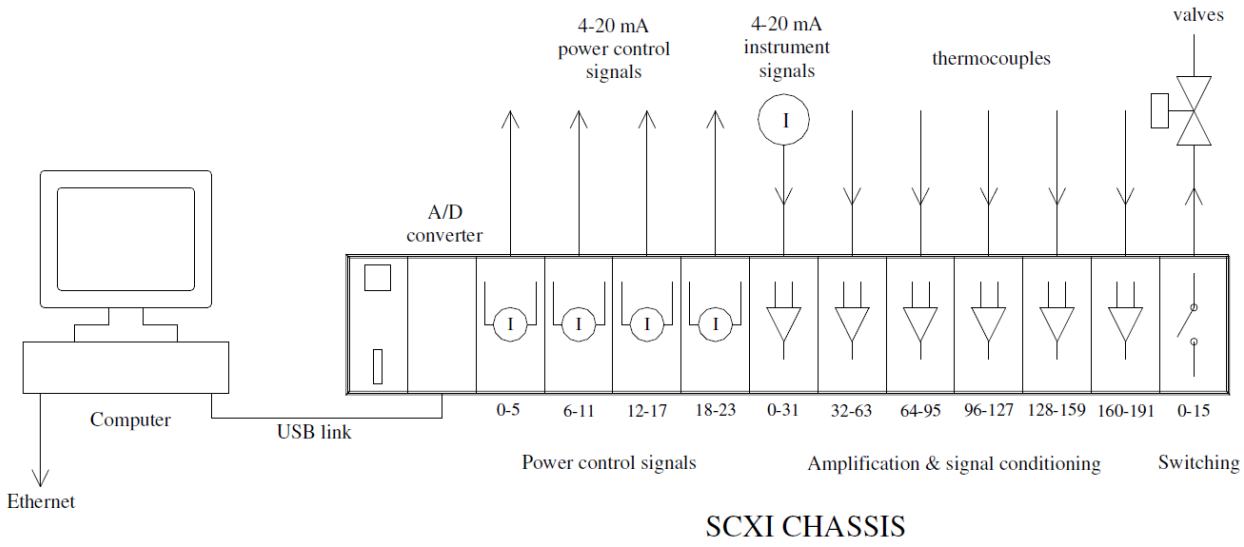

Figure 4.11. Data Acquisition and Control Systems

*Division
Argonne National Laboratory
9700 South Cass Avenue, Bldg. 208
Argonne, IL 60439

www.anl.gov

Argonne National Laboratory is a U.S. Department of Energy
laboratory managed by UChicago Argonne, LLC